ABSTRACT

Title of dissertation: A RING WITH A SPIN: SUPERFLUIDITY
IN A TOROIDAL BOSE-EINSTEIN
CONDENSATE

Anand Krishnan Ramanathan, Doctor of Philosophy, 2011

Dissertation directed by: Steve Rolston
Chemical Physics Program

Superfluidity is a remarkable phenomenon. Superfluidity was initially characterized by flow without friction, first seen in liquid helium in 1938, and has been studied extensively since. Superfluidity is believed to be related to, but not identical to Bose-Einstein condensation, a statistical mechanical phenomena predicted by Albert Einstein in 1924 based on the statistics of Satyendra Nath Bose, where bosonic atoms make a phase transition to form a Bose-Einstein condensate (BEC), a gas which has macroscopic occupation of a single quantum state.

Developments in laser cooling of neutral atoms and the subsequent realization of Bose-Einstein condensates in ultracold gases have opened a new window into the study of superfluidity and its relation to Bose-Einstein condensation. In our atomic sodium BEC experiment, we studied superfluidity and dissipationless flow in an all-optical toroidal trap, constructed using the combination of a horizontal “sheet”-like beam and vertical “ring”-like beam, which, like a circuit loop, allows flow around the ring. On inducing a single quantum of circulation in the condensate, the smoothness and uniformity of the toroidal BEC enabled the sustaining of a persistent current lasting 40 seconds, limited by the lifetime of the BEC due to background gas pressure. This success set the stage for further experiments studying superfluidity.

In a first set of experiments, we studied the stability of the persistent current by inserting a barrier in the flow path of the ring. The superflow stopped abruptly at a barrier strength such that the local flow velocity at the barrier exceeded a critical velocity, which supported decay via the creation of a vortex-antivortex pair. Our precise control in inducing and arresting superflow in the BEC is a first step toward studying other aspects of superfluidity, such as the effect of temperature and dimensionality.

This thesis discusses these experiments and also details partial-transfer absorption imaging, an imaging technique developed in the course of this work.

A Ring with a Spin : Superfluidity in a toroidal Bose-Einstein condensate

by

Anand Krishnan Ramanathan

Dissertation submitted to the Faculty of the Graduate School of the
University of Maryland, College Park in partial fulfillment
of the requirements for the degree of
Doctor of Philosophy
2011

Advisory Committee:
Professor Steven Rolston, Chair
Doctor Gretchen Campbell
Professor Kristian Helmerson
Professor Wendell Hill
Professor Christopher Lobb, Deans's Representative
Professor William Phillips

To my Father,

who has been a source of inspiration and strength
throughout my education and my life so far.

Acknowledgments

I owe my gratitude to all the people who have made this thesis possible and because of whom my graduate experience has been one that I will cherish forever. The Laser Cooling and Trapping (LC) Group at NIST has been a fantastic place to work at, and I am indebted for the extremely friendly and helpful atmosphere, and all the people whom I have had a chance to interact with.

First, I would like to thank my advisors Kris Helmerson and Gretchen Campbell. I feel very fortunate to have had the opportunity to interact and to learn from both of them. The support and encouragement shown by Kris was crucial during my first few months at NIST. Kris has always shown the readiness to help right from choosing the right conference to attend to setting things right in the lab. I have admired Kris for his diverse interests, from BEC physics to biophysics, and for the many collaborators he has around the world.

Gretchen, who joined the group in my fourth year, has been immensely helpful during the later part of my PhD, and more than once, has prevented me from making a mistake that would have been detrimental to my career. She has always gone out of the way to make sure that I got the help and advice that I needed. She has been key in checking on the progress of my thesis and setting goals for completion. She has given prompt feedback on anything I have sent her. I've always admired how she has been on top of things, and follows up on even the smallest thing such as a question about Latex, despite her several commitments at NIST and UMD and her new Strontium lab.

Bill Phillips has been the biggest inspiration through my PhD. His enthusiasm for physics has always been infectious, and kept me going when nothing seemed to work int the lab. He has asked some of the best questions, which have stimulated many thought-provoking discussions. Bill started our group's Wednesday meetings, where we met with Chris Lobb and Wendell Hill and others from UMD. Although I've often felt that the discussions in such meetings led to nowhere, they fostered our best collaboration, without which a lot of this work would not have happened. Bill has the amazing ability to reach out to people from different backgrounds, and stimulate a discussion that brings about interesting physics. As a group leader, Bill has also been a role model in many ways. He is always approachable even when his schedule is busy. He takes time to give some carefully thought out advice. He is encouraging of everyone.

I feel very fortunate to have discussed physics with Chris Lobb. I started reading about superconductivity during my third year under his guidance, and enjoyed our discussions on the subject. He always found time to guide me through Tinkham's book, despite his hectic schedule, and was very patient through my slow learning of the subject. The little I learned from that time has gone a long way in giving me a different perspective on the physics we have seen. I have also enjoyed the many discussions I have had with Chris at his office. He has been remarkable in the number of wonderful insights he has come up with. Despite that, he has always been keenly aware of any small contribution by someone else and has been very generous in giving credit for it.

I have also benefited from Wendell Hill and Steve Rolston. Wendell has always kept in touch with what I am doing, and has given me useful advice along the way. Steve has had an open door for discussing physics or my thesis and has provided me invaluable administrative support to ensure that I have had no problems in working at NIST, which is off-campus from UMD.

During my time at NIST, I have had the fortune of working with several extremely talented post-docs, Mikkel Andersen, Changhyun Ryu, Pierre Cladé, Sérgio Muniz and Kevin Wright, who have helped me along the way. Mikkel got me started into the lab, helping me with my initial experiment. Chang helped me greatly in understanding the complicated BEC apparatus. He also shared with me, what he had learned about the field, to try and give me a broader perspective. Pierre got me started on analyzing data, which has stood me good right through my PhD. I cannot forget our discussions on BKT physics, which got me enthusiastic about the physics, and along with that, integrated into the science of the experiment. I am grateful to Pierre and Chang into taking care to see that I had a defined PhD project before they left.

I have worked the longest with Sérgio, and we have been through many battles together. Sérgio is one of the warmest and most helpful people I've known. He has taught me a lot of electronics, and an amazing array of other miscellaneous lab-related things. A lot of my skills as an experimentalist were built with him looking over me.

I probably would not be writing this thesis at this point if not for Kevin. Kevin gave the lab its critical mass, and along with Sérgio, we had an extremely productive year, which brought out the best in all of us. From Kevin, just when I thought I knew everything that was there in the lab, I ever so often learned how something could be done better. I have admired his meticulousness and tidiness in working. His knowledge of optics, and his ability to explain it is phenomenal. I have also learned from him, how to be generous with credit.

Apart from post-docs, our lab had several visitors who helped along the way. Of them, I learned a lot from fellow graduate students Russ Anderson and Martin Zelan, who showed me that a lot could be done even in a short visit. I also had the fortune of working with Vasant Natarajan, whom I had known since my undergraduate days. He has provided excellent mentorship right through, and has played an important role in shaping my career.

There are many other people in the LC Group who have helped me along the way. Most notable is the other sodium BEC lab, with Paul Lett, Lincoln Turner, Yingmei Liu, Jianing Han and Jonathan Wrubel. Rani Kishore of the Tweezer lab has also helped me in many ways. I greatly cherish sharing my office with Brooke Hester (previously Cranswick), who provided great company through the years. She was quick to tell me about any opportunity that could be of use to me, and got me involved with the OSA and other activities at UMD, which broadened my horizon beyond the confines of my research. She always there when I had a bad day or when I was worried about something.

I can never forget the administrative help I have received from Gail Griffin-Ferris and Kim Emswiler. They have been extremely prompt with any thing that I requested for or any help that I needed. Gail has, more than once, gone out of her way to cover up for my being late on a poster printing form or a purchase order.

The daily good mornings passing by their office have brightened up my days at the LC group.

At NIST, there have been other wonderful people I have had the opportunity to interact with, most notably Charles Clark and Ludwig Mathey. Charles was instrumental in my coming to NIST, and has helped me throughout my PhD. The discussions I have had with Ludwig have been fascinating, with his remarkable ability to bridge the gap between theorists and experimentalists.

At UMD, Mike Coplan has been a mentor right through my PhD. As program director of the Chemical Physics program, he has always kept in touch with me, and been there to provide guidance in the PhD process when I have been completely lost. I am also indebted to Debbie Jenkins, who has handled the administrative side flawlessly through everything, from my Chemical Physics office space to my qualifier exam to my PhD defense date. Paulina Rirksopa of Physics was always there for help regarding my RA. I can never forget her smiling face.

The PhD process would be a lot duller if not for fellow grad students. I have enjoyed the company of Anzi Hu, Jeremy Clark, Roger Brown, Sam Brewer, Mingdong Li, Kai Li, Suri Vaikuntanathan, Andy Ballard, Baladitya Suri, Sandeep Somani, Debjani Roy, Abigail Perry and a lot of the other JQI grad students.

Some people are placed in the right place and the right time. My short association with Sameer Rahatekar came when I most needed it, and thanks to his help, I was able to navigate through a crisis in my PhD. Sukumar Rajauria, who joined NIST during my fourth year, has guided me through the later part of my PhD. I have gone to him several times when I was unable to figure out what a PhD meant or what was expected of me. He has always been clear-sighted through all this and has been someone whose advice I could blindly trust when I was most confused.

Lastly, my family has been extremely supportive through my PhD. My wife, Shilpa Viswanathan, has stood by me despite all the delays in the completion of my PhD, and all the mistakes that I made. She has helped me through my frustrations in writing proposals and seeing them being rejected, until something finally came through. She always took care to do what was best for my dissertation, even if it meant us spending less time together. I can't thank her enough for all that she has done.

I am indebted to my parents for all that they have done for me. My father, R K Ramanathan, has kept a watchful eye on my PhD, often without my realizing it. He has been far-sighted in so many things, and has taught me to look at the bigger picture, and not be fooled by what I see around me. At all the critical junctures, when I have felt my worst, he has been the pillar of strength to help me get through. He has done his best, despite being more than 10,000 km away, in making sure that despite the many bumps, my PhD went in the right direction, and to him I dedicate my thesis.

It is impossible to remember all, and I apologize to those I've inadvertently left out.

Table of Contents

List of Tables

List of Figures

List of Abbreviations and important Symbols

BEC	Bose-Einstein Condensate
BKT	Berezinskii-Kosterlitz-Thouless
GL	Ginzburg-Landau
JQI	Joint Quantum Institute
MOT	Magneto-Optical Trap
NIST	National Institute of Standards and Technology
LG	Laguerre-Gaussian
OD	Optical Depth
PCI	Phase-Contrast Imaging
PTAI	Partial-Transfer Absorption Imaging
rf	radio frequency
SQUID	Superconducting QUantum Interference Device
S/N	Signal-to-Noise ratio
TF	Thomas-Fermi
TOF	time-of-flight
TOP	Time-averaged Orbiting Potential
UMD	University of Maryland

a	s-wave scattering length of a Bose gas
β	optical depth
c	speed of sound in BEC/superfluid or speed of light
E	Energy or electric field
ϕ	phase of a wave or wavefunction
g	interaction constant, $4\pi\hbar^2 a/m$
Γ	natural linewidth of a transition
Δ	detuning of a laser beam from an atomic transition in Hz
$\tilde{\Delta}$	Δ normalized by $\Gamma/2$
h	Planck's constant 6.63×10^{-34} Js
$\hbar$	$h/2\pi$
I	light intensity
I_{sat}	saturation intensity for an optical transition
k	wave vector of light or matter wave
k_B	Boltzmann's constant 1.38×10^{-23} J/K
log	natural logarithm (base e, not 10)
m	mass of bosonic atom
μ	mean field
μ_0	chemical potential
n_{3D}	3D density of a BEC
p	momentum
σ	scattering cross-section
v	velocity
V	trapping potential
Ω	Rabi frequency

Chapter 1

Introduction

The theory of quantum mechanics, which developed in the early 20^{th} century, brought in several new concepts that changed physics. Several new fields in physics, such as atomic physics, nuclear physics, low-temperature physics and quantum electrodynamics were all born during that time. Quantum mechanics has been successfully applied to nearly every field of physics, and is an integral part of a physicist's education today. On the practical side, quantum mechanics has contributed to many technological advances such as the transistor, the laser, nuclear power and MRI machines.

The liquefaction of helium at 4 K by Kamerlingh Onnes at the University of Leiden led to the field of low-temperature physics, which led to the observation of superconductivity and superfluidity. Both phenomena were demonstrated by conceptually simple experiments that could not be explained by any classical theory. They have played a significant role in the development of some of the formalism for quantum mechanics related to condensed matter physics. Nevertheless, even a century later, many experts feel that phenomena like the origins of high temperature superconductivity [1] or the basic nature of superfluidity [2] are still not fully understood. The observation of Bose-Einstein condensates (BECs) in alkali gases in 1995 opened a new window into the study of low-temperature physics. Studying superfluidity in BECs is now an active area of research with interesting possibilities, such as using BECs for navigation as detectors of rotation.

This thesis is primarily about Bose-Einstein condensates and superfluidity. However, since superfluidity and superconductivity are related, I will mention, wherever applicable, superconducting analogies to phenomena seen in Bose condensates.

1.1 Liquid helium and the "old" superfluidity

Prior to the creation of atomic BECs in 1995, superfluidity was associated exclusively with helium. Almost all theory and modeling of superfluids until then was based solely on liquid helium, despite the fact that the strong interaction in liquid helium makes the theory much more complicated. Given that, it is quite remarkable that the theory could not only model liquid helium well, but also be directly applied to BECs. In this section I will discuss the developments in the field of superfluidity in liquid helium.

1.1.a Origins

The concept of superflow, or dissipationless flow, first arose in the context of superconductivity in 1911, when Onnes [3] found that the resistance of solid mercury went to zero below 4 K. While it was known that resistance decreased with temperature, the sudden drop to zero at non-zero temperature was unexpected. It was reasoned that if the resistance of a substance were truly zero, any current set in it would last forever, leading to a concept of a persistent current. Careful experiments in the many decades since, have shown, with increasing precision, that persistent currents can, in principle, last longer than the age of the universe [4, 5].

While superfluidity in liquid helium was not observed until 1938, some important developments in bosonic statistics occurred earlier. In 1924, Satyendranath Bose [6] explained Max Planck's formula for black body radiation based on simple combinatorics. Einstein [7, 8] applied Bose statistics to material particles, and predicted a special condensation to occur at low temperatures. The condensation did not require interactions, and was characterized by a macroscopic occupation of the single-particle ground state. After the development of wave mechanics, the basis of Bose-Einstein statistics could be understood in terms of a wavefunction symmetry under exchange. Although Bose-Einstein condensation itself was not realized until much later, the extensive theoretical work in the first half of the 20th century set up the framework for understanding bosonic particles.

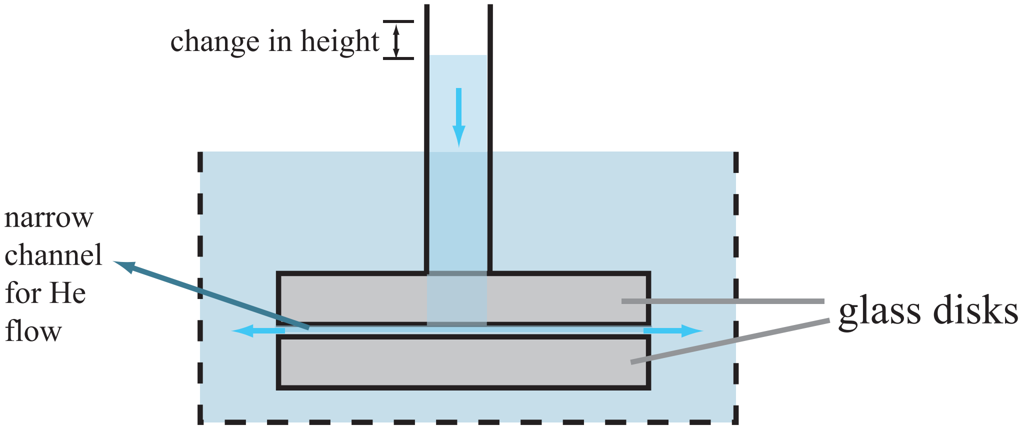

Figure 1.1: Observation of superflow in helium (from Kapitza [9]): By observing the rate of flow of liquid helium from the inner column to the outer reservoir via the narrow gap (about 0.5 micron) between large (3 cm diameter) glass disks, Kapitza found that the viscosity of helium dropped by a factor of at least 1500 as the temperature dropped below the λ-point. The rate of flow was determined by the change in height in the inner column as a function of time.

In the years following the liquefaction of helium in 1908, strange properties of helium below 2.2 K (known as the λ-point) were noted, such as an abrupt change in specific heat and the sudden ability of the liquid to pass through small leaks. In the second issue of the journal Nature in January 1938, two groups showed evidence of superflow in helium II (helium below the λ-point). Kapitza [9] measured the rate of flow of helium through a narrow gap between two large disks (schematic shown in figure 1.1) and found that the viscosity was lower by a factor of at least 1500 below the λ-point. As an analogy to superconductivity, Kapitza termed helium below the λ-point as ‘superfluid’. Simultaneously, Allen and Misener [10] measured the rate of flow of liquid helium through narrow capillaries, and found that the viscosity of helium II was below 10^{-9} Pa s, consistent with the measurements of Kapitza.

In April 1938, London [11] came up with a qualitative explanation for the phenomena of superfluidity, relating it to Bose-Einstein condensation. Since ^{4}He has an even number of protons(2), neutrons(2) and electrons(2), it would come under the class of particles which obey Bose-Einstein statistics. Using a simple ideal gas model for helium (he states *"...model which is so far away from reality..."*), London obtained a transition temperature of 3.09 K, which was reasonably close to the λ-point. Shortly after, Tisza [12] extended London's idea and described the superfluid as having two components, a 'condensed' fraction which is responsible for the zero viscosity and the remaining excited state fraction which can undergo dissipation. Tisza's formalism helped understand superfluidity in a framework based on Bose-Einstein condensation.

1.1.b Landau theory: quantitative description of superfluidity

While London and Tisza had an intuitive and qualitative explanation for superfluidity, there was no quantitative model with experimentally testable predictions until Landau. In a landmark paper, Landau [13] came up a with a quantitative description of superfluidity that introduced several key concepts, which still remain the basis for understanding superfluidity. The theory could explain the transition temperature and flow without viscosity. While Landau rejected Tisza's idea of Bose-Einstein condensation, he nevertheless used a two-fluid model, consisting of a ground state "superfluid" and an excited state "normal" fluid. He clarified that the two-fluid model was only a convenient way of expressing the formalism, and that there were no separate ground state and excited state atoms. The excited state spectrum consisted of phonons (analogous to the lattice excitations in a solid) and rotons[1] (Landau referred to these as the vortex spectrum), and the occupation level of these states depended on the temperature. Landau theory also predicted second sound, which consists of waves where the superfluid and normal fluid oscillate out of phase. Second sound was observed by Peshkov [14].

At this point, it is relevant to point out that a similar formalism was used to describe superconductivity. The Ginzburg-Landau (GL) theory [15] used the concept of a superconducting ground state with an excitation spectrum to treat the problem of superconductivity. Despite the fact that superconductivity and superfluidity

---

[1] See section 2.4 for a brief discussion on rotons. Landau had assumed that rotons came from the vortex spectrum. However, this is not believed to be true anymore.

involved fundamentally different particles (the former involved electrons, which are fermions, and the latter involved bosons), Landau's generalized formalism based on the second-order phase transition was successful in quantitatively describing both phenomena.

While Landau's theory was largely successful in many ways, it still lacked a microscopic explanation. Bogoliubov [16] bridged some of the gap between Landau's model and Bose-Einstein condensation. By considering the case of a weakly interacting BEC, he showed that the excitations needed to be transformed into collective modes. The excitation spectra of these modes had a linear dispersion relation similar to that of the phonon modes. It is unfortunate that helium was the only superfluid available back then. While the Bogoliubov approach was not very popular with helium II, it has been hugely successful with ultracold gas BECs and accurately models the excitation spectrum and dynamics. Still, even in the context of liquid helium, Bogoliubov made the connection between Landau's two-fluid approach to a microscopic theory of Bose-Einstein condensation.

Further research on the connection between helium II and Bose-Einstein condensation [17] made the distinction between the BEC fraction and superfluid fraction. The former refers to the fraction of atoms in a single quantum state. Penrose and Onsager [17] estimated that, at absolute zero, $\approx$ 8% of the atoms were Bose condensed, while according to the Landau theory, at absolute zero, the superfluid fraction should approach unity. Neutron scattering experiments [18] have more or less confirmed the predicted (the $\approx$10%) Bose condensed fraction in nearly zero temperature liquid helium (see Griffin [19] for an extensive discussion).

Before we move on, there is one final point of Landau's theory relevant to our experiment. The theory predicts the existence of a critical velocity that depends on the energy-momentum dispersion of the low energy excitations, above which superfluid flow can dissipate into other excitations. However, experiments of that time showed that superfluid critical velocity was about 2 orders of magnitude less than what one would expect from the superfluid phonon and roton excitation spectrum [20]. The discrepancy was explained later in terms of quantized vortices, which could also contribute to dissipation. Nevertheless, the Landau theory set the framework for understanding superfluidity, upon which further developments could take place.

1.1.c Rotation and vortices in helium II

Landau stated that the superfluid fraction was irrotational ($\nabla \times \mathbf{v} = 0$, where $\mathbf{v}$ is the velocity field), and that only the normal component would move if helium II were placed in a rotating vessel. However, experiments at the time indicated that the superfluid was not irrotational [21, 22]. Onsager [23] and Feynman [24] made an important addition to the superfluid theory, introducing the notion of quantized vortex lines[2] in a superfluid, which could allow the superfluid to rotate. Since the superfluid density is zero at the vortex line, the geometry becomes multiply connected and the irrotationality condition of Landau's theory is not violated. Feynman also suggested that a vortex line closed into itself (vortex-ring) of appropriate size could be the roton excitation of the Landau theory.

Evidence of quantized vortex lines in liquid helium was seen in various ways. Vinen [25, 26] studied the oscillation modes of a fine wire in rotating helium superfluid, and observed a stable single quantum of circulation around the wire. Steyert *et al.* [27] used hydrogen-deuterium mixture "snow flakes" (H-D mixture adjusted to give particles of the same density as He) to track the rotation of helium, and saw evidence of quantized flow. Other experiments [28–30] have studied quantized vortices using charged ions trapped in the vortex core. Of them, Yarmchuk and Packard [30] obtained a lattice pattern for the arrangement of quantized vortices that matched theoretical predictions.

Another consequence of quantized vortex lines [24] is a modification of the superfluid excited state spectrum, particularly in finite geometries. For flow in a cylindrical channel, dissipation occurs at lower flow velocities via a vortex-ring

---

[2] While the standard definition of a vortex line is something that is straight with circulation around it, vortex lines may be curved. Vortex lines can either end at the superfluid boundary or can close upon themselves.

mechanism rather than by phonon or roton mechanisms. The reduced critical velocity is referred to as the Feynman critical velocity (see Wagner [31] or Varoquaux [32]). Evidence of quantized vortex-ring dissipation events has been observed in flow of helium II through a channel [33–35]. The critical flow velocities for such experiments were found to be consistent with estimates of the Feynman critical velocity [32].

At this point, I need to emphasize that this introduction covers only a tiny fraction of the literature on superfluid helium. There have been a lot of studies on various other aspects, such as the specific heat of helium II (discussed by Landau [13]), superfluidity in ^{3}He [36, 37], the third sound [38], helium gyroscopes [39, 40], etc., which are beyond the scope of this thesis. We will now turn to the more recent history of superfluidity in atomic Bose gases.

1.2 Ultracold gases and superfluidity

Advances in laser cooling of atoms in the 1980s opened up the field of ultracold gases and led to the observation of Bose-Einstein condensation in alkali gases [41–43] in 1995. Atomic Bose-Einstein condensates (BECs) are very different from liquid helium, typically involving 10^6 atoms or less, which amounts to $\sim 10^{-17}$ grams of atoms (densities $< 10^{20}$ atoms/m^{-3}), compared to the $\gtrsim 10^0$ grams (density $\approx 10^{28}$ atoms/m^{-3}) for liquid helium. Ultracold gases also have weak interactions compared to the case of liquid helium, which has made observing Bose-Einstein condensation relatively easier. Some of the aspects of superfluidity such as quantized vortices have been clearly observed [44–47], but others such as dissipationless flow are more involved. Ironically, some of the first experiments showing superfluidity in liquid helium [9, 10] are nearly impossible to replicate in ultracold gases owing to constraints of the system. However, it is still possible to observe dissipationless flow in a BEC, which is an important part of this thesis.

There are several advantages to using ultracold gases for studying superfluidity, compared to the superfluid helium experiments.

- Pure ground state : The ability to attain a nearly pure BEC enables one to reach the ground state of the system with almost no thermal excitations or quantum depletion. This allows a better study of the condensed phase, with thermal excitations being introduced as and when needed.

- Arbitrary, dynamic potentials : With cold atoms, one can create almost arbitrary potentials with light fields and magnetic gradients. This is particularly advantageous when trying to produce strong confinement for atoms. One can also create time varying potentials, both adiabatic and sudden, and so can conveniently switch between one potential and another.

- Direct imaging : Exploiting the strong interaction of ultracold gases with light, one can directly image the atom density. In addition, one can make interferometric measurements to obtain the coherence length and phase.

- Simpler system : Atomic BECs have low densities and atom-atom interactions can be completely determined by the s-wave scattering length, in contrast with helium, where both the attractive van der Waal's interactions and the short range repulsion play a role. Hence, one can more exactly model atomic BECs from first principles.

Atomic BECs are typically held in traps having dimensions of around 100 μm. Creating flow in such a system is not easy, and observing superflow even more tricky. A first step in that direction is to look for vortices. While experiments at JILA [44] were the first to create a vortex in a BEC, experiments at ENS, Paris [45, 46] were the first to observe the hydrodynamic nature of superfluidity, which was done by stirring a BEC with a focused laser beam. For low stirring speeds, there were no excitations seen. As the speed was increased, vortices began to appear.

The experiments tell us two things. First, the appearance of vortices in these experiments indicates hydrodynamic behavior as one would expect for a fluid (as opposed to a gas) and evidence of quantized vortices, which is an indication of superfluidity. Second, the lack of excitations at low speeds for the Paris experiment

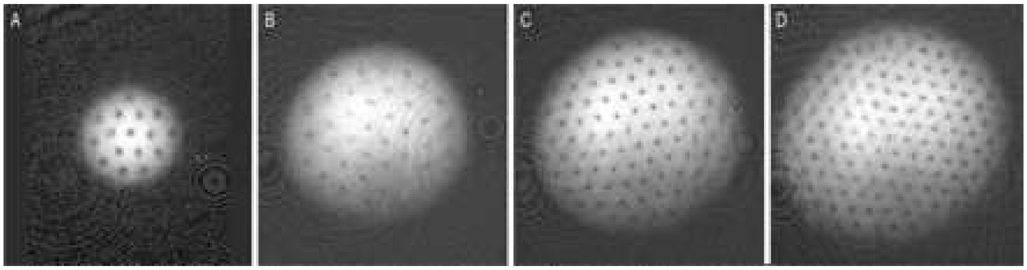

Figure 1.2: Observation of vortex lattices (from Abo-Shaeer *et al.* [47]): The figure show density distributions of an image of a circular cloud. The density holes in the cloud are vortices. The images show a BEC with approximately (A) 16, (B) 32, (C) 80, and (D) 130 vortices. The triangular lattice pattern minimizes the energy of the rotating superfluid.

is an indication of superflow, where there is dissipationless flow in the BEC around the laser beam.

In further experiments in stirring a BEC, Abo-Shaeer *et al.* [47] observed the formation of a stable vortex lattice (see figure 1.2). These experiments made the connection between angular momentum in a BEC to magnetic field in a type-II superconductor. When the magnetic field exceeds a certain critical value, the magnetic flux penetrates through singly quantized lines of flux with non-superconducting cores. Analogously, in a BEC, the rotation penetrates through quantized vortices of rotation flux, which have cores where the BEC density goes to zero.

There have been other experiments indirectly looking for superflow by studying the effect of dragging an object (a focused laser beam, which serves as a repulsive potential) through a BEC [48–51]. In all these experiments, there was an onset of excitations only when the speed of the moving object crossed a certain threshold, indicating dissipationless flow for low speeds. This was taken further in experiments observing persistent currents. Ryu *et al.* [52] observed stable persistent flow in a multiply connected BEC. The flow was found to persist without decay for up to 10 s, limited only by experimental factors such as disortion of the trap geometry due to relative drift between trapping fields, and the BEC lifetime in the trap. Since there was only one quantum of flow, any dissipation would lead to a complete loss of circulation. While 10 seconds of dissipationless flow may seem a short time for something that is supposed to be persistent, it needs to be seen in context of the timescales on which BEC dynamics (based on the kinetic and interaction energies) occur, which are of the order of tens of milliseconds. This experiment makes the connection back to the original superfluidity experiments of Kapitza [9] and Allen and Misener [10].

Having realized persistent flow, the question may arise: What is left to study in superfluidity of atomic BECs besides pushing the flow lifetime to longer timescales?

While superfluidity may have been observed in BECs, there are still several unanswered questions. The observed critical velocities for the breakdown of superflow have been found to be lower than simple predictions. The mechanisms for decay have not been fully understood. The role of temperature in the decay of superflow has not been fully explored.

The relation of the dimensionality of the cloud to superfluidity opens several questions. While a three-dimensional (3D) Bose gas is expected to Bose condense with the BEC being superfluid, a two-dimensional (2D) Bose gas is expected to undergo a superfluid transition (but not BEC). Is it possible to observe superfluidity in a 2D Bose gas? In the case of a highly anisotropic trap, will reduced dimensional effects play a role? What kind of transition will a quasi-2D Bose gas undergo?

Several of these questions boil down to a single fundamental question. What is the relation between Bose-Einstein condensation and superfluidity? Both phenomena involve Bose gases at low temperatures. However, superfluidity requires interaction, while BEC does not [7, 8]. While theoretical frameworks, such as the Bogoliubov formulation [16] do bridge some of the gap, it is nevertheless important for experiments to validate the theoretical predictions, and to probe interesting dimensional cross-overs which are not easily understood by theory.

As an extension, there is also a need to better understand the connection between bosonic superfluidity (and BECs) and superconductivity. Superconductors have been used in several practical applications. Principles of superconductivity are used in making SQUIDs for sensitive detection of magnetic fields. Since magnetic field in a superconductor is analogous to rotation in a BEC, building an analogous device using a BEC could make sensitive measurements of angular velocity. Hence, while superconductors may be fundamentally different from BECs, it is important to make connections wherever possible.

1.3 In this thesis

In this thesis, I will present my research work at NIST. The work was done working with other researchers at NIST, Gaithersburg, during the period 2006 to 2010. In a first set of experiments [53], we studied the 2D superfluid transition in a sheet-like trap, which I will only briefly talk about. In a second set of experiments, we studied the breakdown of superflow [54] in a toroidal trap. During this time, we developed a new imaging technique [55] and an extensive set of tools for creating and manipulating a BEC in a toroidal trap.

In chapter 2, I will give an introduction to the theory of BECs and superfluidity. Chapter 3 gives an overview of the experimental setup and introduces the concepts of atomic physics that are crucial for the creation and manipulation of BECs. Chapter 4 deals with partial transfer absorption imaging, the new technique developed to image optically thick clouds, largely based on Ramanathan *et al.* [55]. In chapters 5 and 6, I will go over details about the ring trap, and persistent currents respectively. In chapter 7, I will discuss our experiments studying the breakdown of superflow, before concluding in chapter 8.

Chapter 2

Theory of superfluidity and Bose-Einstein condensates

Historically, the study Bose-Einstein condensation was ruled by liquid helium, and was understood in terms of the Landau two-fluid model (see Landau and Lifshitz [56], Daunt and Smith [57], Khalatnikov [58] or Tilley and Tilley [59] for example). However, with the advent of atomic Bose-Einstein condensates (BECs), the phenomenon is now understood in terms of the weakly interacting Bose gas model, using the formalism first developed by Bogoliubov [16]. Since the formalism has a microscopic basis, derived by adding a perturbation to the non-interacting Bose gas, it is more useful as a starting point for understanding superfluidity in BECs than the original Landau theory. Nevertheless, it is important to remember that a lot of the theory for superfluidity and BECs, such as coherence, excitations, vortices and the critical velocity had been developed prior to atomic BECs, despite the fact that liquid helium was the only available superfluid. For a more complete review on superfluidity in liquid helium, see Khalatnikov [58] or Tilley and Tilley [59].

In this chapter, I will introduce the concepts of Bose-Einstein condensation and superfluidity relevant to this thesis, starting from the ideal Bose gas, and then moving to the weakly interacting gas. I will discuss the excitations of a BEC, rotation and the critical velocity of flow. The approach used is similar to that of Pitaevskii and Stringari [60].

2.1 Bose-Einstein condensation in an ideal Bose gas

Before jumping to Bose statistics, we first review the familiar expression for the occupancy of an energy level, ε of a classical gas, given by the Maxwell-Boltzmann statistics:

$$n(\varepsilon) = \exp\left(\frac{\mu - \varepsilon}{k_B T}\right), \tag{2.1}$$

where μ is the chemical potential, k_B is the Boltzmann constant and T is the temperature. At a given chemical potential and temperature, states at lower energies tend to have higher occupancies than states at higher energies. Looking at equation (2.1), we see that on raising the chemical potential, the occupancy of all states increase. On lowering the temperature, the occupancy of high energy states sharply decreases. This characterizes the general description of Maxwell-Boltzmann statistics. The reader should note that in practice (for example, in 3D space), the density of states at higher energies is larger, which leads to a peak in the density distribution at a non-zero energy ($\propto k_B T$ for a 3D gas with only translation energy).

For bosons, the indistinguishability of particles has to be factored in when obtaining the occupancy of a given energy level. The effect of indistinguishability has been explained in Cornell *et al.* [61] and illustrated beautifully by Stamper-Kurn [62]. At low occupancies (equivalently low phase-space density), where the probability of two particles being in the same state is nearly zero, the indistinguishability plays little role and one can assume Maxwell-Boltzmann statistics for the system. However, at higher occupancies (which tend to occur at low temperatures and high density), one needs to account for Bose-Einstein statistics, which leads to (see Pitaevskii and Stringari [60] for a derivation):

$$n(\varepsilon) = \frac{1}{\exp\left(\frac{\varepsilon-\mu}{k_B T}\right) - 1}. \tag{2.2}$$

As one can see, at a low chemical potential (for a given temperature) such that $\frac{\varepsilon-\mu}{k_B T} \gtrsim 4$ ($e^{\frac{\varepsilon-\mu}{k_B T}} \gtrsim 50$), equation (2.2) can be approximated by equation (2.1), which corresponds to the case of low occupancy. The expression is valid for an ideal Bose gas only when $\mu < \varepsilon_{\min}$, or equivalently when the chemical potential is less than the ground state energy. As the chemical potential approaches the ground state energy ($\mu \to \varepsilon_{\min}$), the occupancy of the ground state, $n(\varepsilon_{\min})$ becomes large, which corresponds to a macroscopic occupation of the ground-state.

For a derivation of Bose-Einstein condensation, one needs to include the density of states, $\rho_\varepsilon(\varepsilon)$. The density of states determines the scaling of the number of particles (or density of particles in space) with μ. Although the effects of indistinguishability do play a role at low temperatures (and μ approaching $\varepsilon_{\min}$), those effects may or may not translate to Bose-Einstein condition, depending on $\rho_\varepsilon(\varepsilon)$. A full discussion of this can be found in several standard textbooks (Pitaevskii and Stringari [60] for example). For this chapter, it suffices to say that for a gas in free space (homogeneous infinite system), only in 3D (or higher dimensions), Bose-Einstein condensation occurs at non-zero temperatures.

To obtain the conditions for Bose-Einstein condensation, one can take a semi-classical approach (see Dalfovo *et al.* [63]) and look at the 3D phase-space density $\rho\lambda_T^3$, where $\rho = N/V$ is the spatial density (number of particles divided by the volume of the sample) and $\lambda_T = \sqrt{2\pi\hbar^2/mk_BT}$ is the thermal de Broglie wavelength, which defines a characteristic length scale. When $\rho\lambda_T^3 \ll 1$, the phase-space density is low and the gas behaves like a classical gas. When $\rho\lambda_T^3 \gtrsim 1$ [1], Bose-Einstein condensation occurs. This can be seen as the overlap of de Broglie waves of different particles to form a macroscopic wave. For Bose-Einstein condensation, the critical density as a function of temperature, from the expression of phase-space density, is

$$\rho \sim \left(\frac{mk_BT}{2\pi\hbar^2}\right)^{3/2}. \tag{2.3}$$

In practice, rather than ρ, it is easier to measure N, the total number of atoms, which can be directly measured by absorption or other imaging techniques. One can express the equation (2.3) in terms of the number of atoms to obtain the transition temperature at which atoms are expected to Bose condense [64]. For a 3D (harmonically) trapped Bose gas, the critical number is given by,

$$N_c \sim \left(\frac{k_BT}{\hbar\omega_0}\right)^3, \tag{2.4}$$

where ω_0 is the harmonic oscillator frequency of the trap (assuming it to be isotropic in 3D). As can be seen in equations (2.3) and (2.4), for a non-interacting Bose gas, the critical number of atoms (or density) for Bose-Einstein condensation has a direct relationship with the temperature. As the temperature increases, the critical number also increases.

---

[1] The exact value is a number that can obtained by a rigorous calculation involving the zeta function integral [56].

The non-interacting ideal Bose gas model is very useful to illustrate the Bose-Einstein condensation process, obtain the temperature-number relation and estimate the transition temperature. However, it does not account for superfluidity and so has limited value. For the interested reader, there are several sources which contain a more detailed and rigorous derivation of the above relations (Dalfovo *et al.* [63], Pitaevskii and Stringari [60], Pethick and Smith [65]).

While in theory a Bose condensate can be obtained at any temperature, there are some obvious practical considerations. For example, consider a room temperature gas of sodium, which is bosonic: The critical density for Bose condensation is $\rho_c \approx 10^{32}$ atoms/ m^3 $= 10^6$ kg/m^3, which is 3 orders of magnitude denser than sodium metal. Apart from the fact that such densities are impossible to attain at room temperature, a gas under such conditions would be solid. To get away from the problem of liquefaction or solidification, one needs to work with gases at low densities[2]. In our sodium BEC experiment, we work at temperatures around 40 nK, and densities of $\rho \sim 10^{19}$ atoms/m^3 $> \rho_c \sim 10^{17}$ atoms/m^3. In terms of atom numbers, we obtain $N \sim 10^5 > N_c \sim 100$ (using $\omega_0 \approx 70$ Hz).

2.2 The weakly interacting Bose gas

The previous section described an ideal non-interacting Bose gas. Just to reiterate, Bose-Einstein condensation occurs as a consequence of indistinguishability and Bose-Einstein statistics, and occurs even in the case of a non-interacting gas. We will now deal with the practical case of an interacting Bose gas.

Taking the general situation, interaction in gases can cause a variety of effects, such as condensation to liquids or solids or forming molecules. However, with ultracold gases, we work at low densities and ultra-high vacuum. From an experimental point of view, such conditions prevent any of those processes from taking place and

---

[2] In fact, even at BEC temperatures, the equilibrium state of sodium, or any other Bose gases is solid. The BEC is a metastable state. The low densities which we work with make the time constant for forming molecules much longer than experimental timescales and hence the Bose condensate behaves as an equilibrium state [61].

allow atoms to be cooled to the nanokelvin BEC temperatures. From a theoretical point of view, such conditions greatly simplify the picture and allow us to characterize the interaction of the cloud based on the atom-atom low-energy scattering. The experimental setup and techniques to reach condensation are discussed in chapter 3. We will now talk about the treatment of interactions.

2.2.a Atom-atom interactions

Ultracold gas experiments are typically performed under ultra-high vacuum (10^{-14} atm for background gas), to ensure minimal collisions and consequently heating from background gas. For the atomic species under considerations, we work at low densities, 5-10 orders of magnitude below a gas at STP (Standard Temperature and Pressure: 20 Celsius, 1 atmosphere). Under such conditions, simultaneous interaction between three or more atoms can be safely neglected, and the formation of molecules is unlikely. This leaves us with just the two-body interaction. The two-body interaction is normally characterized by the van der Waals potential (see Pethick and Smith [65] for a detailed description of how the potential plays a role), the long-range attraction that arises from the (induced) electric dipole-dipole interaction, and the strong repulsive core due to the repulsion from the overlap of the electron clouds. However, given the low temperature of the sample, we can make a further simplifying assumption. Atoms scatter at low momenta $\hbar k$ (k is the magnitude of the wave-vector of the atom-atom scattering wavefunction), such that the kinetic energy is much below the angular momentum barrier of p-wave (scattering process that has one unit of angular momentum, $l = 1$) and higher modes ($l > 1$):

$$\frac{\hbar^2 k^2}{2m} \ll \frac{\hbar^2}{2mr_0^2} \quad \Leftrightarrow \quad k \ll \frac{1}{r_0}, \tag{2.5}$$

where m is the mass of the atom, and r_0 is the range of the potential. For any scattering process that has $l \geq 1$, the interacting atoms do not get within the range of the inter-atomic potential. To give an estimate of a typical scenario, for sodium atoms at a temperature T=10 μK, $\hbar^2 k^2/2m \sim k_B T \approx 10^{-5} \times \hbar^2/2mr_0^2$ ($r_0 < 1$ nm, or twenty Bohr radii [65]), and hence the interaction can be characterized by the s-wave scattering length, which arises from the $l = 0$ scattering process.

For atom-atom collision processes, it is impossible from theory alone to evaluate scattering properties of cold atoms because the atom-atom interaction potentials cannot be calculated with sufficient accuracy [65]. However, using photoassociation spectroscopy and the study of Feshbach resonances (see Weiner *et al.* [66]), information about the interaction potentials can be obtained, which could then be used to characterize the scattering process and make further experimental predictions. Hence, the scattering process is determined, based on experiments.

In an elastic scattering process, there is an incoming wave and an outgoing wave (both with wave vector magnitude k). The phase-shift of the outgoing wave with respect to the incoming wave determines the strength of the scattering process. The phase-shift, δ_0, in the long wavelenght limit of k, $k \rightarrow 0$, can be expressed as $\delta_0 = -ka$, where a is the scattering length. Consequently, the scattering length can be expressed as

$$a = \left.\frac{\delta_0}{k}\right|_{k\rightarrow 0} . \tag{2.6}$$

Nearly all the properties of low-energy scattering can be obtained from the s-wave scattering length a. As for the nature of the interaction, $a > 0$ implies repulsive interaction, while $a < 0$ implies attractive interaction. The strength of the scattering process is given by the total scattering cross-section, $4\pi a^2$. The scattering cross-section is used in calculating the elastic collision rate, which is important to model evaporative cooling. The scattering length also plays a role in BECs, where the interaction energy term of the hamiltonian is proportional to a.

2.2.b The ground state

The problem of the weakly-interacting Bose gas was first treated by Bogoliubov [16], using a mean-field based approach, where the many-body wavefunction (or field operator) was expressed in terms of a single particle wavefunction basis. In this section and the next, we will discuss the ground state properties of a Bose gas and then solve for the low-excitation spectrum, based on the Bogoliubov theory of a weakly-interacting Bose gas.

In a uniform system, the density is constant in space and it is useful to go into a momentum basis, $\psi(\mathbf{p})$. Such a basis also separates the zero-momentum Bose-condensed ground state from excited states. The normalization condition gives $\int \psi^*(\mathbf{p})\psi(\mathbf{p})d\mathbf{p} = N$, where N is the number of particles. The energy of the system can be written as:

$$\begin{aligned} E = \langle \bar{H} \rangle &= \int \psi^*(\mathbf{p})\frac{p^2}{2m}\psi(\mathbf{p})d\mathbf{p} \\ &+ \frac{1}{2V}\int d\mathbf{p}_1 d\mathbf{p}_2 \psi^*(\mathbf{p}_1)\psi^*(\mathbf{p}_2)\psi(\mathbf{p}_1+\mathbf{q})\psi(\mathbf{p}_2-\mathbf{q})\mathbf{V}_\mathbf{q} d\mathbf{q}, \end{aligned} \tag{2.7}$$

where $\mathbf{p}_1 + \mathbf{q}$, $\mathbf{p}_2 - \mathbf{q}$ are the incoming wave vectors, $\mathbf{p}_1$ and $\mathbf{p}_2$ are the outgoing wave vectors, $\mathbf{V}_\mathbf{q}$ is the scattering angle-dependent time-averaged scattering potential, and V is the volume of the system. As discussed in the previous section, at low temperatures, only the spherically symmetric s-wave scattering plays a role, and $\mathbf{V}_\mathbf{q}$ can be integrated over $\mathbf{q}$ to give $4\pi\hbar^2 a/m$. The energy functional can then be simplified to

$$E = \int \psi^*(\mathbf{p})\frac{\mathbf{p}^2}{2m}\psi(\mathbf{p})d\mathbf{p} + \frac{g}{2V}\int d\mathbf{p}_1 d\mathbf{p}_2 \psi^*(\mathbf{p}_1)\psi^*(\mathbf{p}_2)\psi(\mathbf{p}_1)\psi(\mathbf{p}_2), \tag{2.8}$$

where $g = 4\pi\hbar^2 a/m$. At $T = 0$, all the atoms are in the ground state, $\mathbf{p} = 0$, giving

$$|\psi(\mathbf{p})|^2 = |\psi_0|^2 = N\delta(\mathbf{p}). \tag{2.9}$$

The $\delta(\mathbf{p})$ expresses the fact that for a non-interacting Bose gas, the ground state is the zero momentum state. The ground state energy E_0 is given by,

$$E_0 = \frac{N^2 g}{2V} = \frac{Ng\rho}{2}, \tag{2.10}$$

where $\rho = N/V$. The ground state energy per particle E_0/N is proportional to the particle density and the interaction strength. Using equation (2.10), we can now go ahead and calculate the sound speed, c, which is the speed of propagation of compression waves, for the system. The thermodynamic pressure of the weakly interacting Bose gas can be obtained using

$$P = -\frac{\partial E_0}{\partial V} = \frac{g\rho^2}{2}. \tag{2.11}$$

The compressibility of the system can be expressed as

$$\frac{\partial \rho}{\partial P} = \frac{1}{g\rho}. \tag{2.12}$$

The sound speed is given by the ratio of the square root of the elasticity, $\rho\frac{\partial P}{\partial \rho}$, divided by the (mass) density $m\rho$, giving

$$c = \sqrt{\frac{g\rho}{m}}. \tag{2.13}$$

In taking the square-root, we assume that g, and hence the s-wave scattering length (a) are positive, implying repulsive interaction[3].

2.2.c Low-energy excitation spectrum

The physics of a weakly interacting Bose gas depends strongly on the low-energy excitations. For example, the decay of superflow occurs via the transfer of energy to such excitations. The low-energy excitation spectrum is derived using the Bogoliubov-de Gennes method [67]. While this is generally worked out using the second-quantization operator notation [60], I will write it in terms of the wavefunctions. We begin with writing out the time-dependent Schrödinger equation[4] for the energy functional in equation (2.8), using $i\hbar\partial\psi/\partial t = \delta E/\delta\psi^*$ (see Pitaevskii and Stringari [60] for more details) to get

$$\frac{p^2}{2m}\psi(\mathbf{p}) + g\rho\psi(\mathbf{p}) = i\hbar\frac{\partial\psi(\mathbf{p})}{\partial t}. \tag{2.14}$$

The above equation is valid only when ψ is the order parameter. The order parameter characterizes the macroscopically occupied states. For a degenerate, weakly-interacting Bose gas in thermal equilibrium, the order parameter refers to the ground state wavefunction (for a non-interacting gas, this is identical to the single particle ground state). However, often the superfluid has been perturbed (and hence it is not in thermal equilibrium), in which case the order parameter need not be the ground state.

---

[3] In general, interactions cause an attractive BEC having $a < 0$ to collapse upon itself [63].

[4] If written in a position basis, equation (2.14) would be a variant of the Gross-Pitaevskii equation, which is discussed in section 2.3.

We continue to use the momentum basis (will not explicitly show $\mathbf{p}$ dependence), and set a trial wavefunction, that consists of the ground state ψ_0, with a small additional perturbation ψ' added to it:

$$\psi = \psi_0 + u\psi' + v\psi'^*, \tag{2.15}$$

where u and v are complex numbers. This is known as the Bogoliubov transformation, where ψ'^* is the Hermitian conjugate of ψ'. Expressing ψ_0 explicitly in terms of the condensate number and phase,

$$\psi_0(\mathbf{p}) = \sqrt{N_0\delta(\mathbf{p})}e^{i\phi}, \tag{2.16}$$

we assume that the amplitude, the square-root of the condensate number, is time independent, while the phase, ϕ, can evolve in time. In the formalism we are using, the wavefunctions ψ' and ψ'^* are constant, and all the variation lies in the complex amplitudes u and v. We now substitute ψ into equation (2.14) to obtain

$$\begin{aligned}\frac{p^2}{2m}(\sqrt{N_0\delta(\mathbf{p})}e^{i\phi} + u\psi' + v\psi'^*) &+ g(\sqrt{N_0\delta(\mathbf{p})}e^{i\phi} + u\psi' + v\psi'^*)^2 \\ &\times(\sqrt{N_0\delta(\mathbf{p})}e^{-i\phi} + u^*\psi'^* + v^*\psi') \\ &= i\hbar\frac{\partial}{\partial t}(\sqrt{N_0\delta(\mathbf{p})}e^{i\phi} + u\psi' + v\psi'^*).\end{aligned} \tag{2.17}$$

We now make the assumption that the excitation, ψ' has a definite momentum, p', and correspondingly, ψ'^* has a momentum, $-p'$. The ground state corresponds to a zero momentum eigenstate. Multiplying through, we keep terms to first order in u and v:

$$\begin{aligned}\frac{p'^2}{2m}(u\psi' + v\psi'^*) &+ g\rho_0(\sqrt{N_0\delta(\mathbf{p})}e^{i\phi} + 2u\psi' + 2v\psi'^* + e^{i\phi}u^*\psi'^* + e^{i\phi}v^*\psi') \\ &= i\hbar\frac{\partial}{\partial t}(\sqrt{N_0\delta(\mathbf{p})}e^{i\phi} + u\psi' + v\psi'^*).\end{aligned} \tag{2.18}$$

We can now separate terms containing individual wavefunctions in order to solve for u, v and ϕ:

$$\frac{p'^2}{2m}u\psi' + g\rho_0(2u\psi' + e^{2i\phi}v^*\psi') = i\hbar\frac{\partial u}{\partial t}\psi', \tag{2.19}$$

$$\frac{p'^2}{2m}v\psi'^* + g\rho_0(2v\psi'^* + e^{2i\phi}u^*\psi'^*) = i\hbar\frac{\partial v}{\partial t}\psi'^*, \tag{2.20}$$

$$g\rho_0\sqrt{N_0}e^{i\phi} = i\hbar\sqrt{N_0}\frac{\partial e^{i\phi}}{\partial t}. \tag{2.21}$$

Solving for ϕ from equation (2.21), we obtain

$$\phi = -\frac{g\rho_0 t}{\hbar}. \tag{2.22}$$

We now multiply $e^{-i\phi}$ through equations (2.19) and (2.20) and substitute, $u = u'e^{i\phi}$ and $v = v'e^{i\phi}$ to obtain the matrix differential equation

$$\begin{bmatrix} \frac{p'^2}{2m} + g\rho_0 & -g\rho_0 \\ g\rho_0 & -\frac{p'^2}{2m} - g\rho_0 \end{bmatrix} \begin{bmatrix} u' \\ -v'^* \end{bmatrix} = i\hbar\frac{\partial}{\partial t} \begin{bmatrix} u' \\ -v'^* \end{bmatrix}. \tag{2.23}$$

By taking the complex conjugate of equation (2.20), we have obtained two linear first order differential equations, shown in equation (2.23). The stationary solutions of the excitation (amplitudes of u' and v' are constant in time) are the eigenmodes of the matrix, of the form $\beta_1\psi' + \beta_2\psi'^*$ which have energies corresponding to the eigenvalues of the matrix. The energy of the excitation, $\varepsilon(p')$ from the positive eigenvalue is:

$$\varepsilon(p') = \sqrt{\left(\frac{p'^2}{2m}\right)^2 + \frac{p'^2 g\rho_0}{m}}. \tag{2.24}$$

This is the fundamental expression for Bogoliubov excitation modes, containing the energy-momentum dispersion relation. At low momenta, $p'^2 \ll g\rho_0 m$, the modes resemble a phononic excitation spectrum, which can be expressed in terms of the sound speed

$$\varepsilon(p') = cp'. \tag{2.25}$$

In this derivation, we have assumed a uniform, infinite system, and the excitation spectrum is phononic at low momenta and single particle-like at high momenta ($p'^2 \gg g\rho_0 m$). In a finite and therefore nonuniform system, however, excitations such as vortex rings have a lower energy [24].

As mentioned previously, Landau predicted the decay of superflow to occur when the flow velocity exceeds a critical velocity set by the energy-momentum dispersion of the lowest energy excitations. Given the Bogoliubov energy-momentum relation, shown in equation (2.25), the Landau critical velocity is the speed of sound c (derived in the section 2.4).

2.3 Bose gas in an inhomogeneous system: The GP equation

Until now, we have talked about a Bose condensate in a uniform system. The assumption of uniformity holds better for liquid helium (although the weakly-interacting Bose gas model does not apply), since it is produced in large quantities and is reasonably incompressible. As mentioned previously, in contrast to helium, atomic BECs consist of relatively very few atoms. In addition, they are held at very low temperatures (<1 μK as opposed to ≈ 0.1 K of superfluid helium) and so any heat absorbed from the surroundings would be catastrophic to the sample. For this reason, atomic BECs are held in traps created by electromagnetic fields and are suspended in ultra-high vacuum so that there is no contact with the surroundings. A consequence of such traps is that atomic BECs are always in an inhomogeneous trapping potential.

To model atomic BECs accurately, which due to their diluteness are also much more compressible, we modify equation (2.14) to include a spatially varying trapping potential. Also, we use the wavefunction defined in the position basis. This non-linear Schrödinger equation, known as the Gross-Pitaevskii (GP) [68–70] equation, is given by

$$i\hbar\frac{\partial}{\partial t}\psi(\mathbf{r},t) = \left(-\frac{\hbar^2\nabla^2}{2m} + V(\mathbf{r}) + g|\psi(\mathbf{r},t)|^2\right)\psi(\mathbf{r},t), \tag{2.26}$$

where $\psi(\mathbf{r},t)$ is the order parameter and $V(\mathbf{r})$ is the externally applied potential. The condensate density is given by $\rho(\mathbf{r},t) = |\psi(\mathbf{r},t)|^2$. The stationary solution of the GP equation gives the ground state wavefunction, and its eigenvalue, μ, corresponds to the ground state energy (per particle). μ can also be taken as the chemical potential of the system, which is the energy cost of adding a particle to the BEC. The stationary GP equation is

$$\mu\psi(\mathbf{r}) = \left(-\frac{\hbar^2\nabla^2}{2m} + V(\mathbf{r}) + g|\psi(\mathbf{r})|^2\right)\psi(\mathbf{r}). \tag{2.27}$$

Once the ground state wavefunction and ground state energy are obtained, the low-energy excitations can be perturbatively obtained by the Bogoliubov-de Gennes method, using a trial wavefunction similar to equation (2.15).

While the full GP equation is not easy to solve, there are simple analytic solutions in certain limits. We start by looking at the terms contained in the GP Hamiltonian, namely the kinetic energy, the potential energy and the interaction energy, and consider the cases where one of the terms can be ignored.

The potential energy term is always present, except for when the cloud is released in time-of-flight, and hence cannot be ignored for the trapped cloud.

In the absence of interaction ($g = 0$) and hence zero interaction energy, the GP equation becomes a linear Schrödinger equation, and one can use the single particle solution. For a harmonic confinement potential along one dimension ($V(x) = \frac{1}{2}m\omega^2x^2$, with ω being the oscillator angular frequency), using the single particle ground state, ψ_0 in that dimension is given by (see, for example, Sakurai [71])

$$|\psi_0(x)|^2 \propto \exp\left(-\frac{x^2}{x_0^2}\right), \tag{2.28}$$

where $x_0 = \sqrt{\hbar/m\omega}$ is the harmonic oscillator length (plotted in figure 2.1 (left)). Even for traps that are not perfectly harmonic (have small quartic or higher order terms), the harmonic oscillator approximation can be used. Corrections to the ground state are typically small, and usually do not affect the physics. For a 3D trap in the absence of interaction, one gets solutions of the form of equation (2.28) for all 3 directions. This harmonic oscillator limit solution is valid at low densities, where the mean-field is small compared to the kinetic energy.

In the opposite limit, where the interaction energy is much larger than the kinetic energy, the GP equation is no longer a differential equation and the ground state of the GP equation can be easily solved, given by

$$\begin{aligned} g|\psi_0(\mathbf{r})|^2 &= \mu - V(\mathbf{r}) \quad \text{for } \mu > V(\mathbf{r}) \\ &= 0 \qquad \text{for } \mu < V(\mathbf{r}). \end{aligned} \tag{2.29}$$

This limit is known as the Thomas-Fermi (TF) limit[5]. The TF approximation

---

[5] The Thomas-Fermi limit model, developed shortly after the introduction of the Schrödinger equation, was originally used to model an electron gas (Thomas [72], Fermi [73]) and has been supplanted by density functional theory for electrons.

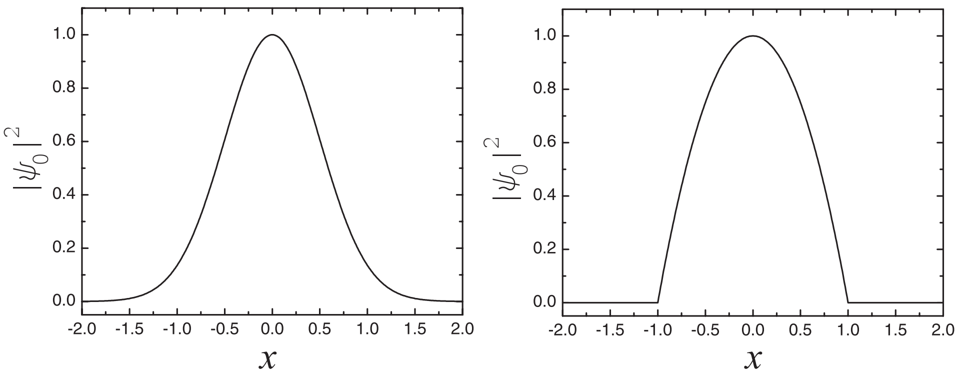

Figure 2.1: Solution to GP equation for a 1D harmonic trap in certain limits : The condensate density $|\psi_0|^2$ is plotted as a function of the position. (left) The harmonic oscillator ground state solution in the absence of interactions shows a Gaussian profile. (right) The Thomas-Fermi solution for strong interactions, where the kinetic energy has been neglected, follows the shape of the trap leading to the profile of an inverted parabola. note: While the figures show the two solutions having the same length scale, this need not be the case.

can be applied when the interaction energy is significantly higher than the ground state kinetic energy, i.e. $g|\psi_0|^2 \gg \frac{\hbar\omega}{4}$.

Applying the TF solution to a 1D harmonic oscillator, we obtain a density profile shaped as an inverted parabola (plotted in figure 2.1 (right)):

$$\begin{aligned} |\psi_0(x)|^2 &\propto \left(1 - \frac{x^2}{x_0^2}\right) \quad \text{for } |x| < x_0 \\ &= 0 \qquad \text{for } |x| > x_0 \end{aligned} \tag{2.30}$$

where $x_0 = \sqrt{2\mu/m\omega^2}$. The TF solution is not valid for a small region (discontinuity of the slope seen in the plot at $x = \pm 1$), where x is close to x_0. However, so long as we are looking at the overall shape and dynamics, and not focusing on that region, the TF approximation works very well.

In this section, we have seen the solutions of the GP equation in both the non-interacting and the TF regimes, for a sample problem, the 1D harmonic oscillator. While such solutions are not complete, they are nevertheless instructive about what physics to expect. We will be discussing the BEC in a ring in chapter 5.

Before we move on, the reader should note that the GP equation is very important in characterizing a BEC. While most of the theory in this chapter has been presented assuming a uniform system so that the physics is more apparent, nearly all the theory from the low-energy excitations to the critical velocities have to be modified suitably for a non-uniform BEC, using the GP equation. We will now move on to other properties of a Bose superfluid, while still using the weakly-interacting Bose gas model to illustrate the physics.

2.4 The Landau critical velocity

In Landau's 1941 paper [13], Landau made the argument that *"... If such a liquid is considered when flowing as a whole along a capillary, it can be easily shown that the interactions between it and the walls of the capillary cannot lead (when the velocity of flow is not too great) to an excitation of internal motion, i.e. to an energy dissipation;"* The Landau critical velocity is based on an energetic argument, which I will derive here.

We consider an excitation which is characterized by a velocity field $\mathbf{v}(\mathbf{r})$, and a number density field $\rho(\mathbf{r})$. The energy of the ($\mathbf{v}(\mathbf{r})$, $\rho(\mathbf{r})$) excitation in an otherwise stationary fluid is (from $\varepsilon = \frac{1}{2}m\mathbf{v}^2$)

$$\varepsilon = m \int d\mathbf{r} \left(\frac{1}{2}\rho(\mathbf{r})\mathbf{v}(\mathbf{r}) \cdot \mathbf{v}(\mathbf{r}) \right), \tag{2.31}$$

where the integral is over the superfluid volume. We now consider the same excitation in a superfluid moving with velocity $\mathbf{v}_s$. By Galilean invariance, the energy of the same excitation with respect to the moving fluid is

$$\varepsilon' = m \int d\mathbf{r} \left(\frac{1}{2}\rho(\mathbf{r})(\mathbf{v}(\mathbf{r}) + \mathbf{v}_s) \cdot (\mathbf{v}(\mathbf{r}) + \mathbf{v}_s) - \frac{1}{2}\rho(\mathbf{r})\mathbf{v}_s \cdot \mathbf{v}_s \right). \tag{2.32}$$

Substituting $\mathbf{p} = m\int \mathbf{dr}\rho(\mathbf{r})\mathbf{v}(\mathbf{r})$, we can express ε' as

$$\varepsilon' = \varepsilon + \mathbf{p} \cdot \mathbf{v}_s. \tag{2.33}$$

In the rest (lab) frame, there is always an energy cost to create the ($\mathbf{v}(\mathbf{r})$, $\rho(\mathbf{r})$) excitation, which is ε. However, in the moving frame, for a velocity $\mathbf{v}_s$, such that,

$$\mathbf{p} \cdot \mathbf{v}_s + \varepsilon < 0,$$

or equivalently, for an appropriately chosen direction for v_s, and

$$v_s > \frac{\varepsilon}{p}, \tag{2.34}$$

it will be energetically favorable to create the excitation. In creating the excitation, energy from the flow is transferred to the excitation, and the flow dissipates. From this, we can deduce that the critical velocity at which superflow breaks down is given by

$$v_c = \min\left\{\frac{\varepsilon}{p}\right\}, \tag{2.35}$$

where the minimum refers to the excitation with the lowest ε/p ratio. Below this critical velocity, it is always energetically unfavorable to create any excitation.

For a phononic excitation spectrum, with a dispersion relation approximated by equation (2.25), the critical velocity is given by the speed of sound,

$$v_c = c. \tag{2.36}$$

In Landau's original paper, he postulated the existence of roton excitations in liquid helium, which modify the critical flow velocity. Landau referred to rotons as the vortex spectrum, and computed the exact energy of rotons on the basis of experimental measurements of specific heat. While the exact nature of rotons are still not fully understood, they are a consequence of the strong inter-particle interaction in liquid helium, and do not play a role in weakly interacting Bose gases. The excitation spectra of atomic Bose gases have been found to agree with Bogoliubov theory (see Dalfovo *et al.* [63]).

2.5 Irrotational flow and quantized vortices

To treat vortices in Bose gas, as with the Bose gas in an inhomogeneous system (section 2.3), we use the wavefunction in spatial coordinates, $\psi(\mathbf{r}) = |\psi(\mathbf{r})|e^{i\phi(\mathbf{r})}$, where the density is given by $\rho(\mathbf{r}) = |\psi(\mathbf{r})|^2$. The flow velocity, $\mathbf{v}_s(\mathbf{r})$ for such a wavefunction is given by

$$\mathbf{v}_s(\mathbf{r})\psi(\mathbf{r}) = -i\frac{\hbar}{m}\nabla\psi(\mathbf{r}). \tag{2.37}$$

If the fluid is uniform, $|\psi(\mathbf{r})| = \text{constant}$, we get

$$\mathbf{v}_s(\mathbf{r}) = \frac{\hbar}{m}\nabla\phi(\mathbf{r}). \tag{2.38}$$

From equation (2.38), we can see that,

$$\nabla \times \mathbf{v}_s(\mathbf{r}) \;\propto\; \nabla \times \nabla\phi(\mathbf{r}) \;=\; 0, \tag{2.39}$$

and hence superfluid flow for a uniform system is irrotational[6]. We now look at the more general case of a simply-connected geometry (see Fig 2.2 (left))[7] and the integral of the flow velocity along a path from $\mathbf{r}_1$ to $\mathbf{r}_2$, using equation (2.37), we obtain

$$\frac{m}{\hbar}\int_{\mathbf{r}_1}^{\mathbf{r}_2} \mathbf{dl}\cdot\mathbf{v}_s(\mathbf{r}) = \phi(\mathbf{r_2}) - \phi(\mathbf{r_1}). \tag{2.40}$$

If the path were closed, $\mathbf{r_1} = \mathbf{r_2}$, the integral goes to zero[8], and hence for a simply connected geometry (see figure 2.2 left),

$$\frac{m}{\hbar}\oint \mathbf{dl}\cdot\mathbf{v}_s = 0, \tag{2.41}$$

which implies that there cannot be any flow along a closed path. This is a larger statement of no rotation than the local irrotational flow condition of equation (2.39). In essence, the single-valuedness of $\phi(\mathbf{r})$ implies that there is no closed loop flow in any simply-connected geometry.

In multiply-connected geometry[9] (where the condition of simply-connected geometry does not hold, see Fig 2.2 (right)), however, if one were to integrate the

---

[6] This is in general true for any superfluid [2], but easier to show for the case of the uniform system.

[7] A simply-connected geometry is defined as a geometry, where given two points $\mathbf{r}_1$ and $\mathbf{r}_2$ connected by a path $\mathbf{l}$ (that stays within the geometry), one can continuously deform the path to obtain all possible paths between $\mathbf{r}_1$ and $\mathbf{r}_2$.

[8] This can also be arrived at by applying Stoke's theorem to equation (2.39 [2].)

[9] Multiply-connected geometry can arise in two ways. The trap or the container itself could be multiply-connected, or, there maybe a vortex in the system which causes a density zero at its core, leading to a multiply-connected geometry. Here, I am using multiply-connected in the general sense.

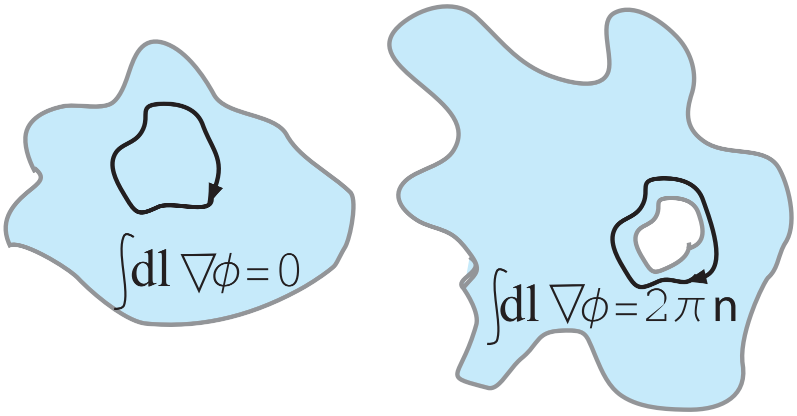

Figure 2.2: In the case of simply-connected geometry (left), the phase winding around any closed path is zero implying no closed loop flow, while in the case of multiply-connected geometry (right), by taking the path shown in the diagram, the phase winding can be any integral multiple of 2π, and there can be closed loop flow.

phase over a path which encloses an area that contains the region of no superfluid (shown in figure 2.2 right), one obtains

$$\frac{m}{\hbar}\oint \mathbf{dl}\cdot\mathbf{v}_s = 2\pi n, \tag{2.42}$$

where n is an integer. Equation (2.42)[10] shows two things. Superfluid flow in multiply-connected geometry can have closed loop flow; and circulation is quantized in units of 2π.

In addition to the concept of circulation in multiply-connected geometry, Onsager [23] and Feynman [24] also introduced the concept of quantized vortex lines, which can carry circulation in a superfluid. At the center of each vortex line is a vortex core, where the superfluid density goes to zero and the superfluid phase has a singularity. A vortex line in a simply-connected geometry breaks the simply-connected condition (see figure 2.3 (left)), since the superfluid density goes to zero at its core. Hence, even a simply-connected (or what appears to be simply-connected)

---

[10] While equation (2.42) looks identical to equation (2.41), the non-superfluid region enclosed by the path prevents the application of Stoke's theorem. Given that $\psi(\mathbf{r})$ is a complex field, the integral need not be zero and can be any integer multiple of 2π [2].

superfluid can sustain rotation (closed loop flow) via quantized vortex lines. A rotating superfluid is expected to relax to a state with quantized vortex lines, each having a 2π phase winding. A path enclosing N lines will have a phase winding of $2\pi N$. For the interested reader, the structure of the vortex core as well as the lattice-like arrangement of quantized vortices have been studied extensively, and are reviewed by Glaberson and Donnelly [74].

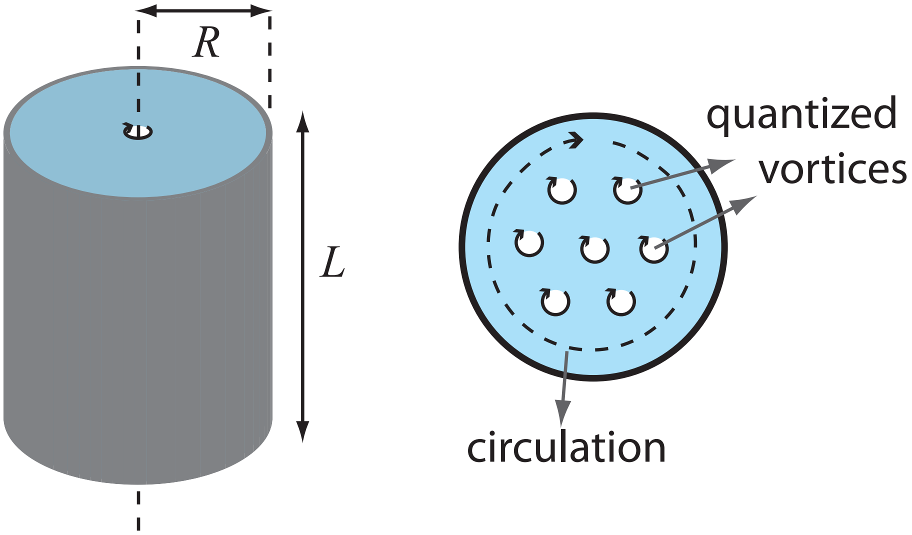

Figure 2.3: Quantized vortices: (left) A single quantized vortex in a large cylinder. The vortex line extends all the way from the bottom of the cylinder to the top. Quantized vortices, by virtue of the density zero at the center of the vortex core, allow even simply-connected superfluids to sustain rotation. (right) An array of quantized vortices carrying a circulation of 7π is shown. While the phase winding around each vortex is 2π, the phase winding along the dashed arrow adds up to 14π.

2.5.a Energy of single vortex

We now consider the case of a single quantized vortex in a large uniform system. For the sake of simplicity, we assume the system to be a large cylinder of height L and radius R, shown in figure 2.3 (left). The vortex line is at the center of the cylinder and extends from the bottom to top[11]. As mentioned previously, the superfluid density goes to zero at the center of the vortex line. Owing to cylindrical symmetry, the phase of the superfluid can be written in terms of $\mathbf{r}(r, \theta, z)$ coordinates as

$$\phi = \theta. \tag{2.43}$$

The flow velocity is given by

$$\mathbf{v}_s = \frac{\hbar}{mr}\hat{\theta}. \tag{2.44}$$

The $1/r$ dependence of the velocity means that atoms close to the core move the fastest, while those furthest away move the slowest. This is the exact opposite of rigid body rotation, where the velocity has an r dependence. The energy of a single vortex is given by

$$\begin{aligned} \varepsilon_v &\approx \int \mathbf{dr}\frac{1}{2}\rho_0 m v_s^2 \\ &\approx \frac{\pi\hbar^2\rho_0 L}{m}\ln\frac{R}{r_v}, \end{aligned} \tag{2.45}$$

where r_v is the size of the vortex core. While the exact calculation has additional correction terms [60] for small regions of small r, equation (2.45) captures the scaling necessary for understanding and predicting the physics. The vortex core size r_v is an artificial cut off, put in to avoid the singularity at the center. The value of r_v is obtained by finding the distance at which the kinetic energy of high velocity field (close to the center of rotation) equals the repulsive mean-field potential of the superfluid. The vortex-core size (< 1 nm for liquid helium, $\sim$1 μm for ultracold gases) is usually much smaller than the size of the system and is often approximated to be the healing length [63], which is given by

$$\xi = (8\pi\rho a)^{-1/2}. \tag{2.46}$$

The healing length is the characteristic length at which the superfluid density changes. For example, for a superfluid in a container with hard walls, the superfluid density has to go to zero at the walls. The superfluid density cannot change

---

[11] The reader should note that a vortex line can only terminate at the superfluid boundary or with itself, as in a vortex ring

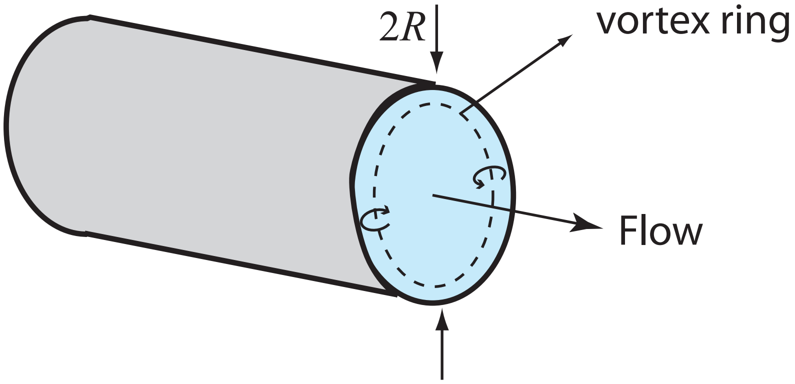

Figure 2.4: Flow decay via formation of vortex ring: The lowest energy excitation is a vortex ring the size of the channel.

discontinuously. The distance from the hard wall, at which the superfluid density approaches the mean density in the container scales as the healing length.

Having discussed the case of a simple vortex excitation, we will now talk about other vortex-like excitations and their role in superfluid dynamics.

2.5.b Decay of flow by vortex excitations

Equation (2.45) also shows that the energy of a vortex diverges with system size, with both L and R. Consequently, a vortex ring in 3D or a vortex-antivortex pair in 2D have a lower energy, since their energies do not diverge with system size. The energy of a vortex ring of radius R_v is proportional to $R_v \log(R_v/r_v)$ [75]. The energy of a vortex-antivortex pair in 2D separated by r_s is proportional to $\log(r_s/r_v)$. Hence, these excitations are more likely to play a role in any decay of flow compared to just a simple vortex line. We shall now discuss the breakdown of superflow in a cylindrical channel via the formation of a vortex ring.

We consider superfluid flow through a cylinder of radius R (see figure 2.4). The energy and momentum of a vortex ring excitation are given by [32, 75]

$$\varepsilon_{\mathrm{vr}} \approx \frac{2\pi^2\hbar^2\rho R_v}{m}\left(\log\frac{R_v}{r_v}-\frac{7}{4}\right), \tag{2.47}$$

$$p_{\mathrm{vr}} = 2\pi^2\hbar\rho R_v^2. \tag{2.48}$$

Using equation (2.35), we can find the critical velocity for creating such an excitation:

$$v_c \approx \min\left\{\frac{\hbar \log(R_v/r_v)}{mR_v}\right\} \tag{2.49}$$

The vortex ring with the largest radius, R_v has the lowest critical velocity (shown in figure 2.4), and hence $R_v \sim R$, giving the Feynman critical velocity [24],

$$v_c \simeq \frac{\hbar \log(R/r_v)}{mR}. \tag{2.50}$$

The above expression is only an approximation and can only give an estimate of what the critical velocity should be. The expression shows a decreasing trend with increasing channel size, R. This is counter-intuitive to the notion that flow is most likely to break at the "weakest" connection or narrowest part of the tubing. In fact, superflow is expected to decay more easily in wider channels. This could explain why the original experiments of Kapitza and Allen and Misener had to use extremely narrow channels in order to observe dissipationless flow. Experiments studying the critical flow velocity in superfluid helium have been more consistent with the Feynman critical velocity than the critical velocity for phonon or roton excitations [76].

Chapter 3

Sodium Bose-Einstein condensate apparatus

A typical Bose-Einstein condensate (BEC) in our lab consists of 10^5 sodium atoms at a temperature of around 40 nK. Such temperatures are orders of magnitude colder than liquid nitrogen ($\approx$80 K), liquid helium ($\sim$1 K) and even the most sophisticated refrigeration techniques (dilution refrigerators go down to $\lesssim$10 mK). Getting atoms to such low temperatures requires a specialized setup and several steps of cooling and trapping. These cooling and trapping techniques are based on certain properties of the atom. Although the physics of BECs does not require many of these atomic properties, they are nevertheless important for cooling, trapping, manipulating and detecting the atomic cloud.

The choice of atom for making a BEC is limited to atoms that can be laser cooled (or in some cases helium buffer gas cooled). The electronic structure of alkali atoms makes them easy to laser cool and hence the first atoms laser cooled and the first BECs were all alkali atoms. The apparatus I worked on in the Laser Cooling and Trapping group was the first BEC apparatus (BEC achieved in 1998 [77]) of the group, and is one of the older surviving BEC apparatuses. For this reason, the choice of using sodium atoms is purely due to historic reasons. Since most of the apparatus was built before my time, I will focus on explaining only their principles of operation. I will go over the more recent developments, such as the optical trap, in more detail.

3.1 Atomic physics and the two-level atom

While there are no two-level atoms, the two-level atom model can nonetheless explain several aspects of the physics relevant to the cooling, trapping and manipulation of atom clouds (the atomic physics tool set). The two-level atom consists of an atom interacting with an oscillating electromagnetic field, which causes coupling between the two levels. To begin, we consider a simple atom-field interaction, which can be treated in the following ways:

1. Fully classically : Here both the atom and field are treated classically. The atom is modeled as a charge dipole with a spring constant and the field is modeled as a classical Maxwellian electromagnetic field.

2. Semiclassically : Here the atom is treated as a two-level quantum mechanical system with a dipole coupling between the levels. The field is treated classically.

3. Fully quantum mechanically : Here, along with the atom, the field is also treated quantum-mechanically with discrete energy levels, and can exchange energy with the atom.

While the fully quantum treatment is required for explaining cavity quantum electrodynamic and other experiments, the semiclassical treatment is illustrative and sufficient for the purposes of this thesis. The treatment shown in this section is quite standard and is presented in several textbooks (Scully and Zubairy [78], Metcalf and van der Straten [79]), which also discuss the subtleties and details of the various approximations involved.

I will take the case of a two-level atom with an electric dipole transition, which is a good approximation for the D-line transitions of an alkali atom. Although magnetic dipole transitions arise from coupling to the magnetic dipole moment of the atom, some of the most general spin selection rules and phenomena such as Rabi flopping can nevertheless be treated analogously. The electromagnetic field (or light field) is assumed to be homogeneous and monochromatic. The electric field can be written as

$$E(t) = E_0 \cos(\omega t), \tag{3.1}$$

where E_0 is the amplitude of the field, ω is the frequency and t is time. For simplicity, I will only be considering the electric dipole moment of the atom in the direction of the field and hence the electric field can be written as a scalar. The cosine term in the expression can be split up to give

$$E(t) = \frac{E_0}{2}(e^{i\omega t} + e^{-i\omega t}). \tag{3.2}$$

The atom is modeled as having two levels, the ground state $|0\rangle$ and the excited state $|1\rangle$, with an energy difference of ω_0 (in frequency units). The detuning of the light field from the atom is given by $\Delta = \omega - \omega_0$ (see figure 3.1).

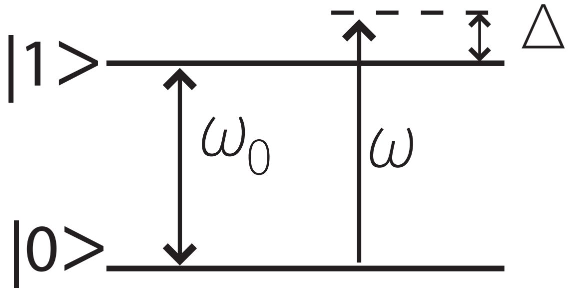

Figure 3.1: Two-level atom : The light field of frequency ω is detuned by Δ from the atomic resonance.

The atom and light field interact via the electric dipole transition moment of the atom, d, giving a cross-coupling energy term $d \cdot E(t)$. The transition dipole moment d results from the dipole operator connecting the ground and excited states. The hamiltonian of the atom in the presence of the field can be written as

$$H = H_0 + H_E, \tag{3.3}$$

where H_0 is the unperturbed hamiltonian, and $H_E = d \cdot E(t)$. In matrix form in terms of states $|0\rangle$ and $|1\rangle$, the hamiltonian can be written as

$$H = \begin{bmatrix} 0 & 0 \\ 0 & \hbar\omega_0 \end{bmatrix} + \begin{bmatrix} 0 & d \cdot E(t) \\ d \cdot E(t) & 0 \end{bmatrix}, \tag{3.4}$$

using a $|0\rangle = \begin{bmatrix} 1 \\ 0 \end{bmatrix}$, $|1\rangle = \begin{bmatrix} 0 \\ 1 \end{bmatrix}$ basis.

Equation (3.4) is the basic two-level atom-light hamiltonian. I will now discuss two specific solutions of the equation, the resonant case and the far off-resonant case.

In the resonant case, $\Delta = 0$, and the primary effect of the light field is Rabi flopping, transferring atoms from $|0\rangle$ to $|1\rangle$ and back. In the far off-resonant case, the primary effect is to cause a shift in the energy levels.

3.1.a Resonant interaction and Rabi flopping

We begin with equation (3.4) and use the time-dependent Schrödinger equation

$$H\psi(t) = i\hbar\frac{\partial\psi(t)}{\partial t}, \tag{3.5}$$

where the time-dependent two-level atom wavefunction is given by $\psi(t) = c_0(t)|0\rangle + c_1(t)|1\rangle$, or $\psi(t) = \begin{bmatrix} c_0(t) \\ c_1(t) \end{bmatrix}$, with the normalization condition $|c_0|^2 + |c_1|^2 = 1$. Substituting H and ψ, we obtain

$$\begin{bmatrix} 0 & d \cdot E_0\cos(\omega t) \\ d \cdot E_0\cos(\omega t) & \hbar\omega_0 \end{bmatrix}\begin{bmatrix} c_0(t) \\ c_1(t) \end{bmatrix} = i\hbar\begin{bmatrix} \dot{c}_0(t) \\ \dot{c}_1(t) \end{bmatrix}, \tag{3.6}$$

where the dot above c indicates derivative with respect to time. This matrix equation gives us two linear differential equations,

$$\begin{aligned} \hbar\omega_0 c_1(t) + d \cdot \frac{E_0}{2}(e^{i\omega t} + e^{-i\omega t})c_0(t) &= i\hbar\dot{c}_1(t) && (3.7) \\ d \cdot \frac{E_0}{2}(e^{i\omega t} + e^{-i\omega t})c_1(t) &= i\hbar\dot{c}_0(t), && (3.8) \end{aligned}$$

where the cosine terms have been expanded out. In order to solve these equations, one can make a simplifying substitutions $b_0(t) = c_0(t)$ and $b_1(t) = c_1(t)e^{i\omega t}$. For the resonant case, $\Delta = 0$ and hence $\omega = \omega_0$, giving

$$\begin{aligned} d \cdot \frac{E_0}{2}(e^{i\omega t} + e^{-i\omega t})b_0(t) &= i\hbar\dot{b}_1(t)e^{-i\omega t} && (3.9) \\ d \cdot \frac{E_0}{2}(e^{i\omega t} + e^{-i\omega t})b_1(t)e^{-i\omega t} &= i\hbar\dot{b}_0(t). && (3.10) \end{aligned}$$

We now use the rotating-wave approximation, where we average over fast oscillations of the order of the carrier frequency ω. These oscillations are typically too fast (particularly for optical transitions) for the atoms to follow or for any detector to measure and most of the relevant dynamics happen on much slower timescales. After multiplying through with $e^{i\omega t}$ for the first equation and removing terms containing $e^{\pm 2i\omega t}$, we are left with

$$
\begin{aligned}
d \cdot \frac{E_0}{2} b_0(t) &= i\hbar \dot{b}_1(t) && (3.11)\\
d \cdot \frac{E_0}{2} b_1(t) &= i\hbar \dot{b}_0(t), && (3.12)
\end{aligned}
$$

which has solutions of the form

$$b_0(t) = b_0(0)\cos(\Omega t/2) - i b_1(0)\sin(\Omega t/2) \tag{3.13}$$

$$b_1(t) = b_1(0)\cos(\Omega t/2) - i b_0(0)\sin(\Omega t/2), \tag{3.14}$$

where

$$\hbar\Omega = d \cdot E_0 \tag{3.15}$$

defines the Rabi frequency Ω. If one started with an atom in state $|0\rangle$ at time $t = 0$, the state probability coefficients are given by

$$
\begin{aligned}
|c_0(t)|^2 &= |b_0(t)|^2 = \cos^2\left(\frac{\Omega t}{2}\right), && (3.16)\\
|c_1(t)|^2 &= |b_1(t)|^2 = \sin^2\left(\frac{\Omega t}{2}\right). && (3.17)
\end{aligned}
$$

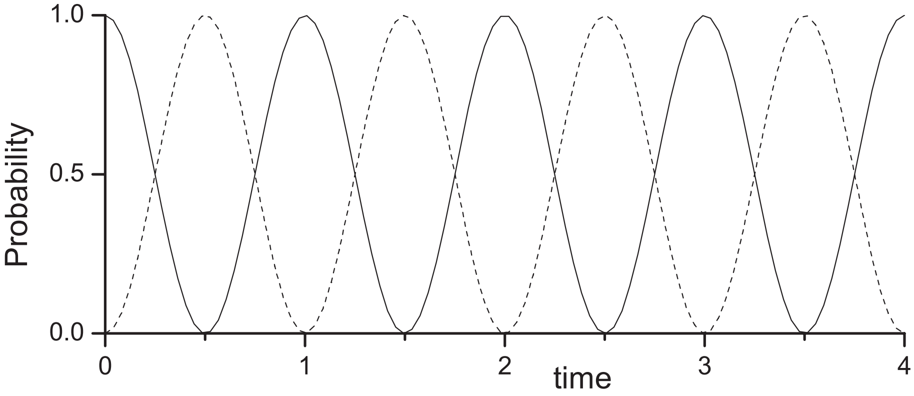

Figure 3.2: Resonant Rabi flopping : The figure shows the $|0\rangle$ probability coefficient $|c_0(t)|^2$ (solid) and the $|1\rangle$ probability coefficient $|c_1(t)|^2$ (dashed) for a resonant light field incident on the two-level atom. The time units are in $2\pi/\Omega$, where Ω is the Rabi frequency.

As one can see in figure 3.2, the atom flops between states $|0\rangle$ and $|1\rangle$. The time $2\pi/\Omega$ is known as the 2π-pulse time. If the field is turned on for the duration of a π-pulse, the atom is shifted from state $|0\rangle$ to state $|1\rangle$. A $\pi/2$-pulse puts the atom in an equal superposition of $|0\rangle$ and $|1\rangle$.

3.1.b Far off-resonant interaction and energy level shifts

When the light field is significantly far detuned from the energy separation of the two levels of the atom, the light causes little transfer from the ground to the excited state. Rather, it causes a light-shift in the energies of the two levels. In order to eliminate the time dependence of the electromagnetic field, we go into the rotating frame $e^{-i\omega t}$ of the field, and just like in the resonant case, apply the rotating-wave approximation[1] eliminating terms of the order $e^{\pm i\omega t}$. We start with equation (3.6), and set $b_0 = c_0(t)$ and $b_1 = c_1(t)e^{i\omega t}$ to obtain

$$\begin{bmatrix} 0 & d\cdot\frac{E_0}{2}(e^{i\omega t}+e^{-i\omega t}) \\ d\cdot\frac{E_0}{2}(e^{i\omega t}+e^{-i\omega t}) & \hbar\omega_0 \end{bmatrix}\begin{bmatrix} b_0 \\ b_1 e^{-i\omega t} \end{bmatrix} = i\hbar\begin{bmatrix} \dot{b}_0 \\ e^{-i\omega t}(\dot{b}_1 - i\omega b_1) \end{bmatrix}.$$

Applying the rotating wave approximation and expressing the equation in terms of $\begin{bmatrix} b_0 \\ b_1 \end{bmatrix}$, we get a time-dependent Schrödinger equation of the form

$$\begin{bmatrix} 0 & d\cdot\frac{E_0}{2} \\ d\cdot\frac{E_0}{2} & -\hbar\Delta \end{bmatrix}\begin{bmatrix} b_0 \\ b_1 \end{bmatrix} = i\hbar\begin{bmatrix} \dot{b}_0 \\ \dot{b}_1 \end{bmatrix}, \tag{3.18}$$

which can be written as a hamiltonian in the $(|0\rangle, e^{-i\omega t}|1\rangle)$ basis:

$$H' = \hbar\begin{bmatrix} 0 & \Omega/2 \\ \Omega/2 & -\Delta \end{bmatrix} = \hbar\begin{bmatrix} -\Delta/2 & 0 \\ 0 & -\Delta/2 \end{bmatrix} + \hbar\begin{bmatrix} \Delta/2 & \Omega/2 \\ \Omega/2 & -\Delta/2 \end{bmatrix}. \tag{3.19}$$

By solving for the eigenvalues of the new hamiltonian, the modified energy levels come out to be

$$\epsilon_\pm = \left(-\frac{\Delta}{2} \pm \frac{\bar{\Omega}}{2}\right)\hbar, \tag{3.20}$$

where $\bar{\Omega} = \sqrt{\Omega^2 + \Delta^2}$. In the limit of large detunings, $\Delta \gg \Omega$, $\bar{\Omega}$ simplifies to $\Delta(1 + \frac{\Omega^2}{2\Delta^2})$, which gives a ground state energy shift of

$$\delta\epsilon_0 = \hbar\frac{\Omega^2}{4\Delta}, \tag{3.21}$$

---

[1] The rotating-wave approximation is valid so long as one is not too far detuned. If $\omega \ll \omega_0$, then there is not much difference between $|\omega + \omega_0|$ and $|\omega - \omega_0$—.

and the excited state energy shift of

$$\delta\epsilon_1 = -\hbar\frac{\Omega^2}{4\Delta}. \tag{3.22}$$

The energy shifts are proportional to the intensity of the radiation (E_0^2). When the applied field is blue-detuned, $\Delta > 0$, the ground state energy is raised and the excited state energy is lowered, whereas when the applied field is red-detuned, $\Delta < 0$, the ground state energy is lowered and the excited state energy is raised (see figure 3.3). If one were to apply a red-detuned light field, an atom in the ground state will be attracted towards regions of higher intensity, due to the lower potential there. Hence, red-detuned fields with localized maxima can be used to trap atoms via the dipole force. Blue-detuned light fields have the opposite effect and can be used to create a repulsive potential.

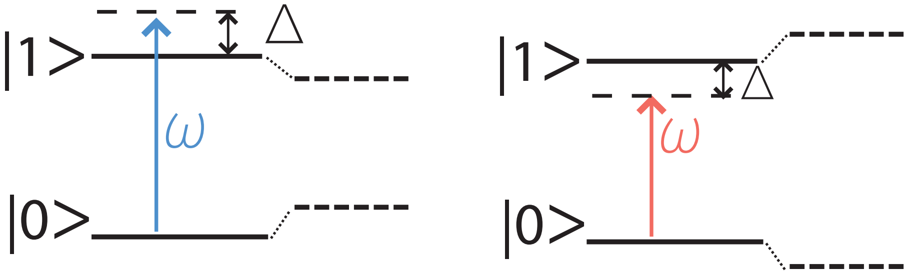

Figure 3.3: Light shift on a two-level atom: The effect of blue-detuned (left) and red-detuned (right) light on the two level atom. The effect shown is exaggerated for clarity. The light shift is typically orders of magnitude smaller than the detuning.

3.1.c Spontaneous emission

In practice, an atom in the excited state will emit a photon and decay to the ground state even in the absence of an applied coupling field[2], via a process known as spontaneous emission. The rate of spontaneous emission depends on the strength

---

[2] Spontaneous emission can also be viewed as the coupling of an atom to the vacuum field, which according to quantum electrodynamics is nonzero.

of the transition and the resonance frequency, and is given by [80]

$$\Gamma = \frac{\omega_0^3}{3\pi\epsilon_0\hbar c^3}|\mathbf{d}|^2, \tag{3.23}$$

where ϵ_0 is the permittivity of vacuum, c is the speed of light and $\mathbf{d}$ is the total dipole moment of the atom (in calculating the Rabi frequency, we used only the component in the direction of the electric field of the light). The expression for spontaneous emission can be derived quantum mechanically from the coupling of an atom to the free space vacuum modes (originally in Weisskopf and Wigner [81], also shown, for example, in Scully and Zubairy [78] and Steck [80]). Equivalently, it can also be derived by comparing the thermodynamic steady state of an atom in a light field with the Planck blackbody distribution [82].

The ω_0^3 dependence of the spontaneous emission decay rate causes optically excited states with electric dipole moment transitions to decay at rates of 10^7 s^{-1}. Microwave and rf transitions, which are typically magnetic dipole and have a lower transition frequency, tend to have decay times much longer than experimental timescales and hence can be neglected.

Spontaneous emission causes an atom in a light field to reach a steady state, as opposed to undergoing Rabi oscillations. In contrast to Rabi oscillations where the photon is emitted coherently into the driving field, spontaneous emission causes photons to be emitted incoherently in all directions. This process is key to imaging techniques, which either measure the loss of photons as they pass through an atomic sample (absorption imaging, discussed in 3.8), or the number photons scattered in other directions (fluorescence imaging). The steady state excited population fraction of atoms in a radiation field depends on the intensity and detuning of the radiation, and is given by [80]

$$|c_1(t \to \infty)|^2 = \frac{(\Omega/\Gamma)^2}{1 + 4(\Delta/\Gamma)^2 + 2(\Omega/\Gamma)^2}. \tag{3.24}$$

The spontaneous scattering rate per atom is $R_s = \Gamma|c_1(t \to \infty)|^2$, leading to

$$R_s = \left(\frac{\Gamma}{2}\right) \frac{(I/I_{\text{sat}})}{1 + 4(\Delta/\Gamma)^2 + (I/I_{\text{sat}})}, \tag{3.25}$$

where we have defined a saturation intensity I_{sat}, such that $I/I_{\text{sat}} = 2(\Omega/\Gamma)^2$, and I is the intensity of the light field (in energy per area per time), given by $I = (1/2)c\epsilon_0 E_0^2$. The saturation intensity can be expressed in terms of the dipole interaction:

$$I_{\text{sat}} = \frac{c\epsilon_0 \Gamma^2 \hbar^2}{4|\hat{\epsilon} \cdot \mathbf{d}|^2}, \tag{3.26}$$

where, to remind the reader, $\hat{\epsilon} \cdot \mathbf{d}$ is the component of the dipole moment in the direction of the electric field.

The effect of detuning is to lower the steady state population in the excited state and hence the spontaneous scattering rate. However, this can be overcome by using a higher intensity of light. For a fixed detuning, in the limit of low intensity, the population fraction of the excited state is linearly proportional to the intensity (or Ω^2) of the radiation. In the limit of high intensity, the population saturates to 0.5 (50 %), and the scattering rate saturates to $\Gamma/2$.

3.1.d Light forces

In the previous section, we discussed the steady state of an atom in a light field. If such a light field were unidirectional as is typical of an optical beam (see figure 3.4), there is a net force on the atom due to the difference in momenta between the photons absorbed from the incident beam and the photons spontaneously emitted in all directions[3].

For an atom in free space (assuming no collisions with other atoms), the atom undergoes a momentum change due to the net force. The velocity shift due to the momentum change in turn causes a Doppler shift in the light frequency that the atom sees, which eventually takes the light field off-resonance, and the atom is no longer affected by the field. The Doppler shift of a moving atom can also be used to slow it down. This was first proposed independently by Hänsch and Schawlow [85] and by Wineland and Dehmelt [86] and later demonstrated in ions by Wineland

---

[3] The effect of light on an atom also depends on the state of matter in which it is in. For example, for atoms in a conducting solid, light can cause pairing of electrons [83]. In this thesis, we only consider the effect of light on a pure sample of neutral atoms in the gaseous state.

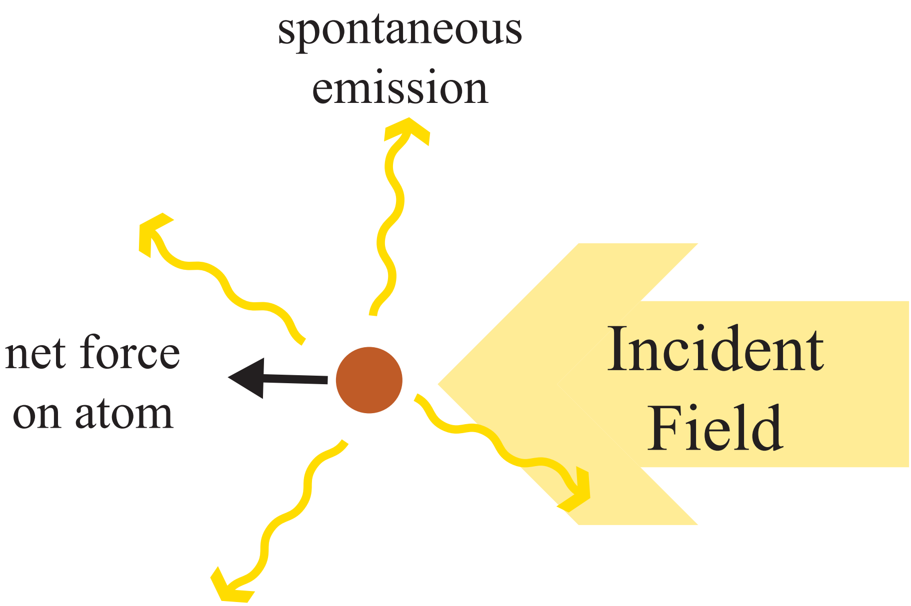

Figure 3.4: Light force on a two-level atom: An atom in a light field in steady state absorbs radiation from the incident light field, and emits radiation in nearly all directions (dipole radiation pattern [84]) via spontaneous emission. Through this process, the atom undergoes a net force in the direction of incidence of the light field.

et al. [87] and Neuhauser *et al.* [88]. For a gas of atoms, where the energy is primarily translational, slowing down atoms corresponds to cooling, and hence the technique is known as laser cooling, which enables nearly all BEC experiments. We will now see a simple example of laser cooling.

In figure 3.5, the effect of a 1D pair of counter-propagating beams is shown. The beams are near red-detuned. For an atom moving towards one of the beams, the atom sees the beam with a blue Doppler shift (closer to resonance) and experiences a stronger light force from that beam. Since it is moving away from the other beam, it sees the beam with a red Doppler shift (further red-shifted) and experiences a weaker force from that beam. The net result of the two beams is to damp the velocity of the atom along the beams' axis. An atom that is not moving (in the axis of the beams) feels no net force. This velocity-sensitive damping force can be used to slow and hence cool the atoms down.

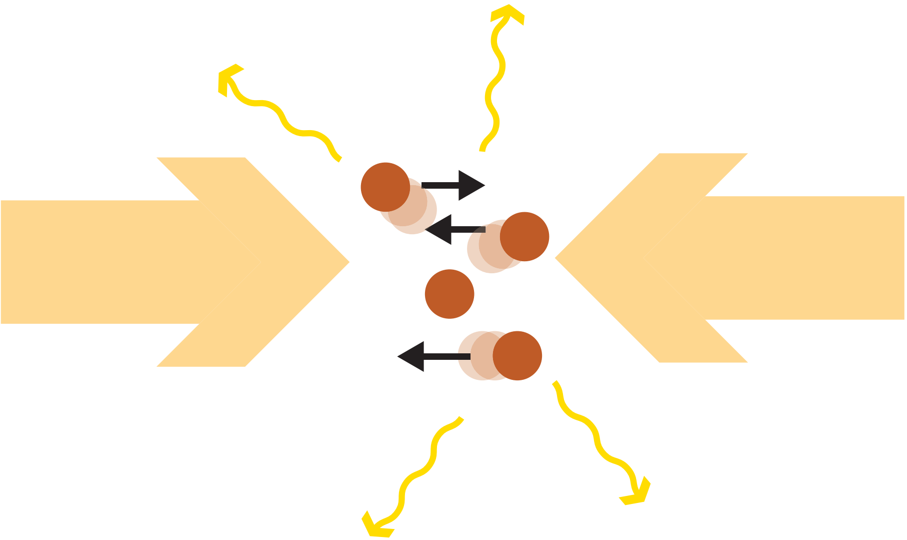

Figure 3.5: Velocity sensitive light forces: An atom in a field created by a pair of near red-detuned counterpropagating beams undergoes a light force opposing the direction of its velocity, shown by black arrows. An atom at rest (center) feels no net force. This acts as a damping force and can be used slow atoms down.

Using the scheme shown in figure 3.5 along all 3 axes, atoms can be cooled down to millikelvin temperatures. This scheme is known as optical molasses and has been studied extensively [89–94]. The simple two-level atom picture described here cannot fully explain laser cooling from optical molasses. In fact, the magnetic sublevel structure of alkali atoms causes further cooling of the atoms, known as sub-doppler cooling [90]. The exact effect of light forces due to sub-doppler cooling is complicated and beyond the scope of this thesis. For a good review on the subject, see Cohen-Tannoudji [89], Cohen-Tannoudji [95] or Phillips [96].

Having described the various interactions of the two-level atom with laser light, we can now focus our attention towards the more practical aspects of atomic physics and our system.

3.2 Atomic structure in real world atoms

Unlike their imaginary counterparts, real world atoms have a more complicated energy level structure. As mentioned before, the energy level properties of the atom are important mainly for cooling, trapping, manipulating and imaging the atoms, and function as the basis of "engineering tools" for the atom. So long as we are able to cool and trap atoms, we need not delve into details of the internal structure of the atom. In that respect, as engineers, all we need to know are the energy level "specifications" of the atom. Nevertheless, I feel it is instructive to go through some background as to how the energy level structure of the atom arises.

The basic energy level structure, namely the principal quantum number n ($n \in \{1, 2, ...\}$), and the orbital angular momentum quantum numbers l and m_l (l, m_l: $0 \leq l < n$, $m_l \in \{-l, ...0, ...l-1, l\}$), come from solutions of the Schrödinger equation for the hydrogen atom (see Schiff [97] or Johnson [98] for example). Electrons being spin $\frac{1}{2}$ fermions have the additional spin degree of freedom s, where there are two spin states ($s = \frac{1}{2}$, $m_s \in \{-\frac{1}{2}, \frac{1}{2}\}$) for every ($n$,$l$,$m_l$) state. Finally, there is additional fine and hyperfine structure to this basic (n,l,m_l,s,m_s) structure.

Atomic fine structure[4]. arises from spin-orbit coupling, by which m_l and m_s are no longer good quantum numbers. Rather, l and s combine to give a spin-orbit angular momentum j (for information on angular momentum addition, see Sakurai [71] or for a more atomic physics based reference, see Johnson [98]), denoted by

$$\mathbf{j} = \mathbf{l} + \mathbf{s}, \tag{3.27}$$

where $j \in \{|l - s|, |l + s|\}$. The electronic state in the new basis is given by (n,l,s,j,m_j), where the relationship between m_j and j is analogous to that of m_l and l (m_j: $m_j \in \{-j, ...0, ...j-1, j\}$).

For atoms that have multi-electron outer states, one needs to add the spins ($\mathbf{S} = \mathbf{s}_1 + \mathbf{s}_2 + ...$) and orbital angular momentum ($\mathbf{L} = \mathbf{l}_1 + \mathbf{l}_2 + ...$) of individual electrons before computing the spin-orbit coupling J state ($\mathbf{J} = \mathbf{L} + \mathbf{S}$), or alternatively,

---

[4] Fine structure is a more general term, and can be used to describe the splitting of spectral lines due to a variety of sources, for example from the Brillouin effect [99].

add the total spin of each electron ($\mathbf{j}_1 = \mathbf{l}_1 + \mathbf{s}_1$, $\mathbf{j}_2 = \mathbf{l}_2 + \mathbf{s}_2$, ...) and combine the spins of all electrons ($\mathbf{J} = \mathbf{j}_1 + \mathbf{j}_2 + ...$), depending on which is applicable. Finally, in denoting an electron state, one uses the notation $n^{2S+1}\mathbf{L}_J$, where the orbital angular momentum is denoted by $\mathbf{L} =$ S, P, D, F for $L = 0, 1, 2, 3$. For hydrogen-like atoms, having only one electron in its outermost shell, one can simply use $\mathbf{S} = \mathbf{s}$, $\mathbf{L} = \mathbf{l}$, $\mathbf{J} = \mathbf{j}$. Since sodium is a hydrogen-like atom, I will not talk about multi-electron atoms (there are several books that cover this, such as Johnson [98]).

Analogous to electron spin, atomic nuclei also have spin associated with them. The total spin depends on the number of nucleons and the nuclear structure, and can take integer or half-integer values. Hyperfine structure arises from coupling of the spin-orbit angular momentum J with the nuclear spin I (if non-zero) to give the total angular momentum F, denoted by

$$\mathbf{F} = \mathbf{J} + \mathbf{I}, \tag{3.28}$$

where $F \in \{|I - J|, |I - J| + 1, ..., |I + J|\}$. Including nuclear spin, the final electron state is given in the (n,L,S,I,J,F,m_F), where $m_F \in \{-F, ..., 0, ..., F - 1, F\}$. The electron state is denoted by $n\mathbf{L}_J$ followed by the hyperfine state F and sublevel m_F. Here, since only one electron is involved, the spin state is always $S = 1/2$, and so is omitted from the notation. Hyperfine interactions are much weaker than spin-orbit coupling and other electronic interactions, and add only a small perturbation to energy levels. However, they do change the nature and degeneracy of the ground state.

In applying an external magnetic field to an atom, the degeneracy of the m_F sublevels of the F manifold is broken, and the different sublevels undergo different energy shifts. This is known as the Zeeman effect. The Zeeman effect is an important tool in atomic physics and forms the basis of magnetic trapping, where atoms in a weak-field-seeking hyperfine state are trapped at the minimum of a spatially varying applied external magnetic field. The exact Zeeman splitting depends on the coupling strengths of the various individual basis states (L,S,I) to the external magnetic field, and their vector combination that results in F.

3.3 The Sodium atom

We now move to sodium, the atom used in the experiments. Sodium has been isolated and studied from as early as the 1800s [100]. However, most of the aspects for which sodium is known, such as its metallic structure, reactivity, chemistry, role in physiological processes and other uses are irrelevant to us. The key properties that matter to our experiment are:

- Sodium's bosonic nature (it has 11 protons, 11 electrons and 12 neutrons, making an even number of spin $\frac{1}{2}$ particles).
- The hydrogen like structure ($1s^2\ 2s^2\ 2p^6\ 3s^1$), which allows cooling, trapping and probing.
- The sodium-sodium scattering properties, which are favorable for evaporative cooling and BEC, including the repulsive low energy s-wave interactions, which are key to observing superfluidity.

Analyzing the atomic structure of sodium along the lines of the discussion of the previous section, the $1s$, $2s$ and $2p$ orbitals are completely filled, leaving a lone electron in the $3s$ state. The ground state has $S = 1/2$, $L = 0$, giving a $3S_{1/2}$, spin-orbit ground state. Sodium has a nuclear spin of $I = 3/2$, which leads to two ground hyperfine states, $F = 1$ and $F = 2$ (see figure 3.6).

The lowest electronically excited state is the $3p$ state ($L = 1$). Spin-orbit coupling causes a split into $3P_{1/2}$ and $3P_{3/2}$ states. The $3P_{1/2}$ state combines with the nuclear spin to give 2 hyperfine states ($F' = 1$ and $F' = 2$, prime denotes excited state, otherwise ground state). The $3P_{3/2}$ state combines with the nuclear spin to give 4 hyperfine states ($F' = 0, 1, 2, 3$ shown in figure 3.6).

The sodium $3S_{1/2}$ to $3P_{3/2}$ transition (called the D_2 transition) is shown in figure 3.6. Nearly all the cooling and probing is done on the $3S_{1/2}$ $F = 2$ to $3P_{3/2}$ $F' = 3$ cycling transition[5] . The transition is termed a cycling transition, since any

---

[5] I am using cycling transition in the more general sense. The cycling transition is often referred to the $F = 2, m_F = \pm 2$ to the $F' = 3, m'_F = \pm 3$ transition with circularly polarized light, which

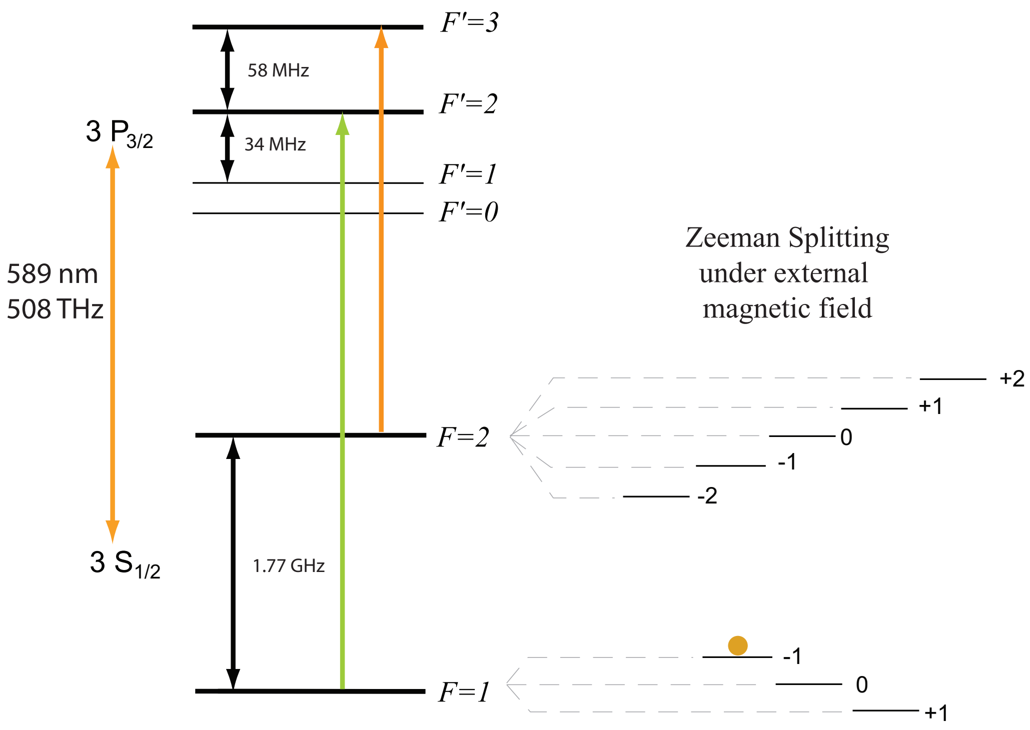

Figure 3.6: Sodium D_2 transition hyperfine structure : The $3S_{1/2}$ to $3P_{3/2}$ levels are shown. Most of the cooling and probing is performed on the cycling transition, $F = 2$ to $F' = 3$, shown by the orange arrow. The repumping transition, $F = 1$ to $F' = 2$, is shown with a green arrow. An externally applied magnetic field breaks the degeneracies of the hyperfine ground states, with sublevels shown on the right. Magnetic trapping and evaporative cooling is performed in the $F = 1$, $m_F = -1$ state (indicated above).

atom excited to the $F' = 3$ state has to decay (via spontaneous emission) to the $F = 2$ state due to spin selection rules (see Schiff [97]). Atoms in the $F = 2$ state can get off-resonantly excited to the $F' = 2$ state, which has an equal probability of decaying to the $F = 2$ or $F = 1$ ground states. Although rare (around 1/100 if the light is linearly polarized and even less if it is circularly polarized), this off-resonant excitation ultimately leads to all the atoms being transferred to the $F = 1$ state. This process is known as optical pumping. To prevent optical pumping, additional $F = 1$ to $F' = 2$ resonant light is used to optically *repump* the atoms back into the

---

is closed within itself and does not involve other magnetic sublevels.

$F = 2$ state (also shown in figure 3.6).

While the $F = 2$ state is convenient for cooling and probing, it has a larger s-wave scattering length than the $F = 1$ state [101]. This leads to shorter trap lifetime due to the higher three-body collision rate and molecule formation. To minimize losses and allow for longer, slower evaporative cooling, we create and work with condensates in the $F = 1$ ground hyperfine state. The effect of a magnetic field on the $F = 1$ manifold is shown in figure 3.7. Of the three magnetic sub-levels, the energy of the $m_F = -1$ sublevel initially increases with magnetic field. Atoms in the $m_F = -1$ state are attracted to low-field regions, making them magnetically trappable (magnetic trapping will be discussed in 3.4.d). All our magnetic trapping and cooling is done in the $F = 1$, $m_F = -1$ state.

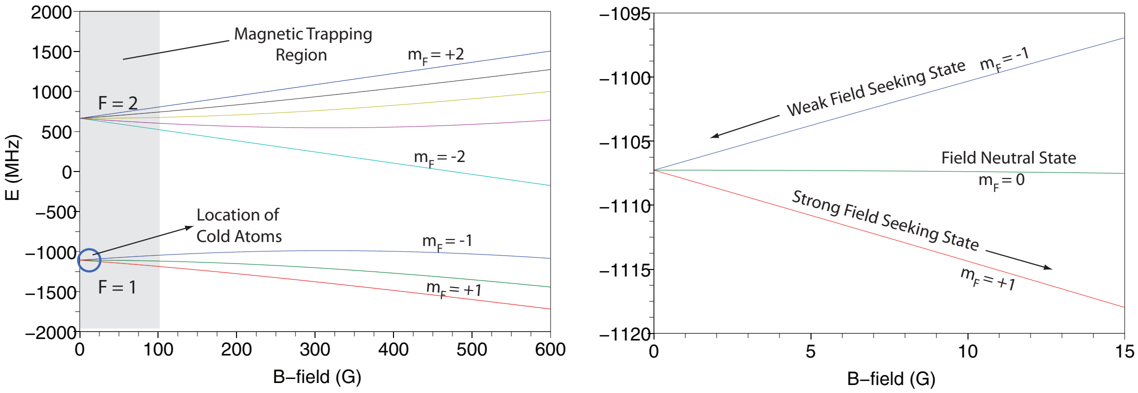

Figure 3.7: Sodium ground state Zeeman shift : Under small fields ($B < 10$ G), the hyperfine splitting is essentially linear ($\propto m_F B$), while at larger fields, the (F,m_F) basis is no longer valid, as seen in the plot on the left. The plot on the right shows a zoomed-in version of the low field Zeeman shifts of the $F = 1$ manifold (circled on left). The $m_F = -1$ state, the weak-field seeking state, is attracted to lower B-fields and can be trapped at the magnetic field minimum. Magnetic trapping will be discussed in section 3.4.d

3.4 Creating a BEC

Though fairly standard now, achieving Bose-Einstein condensation was the result of several innovative techniques and amazing feats of engineering. While technology has greatly improved and most techniques have become standard (and recipe-like), BEC apparatuses still require large investments in equipment and people. In our BEC lab, most of the equipment one sees is solely for the purpose of reaching (and maintaining) BEC temperatures, as opposed to performing the scientific experiment. Most of the steps in the creation of the BEC have been previously thought through and optimized. In my time at NIST, except for minor modifications, the core vacuum system and magnetic coils and the process to obtain a BEC have remained the same, and hence I will only give a qualitative explanation of these. There are several sources which discuss the design considerations of a BEC system [102–108], and the standard cooling and trapping techniques [79, 109].

Our BEC chamber (see figure 3.8) consists of two parts, the main chamber, which is kept under ultra-high vacuum and the oven chamber, which is kept at lower vacuum. In the main chamber, atoms are trapped and cooled down to ultracold temperatures at the center of a glass cell. The glass cell has magnetic coils mounted close to the surface in order to capture atoms from the atomic beam and trap them. In a typical experimental sequence, we start with hot atoms from the oven, which are then slowed (and cooled) by the Zeeman slower (shown in figure) and the slower laser beam, before being trapped in the Magneto-Optical Trap (MOT). By subsequent magnetic trapping and evaporative cooling, we are able to get a million-atom BEC in the magnetic trap.

The experiments discussed in this thesis were performed in an optical dipole trap. Rather than condensing the atoms in the magnetic trap, we transfer them to an optical dipole trap while they are yet to condense. Subsequently, we perform the experiments on the BEC and image the atoms, by measuring the absorption of a resonant probe passing through the cloud. The imaging process causes heating and destroys the sample. The entire process, which lasts around 40 seconds, is controlled by a computer which provides the timing for all the devices participating in the experiment.

In the following sub-sections, the different stages of trapping and cooling will be briefly discussed.

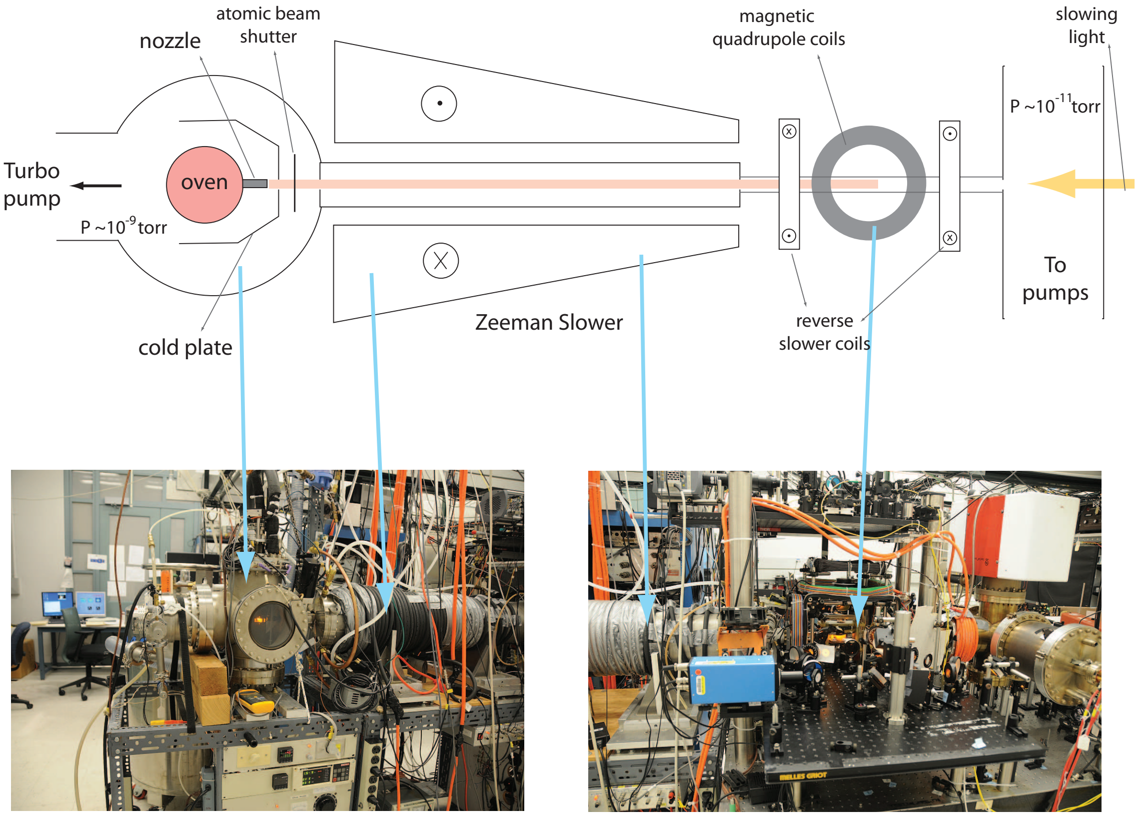

Figure 3.8: Schematic and photos of the BEC setup: The figure (top) shows a schematic of the physical apparatus. Atoms start from the oven (left), travel along the Zeeman slower (atomic beam path shown in light red) and are captured at the center of the quadrupole coils (right). All further evaporation and condensation takes place there. The corresponding parts are shown in photos of the lab. For scale, the Zeeman slower is about 1.5 meters long.

3.4.a Vacuum chamber

The main vacuum chamber is kept under ultra-high vacuum ($\approx 10^{-11}$ torr), pumped by an ion pump and a titanium sublimation pump. There is a differential pumping stage between the main chamber and the oven chamber. The oven chamber is kept at high vacuum, $\approx 10^{-9}$ torr, and is pumped by a turbo pump which is backed by a roughing pump. The oven consists of a sealed metal container, loaded with metallic sodium, and has a nozzle protruding outwards towards the main chamber.

3.4.b Oven and Zeeman slower

Atoms coming out of the oven are at 500 K. The collimation from the oven nozzle and the cold plate (shown in figure 3.8) ensures that the transverse velocity distribution of the atomic beam is small. The slower beam (shown in figure 3.8) slows down atoms by using laser light. The longitudinal magnetic field profile of the Zeeman slowing coils creates a spatially varying Zeeman shift, and compensates the changing Doppler shift due to the slowing of atoms, allowing the atoms to stay in resonance with the slower beam through the distance of the Zeeman slower. In our BEC setup, the Zeeman slower magnetic field is highest at the oven chamber end, passes through a zero between the slower and reverse slower coils (see figure 3.8) as it inverts, before going to zero at the location of the MOT. The inverted field allows the slowing laser to pass through the Magneto-optical trap (MOT) without affecting it[6]. The inverted field also extends the velocity slowing range of the Zeeman slower without having to use higher magnetic fields. The effect of the Zeeman slower is to lower the velocity of atoms from 100-400 m/s down to < 10 m/s. The slowing of atoms is critical to the loading of the MOT from the atomic beam.

3.4.c Magneto-optical trap (MOT)

The MOT is used to capture atoms from the Zeeman slowed atomic beam, which are then transferred to the magnetic trap, where they can be further cooled. A MOT consists of 3 pairs of circularly polarized counter-propagating beams along 3 perpendicular axes, along with a quadrupole magnetic field gradient (see figure 3.9). The magnetic field creates a force gradient, where atoms away from the center are Zeeman shifted to be closer to resonance with the light and hence experience a force towards the center. In addition, the red-detuning of the MOT beams contributes to an overall cooling of the cloud, as was discussed in 3.1.d. We typically load about

---

[6] In the inverted field Zeeman slower, the field starts high, decreases, goes past zero to a negative field before returning to zero. The final change in slope (from negative to positive) allows the Zeeman slower beam to be off-resonant to the slowed atoms and also the atoms in the MOT.

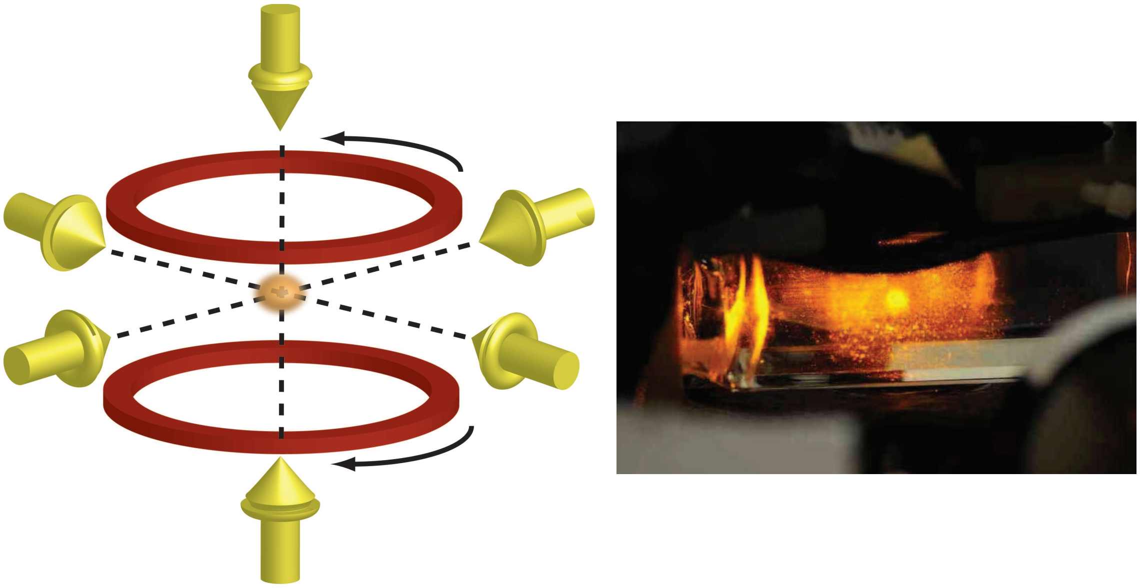

Figure 3.9: The magneto-optical trap consists of a pair of anti-Helmholtz coils (see left), along with 3 pairs of mutually perpendicular counter-propagating beams. The trap captures slowed atoms from the atomic beam, and cools them down to sub-millikelvin temperatures. On the right is a photo of the MOT, as seen by the naked eye.

1.5×10^9 atoms in our MOT, which are cooled to 500 μK[7], before being transferred to the magnetic trap.

3.4.d Magnetic trapping and evaporation

We have two stages of magnetic trapping, the quadrupole trap and the time-averaged orbiting potential (TOP) trap. The magnetic trap works on the principle that atoms that are in the weak B-field seeking state ($F = 1$, $m_F = -1$ for sodium) are attracted towards the magnetic field minimum of the potential.

The quadrupole magnetic trap is constructed using an “anti-Helmholtz” (not at the Helmholtz spacing) pair of coils (see figure 3.10) and has a minimum (field magnitude goes to zero) at the center with linearly increasing field as one moves away from the origin. This causes a spatially dependent potential for the atoms, which traps $F = 1$, $m_F = -1$ atoms.

---

[7] We do not do optical molasses.

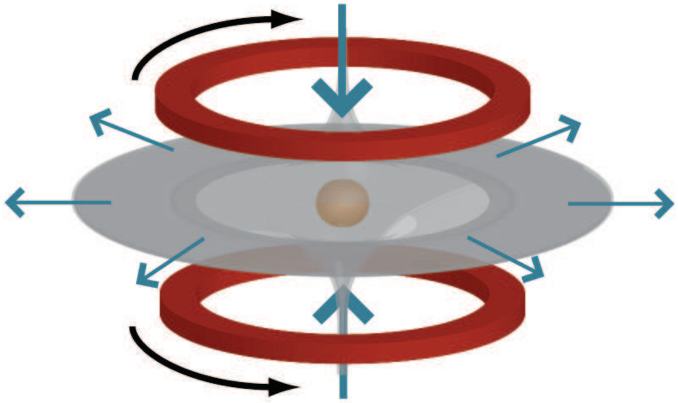

Figure 3.10: Magnetic quadrupole trap : The gray surface traces magnetic field lines, while the magnetic field directions are shown in blue. Atoms are attracted to the magnetic field minimum at the center of the trap.

The energy of an atom is distributed between kinetic and potential energy (the sample is dilute enough to neglect interaction energy). Atoms with higher energy spend more time in higher field areas. Removing such atoms would cause the average energy per particle to decrease. This is done by applying an rf field with a frequency corresponding to the magnetic sub-level splitting at the high-field areas, causing the higher energy atoms to go from the trapped to the anti-trapped states ($F = 1$, $m_F = +1$ for sodium). The remaining atoms thermalize through collisions, thereby lowering the temperature of the atom cloud.

The field zero at the center of the quadrupole traps causes Majorana spin flips [110], where atoms at the center of the trap change their hyperfine magnetic sub-level due to the absence of a well defined quantization axis for their spin. This causes a loss of atoms as the cloud gets colder, not allowing one to reach BEC temperatures.

To overcome the problem of the field zero, the TOP trap is used (first demonstrated by Petrich *et al.* [110]). The TOP trap consists of the superposition of the quadrupole field with a rotating bias field of constant magnitude. For a sufficiently fast rotation (faster than timescales associated with atomic motion but slower than the timescale associated with the energy splitting of the hyperfine levels), atoms see the time-averaged potential. The addition of the rotating bias field moves the field zero away from the center, and while the TOP trap has a time-averaged minimum at the center, the spin quantization axis near the center is always well defined. Using rf evaporation in the TOP trap, we can cool atoms in the TOP trap down to BEC temperatures (transition around 250 nK).

We typically transfer uncondensed atoms from the TOP trap to the optical dipole trap. If we were to allow the cloud to condense in the TOP trap, the typical BEC temperatures would be of the order of 100 nK.

3.5 Laguerre-Gaussian beam

Before we go on to the optical dipole trap, I would like to talk about Laguerre-Gaussian (LG) beams. The LG beam, a crucial component to our experiment, is used for two purposes, creating the toroidal optical dipole trap and transferring orbital angular momentum (OAM) to atoms in the toroidal trap. However, while in the former case, the LG beam is used for its intensity profile, in the latter, it is used for its phase-winding. In this section, I will go over the general properties of the LG beam.

The Gaussian beam can be described as

$$\mathbf{E}_G(r, \phi, z) \propto e^{-r^2/w^2} e^{-ikz} \hat{\epsilon}_p, \tag{3.29}$$

where $\mathbf{E}_G$ is the electric field given in (r, ϕ, z) cylindrical coordinates, $\hat{\epsilon}_p$ is the direction of polarization and w is the beam waist. The wave vector k points along z, which is the direction of propagation. Here, for simplicity, I am assuming monochromatic light of wavelength $\lambda = 2\pi/k$ and am ignoring the curvature of the wavefront and the Gouy phase [111]. Gaussian beams are discussed in detail in several books such as Mandel and Wolf [112], Siegman [113] or Ghatak and Thyagarajan [114].

In equation (3.29), for any plane $z = z_0$, the phase of the wave is nearly uniform, e^{-ikz_0}. In an LG beam, the phase of the wavefront of any plane is modified, and has a winding of $2\pi m$, where m is an integer. An LG beam is denoted by LG_l^m, where the superscript denotes the winding and the subscript denotes the radial order of LG mode, which will not be discussed here (see Pampaloni and Enderlein [115] for details). An LG_0^m beam can be described as

$$\mathbf{E}_{LG}(r,\phi,z) \propto \mathbf{E}_G(r,\phi,z)\left(\frac{r}{w}\right)^{|m|} e^{im\phi}, \tag{3.30}$$

having an intensity node at the center, with the $2\pi m$ phase-winding around it. It should be noted that the LG beam is also a solution of the Helmholtz equation $\nabla^2\mathbf{E} + k^2\mathbf{E} = 0$ [115]. An LG beam can be thought of as an optical vortex with angular momentum of $m\hbar$ per photon [116]. In this thesis, I will only discuss the LG_0^1 beam, which we used in the experiment. The intensity cross-section (time averaged) of the LG_0^1 beam is shown in figure 3.11(b), showing the central node and peaks at $r = \pm w/\sqrt{2}$. In an LG beam, regions that satisfy a spiral shaped $m\phi - kz = \phi_0 \bmod [2\pi]$ will have a uniform phase (shown in figure 3.11(c)), while regions that satisfy $m\phi - kz = \pi + \phi_0 \bmod [2\pi]$ will be phase shifted by π.

An LG beam should not be confused with a circularly polarized Gaussian beam, both of which carry angular momentum. In the former, the polarization $\hat{\epsilon}_p$ is uniform, while in the latter, the polarization goes as $\hat{\epsilon}_p = \hat{\mathbf{x}}\cos kz + \hat{\mathbf{y}}\sin kz$. The LG beam has spiral wavefronts with a central node, while the circularly polarized Gaussian beam has planar wavefronts (assuming no curvature) and an intensity distribution that is identical to a linearly polarized Gaussian beam. The relation between the OAM of an LG beam and the circular polarization of a photon can be seen as the photon analogy to OAM and spin angular momentum of an electron [116]. OAM is associated with the spatial mode, while spin is intrinsic to the particle. However, in the case of light, there is no coupling between the two angular momenta.

LG beams have a breadth of applications, ranging from astronomy to microscopy [117–125]. They are used for their phase-winding, their OAM, or their intensity profile. The phase winding of an LG beam has interferometric applications in phase-contrast optical microscopy [118] and in astronomy, where it is used to remove the glare of a bright star while looking for extrasolar planets [119]. The OAM properties of LG beams have been used to rotate microscopic objects [120, 121]

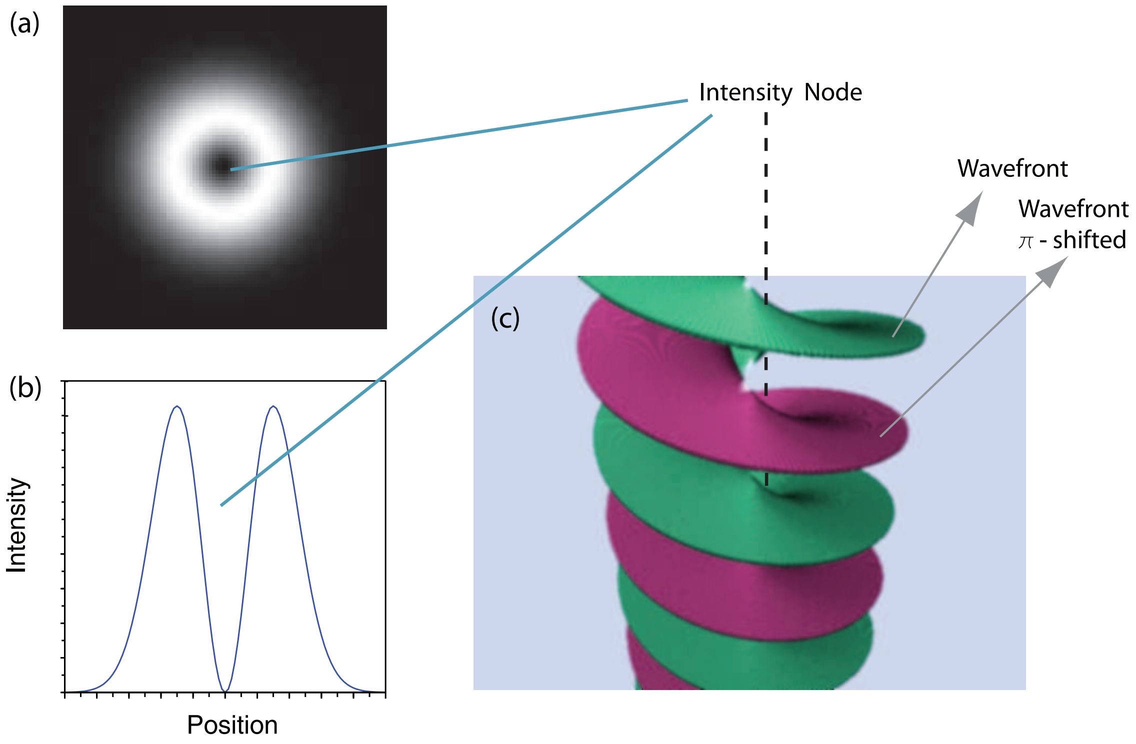

Figure 3.11: Laguerre-Gaussian beam : (a) transverse intensity profile of an LG_0^1 ($m = 1$) beam; (b) An intensity cross-section of the profile; (c) A 3D rendering (approximate) of regions of constant phase for an LG_0^1 beam. As opposed to nearly flat planar wavefronts of a Gaussian beam, the wavefront of an LG beam spirals around the central intensity node. The purple wavefronts have a π phase-shift with respect to the green wavefronts.

and BECs [117, 126]. Rotating of a BEC with an LG beam will be discussed in detail in section 6.2.

When compared to a masked Gaussian beam that has a hole in the center, LG beams have a true node owing to the phase singularity, which is stable under propagation and aberrations. Hence, they are used in applications where a ring shaped beam is required such as sub-diffraction optical microscopy [122, 123], trapping microscopic objects [127] and trapping or guiding[8] cold atoms [129–133], where depending on the light detuning, atoms reside either in the ring-shaped intensity maximum or the central node. In our experiment, we use the LG beam to trap in

---

[8] Ring shaped cold atom guides have also been demonstrated using Bessel beams [128].

the high intensity regions.

Finally, LG beams have been used in several other miscellaneous application such as encoding information [124] and entangling photons [125]. Recently, analogous to LG optical beams, LG electron beams with OAM [134, 135] have also been demonstrated.

3.6 The optical dipole trap

As discussed earlier in this chapter, off-resonant coupling of the ground state of an atom to higher internal excited states can cause a shift in the ground state energy level. Optical dipole traps work on the principle of using such off-resonant light to trap atoms. They have the following advantages over magnetic traps:

- They trap all spin states: This allows one to use the spin degree of freedom of atoms.
- They allow for more varied trap shapes: Using lenses, holograms and other optics, one can create nearly arbitrary shaped traps.
- They can be easily turned off nearly instantly: In contrast to magnetic traps which use high currents and require careful engineering so that they can be turned off rapidly (sub-millisecond time scale), optical traps are usually switched using acousto-optical modulators (AOMs), that can be turned on and off in the microsecond timescale, faster than all the relevant timescales for atoms.

Sodium's $3s$ to $3p$ transition is at 589 nm. Light red-shifted of the D-line (wavelengths longer than 589 nm) lower the ground state energy, causing atoms to be attracted to regions of higher intensity. Conversely, light blue-shifted of the D-line causes atoms to be repelled from regions of higher intensity (so long as there is no significant coupling to other higher excited levels such as 4s 4p, etc.).

We perform our experiments in an optical dipole trap, created by attractive, red-detuned 1030 nm light.

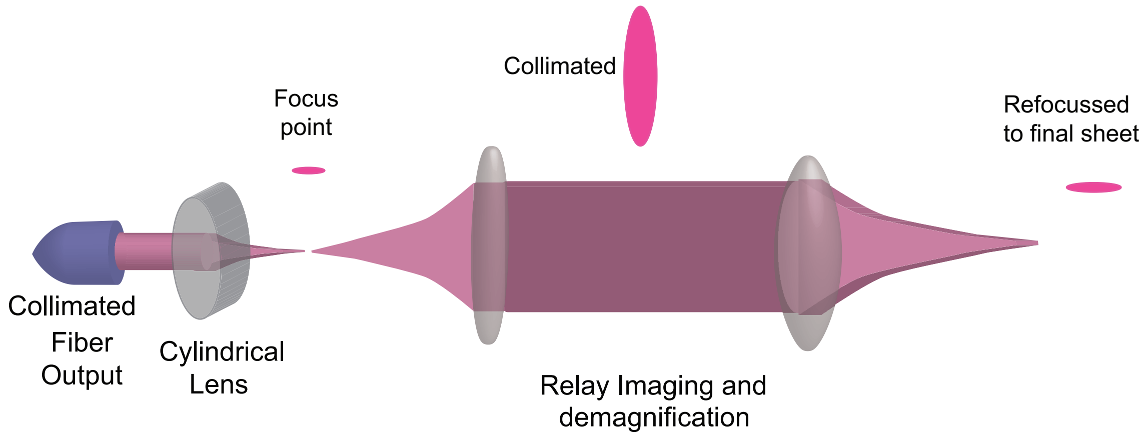

Figure 3.12: Schematic of the optical system for the sheet trapping beam: The sheet trapping beam is created by relay imaging a beam focused by a cylindrical lens. The labelled profiles refer to only the beam along the vertical axis. The horizontal axis of the beam is not focused strongly or collimated at any particular point.

3.6.a The sheet trap

The sheet trapping beam provides tight confinement in the vertical direction, necessary to prevent atoms from falling due to gravity. It also confines in the other two axes, transversely due to its horizontal size and along its direction of propagation due to the Rayleigh range. The beam is created using a cylindrical lens (see figure 3.12). At the focus, the beam has dimensions of about 9 μm in the vertical and around 800 μm in the horizontal ($1/e^2$ radius).

Since the in-plane confinement of the sheet is weak, the addition of any potential in the plane will cause the BEC to take the shape of the other potential. In figure 3.13, we demonstrate some arbitrary potentials created using a spatial light modulator. This will be discussed in detail in chapter 5.

3.6.b The ring trap

For toroidal confinement, we intersect an LG_0^1 beam mode with the sheet. We create the beam using a hologram (see figure 3.14), which consists of a diffraction grating with a single defect. The effect of the defect can be intuitively understood

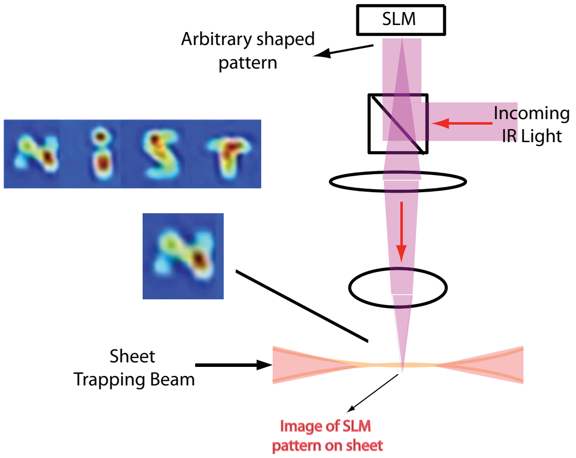

Figure 3.13: Arbitrary shaped BEC: Using a spatial light modulator to image a pattern on the plane of the sheet trap, we can create arbitrary shaped potentials. In the "NiST"picture (with four images), we show BEC realizations shaped 'N', 'i', 'S' and 'T' respectively.

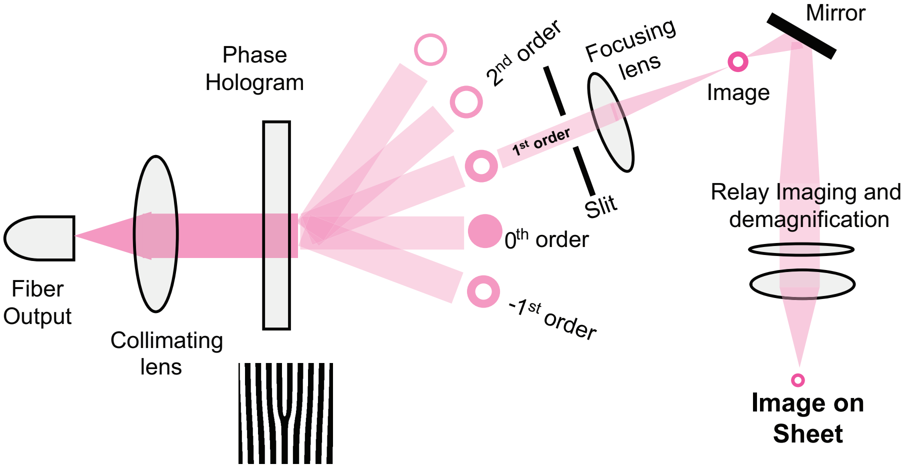

Figure 3.14: Schematic of the optical system for the ring trapping beam: The ring beam is created using a hologram (pattern shown).

as follows. If one were to consider the upper and lower halves of the grating shown in figure 3.14, they can be thought of as being offset by a single half-line (bright on top corresponds to dark on bottom). While both halves will individually diffract light into the same angles, for the first order, the light from the top half will have a phase-offset of π, which causes a phase-winding of 2π in that order ($m = 1$). Higher orders will have increasingly higher integer 2π phase-windings.

The hologram we use is blazed so that the majority of power goes into the first diffracted order, which has a phase-winding of 2π. Although the near-field diffracted beam mode does not have the LG radial profile, with propagation, higher spatial frequencies get filtered out and we obtain the fundamental LG_0^1 mode. Since we focus the beam down to around 40 μm diameter, which is much larger than our diffraction limited spot size of $\approx$4 μm, we obtain a relatively aberration-free ring.

3.7 The microwave system

Before we go on to how we image the BEC, I would like to describe the microwave system that was used to drive transitions between the F=1 and F=2 hyperfine ground states of sodium. The system was implemented during my time at NIST.

As seen in Figure. 3.6, the splitting between the hyperfine ground states of sodium is around 1.77 GHz, which corresponds to the microwave region. At such high frequencies, one needs specialized function generators and amplifiers, and we could not use the exisiting rf circuitry which is used for evaporation in the magnetic trap. Our microwave system consists of four basic components, a synthesizer, a switch, an amplifier and an antenna close to the atoms. I will now describe the components of the microwave system implemented in the lab (schematic shown in figure 3.15).

The synthesizer needs to be able to provide a precise, stable frequency, that is programmable. We used a Holzworth HS2001A synthesizer, which is specified to generate frequencies from 8 MHz to 2 GHz with low phase noise. The device

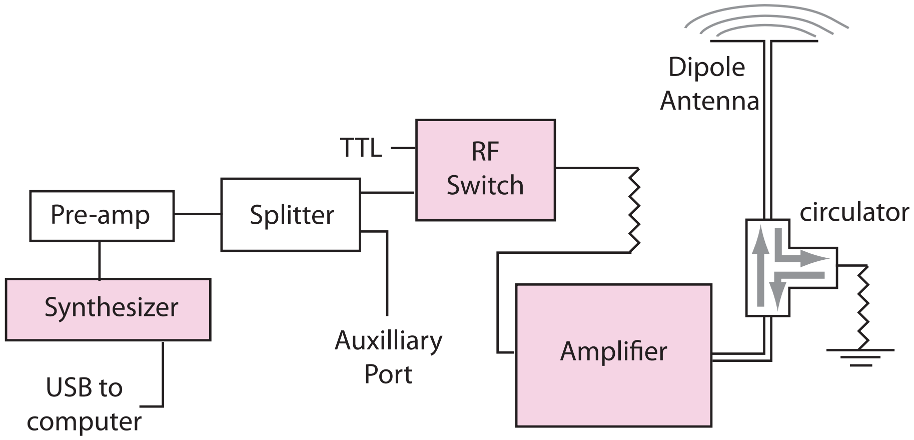

Figure 3.15: Schematic of the microwave system: We use an amplified signal from a precision signal generator (synthesizer) to drive microwave transitions in the sodium atom. The key parts of the system are highlighted. The zig-zag lines denote attenuators.

is programmed via a USB connection to a computer and hence has no display or buttons, which makea it compact. The output passes through a 10 dB preamplifier to boost the signal before it is fed to a splitter. The splitter provides an additional port, which could be used for monitoring the frequency. The microwave signal then passes through a high isolation rf switch (Minicircuits ZASWA-2-50DR), which is controlled by a TTL (transistor-transistor-logic) signal before being fed to the amplifier.

The amplifier (Minicircuits ZHL-10W-2G) provides an amplified output for the antenna. In order to prevent any reflected signal from the antenna from reaching the amplifier, we insert a circulator (directional coupler), which diverts the reflected power into an alternate port, which is terminated. For radiating the ≈17 cm wavelength microwave, we use a simple dipole antenna (see Jackson [84]). To maximize the efficiency, the length of each arm of the antenna is about 4 cm, a quarter of the wavelength. The antenna is aligned along the horizontal plane at an angle of around 45 degrees from the axis of the Zeeman slower.

The magnetic bias field (quantization axis) of our system is along the axis of the Zeeman slower (see figure 3.8). The microwave antenna is oriented at 45

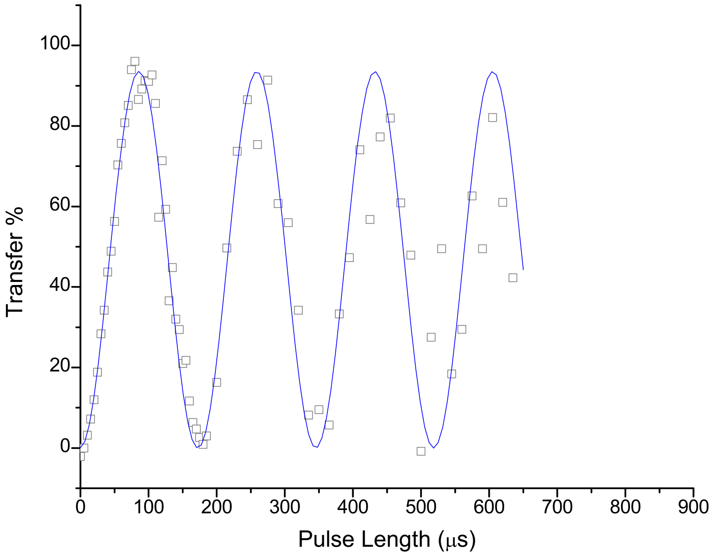

Figure 3.16: Microwave Rabi flopping: A microwave field is turned on for a certain pulse duration, shown on the horizontal axis. The atoms are initially in the $F = 1$, $m_F = -1$ state. The microwave pulse transfers atoms to the $F = 2$, $m_F = -2$ state. At the end of the pulse, we measure the populations in each of the states, and determine the transfer % to the $F = 2$, $m_F = -2$ state. On tuning the microwave frequency to the resonance condition for the $F = 1$, $m_F = -1$ and the $F = 2$, $m_F = -2$ states, we observe Rabi flopping where the population oscillates between the two states. The line is a least squares fit to the initial 2 oscillations. Over long times (>200 μs), fluctuations in the magnetic bias field dephase the oscillations.

degrees to the Zeeman slower axis, in the horizontal plane. The magnetic field of the microwaves are oriented along the vertical, perpendicular to the magnetic bias field direction, allowing hyperfine transitions that change m_F by ±1 (see Jackson [84]). We use our microwave system primarily to couple from the initial $F = 1$, $m_F = -1$ state to the $F = 2$, $m_F = -2$ state. Given our typical magnetic bias fields ($B < 5G$), the $F = 1$, $m_F = -1$ to $F = 2$, $m_F = -2$ transition frequency ranges from 1.761 to 1.771 GHz. By varying the pulse duration, we can choose the fraction we want to transfer to the $F = 2$, $m_F = -2$ state. The transfer fraction follows Rabi flopping and sinusoidally oscillates (Figure. 3.16). The variability of the transfer fraction was the key to partial transfer absorption imaging, which is discussed in chapter 4.

3.8 Imaging

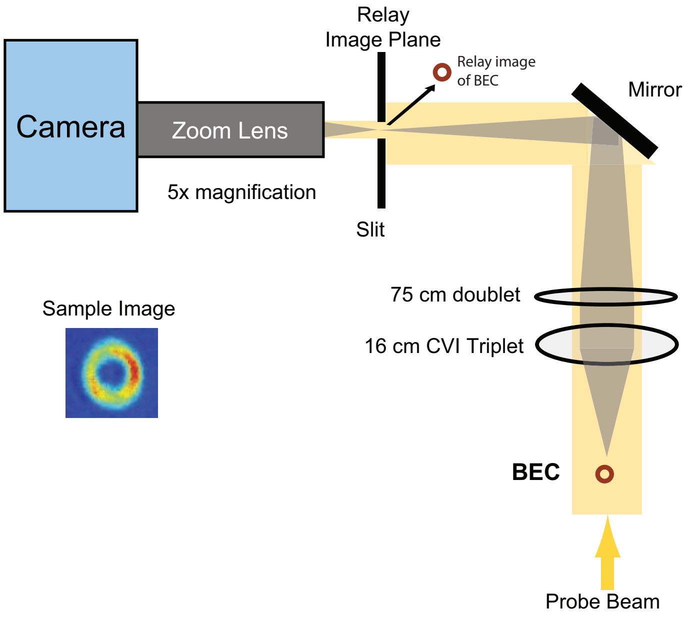

Figure 3.17: Schematic of the imaging system: Our image system images the plane of the sheet and has a resolution of about 4 μm. We use a rectangular slit in the relay image plane to reduce ambient light falling on the camera. While a hole would be more appropriate, using a slit allowed us to independently vary the x and y dimensions of the image.

For our experiment, we use simple absorption imaging. Chapter 4 discusses partial-transfer absorption imaging, which, while a different technique, is still based on absorption imaging. We have the capability to image along both the horizontal and the vertical axes. For most of the data, we image along the vertical axis (see figure 3.17), which images the plane of the sheet yielding more spatial information. Our imaging system uses two steps of relay imaging, each providing magnification. In the first step, which uses the same optics that are used to focus down the LG trapping beam, using a lens pair that consists of a 16 cm triplet (5.08 cm diameter, ≈f/3) and a 75 cm doublet (5.08 cm diameter), a 3x magnified relay image is produced. The optical resolution of our system is limited by the diffraction limit of the triplet (diffraction limited spot size = 0.61 λ/NA ≈2 μm, NA = numerical aperture). Aberrations due to the triplet further reduce it. The relay image is then magnified using a 5x zoom lens on to the Andor Iχon camera. While the total magnification is 15x, with each camera pixel corresponding to 1.2 μm in the plane of the atoms, the actual $1/e$ optical resolution is around 4 μm.

We will now calculate the effect of a certain column density of atoms on resonant ($\Delta = 0$) probe light. The scattering cross-section, σ, is defined as the ratio of the scattered power, $R_s \times \hbar\omega$ to the incident intensity (or energy flux), I. Using equation (3.25), we obtain the scattering cross-section

$$\sigma = \frac{\Gamma\hbar\omega}{2I_{\text{sat}}(1 + I/I_{\text{sat}})}, \tag{3.31}$$

where the saturation intensity I_{sat} is defined in equation (3.26). The next chapter will discuss absorption imaging in detail and exactly solve the absorption imaging problem. For the sake of completeness, I will briefly mention how the basic imaging process works. In the limit of low intensity ($I_i \ll I_{\text{sat}}$), for a given incident intensity I_i, the transmitted intensity is given by

$$I_t(x, y) = I_i e^{-\sigma_0 \hat{\rho}(x,y)}, \tag{3.32}$$

where $\hat{\rho}(x, y)$ is the atom number density, and σ_0 is the scattering cross-section in the low intensity limit (σ in the limit of $I_i/I_{\text{sat}} \ll 1$. σ_0 is the largest scattering cross-section). Using equation (3.32), we can obtain the column density of the atoms from the knowledge of the incident and transmitted light intensity. In practice, this is done by taking 3 images per run; an absorption image in the presence of atoms $I_1(x, y)$, a reference image of the probe in the absence of atoms $I_2(x, y)$, and an image of the background in the absence of probe light $I_3(x, y)$. The column density of atoms (at low probe intensities) is given by

$$\hat{\rho}(x, y) = \sigma_0 \log\left(\frac{I_2(x, y) - I_3(x, y)}{I_1(x, y) - I_3(x, y)}\right). \tag{3.33}$$

3.9 Conclusion

In this chapter, I hope to have given the reader an introduction to atomic physics and some idea of how experiments are performed. Since atomic physics is a large field in itself on which several textbooks have been written, I have been brief, only introducing concepts that are relevant to this thesis.

Likewise, a complete description of the details of the experimental apparatus is beyond the scope of this thesis, and I have only given a general overview of our setup. There are several theses, such as Stamper-Kurn [62], that provide details of the apparatuses and experimental techniques.

Having described our experimental apparatus, and given some background on atomic physics and the sodium atom, which we use, we are ready to delve into the experiments and science that constitute this thesis. In chapter 5, I will discuss our experiments on the toroidal BEC. However, before that, I wish to take the reader on a slight detour and discuss partial-transfer absorption imaging, a technique developed during the course of this work. The reader can feel free to skip chapter 4 and get to the ring trap experiments in chapter 5.

Chapter 4

Partial-transfer absorption imaging

Most BEC experiments take images in time-of-flight as opposed to *in situ*, largely because features in the BEC are too small to image *in situ* and so the cloud of atoms is allowed to expand before imaging[1]. In addition, the time-of-flight expansion provides information about the momentum distribution, which often is more useful than the spatial distribution[2]. In contrast, when we began experiments using the toroidal optical dipole trap, it was important to obtain *in situ* density profiles to be able to create a smooth, uniform ring BEC.

When performing simple absorption imaging on the ring BEC, we found that the probe beam was completely extinguished in regions of high density, preventing us from making accurate quantitative measurements of uniformity. That information was also lost in time-of-flight because of the ring closing on itself. While we could have used an off-resonant probe and tried to deconvolve the distortion from its refraction through the cloud, we developed a new technique, partial-transfer absorption imaging. As it turned out, the technique could also be used to take multiple images of the same cloud. In this chapter, I will describe the technique in the context of other imaging techniques and compare its performance to the more established phase-contrast imaging.

4.1 Introduction

In choosing an imaging technique for an ultracold gas cloud, one traditionally has three choices: absorption imaging, fluorescence imaging or phase-contrast

---

[1] Also, in many experiments, the optical depth of the cloud *in situ* is too high to perform absorption imaging, and hence the cloud is imaged after time-of-flight.

[2] Since most of the early BEC experiments were performed in magnetic traps, magnetic field gradients would distort the *in situ* images, requiring, at the very least, a short time-of-flight before imaging to allow the magnetic fields to shut off.

imaging. Absorption imaging exploits the strong interaction of ultracold gases with resonant laser light. However, the scattering of photons by the ultracold gas cloud leads to heating and destruction of the sample, allowing only one image to be taken per sample. In addition, on-resonant absorption imaging cannot be used for optically thick condensates, due to attenuation of the probe beam. Modifications such as imaging off-resonance, or imaging after expanding the cloud in time-of-flight, can overcome this limitation, but make reconstructing the original cloud profile more difficult. Fluorescence imaging works similarly to absorption imaging, detecting the scattered photons from the cloud instead of the transmitted probe beam. However, the small solid angles for capturing fluorescent light typically make it inferior to absorption imaging for ultracold gas clouds.

Phase-contrast imaging (PCI) [136, 137] and other dispersive techniques [138, 139] are typically used to image clouds of high optical depth (OD). Such techniques use off-resonant probe light, where a relative phase-shift, imparted by the cloud, is detected on the transmitted probe beam. Since the scattering cross-section is severely reduced by going off-resonance, the perturbation to the sample is small, allowing the cloud to be imaged multiple times. PCI is unsuitable for imaging clouds of low OD as it gives a weak signal[3].

Using partial-transfer absorption imaging (PTAI), one retains the advantages of absorption imaging for optically thin clouds while also being able to image optically thick clouds. In this technique, a portion of the cloud from the initial state is first coherently transferred to an auxiliary internal state that has a cycling transition. The transferred cloud is then resonantly imaged on the cycling transition. The recoil energy imparted by scattered photons from the imaging light cause the transferred cloud to be ejected from the trap, while the cloud remaining in the initial state is almost unperturbed, and can subsequently be re-imaged.

In any measurement process, there is a certain amount of perturbation to the

---

[3] One could use an intense probe beam (or a long probe pulse) to overcome the problem of a weak signal. However, even in such situations, the small relative change in the intensity of the probe beam on the detector uses only a small part of the dynamic range of the detector.

sample. In a minimally-destructive imaging technique, that perturbation depends on the desired information, quantified as a signal-to-noise ratio (S/N), leading to a trade-off between the obtained S/N and the sample perturbation. For example, in PCI, reducing the probe light detuning improves the S/N but also causes a greater perturbation to the system [140]. PTAI extends absorption imaging to a minimally-destructive regime, where, by transferring a larger fraction to the auxiliary state for imaging, one obtains a better S/N at the cost of a larger perturbation to the initial cloud.

A key advantage of PTAI over PCI is the ability to easily vary the degree of perturbation to the sample, even for different images within the same experimental run, which is useful in situations where the final cloud is optically much thinner than the initial cloud, such as in characterizing Feshbach resonances [141–143] or Efimov states [144, 145]. PTAI is also useful for studying *in situ* dynamics of quasi two-dimensional condensates where the cloud optical depth in the tightly confined direction may not be high enough to obtain a good phase-contrast image [53, 146, 147].

There have been several techniques used to overcome the problem of high OD [148–150]. However, such schemes have been destructive and cannot be used to take multiple images. Ref. [151] used a partial microwave out-coupling technique, similar to PTAI, in a magnetically trapped BEC. However, since the focus of the work was to study vortex dynamics, the atoms were imaged in time-of-flight. In this chapter, I will focus on using PTAI to obtain an accurate minimally-destructive image of the *in situ* density profile.

The structure of this chapter is as follows: In section 4.2, I will go over the basics of absorption imaging. In section 4.3, I will discuss the PTAI technique and its applicability. In section 4.4, I will present some practical uses of the technique in our experiment. In section 4.5, I will discuss the noise in the measurement process and compare the technique to PCI as a minimally-destructive imaging technique. In section 4.6, I will derive expressions to correct for optical pumping. In section 4.7, I will discuss some of the practical aspects before concluding.

4.2 Absorption imaging

Before we go on to PTAI, let us quickly go over the basics of absorption imaging. Absorption imaging is a standard technique used in many fields to image a sample. The fundamental scatterer is an atom (or molecule), which has a (on-resonant) scattering cross-section $\sigma = \Gamma\hbar\omega/[2I_{\text{sat}}(1+I/I_{\text{sat}})]$ (from equation (3.31)), where, to remind the reader, $\hbar$ is Planck's constant, ω is the frequency of the resonant light, Γ is the natural linewidth of the transition and I_{sat} is the saturation intensity of the transition (defined in equation (3.26)). We factor out the intensity dependence of the (on-resonant) scattering cross-section, expressing it as

$$\sigma = \frac{\sigma_0}{1 + I/I_{\text{sat}}}, \tag{4.1}$$

where σ_0 is the scattering cross-section in the low intensity limit ($I_i \ll I_{\text{sat}}$), given by

$$\sigma_0 = \frac{\hbar\omega\Gamma}{2I_{\text{sat}}}. \tag{4.2}$$

For a cloud density of $\rho(x, y, z)$, where (x, y, z) is the position in space, the change in light intensity, I, for a resonant light beam propagating along the z-direction is given by [80]

$$\frac{dI}{dz} = -I\sigma\rho(x, y, z) = -\frac{I\sigma_0\rho(x, y, z)}{1 + I/I_{\text{sat}}}. \tag{4.3}$$

4.2.a Limit of Low Intensity

In the limit of low intensity, $I \ll I_{\text{sat}}$, equation (4.3) simplifies to

$$\frac{dI}{dz} = -I\sigma_0\rho(x, y, z), \tag{4.4}$$

where one can see that the absorption is linearly proportional to the intensity of the light. Equation (4.4) can be integrated along z, giving an expression for the transmitted light intensity, I_t as a function of the incident light intensity I_i and the column density of the atoms. We will assume that the cloud extends from z_i to z_f. This implies that $I(z_i) = I_i$ and $I(z_f) = I_t$. The column density of the atoms is given by, $\hat{n}(x,y) = \int_{z_i}^{z_f} dz \rho(x,y,z)$. Integrating equation (4.4), we obtain:

$$\begin{aligned}
\int_{I_0}^{I_t} \frac{dI}{I} &= -\int_{z_i}^{z_f} \sigma_0 \rho(x,y,z) dz \\
\log \frac{I_t}{I_i} &= -\sigma_0 \hat{n}(x,y) = -\beta & (4.5) \\
I_t &= I_i \exp\left(-\beta(x,y)\right), & (4.6)
\end{aligned}$$

where $\beta(x,y)$, the (on-resonance) optical depth, is defined as $\beta(x,y) = \sigma_0 \hat{n}(x,y)$ (see appendix C for a sample calibration of σ_0). The optical depth (OD) is a dimensionless quantity which is useful for parameterizing the absorption through the sample. An OD of less than 0.5 corresponds to little absorption. An OD of 1 corresponds to a $1/e$ (37%) transmission. An OD of 4 corresponds to almost complete absorption (nearly 99%).

As one can see in equation (4.6), the transmitted intensity is related to the OD by a simple exponential function. Similarly, the optical depth can be expressed analytically in terms of the transmitted intensity (equation (4.5)).

In practice, analyzing an image using equation (4.5) underestimates the column density. For good image quality, one typically uses an intensity of $I \approx I_{\text{sat}}/2$, which underestimates the column density by about 30%. If one were to weaken the probe down to $I = I_{\text{sat}}/5$, there is still a 20% correction. Hence, while simple analysis of an absorption image can give good qualitative information about an atom cloud, it needs to be corrected for saturation to obtain a quantitatively accurate picture.

Equation (4.5) will be used as a basis for getting a naive estimate of the optical depth and subsequently adding corrections to get the true optical depth.

4.2.b Effect of saturation

The first correction to the analysis of an absorption imaging is saturation. We can rewrite equation (4.3) to separate the variables:

$$\left(\frac{1}{I} + \frac{1}{I_{\text{sat}}}\right) dI = -\sigma_0 \rho(x,y,z) dz. \tag{4.7}$$

Integrating over the the propagation direction, z, similar to the simple case, we get:

$$\int_{I_i}^{I_t}\left(\frac{1}{I}+\frac{1}{I_{\mathrm{sat}}}\right)dI = -\int_{z_i}^{z_f}\sigma_0\rho(x,y,z)dz \tag{4.8}$$

$$\log\left(\frac{I_t}{I_i}\right)+\frac{I_t-I_i}{I_{\mathrm{sat}}} = -\sigma_0\hat{n}(x,y)=-\beta \tag{4.9}$$

Equation (4.9) is identical to equation (4.5) except for a correction term due to the saturation given by $(I_t - I_i)/I_{\mathrm{sat}}$ (see appendix C for a sample calibration of I_{sat}). In the limit of low incident intensity $I_i, I_t \ll I_{\mathrm{sat}}$, the correction term goes to zero.

For a given incident and transmitted intensity, equation 4.9 gives an expression for the optical depth. From a practical standpoint, this suffices for a calculating the optical depth. However, if one were to try and invert the expression (*i.e.* $I_t = f(\beta)$), there is no simple analytic way (using commonly used functions) of obtaining the transmitted intensity for a given optical depth. This makes incorporating further corrections messier, even though the fundamental differential equation is simple.

Having gone through the basics of absorption imaging, we are now set to introduce PTAI.

4.3 Imaging with PTAI

In this section, I will first discuss the requirements for implementing PTAI in the general case before applying it to alkali atoms, and, as is relevant to this thesis, sodium.

4.3.a Requirements for implementing PTAI

PTAI can be used for any atomic species with the following properties (see figure 4.1a). In addition to the initial atomic ground state, $|g\rangle$, the species needs to have an auxiliary state, $|i\rangle$ to which the atoms can be coherently transferred. The state $|i\rangle$ should have access to a cycling transition to a state $|c\rangle$ for optical imaging, where ideally the species only decays from $|c\rangle$ to $|i\rangle$. The lifetime of $|i\rangle$ must exceed imaging timescales. The energy splitting between the two states, $\hbar\omega_{ig}$

should be large enough so that the imaging light does not affect the initial state, *i.e.*, $\omega_{ig} \gg \Gamma_c$, where Γ_c is the natural linewidth of the imaging transition.

In most cases, there is some off-resonant excitation from $|i\rangle$ that causes the transferred fraction, which is being imaged, to eventually be optically pumped out of the cycling transition to another state. In certain circumstances, one could use a second optical repumping beam to bring that fraction back to the cycling transition. However, in situations where the transferred fraction is optically pumped back to $|g\rangle$, one cannot use repumping light, but can nevertheless still use PTAI if the optical pumping due to off-resonant excitation is sufficiently low (discussed in section 4.5.c).

PTAI is well suited (but not limited) to optical dipole traps, which have no spatially varying Zeeman shift that could affect the uniformity of the transfer. For most optical traps, the scattering of several photons transfers a sufficient amount of energy and momentum such that the atoms leave the trap in the direction of propagation of the probe beam. Heating due to collisions between atoms leaving the cloud and the remaining atoms can typically be neglected due to the combination of weak atom-atom interactions and the low densities of ultracold gases as was also observed by Ref.[151].

4.3.b Using PTAI with alkali atoms

The hyperfine structure of alkali metal atoms make them suitable for employing PTAI. The $S_{1/2}$ ground state of alkali atoms has two hyperfine levels between which atoms can be coherently transferred. The condition $\omega_{ig} \gg \Gamma_c$ is satisfied for the ground state hyperfine splitting of all alkali atoms. Alkali atoms have the D_2 optical transition to the $P_{3/2}$ state, and due to the hyperfine splitting of the excited state into four levels, spin selection rules allow certain transitions to be used as cycling transitions[4].

---

[4] The small excited state splittings in lithium (both ^{6}Li [152] and ^{7}Li [153]) and potassium [154] (^{39}K, ^{40}K and ^{41}K) are likely to make the cycling transition for the respective atoms less effective due to off-resonant excitation and consequently optical pumping (discussed in section 4.5.c). One could use polarization selection (using circularly polarized light, analogous to sodium, discussed in

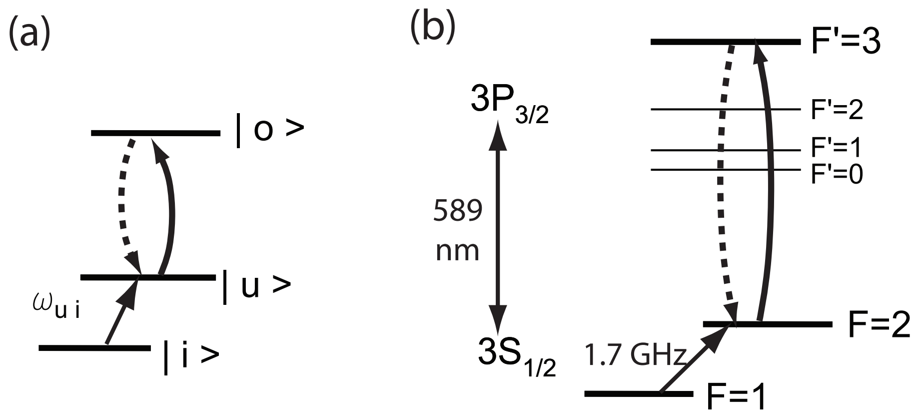

Figure 4.1: (a) General PTAI scheme: PTAI is implemented by coherently transferring a small fraction of the cloud from $|g\rangle$ to $|i\rangle$ and then imaging on the cycling transition $|i\rangle$ to $|c\rangle$. For the scheme to work, the frequency difference ω_{ig} should be much larger than the natural linewidth, Γ_c, of the cycling transition. (b) Sodium D_2 hyperfine structure : Our implementation of PTAI with ^{23}Na uses the F=1 ($|g\rangle$), F=2($|i\rangle$) and F'=3($|c\rangle$) states. For sodium, $\omega_{ig} \gg \Gamma_c$. Optical pumping due to off-resonant excitation to other 3 $P_{3/2}$ states followed by decay to F=1 state is low enough to allow the technique to be used.

For sodium (figure 4.1b), we implement PTAI by keeping the atoms in the initial $S_{1/2}$ F=1 state $|g\rangle$, then transferring a small fraction to the $S_{1/2}$ F=2 state $|i\rangle$ using a single-photon microwave process, and then imaging the transferred fraction on the $S_{1/2}$ F=2 to $P_{3/2}$ F'=3 ($|c\rangle$) cycling transition[5]. For this transition, $\omega_{ig} = (2\pi) \times 1.77\ \text{GHz} \gg \Gamma = (2\pi) \times 9.8\ \text{MHz}$.

4.4 Practical examples using PTAI

In order to illustrate the usefulness of the technique, I will describe three specific case examples of experiments in our setup, which used the PTAI technique, each for a separate reason.

---

the next footnote), to enhance the cycling transition for implementing PTAI.

[5] If one were to use a suitable polarization of light to excite to the $m_F = \pm 3$ magnetic sublevels of the F'=3 state, spin selection rules guarantee that the atom can return only to the F=2, $m_F = \pm 2$ states, which enhances the effect of the cycling transition.

4.4.a *In situ* imaging of an optically thick BEC

PTAI allows for the use of absorption imaging without any change in the optical setup. This is advantageous in situations where one may need to image a high OD cloud *in situ* and a low OD cloud in time-of-flight [52, 54, 155], possibly even within the same experimental run. In our critical velocity experiment (discussed in chapter 7), condensates were created in a ring-shaped trap with a repulsive, permeable barrier cutting across one part of it. The cloud had an on-resonance OD of up to 20 making it unsuitable for absorption imaging *in situ* (shown in figure 4.2d), which obscured the azimuthal density variations. By imaging the cloud using PTAI (figure 4.2b), where we transferred between 15-40% of the atoms depending on the cloud OD, we are able to observe the density variations due to inhomogeneities in the azimuthal potential (figure 4.2c). Plotting the azimuthal profile (figure 4.2e), one can see that PTAI (black) clearly shows the nearly 50% density variation, while absorption imaging (gray) does not.

4.4.b Eliminating trap drift

For calibration purposes of the critical velocity experiment, it was necessary to measure the full profile of the barrier beam. Since the diameter of the repulsive barrier was larger than the annular width of the condensate, we looked at the effect of the beam on a BEC in the sheet optical dipole trap (described in section 3.6). For technical reasons, the sheet trap was found to drift up to 30 μm between shots. Due to this shot-to-shot variation in the position of the dipole trap, we could not use sequential runs to compare images of the BEC with and without the barrier. Instead, by utilizing PTAI, an image with the barrier beam and an image without the barrier beam could be taken in quick succession without destroying the BEC (see figure 4.3) to minimize the relative drift of the BEC and get an accurate reference.

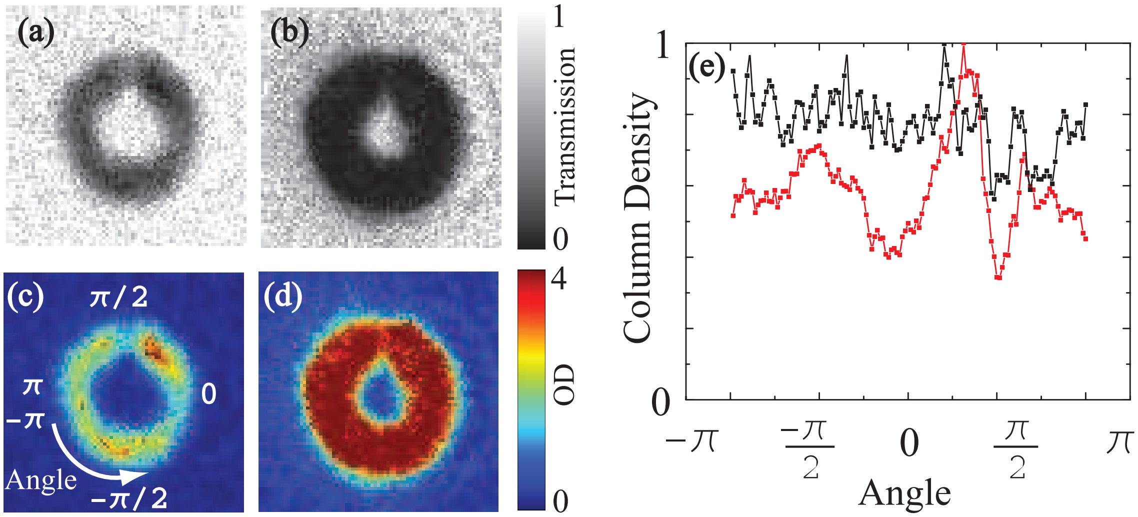

Figure 4.2: Imaging an optically thick cloud: (a) Standard absorption image of an optically thick cloud (grayscale: probe transmission) (b) The corresponding PTAI image of an almost identical cloud using a 16% transfer fraction for the image. From this image we determine the maximum OD to be ≈19. (c),(d) Corresponding column density profiles (colorbar: measured OD). (e) Normalized azimuthal density profiles of the PTAI (black) and absorption (gray) images (angles shown in (d)). Due to the severe attenuation of the probe (seen in (a)), the absorption image fails to show the full optical depth of the cloud and consequently, spatial features such as the azimuthal density variation (plotted in (e)) are unclear and affected by shot noise (discussed in section 4.5). In contrast, the PTAI image shows clear spatial features, particularly the density variations due to azimuthal inhomogeneities of the toroidal potential.

4.4.c Accounting for number fluctuations

In ultracold gas experiments the initial conditions may vary from run to run. This is due to the fact that the process of producing these samples involves several steps of cooling and evaporation, each of which causes fluctuations in the number of atoms and consequently other properties such as the condensate fraction. Although it is possible to average over several experimental runs to overcome the initial fluctuations, one can also, more easily, make a minimally-destructive measurement of the cloud before the experimental procedure to know the initial atom number.

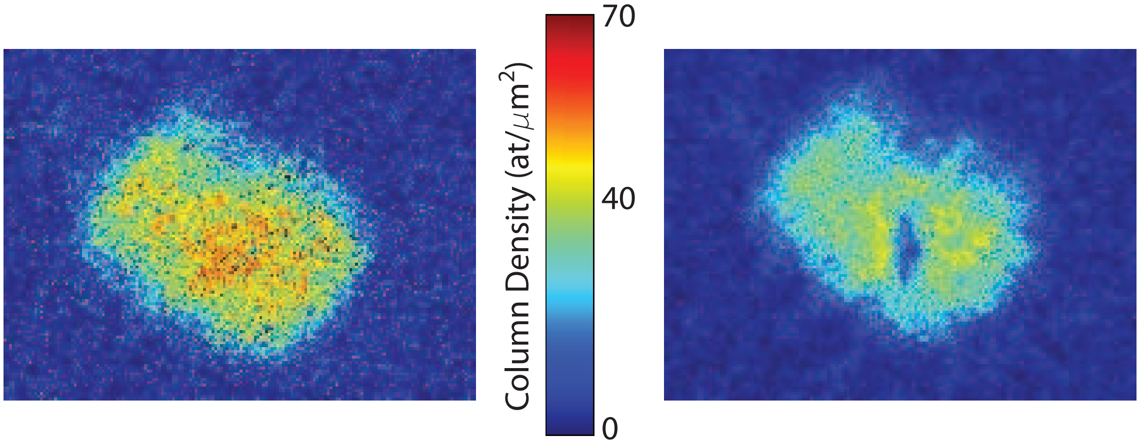

Figure 4.3: Eliminating noise due to shot-to-shot fluctuations in trap position : In one example of an application of PTAI, the effect of drift on measurements of a barrier beam is minimized. In order to obtain the profile of a barrier beam, we take two images, in quick succession, of the BEC in a drifting optical dipole trap, without (left) and with (right) the barrier beam. By keeping the time between the 2 images short (300 ms in this case), we can minimize trap drift to get an accurate comparison of the profile of the atoms, with and without the barrier. Both images are taken with PTAI, transferring 18% and 32% of the atoms respectively. PTAI images have been corrected for saturation and optical pumping using an expression derived in section 4.6

A simple example of this is measuring trap loss of atoms in a sample, which is commonly used to study Feshbach resonances [141–143] and Efimov states [144, 145]. Here, we demonstrate the measurement of the lifetime of a BEC in a trap. The primary loss mechanism is background gas collisions. For every measurement, we take two images, first a reference PTAI image at time $t = 0$, transferring $\approx 15\%$ of the cloud and then a second PTAI image at 300 ms $< t <$ 20 s to determine the final atom number. For the second image, we vary our transfer between $\approx 15\%$ and $\approx 85\%$ to optimally image the cloud. In figure 4.4, we plot the measured condensate lifetime without PTAI (black triangles) and normalized using PTAI (hollow red diamonds). By fitting an exponential decay to the uncorrected data (dashed black line), we obtain a lifetime of 15.4 ± 1.2 seconds, while the corrected data yields 13.5 ± 0.4

seconds. Using PTAI, the uncertainty in the condensate lifetime[6] is reduced by a factor of 3. Hence, PTAI enables one to determine properties such as the vacuum limited lifetime more accurately.

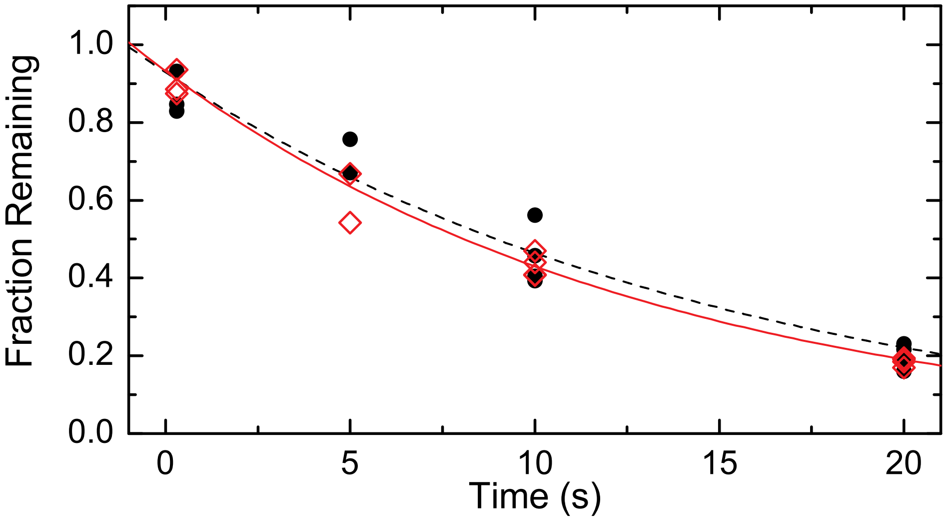

Figure 4.4: Measurement of the BEC lifetime: The circles (filled, black) denote uncorrected values while the diamonds (open, red) denote corrected values, corrected by accounting for the initial number of atoms obtained from a PTAI image (uncertainties lie within points). The respective dashed (black) and solid (red) curves are exponential fits of the points in order to get the decay time. The corrected points produce a better fit and have a smaller variance about the fit. The initial number of atoms is approximately 1.1×10^5.

---

[6] The discrepancy between the two values, being larger than the error bars, is due to a gradual increase in the overall atom number while making the measurements. We made the measurements starting from small hold times and going to large hold times. Had we randomized the order of the measurements, I believe the lifetimes obtained from the uncorrected and the corrected data would agree within the error bars.

4.5 Uncertainty of measurement

To assess the scope and usefulness of PTAI, it is important to obtain an expression for the precision of measurement. In this section, we will do this with a model calculation. We will make some simplifying assumptions and set up the formalism to obtain a figure of merit. We will then derive an expression for the uncertainty of the measurement for PTAI and make a quantitative comparison to PCI for various cloud ODs.

4.5.a Setting up the formalism

To examine the uncertainty, we set up a generalized formalism to analyze the PTAI process. The transmitted probe beam is imaged on a CCD, which consists of a two-dimensional array of photosensors (pixels). Each pixel on the CCD receives probe light transmitted through a specific area of the ultracold gas cloud. For simplicity, we assume that the optical resolution is better than our pixel size and hence can be ignored for this analysis. The precision of the measurement depends on the pixel size, and is ultimately limited by either atom or photon shot noise. One can use a larger pixel size (by binning over adjacent pixels or reducing the optical magnification) to lower shot noise at the expense of spatial resolution. Hence, the choice of pixel size is important.

In the following analysis, we consider a part of the cloud of area A, containing N atoms (see figure 4.5) in the volume enclosed by A along the propagation direction (line of sight). A probe pulse of duration τ passes through the cloud and is incident on the CCD. $\bar{M}$ photons are incident on the imaging area of interest A, and the transmitted photons $\bar{M}_t$, fall on a single effective pixel. We will assume that the probe intensity, $\bar{M}/(A\tau)$ is much lower than the saturation intensity of the transition. The probe time is short enough that atoms are assumed stationary (i.e. $\tau \times v_r \lesssim \sqrt{A}$ where v_r is the total recoil velocity imparted to an atom). The probe light transmitted through the area of interest A, is ultimately incident on a single effective pixel, which is our detector. We will assume a single efficiency coefficient

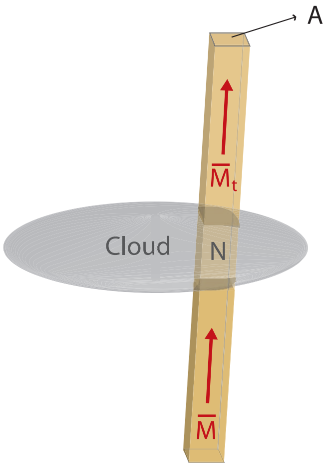

Figure 4.5: Analysis Setup: The imaging area of interest A of an ultracold gas cloud is shown. Within A, the incident probe of $\bar{M}$ photons passes through N atoms giving a transmitted probe of $\bar{M}_t$ photons that are ultimately incident on a single pixel of a CCD, which constitutes the detector.

η for the imaging system, which includes both transmission efficiency of the optical beam path to the CCD and the quantum efficiency of the detector.

In the general case, for a probe pulse of frequency ω, imaging on a cycling transition with resonance frequency ω_0, and linewidth Γ, the normalized detuning $\tilde{\Delta} = (\omega - \omega_0)/(\Gamma/2)$ is used. The (on-resonant) optical depth of the area of interest is $\beta = N\sigma_0/A$ (σ_0 is the resonant scattering cross-section). Assuming that the atom cloud density varies slowly over distances on the order of the wavelength of the light, one can use the eikonal approximation[7] for the light propagation. This gives:

$$\begin{aligned} \bar{M}_t &= \bar{M} \exp\left(-\frac{\beta}{1+\tilde{\Delta}^2}\right), && (4.10) \\ \bar{M}_{\text{abs}} &= \bar{M}\left[1 - \exp\left(-\frac{\beta}{1+\tilde{\Delta}^2}\right)\right], && (4.11) \\ \delta\phi &= \beta\frac{\tilde{\Delta}}{2(1+\tilde{\Delta}^2)}, && (4.12) \end{aligned}$$

where $\bar{M}_{\text{abs}}$ is the number of absorbed photons and $\delta\phi$ is the phase shift imparted to the transmitted probe. For PTAI, imaging is done on resonance ($\tilde{\Delta} = 0$) and hence

---

[7] This is a standard approximation, though not explicitly stated, in classical optics. It is related to the WKB approximation used to model wave-like particles in quantum mechanics.

there is no phase shift ($\delta\phi$=0). In using the PTAI technique, we transfer a desired fraction of atoms, γ, which correspond to a transferred OD of $\beta_f = \gamma\beta$, and number $N_f = \gamma N$. In this calculation, we assume that the atom does not get optically pumped out of the cycling transition through the imaging process. In practice, this puts a limit on the number of incident photons $\bar{M}$, which will be discussed later in this section. With this description, we can now proceed to calculate the uncertainty of the measurement.

4.5.b Shot noise

Shot noise limits the precision of PTAI in two ways, the photon shot noise of the light and the quantum projection noise in the transferred atoms. The detector photon count depends on the light transmitted through the sample, $\bar{M}_t$ and the detection efficiency, η. The photon shot noise, $\mathcal{N}_{\text{phot}}$, of the beam is given by the square-root of the number of photons and is given by,

$$\mathcal{N}_{\text{phot}} = \sqrt{\bar{M}_t\eta} = \sqrt{\bar{M}\eta e^{-N_f\sigma_0/A}}. \tag{4.13}$$

The partial transfer creates a coherent superposition of the cloud in the initial and auxiliary states. The imaging pulse collapses the superposition into an incoherent splitting. The fluctuations from quantum projection give a standard deviation of $\sqrt{N_f}$ for a transfer of N_f atoms, for small N_f/N. Since we ultimately measure the photon count, we need to express the variation in terms of a variation of photon counts. We take the difference in photon counts for the case of the mean value, N_f, and the case of one standard deviation away from the mean, $\sqrt{N_f}$. The atom shot noise, $\mathcal{N}_{\text{at}}$, expressed in terms of photon counts measured by the detector is given by

$$\begin{aligned}
\mathcal{N}_{\text{at}} &= \bar{M}\eta \times \frac{1}{2}\Big[\exp\Big(-(N_f + \sqrt{N_f})\sigma_0/A\Big) \\
&\qquad - \exp\Big(-(N_f - \sqrt{N_f})\sigma_0/A\Big)\Big], \\
\mathcal{N}_{\text{at}} &= \bar{M}\eta e^{-\beta_f}\sinh\left(\sqrt{N_f}\sigma_0/A\right).
\end{aligned} \tag{4.14}$$

We can eliminate the awkward $\sinh(\sqrt{N_f}\sigma_0/A)$, using ($\sinh x \approx x$ for $x \lesssim 1$):

$$\begin{aligned}
\sinh(\sqrt{N_f}\sigma_0/A) &= \sinh(\sqrt{\sigma_0\beta_f/A}), \\
&\approx \sqrt{\sigma_0\beta_f/A} = \beta_f/\sqrt{N_f}, \\
\sinh(\sqrt{N_f}\sigma_0/A) &\approx \beta_f/\sqrt{N_f}.
\end{aligned}$$

Since $\beta_f \sim 1$, $\sigma_0 \leq 6\pi(\lambda/2\pi)^2$ and $A \gtrsim \lambda^2$ (optical resolution limits), $\sqrt{\sigma_0\beta_f/A} \lesssim 1$, and so our approximation is justified[8].

4.5.c Uncertainty in measured optical depth

In using the PTAI scheme, a small β_f gives a poor S/N due to low probe beam absorption. It may appear that the S/N should improve with larger β_f with the best S/N at complete transfer ($\beta_f = \beta$). However, for $\beta_f \gtrsim 4$, there is a loss of contrast due to the severe attenuation of the probe through the sample, which is not accounted for by this simple S/N treatment. For this reason, we choose the uncertainty in the measured optical depth as the metric for the quality of the image, which we will now derive by combining the noise sources and propagating it through the image analysis.

Since the noise sources are independent, they add in quadrature,

$$\begin{aligned}
\mathcal{N} &= \sqrt{\mathcal{N}_{\text{phot}}^2 + \mathcal{N}_{\text{at}}^2}, \\
&= \sqrt{\bar{M}\eta e^{-\beta_f}\left[1 + \bar{M}\eta e^{-\beta_f}\left(\frac{\beta_f^2}{N_f}\right)\right]}. \qquad (4.15)
\end{aligned}$$

Before we move ahead, it is important to consider the effect of off-resonant excitation, which transfers atoms out of the cycling transition. The rate of off-resonant excitation is proportional to the probe light intensity, which puts a limit on $\bar{M}$.

---

[8] The alert reader may wonder if the approximation is justified, given that $\sinh 1 \approx 1.2$. As the purpose of this calculation is to obtain a measure for the uncertainty, the scaling is more important than numerical corrections. The $\lesssim 20\%$ factor comes from the choice of uncertainty limits when we converted the quantum projection noise arising from the partial transfer to detector count variations.

The exact calculation (shown in section 4.6) to account for optical pumping is quite involved and is not completely necessary for the current analysis. For now, I will ignore the effect of optical pumping, but will put a limit on the number of photons each atom can absorb :

$$\begin{aligned} \frac{\bar{M}_{\text{abs}}}{N_f} &\leq \alpha, & (4.16)\\ \bar{M} &\leq \frac{\alpha N_f}{1 - e^{-N_f \sigma_0 / A}}. & (4.17) \end{aligned}$$

where α is the number of photons an atom can absorb and scatter with the effect of optical pumping being small compared to the uncertainty in measurement. The effect of optical pumping should be less than 10% for the comparisons given in section 4.5.d. The exact value of α depends on atomic structure ($\approx$ 75 for our scheme using sodium).

On setting $\bar{M}$ to its maximum allowed value, the total noise, $\mathcal{N}$, is then

$$\mathcal{N} = \sqrt{\frac{\alpha N_f \eta e^{-\beta_f}}{1 - e^{-\beta_f}} \left(1 + \frac{\alpha \eta \beta_f^2 e^{-\beta_f}}{1 - e^{-\beta_f}}\right)} \tag{4.18}$$

As in the case of traditional absorption imaging, the measured optical density is inferred by comparing the image against a reference image taken in the absence of atoms. Here, we assume that the reference is averaged over several images and so has no shot noise associated with it.

The *measured* optical depth is, on average β_f. From the measured optical depth ($\approx \beta_f$), and the chosen transfer fraction γ, we infer the original optical depth β_m. The measurement uncertainty, $\delta\beta_m$, can be calculated from the total noise (see appendix A.1):

$$\delta\beta_m = \frac{1}{\gamma} \sqrt{\frac{1 - e^{-\beta_f} + \alpha \eta \beta_f^2 e^{-\beta_f}}{\alpha \eta \beta_f (A/\sigma_0) e^{-\beta_f}}}, \tag{4.19}$$

The above equation expresses the uncertainty in measurement only in terms of the optical depth of the transferred fraction and the resolution and can be used to find the optimal transfer fraction for a given β. A larger pixel size (i.e. higher A) produces a proportionally lower uncertainty in the measured optical depth. In the limit of wanting to only know the total atom number without any spatial information, one could bin pixels over the entire cloud, thereby grossly reducing the shot noise.

The perturbation to the sample, necessary for characterizing a minimally-destructive technique, can be quantified in terms of N_f (or γ), which corresponds to the number of atoms lost due to the imaging process. From equation (4.19), one can determine $\delta\beta_m$ for a given atom loss N_f. Alternatively, one can determine N_f required to obtain a specific $\delta\beta_m$.

If optical pumping is sufficiently low ($\alpha\eta \gtrsim 50$), and the transferred optical depth is mid-range ($0.5 < \beta_f < 4$), the photon shot noise can be ignored. The terms containing α dominate in equation (4.19), giving

$$\delta\beta_m = \frac{1}{\gamma}\sqrt{\frac{\beta_f^2}{\beta_f(A/\sigma_0)}} = \frac{\beta_f}{\gamma}\sqrt{\frac{1}{N_f}} = \frac{\beta}{\sqrt{N_f}}. \tag{4.20}$$

From the above equation, one can see that the fractional uncertainty $\frac{\delta\beta_m}{\beta_m} \propto \sqrt{\frac{1}{N_f}}$.

4.5.d Comparison with phase-contrast imaging

We compare PTAI with PCI as a minimally-destructive technique by comparing $\delta\beta_m$ for a given perturbation. The uncertainty of the phase-contrast imaging process is (see appendix A.2)

$$\delta\beta_m = \frac{1}{\cos\left(\frac{\beta}{2\tilde{\Delta}}\right)}\sqrt{\frac{\beta}{\eta N_d}} \tag{4.21}$$

where, N_d is the number of atoms undergoing a recoil event, and $\tilde{\Delta}$ is the normalized detuning of the off-resonant probe beam. As with PTAI, the perturbation to the sample can be quantified in terms of N_d, which corresponds to the number of atoms lost in the imaging process. N_f and N_d are equivalent for clouds at BEC or Fermi degeneracy temperatures, where they correspond to atoms that leave the cloud due to the high kinetic energy (compared to other energy scales) acquired during the imaging process.

Comparing equations (4.20) and (4.21), both techniques have $\delta\beta_m \propto 1/\sqrt{N_f}$. In addition, for PTAI, $\delta\beta_m \propto \beta$, while for PCI, $\delta\beta_m \propto \sqrt{\beta}$. This difference is

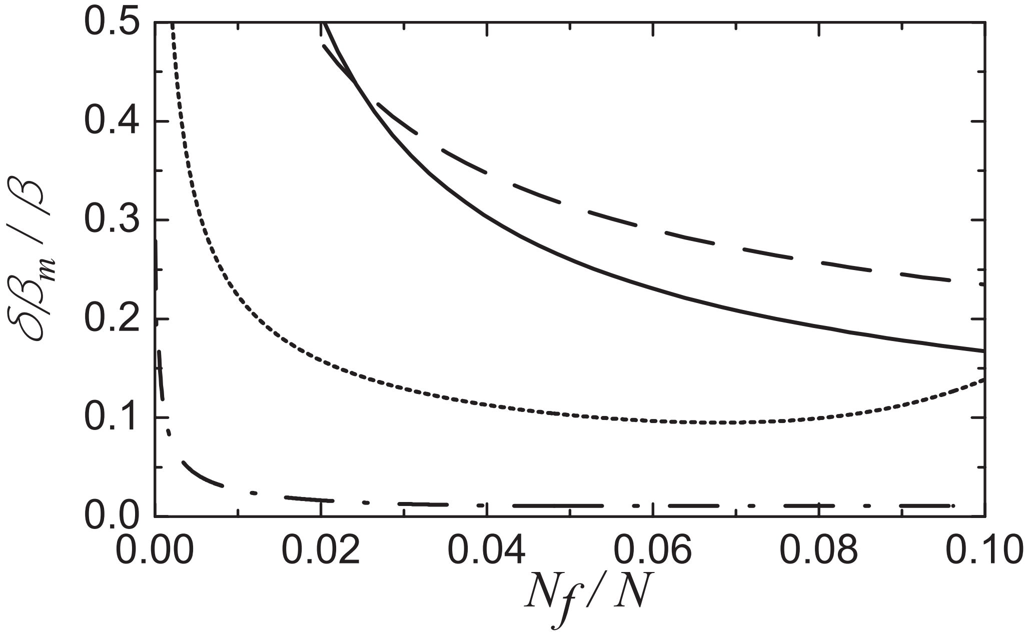

Figure 4.6: Comparison of techniques : (a) For optically thick clouds, $\beta = 100$, PCI (dash) gives a lower uncertainty than the PTAI technique (solid). Pixel size used is 1.5 μm. For PCI, N_f refers to N_d, the number of atoms lost during the imaging process. (b) For optically thin clouds, $\beta = 0.5$, PTAI (solid) works better than PCI (dash). To achieve uncertainty levels comparable to the optically thick clouds, a larger pixel size is needed. Here, we have used a 15 μm pixel size. For both techniques, $\delta\beta_m/\beta$ decreases with increasing N_f/N, showing the trade-off between measurement uncertainty and perturbation of the sample. However, for PTAI, the uncertainty reaches a minimum (as seen in (a)), before increasing with higher transfer fractions (N_f/N) due to attenuation of the probe beam. For PCI, the uncertainty is ultimately limited by the dynamic range of the detector. Here, we assume a detector with a 14-bit dynamic range. The PCI detuning is chosen so that $\Delta^2 \gg 1$ and the phase-shift is modest ($\delta\phi < \pi/4$). In both plots, we have used $\alpha = 75$, the approximate value for our experiments, and have set $\eta = 1$.

because PTAI is usually atom shot noise limited, while PCI is photon shot noise limited.

For situations involving high column densities, $\beta > 20$, typical of some of the largest BECs, PCI gives a lower uncertainty for a given perturbation, while at low column densities ($\beta < 1$), PTAI gives a lower uncertainty as shown in figure 4.6.

For intermediate ODs ($1 < \beta < 20$), typical for many Bose-Einstein condensate experiments, the value of η becomes more important. In this range, PTAI is atom shot noise limited and therefore less sensitive to imaging losses, which often arise due to the complexity of ultracold gas experiments where multiple beams are folded along the imaging path with beamsplitters. In such a scenario, as is the case for our experimental apparatus [54] where $\eta \approx 0.3$, PTAI performs better for a test case $\beta = 2$, even though under ideal imaging conditions, PCI is expected to perform better (figure 4.7).

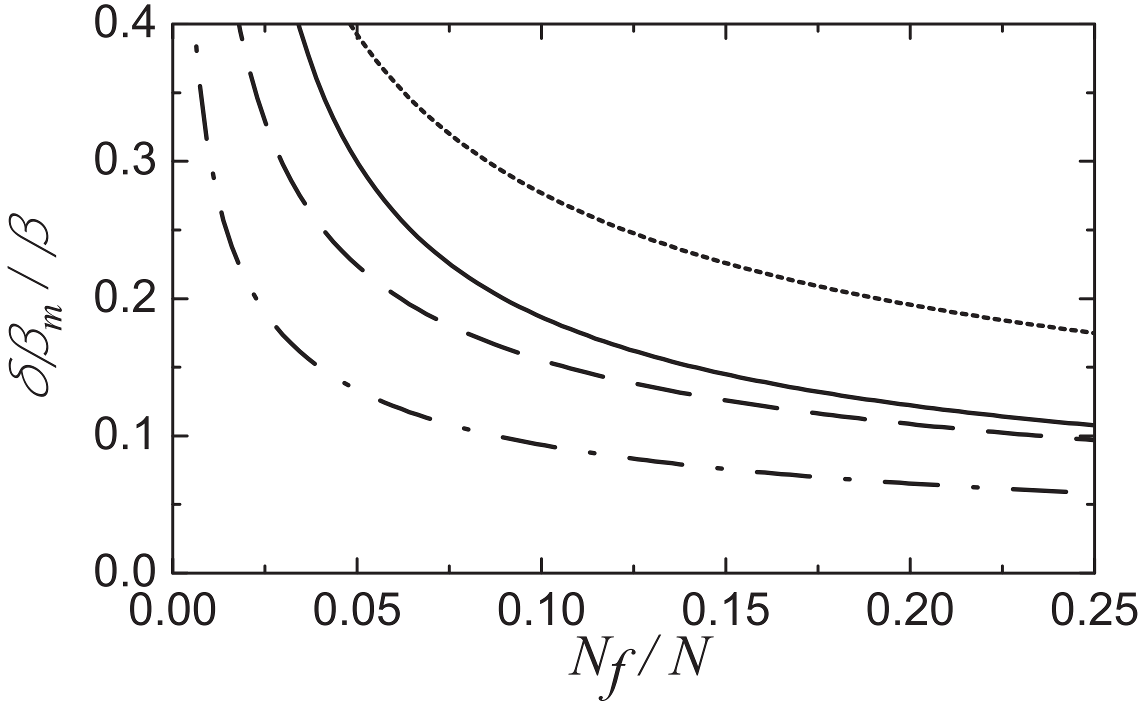

Figure 4.7: Lower sensitivity of PTAI to imaging losses: For $\beta = 2$, PCI (dash-dot) gives a lower uncertainty than the PTAI technique (dot) in the absence of imaging losses ($\eta = 1$). However, when one considers a situation where multiple beams are folded along the imaging beam line leading to high imaging losses ($\eta = 0.3$), the performance of PTAI (solid) is only marginally affected and is better than PCI (dash). A pixel size of 4 μ m has been used. $\alpha = 75$.

4.5.e Scattering of many photons per atom

In the previous section, we set N_f and N_d as equivalent for comparing PTAI to PCI. While for practical purposes they are equivalent, there is one crucial difference. In PCI, the entire atom column contributes to the phase-shift acquired by the probe beam[9]. In the process, every atom has a small probability absorbing and spontaneously scattering a photon. At the end of the imaging pulse, N_d atoms would have undergone a recoil event. In PTAI, only the transferred fraction contributes to the absorption of the probe beam. By imaging on the cycling transition, each transferred atom on average, scatters many photons and therefore acquires several recoil energies, in contrast to PCI where the scattered atoms have only a single recoil energy.

A consequence of the scattering of many photons per atom is that the transferred atoms leave the cloud in the direction of the probe. For most optical dipole traps (trap depth $\approx 1 - 10\mu$K), such atoms are expected to have a sufficient amount of energy (recoil energy $0.5 - 2.5\mu$K per photon for optical transitions, 1.2μK for sodium[10] D2) to leave the trap. However, in PCI, where atoms leave with a single recoil energy, the atoms may oscillate in the trap, and collide with other atoms causing further loss.

In our experiment, we noticed almost no heating when we used PTAI. However, when we used processes that caused atoms to undergo single-photon recoil events[11], similar to recoil events of PCI, we noticed heating and severe loss in the remaining atoms (discussed in chapter 6).

4.6 Correcting for optical pumping

If repumping light was used and the cycling transition for imaging was completely closed, equation (4.9) would suffice. However, with PTAI, in the case of

---

[9] This explains why PCI performs well for optically thick clouds.

[10] 1.2 μK is half the recoil temperature given by $(1/2)k_B T = E_r$, where E_r is the recoil energy.

[11] two-photon Raman transitions and removing an F=1 remnant cloud, which are discussed in chapter 6

sodium, one cannot use repumping light and there is some off-resonant excitation (to the F'=2 state of the $3P_{3/2}$) which decays to the F=1 hyperfine ground state taking the atom out of the cycling transition. This causes a time dependent effect, where the number of atoms participating in the cycling transition decreases with time. Longer pulse lengths give a net lower absorption.

For PTAI to work well, off-resonant excitation should be a factor of 100 or more lower than resonant absorption, because in that case the off-resonant absorption will be significantly less than the on-resonant absorption and will not affect the transmitted intensity I_t. In such situations, the main effect of off-resonant excitation is to create a time dependent optical depth ($\beta(\tau)$), where τ is the time such that $\tau = 0$ is the start of the imaging pulse. This in turn affects the transmitted intensity, $I_t(\tau)$.

Again, we start with the differential equation given in equation (4.3), with an additional time dependence. The z dependence is explicitly shown. For simplicity, I will keep x and y fixed, and omit them from the expressions below.

$$\frac{dI(z,\tau)}{dz} = -\frac{I(z,\tau)\sigma_0\rho(z,\tau)}{1 + I(z,\tau)/I_{\text{sat}}}. \tag{4.22}$$

In addition, we have an off-resonant excitation at a frequency ω_b, which takes atoms out of the cycling transition. This can be expressed as,

$$\frac{d\rho(z,\tau)}{d\tau} = -\frac{I(z,\tau)}{\hbar\omega}\frac{\sigma_b\rho(z,\tau)}{\tilde{\Delta}^2}, \tag{4.23}$$

where $\tilde{\Delta} = (\omega - \omega_b)/(\Gamma/2)$ is the normalized detuning of the excitation from the probe resonance, and σ_b is the optical pumping transition scattering cross-section. It includes the scattering cross-section of the off-resonant excited state and the probability of decay to the other ground hyperfine state. Since the detuning is many linewidths, other terms in the right hand side denominator, including the effect of saturation, are negligible and have been ignored.

To solve for the optical depth, we need to integrate out the z dependence of equations (4.22) and (4.23). Since equation (4.22) is not affected by optical pumping, it can be solved as done in section (4.2.b) to get

$$\log\frac{I_t(\tau)}{I_i} + \frac{I_t(\tau) - I_i}{I_{\text{sat}}} = -\sigma_0\hat{n}(\tau) = -\beta(\tau). \tag{4.24}$$

In order to integrate equation (4.23), we need to solve for the integral of the product of the cloud density and the light intensity $\int_{z_i}^{z_f} dzI(z,\tau)\rho(z,\tau)$. While $\int_{z_i}^{z_f} dz\rho(z,\tau) = \beta(\tau)/\sigma_0$, the product $\int dzI(z,\tau)\rho(z,\tau)$ has not been solved for before. For that, I use some mathematical manipulations. These do not offer any insight and the reader may skip over to section 4.6.b

4.6.a Solving for $\int_{z_i}^{z_f} dzI(z,\tau)\rho(z,\tau)$

We start with the differential equation (4.22), and then rearrange the terms to isolate $I(z,\tau)\rho(z,\tau)$:

$$\begin{aligned} \frac{dI(z,\tau)}{dz} &= -\frac{I(z,\tau)\sigma_0\rho(z,t)}{1+I(z,\tau)/I_{\text{sat}}} \\ \int_{I_i}^{I_t} dI(z,\tau)(1+I(z,\tau)/I_{\text{sat}}) &= -\sigma_0\int_{z_i}^{z_f} dzI(z,\tau)\rho(z,\tau) \end{aligned}$$

By integrating the left hand side over $I(z,\tau)$, and moving σ_0 to the other side, we obtain:

$$\int_{z_i}^{z_f} dzI(z,\tau)\rho(z,\tau) = \frac{1}{\sigma_0}\left(I_i - I_t(\tau) + \frac{I_i^2 - I_t^2(\tau)}{2I_{\text{sat}}}\right) \tag{4.25}$$

4.6.b Obtaining the final expression

Substituting the solved integral from equation (4.25) back into equation (4.23), we obtain an expression,

$$\frac{d\beta(\tau)}{d\tau} = -\frac{\sigma_b}{\hbar\omega\,\tilde{\Delta}^2}\left(I_i - I_t(\tau) + \frac{I_i^2 - I_t^2(\tau)}{2I_{\text{sat}}}\right), \tag{4.26}$$

where the z dependence has been removed. Equation (4.26) has two interdependent variables which are a function of time, the transmitted intensity I_t and the optical depth β. One can then express β in terms of I_t from expression (4.24) giving a master differential equation relating the transmitted intensity I_t and time:

$$\frac{dI_t(\tau)}{d\tau}\left(\frac{1}{I_t(\tau)} + \frac{1}{I_{\text{sat}}}\right) = -\frac{\sigma_b}{\hbar\omega\tilde{\Delta}^2}\left(I_i - I_t(\tau) + \frac{I_i^2 - I_t^2(\tau)}{2I_{\text{sat}}}\right). \tag{4.27}$$

The solution of this equation (see appendix A.3) would give the transmitted intensity as a function of the incident intensity, the initial transmitted intensity and time, i.e. $I_t(\tau) = f(I_i, I_t(\tau = 0), \tau)$. The initial optical depth $\beta(\tau = 0)$ is the transferred optical depth β_f. We can obtain $I_t(\tau = 0)$ from the case when optical pumping is absent (equation (4.9)).

One can then numerically obtain a solution for the measured optical depth given the incident intensity, the transmitted intensity and pulse time.

4.6.c Analytical solutions in special cases

The solution of equation (4.27) shown in appendix A.3 is quite complicated. By making some simplifying assumptions, one can obtain solutions that give a better insight about the physics. I will discuss the case of low optical depth where one can assume that all atoms see roughly the same intensity of light. In this case, one assumes a constant optical pumping and so the rate of loss of atoms is proportional to the incident intensity and the number of atoms:

$$\frac{d\beta(\tau)}{d\tau} = -\frac{\sigma_b}{\hbar\omega\tilde{\Delta}^2} I_i \beta(\tau). \tag{4.28}$$

This can also be derived mathematically from equation (4.27). If one assumed $I_t \approx I_i$ and $I_i \ll I_{\text{sat}}$, one simplify

$$I_i - I_t + \frac{I_i^2 - I_t^2}{2I_{\text{sat}}} \approx I_i\beta,$$

and substitute the result back into the right hand side of equation (4.27) to get the same result.

Equation (4.28) is a first order decay differential equation in β and has a negative exponential solution:

$$\beta(\tau) = \beta_0 \exp\left(-\frac{\sigma_b \tau I_i}{\hbar\omega\tilde{\Delta}^2}\right), \tag{4.29}$$

where $\beta_0 = \beta(\tau = 0)$.

While we have ignored saturation for this expression, it is only a small, indirect contribution as opposed to when we infer the optical depth from the absorption. In fact, it's effect is opposite to that of higher optical depth. In the limit of high saturation, all atoms see roughly the same intensity, but then the optical pumping will be high and the signal to noise ratio will not be good.

Obtaining the optical depth, β_0 in practice, one needs to use the pulse time, τ_p, the incident intensity and the integrated transmitted intensity, $\int I_t(\tau)$. To first order, one can assume an average optical depth over the pulse length, giving us a simple analytical equation:

$$\beta_{av} = \beta_0 \frac{\hbar\omega\tilde{\Delta}^2}{\sigma_b \tau_p I_i}\left[1 - \exp\left(-\frac{\sigma_b \tau_p I_i}{\hbar\omega\tilde{\Delta}^2}\right)\right] \tag{4.30}$$

Using equation (4.9) to correct for saturation, and using equation (4.30) to correct for optical pumping, one can get a reasonable estimate of the actual optical depth.

The effect of the saturation, optical pumping and the analytical correction are show in figure 4.8, calculated for the sodium atom (see Steck [156]). Even at intensities of $I_{\text{sat}}/5$, there is a 10% correction required for saturation. If one corrected for saturation only, one would obtain β_{av} (more or less), which is also plotted. On making the final correction for optical pumping using equation (4.30), one gets a value close to the actual optical depth. For $\beta_0 = 2$, one overestimates the optical depth by 5% at most (see figure 4.8 right).

4.7 Practical considerations in using PTAI

So far in this chapter, we have discussed PTAI, its performance as a minimally-destructive technique and the limitations due to optical pumping. While we quantified perturbation as atom loss, we did not discuss the consequences of sudden atom loss. Although experimental evidence suggests that PTAI does not cause any heating, atom loss affects the equilibrium of a non-linear system like a TF BEC, in which the mean-field energy is balanced by the trap potential. The primary effect is breathing oscillations (discussed in chapter 5), where the sudden[12] lowering of the

---

[12] We have to image faster than the timescale of trap dynamics so as to ensure that we obtain an accurate, undistorted image of the *in situ* cloud. The suddenness of atom loss is unavoidable.

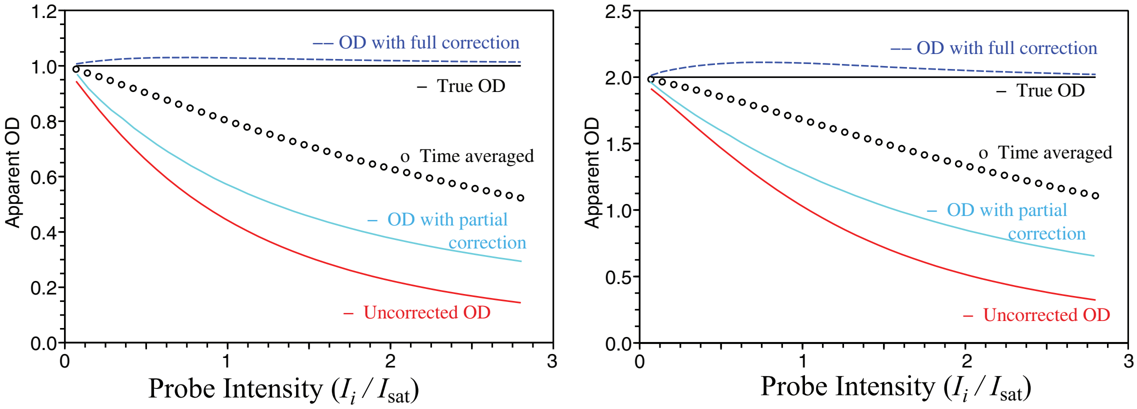

Figure 4.8: Corrected and uncorrected optical depth (OD) as a function of probe intensity for OD=1 (left) and OD=2 (right). The uncorrected OD does not correct for saturation or optical pumping. The partially corrected OD corrects for optical pumping (according to our simple analytical model) only. The fully corrected OD corrects for both saturation and optical pumping. The time-averaged OD gives the mean OD (β_{av}) for the duration of the pulse. For OD=1, our simple analytical correction works well. For OD=2, the correction overestimates the optical depth by about 5% at worst.

mean-field causes a change in equilibrium about which the BEC oscillates. The anharmonicity of the trap then causes the oscillations to populate other modes, which ultimately leads to heating.

The loss of atoms, breathing oscillations and heating, all put limits on what fraction can be transferred (and imaged). Measuring atom loss from the trap (section 4.4.c) is probably the ideal application of PTAI, since the first measurement can use a small transfer fraction[13] and the second measurement is only a measurement of the number of atoms. For other applications, we have to wait until the system equilibrates. In our experiment, even a 5% loss causes observable oscillations *in situ*, which limits any measurement to a time after the oscillations have damped out ($\approx$ 1s). Larger perturbations, such as a 20% transfer cause large oscillations followed by observable heating, which limits any measurement to after a few seconds,

---

[13] As no spatial information is required, the pixel size can be as large as the sample, greatly lowering shot noise.

by which time, rethermalization and background gas scattering cause a nearly 50% loss.

For center-of-mass oscillations, which are often used to measure the harmonic oscillator trap frequency (also known as dipole or sloshing oscillations, discussed in chapter 5), heating or atom loss do not affect the measurement, and PTAI can be used to take repeated measurements when studying center-of-mass oscillations. Repeated measurements in a single experimental run should give a better measurement (compared to a series of experimental runs, with varying oscillation times, and only one measurement per run), and would also yield more data per experimental run.

From practical considerations, for taking actual experimental data, PTAI is most likely to be used as a destructive technique (not minimally-destructive), as with PCI [157], although both techniques have the ability to make minimally-destructive measurements. However, from an experimentalist's point of view, PTAI can be used as a minimally-destructive technique to obtain more data per experimental run, saving time for the experimentalist for measurements that need not be very precise. For example, we have used PTAI to obtain condensate density profiles in our ring trap for a range of atom numbers. Instead of taking several experimental runs, each with different initial conditions, we took several (up to 8) PTAI images of a single BEC. Each successive image had a lower atom number than the previous, and we were able to sample a wide range of atom numbers from a single experimental run.

PTAI (as a minimally-destructive technique) is extremely useful for troubleshooting, allowing the experimentalist to get a snapshot of the BEC at any stage. For example, if one were performing a sequence of procedures on a sample (our experimental sequence to study critical velocity in chapter 7 is one such case), using PTAI, by taking snapshots at different times, one can determine which procedures are working well, and which are not. In particular, if one procedure failed occasionally, say 1 in 10 times, PTAI can help locate the problem, without requiring the experimentalist to specifically test each procedure individually.

PTAI also has some uses as a minimally-destructive technique. PTAI is best suited to take a snapshot of the number of atoms, which typically requires $< 3\%$ perturbation, before any experiment is performed. This is useful either to know what the initial conditions of the sample were, or to use as a check point in a long sequence. Similarly, PTAI can be used to track any sort of trap drift (demonstrated in section 4.4.b), which the experimentalist is unable to eliminate. Also, PTAI can also be used to study center-of-mass oscillations.

4.8 Conclusion

In this chapter, I have discussed the technique of partial-transfer absorption imaging. PTAI can optimally image clouds of the full range of OD and also offers the convenience of being able to easily switch to regular absorption imaging. PTAI is an alternative to PCI as a minimally-destructive technique and performs better for optically thin samples, and for situations which involve imaging losses, such as when multiple beams are folded in along the imaging beam line.

In our lab, PTAI proved to be an invaluable tool in getting a uniform ring trap and was crucial in making accurate measurements of the critical flow velocity. We shall now get back to the BEC physics and study the BEC in the ring trap.

Chapter 5

The ring trap

Superflow, the first evidence of superfluidity observed [9, 10], was the original definition of superfluidity. With Landau's two-fluid model [13] and subsequent theories of quantized vortices in helium [23, 24], the list of characteristic properties of superfluidity expanded. While experiments in atomic BECs have shown convincing evidence of superfluidity [44–51], superflow has been harder to observe. Unlike liquid helium, which could be produced in large quantities and made to flow through long channels, atomic BECs are made in small quantities and hence cannot be made to continuously flow over any long path. A solution to this is to create a multiply-connected geometry and induce flow around a loop.

A vortex in a BEC does create, in a sense, a multiply-connected geometry, since there is a singularity, and hence a "hole", in the vortex core. However, a vortex in a simply-connected BEC is an unstable excitation and can lower its energy by moving towards the edge of the cloud, as has been observed in experiments [45–47, 52, 158]. Hence, one cannot observe truly stable superflow in a simply-connected BEC with a vortex. Given that, the simplest way to realize a multiply-connected geometry for a BEC is by using a toroidal trap. This was a motivation towards building the ring trap.

5.1 Applications of a toroidal potential

Apart from observing superflow, the toroidal potential has other important applications, such as for performing atom interferometry and studying quasi-1D physics, which will be discussed below.

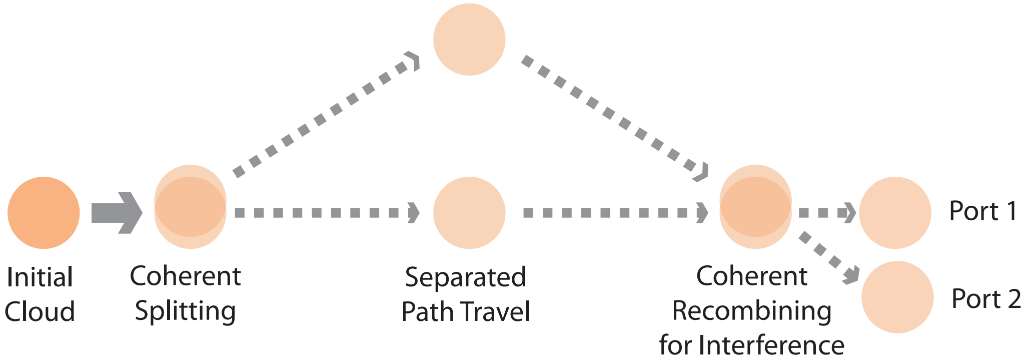

Figure 5.1: Basic scheme of an atom interferometer: As in optical interferometry, atom interferometry requires the coherent splitting and recombining of atoms, giving two complementary interferometer output ports, shown on the right.

5.1.a Atom interferometry

Atom interferometry is performed (figure 5.1) by coherently splitting an atom cloud into two parts, having the two parts travel spatially different paths before recombining and interfering [159]. Atom interferometry is used for gravimetry [160], precision measurements such as measuring the fine structure constant [161–165] and potentially measuring the Newtonian gravitation constant [166–168], and several tests of fundamental physics (see Cronin *et al.* [159]). By making use of the Sagnac effect [169], where the rotation of a closed loop setup causes a differential phase-shift in beams (light or atom) propagating in opposite directions, atom interferometry has also been used to sense rotation [170–172] and cold atom gyroscopes have been demonstrated [173, 174].

While most experiments, including those mentioned above, use free-space atom interferometry, where the coherently split atoms travel in free space, one can implement a configuration where atoms travel along a confined, guided path (or waveguide), akin to optical fibers for light. Guided path atom interferometers have the advantage of operating with higher interaction time and hence yielding a higher signal [159]. Refs. [175–177] used linear waveguides to implement the guided cold atom interferometer. Atoms traveling forward and back on the same waveguide

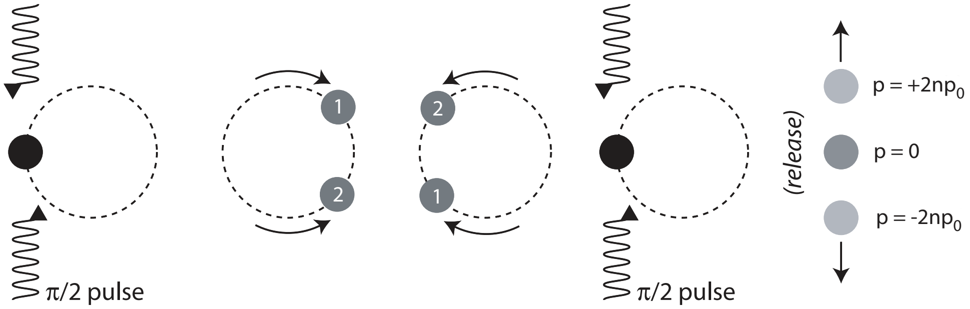

Figure 5.2: Sagnac interferometer using toroidal confinement : Using a $\pi/2$ optical Bragg scattering pulse [77, 178], the atom cloud can be coherently separated into two parts (labeled "1" and "2") which travel in opposite directions around the ring and can be made to interfere by using another $\pi/2$ Bragg pulse when they overlap, giving two interferometric output ports (which have momenta of $\pm 2np_0$, p_0 is the photon-recoil momentum and n is the order of the Bragg pulse). The read out could be the number of atoms in each port, which would change if the apparatus is made to rotate. (from Moore [179])

cancel any accumulated phase-shift to first order. In order to break that symmetry, Wang *et al.* [175] used a magnetic field gradient while Wu *et al.* [176] translated the waveguide perpendicular to its axis.

One can use a toroidal potential as a waveguide for guided path atom interferometry (described in Moore [179]), by placing atoms on one part of the ring, coherently splitting them into two parts that travel along opposite sides on the ring and recombine after they travel the ring in opposite directions (figure 5.2), making an atom Sagnac interferometer.

A BEC in a toroidal geometry can also be used to sense rotation analogous to a SQUID (Superconducting QUantum Interference Device) for sensing magnetic field. A SQUID consists of a superconducting loop [1, 180] with one or two tunnel junctions (or weak links). The quantum coherence of the superconductor across the tunnel junction and around the loop allows for a highly sensitive detection of magnetic field. The neutral superfluid analog of magnetic field in a superconductor is rotation [47]. When one makes the transformation to the rotating frame, the

Coriolis force becomes the effective magnetic field. Hence, a BEC in a toroidal geometry with one or two weak links could be used to make a rotation sensor. Superfluid helium has been used to sense the earth's rotation [181, 182].

5.1.b Quasi-1D physics

A toroidal BEC can also be used to study quasi-1D physics. Since the first BECs, there has been a lot of interest in Bose gases in traps that are highly anisotropic [183], particularly those that are elongated and cigar-shaped [184, 185], making them quasi-1D. Although condensates in such traps are 3D in nature, their transverse lengths being much larger than the thermal de Broglie length and the condensate healing length, they can exhibit 1D-like behavior such as longitudinal phase fluctuations [184, 186], that have been observed by spatial fluctuations in the time-of-flight density profile [187], measuring the spatial correlation function [188, 189], Bragg momentum spectroscopy [190]. The 1D-3D dimensional cross-over has also been theoretically studied [191, 192].

When used to study quasi-1D physics, a narrow, bicycle-tire like toroidal BEC has the advantage of being azimuthally uniform (ideally) over the entire circumference, compared to cigar-shaped clouds, which have a gradual taper as one goes away from the center along the axis. From a theoretical point of view, one can treat the system more exactly using periodic boundary conditions. BEC parameters such as the mean field, the population of thermally excited modes and the longitudinal sound speed are ideally all invariant as one goes around the torus. Another feature of a toroidal BEC is the interference of the entire cloud at the axial center when released in time-of-flight. This feature has been used to detect circulation in the torus [52, 54] and can be used to detect phase fluctuations [193].

5.2 Previous ring trap experiments

There have been several different schemes for making ring traps and ring waveguides. While the first experiments used larger ring traps (millimeters or above) primarily as waveguides, later experiments used smaller traps down to sizes that could hold a BEC in its ground state.

In one of the first such experiments with ultracold gases, Crompvoets *et al.* [194] created a 25 cm diameter hexapole electrostatic circular waveguide for polar deuterated ammonia. The molecules were loaded from a 200 K source using a pulsed solenoid valve followed by a Stark decelerator that produced molecule bunches around 100 m/s with a spread of 4-5 m/s corresponding to a translational temperature of 10 mK. The molecules were found to make up to 6 round trips before the velocity spread caused a broadening of the bunch making it difficult to detect.

Later, Sauer *et al.* [195] created a 2 cm diameter ring waveguide for cold neutral rubidium atoms. The ring waveguide was created using two parallel current carrying wires, which produced 2D confinement and an extended magnetic field zero at the mid-point between them. The $\approx$60 μK atoms were loaded from a magneto-optical trap followed by optical molasses. The atoms were accelerated downwards by gravity and guided with guide wires so that they could be loaded into the ring. The atoms made up to 7 trips around the ring before they were undetectable due to losses, primarily from Majorana spin flips.

In similar work, Wu *et al.* [196] created a 3 cm “stadium”-like ring waveguide for ultracold atoms. The rubidium atoms were loaded directly from a 2D MOT. The atoms were launched bi-directionally around the waveguide using an optical standing wave, and filled the entire ring.

In 2005, the first BECs in circular waveguides were reported. Gupta *et al.* [197] produced a BEC in a horizontal, few-millimeter diameter ring-shaped magnetic waveguide. The waveguide was created by a ring quadrupole with a time-averaged potential to overcome the problem of Majorana losses. The BEC was formed on one side of the tilted ring and then launched into the waveguide. The BEC circulated in the waveguide until its azimuthal expansion filled the entire waveguide uniformly.

Around the same time, Arnold *et al.* [198] created a BEC at the top of a vertical 10 cm diameter quadrupole magnetic ring (see figure 5.3a). The vertical geometry was used to split an atomic cloud into two counter-rotating clouds which were recombined after one revolution. An azimuthal magnetic field from a current carrying wire along the axis was used to overcome the problem of Majorana losses. In both experiments, rubidium-87 was used.

While the experiments discussed so far have involved magnetic traps and waveguides, there have been other proposals for creating ring traps. Several groups have proposed creating ring traps using LG beams. Arlt *et al.* [130] proposed using a tightly focused LG beam to create a ring trap at the focus. A similar scheme was implemented by Olson *et al.* [199], using a blue-detuned high order LG beam, trapping ultracold thermal rubidium-85 atoms. Amico *et al.* [200], proposed using the standing wave created by a retroreflected LG beam to produce a stack of rings. Courtade *et al.* [201] trapped cold atoms in a stack of rings, created by the interference of an LG beam with a counterpropagating Gaussian beam. Carter *et al.* [202] proposed using an LG beam optical molasses to cool and trap atoms in a ring geometry.

Other groups have suggested the use of other electromagnetic fields. Hopkins *et al.* [203] proposed a scheme using magnetoelectrostatic potentials. There have also been proposals using rf dressed atoms [204, 205] in magnetic traps, which have been implemented for thermal atoms [206] and very recently, a BEC [207].

For most applications of toroidal traps, the trap has to have a smooth extended minimum. The roughness in the azimuthal potential has to be less than the mean field (for a BEC) or the temperature (for a thermal cloud), whichever is appropriate. This is particularly difficult to do in some of the larger rings [197, 198], because of the length of the extended minimum and the susceptibility to bumps from inhomogeneities in the wires. Also, in using a small ring (diameter <100 μm), particularly for BECs, the larger mean field[1] is able to overcome small bumps in the potential, something which we will also discuss later in the chapter.

Recently, there have been successful demonstrations of toroidal confinement

---

[1] The number of atoms in a BEC is usually fixed by the experimental setup, and hence in making a smaller BEC, the same number of atoms are confined to a smaller region, which produces a larger mean field.

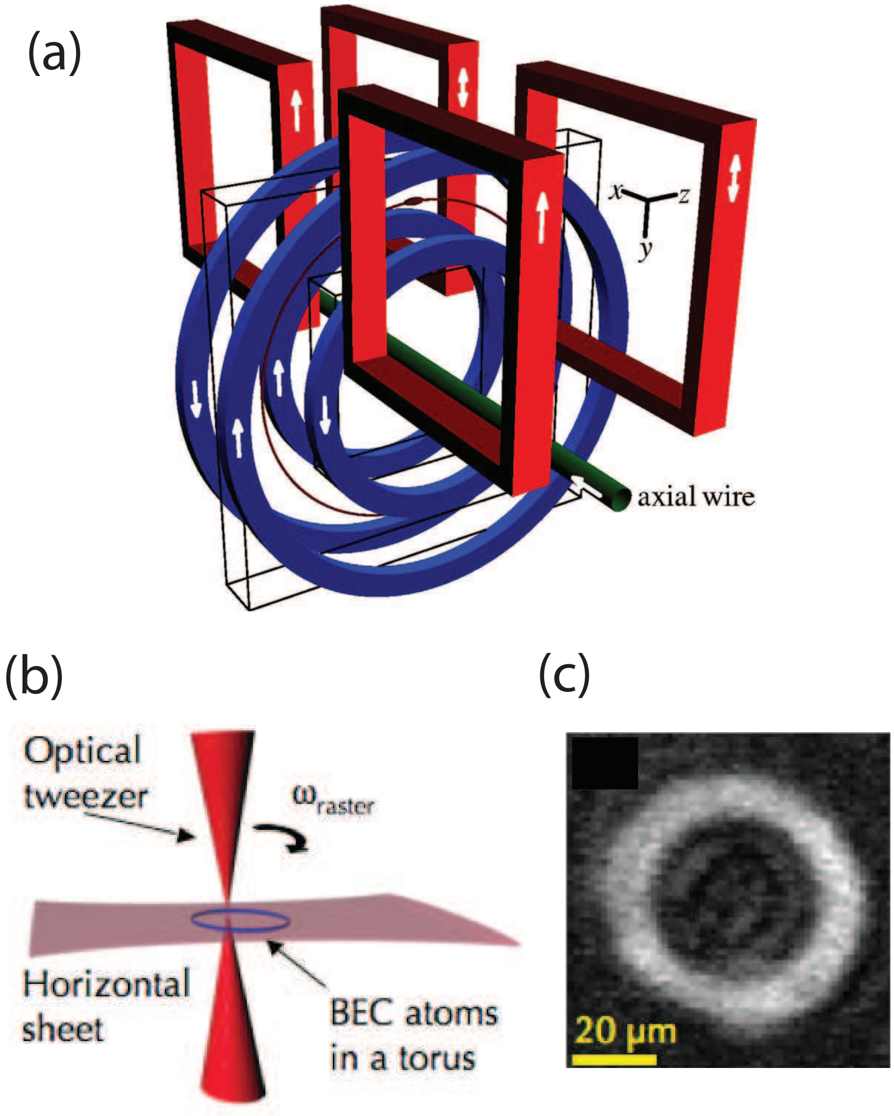

Figure 5.3: Previous ring confinement schemes : (a) Vertical 10 cm diameter ring from Arnold *et al.* [198] using the four circular wires. The BEC (small cigar) is created at the top of the ring with the help of the four square coils. The vertical geometry was used to split an atomic cloud into two counter-rotating clouds which were recombined after one revolution. (b) Toroidal BEC from Henderson *et al.* [147], using the combination of a horizontal sheet beam and a vertical scanning beam. The circular time-averaged scanning beam creates a ring potential, which creates a ring-shaped BEC, shown in (c).

using a combination of magnetic and optical potentials [52, 208], similar to some of the early BEC experiments which explored different shapes [42, 209]. Other groups have shown toroidal confinement using a scanning acousto-optic deflector to pattern the ring confinement [147, 210]. Of them, Henderson *et al.* [147] are the closest to our experiment [54] since they use a combination of two perpendicularly intersecting optical beams (figure 5.3(b), BEC image shown in (c)).

The all-optical traps (and presumably rf dressed traps also) that use a sheet-like potential [54, 147] have the advantage of separating the axes of confinement and hence are insensitive to any small relative drift between the optical beams. Relative drift has been a problem in toroidal traps that use a combination of a magnetic trap and an optical plug [52]. Having discussed the various schemes of creating a toroidal potential, we shall now move on and look at our all-optical ring trap.

5.3 The ring trap potential

To remind the reader, our ring trap is created by the intersection of a horizontal sheet beam that provides vertical confinement and a vertical LG_0^1 beam that provides annular confinement[2] (figure 5.4). In this section, we will calculate the optical potential created by the two beams to obtain an expression for the trapping potential in terms of the trap depth and trap frequencies.

We begin with the LG beam profile (discussed earlier in section 3.5), which has a cross-sectional electric field profile,

$$\mathbf{E}_{\mathrm{LG}}(r,\phi) = \mathbf{E}_0 \left(\frac{r}{r_0}\right) e^{-\frac{r^2}{r_0^2}} e^{i\phi}, \tag{5.1}$$

where $\mathbf{E}_0$ is the field strength, r_0 is the LG beam width, and radial coordinates (r,ϕ) are used. The corresponding intensity profile is given by

$$I_{\mathrm{LG}}(r) = I_0 \left(\frac{r}{r_0}\right)^2 e^{-\frac{2r^2}{r_0^2}}, \tag{5.2}$$

where I_0 represents the intensity of the beam. The azimuthal coordinate has been dropped as I_{LG} has no ϕ dependence.

---

[2] All references to the LG beam henceforth refer to the LG_0^1 beam mode.

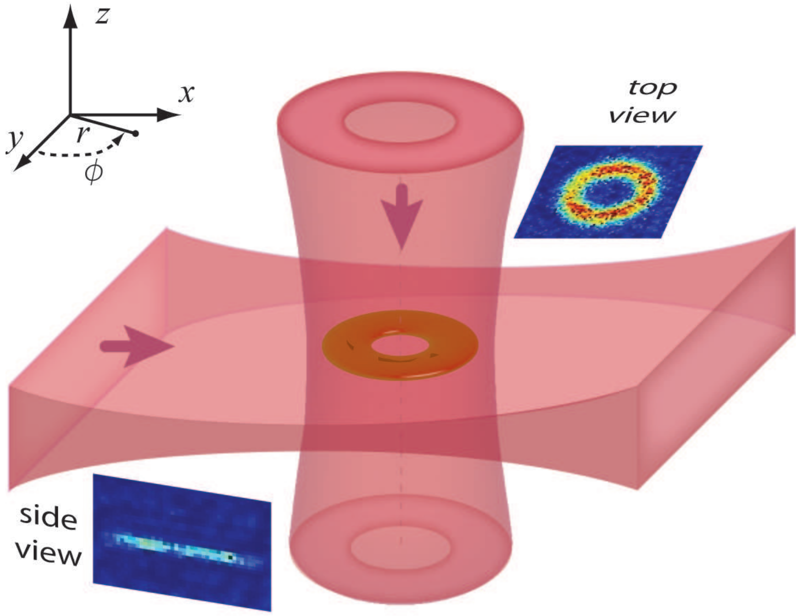

Figure 5.4: Schematic of ring trap (Details of individual beams discussed in section 3.6): Our new toroidal trap is formed by the intersection of a sheet-like horizontal beam and ring-like LG beam. *In-situ* images of atoms in the trap, from both the top and side are shown. The arrows indicate direction of propagation of the respective trapping beams.

Since the strength of the LG beam is normally given in terms of the power of the beam, we shall now express I_0 in terms of the power P_{LG}. We perform the area integration of the intensity profile from 0 to ∞:

$$\begin{aligned} P_{\mathrm{LG}} &= \int_0^\infty 2\pi r dr \left(I_0 \frac{r^2}{r_0^2} e^{-2\frac{r^2}{r_0^2}} \right), \\ P_{\mathrm{LG}} &= \frac{\pi I_0 r_0^2}{4} \qquad (5.3) \\ \Rightarrow I_0 &= \frac{4P_{\mathrm{LG}}}{\pi r_0^2}. \qquad (5.4) \end{aligned}$$

We can now express the cross-sectional intensity profile $I_{\mathrm{LG}}(r)$ in terms of P_{LG} and r_0,

$$I_{\mathrm{LG}}(r) = \frac{4P_{\mathrm{LG}}}{\pi r_0^2} \left(\frac{r}{r_0} \right)^2 e^{-\frac{2r^2}{r_0^2}}. \qquad (5.5)$$

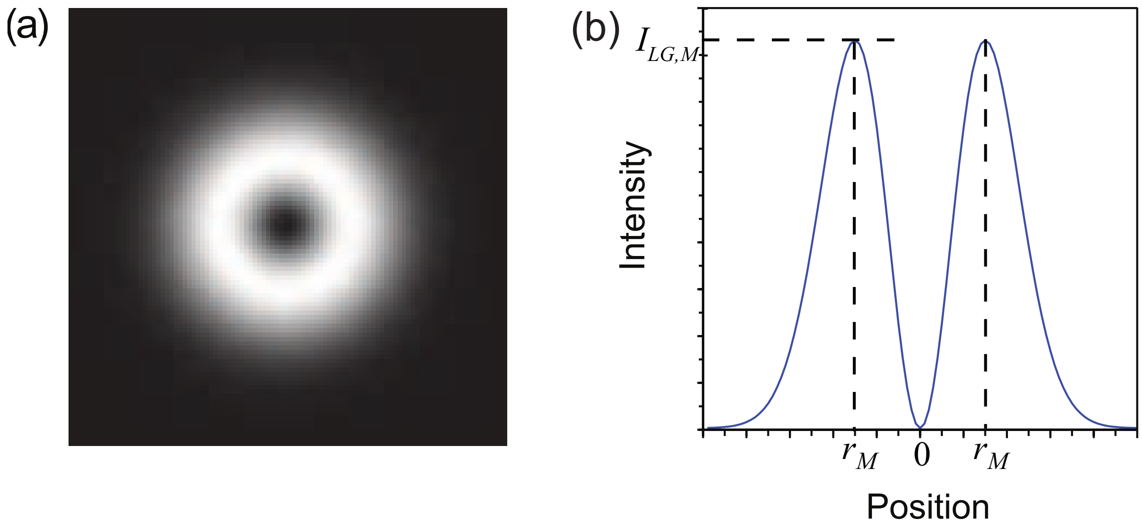

Figure 5.5: (a) Cross-section of an LG_0^1 beam. (b) Radial profile of the cross-section. The LG_0^1 beam has an intensity node at $r = 0$ and a maximum at a radius r_M.

The important characteristics of any cold atom trap are the trap depth and the trap frequencies[3]. The trap depth is proportional to the maximum intensity of the beam and can be calculated using equation (5.5). The trap frequency is obtained by making a harmonic oscillator approximation around the minimum of the trap and obtaining the spring constant from the coefficient of the quadratic term in the expansion of the trap profile about the minimum.

5.3.a The trap depth

To find the LG intensity maximum (or trap minimum), we differentiate equation (5.5) and locate the point at which $dI_{\mathrm{LG}}/dr = 0$:

$$\begin{aligned}\frac{dI_{\mathrm{LG}}}{dr} &= I_0\left(\frac{2r}{r_0^2}e^{-2\frac{r^2}{r_0^2}} - \frac{4r^3}{r_0^4}e^{-2\frac{r^2}{r_0^2}}\right)\\ \frac{dI_{\mathrm{LG}}}{dr} &= I_0\left(1-\frac{2r^2}{r_0^2}\right)\frac{2r}{r_0^2}e^{-2\frac{r^2}{r_0^2}} \qquad (5.6)\end{aligned}$$

---

[3] For optical traps, there is some atom loss due to spontaneous scattering of the trapping light. In our experiment, this is $< 10^{-4}\ \mathrm{s}^{-1}$ per atom, which is negligible compared to scattering from background gas.

The point of maximum intensity occurs at

$$r_M = \frac{r_0}{\sqrt{2}}. \tag{5.7}$$

We can now substitute r_M into equation (5.5) to get the maximum intensity,

$$I_{\mathrm{LG,M}} = \frac{2}{\pi e}\left(\frac{P_{\mathrm{LG}}}{r_0^2}\right) = \frac{P_{\mathrm{LG}}}{\pi e r_M^2}. \tag{5.8}$$

The trap depth can be subsequently obtained using the light shift from the far off-resonant interaction (using equation (3.21), and substituting equation (3.15) for the Rabi frequency). However, we have to be careful here since the detuning, $\omega_L - \omega_0$, is comparable to the transition frequency, ω_0 (in our case $\omega_L \approx \omega_0/2$), and the rotating wave approximation is no longer valid. In such situations, we include counter rotating terms, and simplify the expression by ignoring the fine and hyperfine structure[4]. The light shift simplifies to [211]:

$$V_{\mathrm{trap}} = -\frac{3\pi c^2}{2\omega_0^3}\left(\frac{\Gamma}{\omega_0 - \omega_L} + \frac{\Gamma}{\omega_0 + \omega_L}\right) I_{\mathrm{trap}}, \tag{5.9}$$

where Γ is the natural linewidth of the transition (also known as the rate of spontaneous emission, see equation (3.23)), and c is the speed of light. We set

$$K = \frac{3\pi c^2}{2\omega_0^3}\left(\frac{\Gamma}{\omega_0 - \omega_L} + \frac{\Gamma}{\omega_0 + \omega_L}\right), \tag{5.10}$$

thereby relating the trap depth to the light intensity using $V_{\mathrm{trap}} = -K I_{\mathrm{trap}}$. We obtain the trap depth in terms of the power in the LG beam:

$$V_{\mathrm{depth}} = K I_{\mathrm{LG,M}} = \frac{K P_{\mathrm{LG}}}{\pi e r_M^2}. \tag{5.11}$$

5.3.b The trap frequencies

A harmonic oscillator potential about the trap minimum can be written as

$$V = -V_{\mathrm{depth}} + \frac{1}{2} m \omega_r^2 (r - r_M)^2 \tag{5.12}$$

---

[4] Other excited states do play a role when the rotating wave approximation is no longer valid. However, the electric dipole coupling strengths to other states are low, and can be neglected for this calculation.

Keeping the harmonic oscillator in mind, we will now make a Taylor expansion of I_{LG} about r_M:

$$I_{\text{LG}}(r - r_M) = I_{\text{LG,M}} + \frac{1}{1!}\frac{dI_{\text{LG}}}{dr}\bigg|_{r_M}(r - r_M) + \frac{1}{2!}\frac{d^2 I_{\text{LG}}}{dr^2}\bigg|_{r_M}(r - r_M)^2 + ... \tag{5.13}$$

Since r_M is a maximum, the first derivative in the expansion goes to zero. The second derivative can be obtained by differentiating equation (5.6):

$$\begin{aligned} \frac{d^2 I_{\text{LG}}}{dr^2} &= I_0 \left[\left(1 - \frac{2r^2}{r_0^2}\right)\left(\frac{2}{r_0^2} - \frac{8r^2}{r_0^4}\right) - \frac{8r^2}{r_0^4}\right] e^{-2\frac{r^2}{r_0^2}} \\ \frac{d^2 I_{\text{LG}}}{dr^2}\bigg|_{r_M} &= \frac{-4I_0}{er_0^2} \end{aligned} \tag{5.14}$$

We truncate the expansion beyond $(r - r_M)^2$ and match the expression to equation (5.12). The zeroeth order terms give the expression for trap depth (equation (5.11)). The first order terms are zero. The second order terms give

$$\frac{1}{2}m\omega_r^2 = \frac{1}{2}\frac{16P_{\text{LG}}K}{\pi e r_0^4},$$

from which we obtain

$$\omega_r = \sqrt{\frac{16P_{\text{LG}}K}{\pi e m r_0^4}}. \tag{5.15}$$

The trap frequency is proportional to the square-root of the power of the beam.

5.3.c Vertical confinement

The vertical confinement from the sheet beam holds the atoms against gravity. We will go through the calculation to obtain the vertical trap depth and trap frequency, which are important in characterizing the ring trap.

For an elliptical Gaussian beam, the intensity at the center is given by

$$I_{\text{sh,M}} = \frac{2P_{\text{sh}}}{\pi z_0 r_\perp}, \tag{5.16}$$

where P_{sh} is the power in the beam, z_0 and $r_\perp$ are the $1/e^2$ radius in the vertical (z, see figure 5.4) and horizontal directions (r, ϕ). The trap depth can then be calculated using the light shift from the far off-resonant interaction (equation (3.21)):

$$V_{\text{sh,depth}} = I_{\text{sh,M}}K, \tag{5.17}$$

We can then express the vertical confinement potential due to the sheet in terms of $V_{\mathrm{sh,depth}}$

$$V_{\mathrm{sheet}} = V_{\mathrm{sh,depth}} e^{-2z^2/z_0^2}, \tag{5.18}$$

where we have ignored confinement in the horizontal axes because it is weak compared to the annular confinement of the LG beam. By comparing the terms of the above expression to that of a harmonic oscillator, as was done for the LG beam, we obtain the vertical trapping frequency,

$$\omega_z = \sqrt{\frac{4V_{\mathrm{sh,depth}}}{mz_0^2}} = \sqrt{\frac{8P_{\mathrm{sh}}K}{\pi m z_0^3 r_\perp}}. \tag{5.19}$$

5.3.d Sample calculation of trapping parameters

In practice, we measure the powers in the two beams, P_{sh} and P_{LG}, and their sizes, $z_0 \times r_\perp$, and r_M. We calculate K for sodium using equation (5.10). From these parameters, we can obtain the trap frequencies, ω_r and ω_z, and the trap depth. Table 5.1 gives a sample set of parameters that we have used for the experiment.

5.4 Condensate wavefunction in the ring trap

In the previous section, we modeled our potential as a ring shaped harmonic oscillator. We will now use the model trap potential to solve for the condensate wavefunction in the ring trap. The condensate wave-function can be obtained by solving the Gross-Pitaevskii (GP) equation,

$$E\psi(\mathbf{r}) = \frac{\hbar^2}{2m}\nabla^2\psi(\mathbf{r}) + V_{\mathrm{ext}}(\mathbf{r})\psi(\mathbf{r}) + g|\psi(\mathbf{r})|^2\psi(\mathbf{r}). \tag{5.20}$$

where ψ is the condensate wavefunction, E is the energy of the eigenstate and V_{ext} is the trapping potential, g is the interaction strength and $\mathbf{r}$ is the position in space.

The GP equation cannot be easily solved since it contains a non-linear interaction term. One can model it analytically in one the following limits:

1. Non-interacting regime: In this regime, interactions are low and one neglects the interaction energy compared to the kinetic energy. The many particle ground state in this case is identical to the single particle ground state.

Property	Expression	Value
K	$-\frac{3\pi c^2}{2\omega_0^3}\left(\frac{\Gamma}{\omega_0-\omega_L}+\frac{\Gamma}{\omega_0+\omega_L}\right)$	-7.42 $\times 10^{-37}$ J m^2/W
P_{LG}		27 mW
r_M		19 μm
r_0	$\sqrt{2}r_M$	27 μm
I_0	$4P_{\mathrm{LG}}/\pi r_0^2$	48 $\times 10^6$ W/m^2
V_{depth}	$KP_{\mathrm{LG}}/\pi e r_M^2$	$h\times$ 9.8 kHz
		$k_B\times$ 470 nK
ω_r	$\sqrt{16P_{\mathrm{LG}}K/\pi e m r_0^4}$	$(2\pi)\times$ 218 Hz
P_{sh}		150 mW
z_0		9.1 μm
$r_\perp$		800 μm
$I_{\mathrm{sh,M}}$	$2P_{\mathrm{sh}}/\pi z_0 r_\perp$	13 $\times 10^6$ W/m^2
$V_{\mathrm{sh,depth}}$	$2P_{\mathrm{sh}}K/\pi z_0 r_\perp$	$h\times$ 15 kHz
		$k_B\times$ 700 nK
ω_z	$\sqrt{8P_{\mathrm{sh}}K/\pi m z_0^3 r_\perp}$	$(2\pi)\times$ 560 Hz

Table 5.1: Ring trap parameters: The table lists the measured and calculated parameters for the ring trap in our experiment.

2. Thomas-Fermi regime: In this regime, interactions dominate and kinetic energy does not play a role. The condensate density follows the (inverted) shape of the trapping potential up to the level where $V_{\mathrm{ext}}(\mathbf{r}) = \mu_0$.

We model our ring trap potential $V(r, z, \phi)$ in cylindrical coordinates (r, z, ϕ) as,

$$V(r, z, \phi) = \frac{1}{2}m\omega_z^2 z^2 + \frac{1}{2}m\omega_r^2 (r - r_M)^2, \tag{5.21}$$

where ω_z and ω_r are the vertical and radial trapping frequencies about the annulus, $r = r_M, z = 0$ is the bottom of the potential and m is the mass of the sodium atom. The vertical confinement is tighter than the radial (annular) confinement ($\omega_z > \omega_r$).

There are 3 simplified ways to treat the ground state BEC in the ring trap.

1. Harmonic oscillator ground state regime : In this case, we neglect the interaction energy. The condensate assumes the ground state of the 2D harmonic oscillator. The density distribution n_{3D} is:

$$n_{3D}(r, z, \phi) = n_{3D,0} e^{-z^2/z_w^2} e^{-(r-r_M)^2/r_w^2}, \tag{5.22}$$

   where z_w and r_w are the harmonic oscillator lengths given by $\sqrt{\hbar/m\omega_z}$ and $\sqrt{\hbar/m\omega_r}$ respectively and $n_{3D,0}$ is the maximum (peak) 3D density.

2. Radial Thomas-Fermi and vertical harmonic oscillator : In this case, the condensate expands due to the mean field in the radial (about the annulus) direction, but is still confined to the ground state in the vertical[5]:

$$\begin{aligned} n_{3D}(r, z, \phi) &= e^{-z^2/z_w^2} g \quad \left(\mu_0 - \frac{1}{2} m\omega_r^2 (r - r_M)^2\right) \\ &\qquad\qquad \text{for } |r - r_M| < r_{\mathrm{TF}}, \\ &= 0 \qquad \text{everywhere else} \end{aligned} \tag{5.23}$$

   where $r_{\mathrm{TF}} = \sqrt{\frac{2\mu_0}{m\omega_r^2}}$ is the Thomas-Fermi radius of the cloud, which defines the extent of the cloud in the radial direction.

3. Fully Thomas-Fermi : In this case, the condensate takes the (inverted) shape of the potential and occupies the region enclosed by $V(r, \phi, z) < \mu_0$.

$$\begin{aligned} g n_{3D}(r, z, \phi) &= \mu_0 - \quad \left(\frac{1}{2} m\omega_z^2 z^2 + \frac{1}{2} m\omega_r^2 (r - r_M)^2\right) \\ &\qquad\qquad \text{for } V(r, \phi, z) < \mu_0 \\ &= 0 \qquad \text{everywhere else} \end{aligned} \tag{5.24}$$

The above expressions gives the condensate density distribution in terms of the chemical potential. However, experimentally, we measure the integrated column

---

[5] Here, I will be using $\mu_0 = g n_{3D,0}$ as the chemical potential similar to the fully Thomas-Fermi case. As a consequence, μ_0 does not include the zero point energy along z, which, for the harmonic oscillator ground state, is $\hbar\omega_z/2$.

density (along our imaging direction z) and the total number of atoms. Hence, we need to obtain a relation for the experimentally measured quantities (column density and number of atoms) to the chemical potential.

5.4.a Harmonic oscillator ground state regime

We start with the 3D density distribution:

$$n_{3D}(r, z, \phi) = n_{3D,0} e^{-z^2/z_w^2} e^{-(r-r_M)^2/r_w^2}. \tag{5.25}$$

We can integrate it along z to get the 2D column density distribution, n_{2D}, and the peak 2D column density, $n_{2D,0}$:

$$\begin{aligned} n_{2D}(r, \phi) &= n_{3D,0} z_w \sqrt{\pi} e^{-(r-r_M)^2/r_w^2}, & (5.26) \\ n_{2D,0} = n_{2D}(r = r_M, \phi) &= n_{3D,0} z_w \sqrt{\pi}. & (5.27) \end{aligned}$$

where we have used $\int e^{-z^2/z_w^2} dz = z_w \sqrt{\pi}$. In this case, the column density is Gaussian of width r_w about a circle or radius r_M.

We can further integrate this about ϕ and r to get

$$N = n_{3D,0} z_w r_w \pi \times 2\pi r_M, \tag{5.28}$$

where N is the total number of atoms. We can then express the peak 3D density, $n_{3D,0}$ as

$$n_{3D,0} = \frac{N}{2\pi^2 z_w r_w r_M}. \tag{5.29}$$

We have assumed that the radius of the annulus is large compared to the radial harmonic oscillator width.

5.4.b Radial Thomas-Fermi regime

The 3D density distribution in this case has the same z dependence to the harmonic oscillator case:

$$\begin{aligned} n_{3D}(r, z, \phi) &= e^{-z^2/z_w^2} \frac{1}{g} \left(\mu_0 - \frac{1}{2} m \omega_r^2 (r - r_M)^2 \right), \text{ for } (r - r_M) < r_{\text{TF}} & (5.30) \\ &= 0 \quad \text{everywhere else.} \end{aligned}$$

We can integrate along z similar to the harmonic oscillator case to get:

$$\begin{aligned} n_{2D}(r,\phi) &= \frac{\sqrt{\pi} z_w}{g}\left(\mu_0 - \frac{1}{2} m\omega_r^2 (r-r_M)^2\right), \text{ for } |r-r_M| < r_{\text{TF}} \\ &= \frac{\mu_0\sqrt{\pi} z_w}{g}\left(1 - \frac{(r-r_M)^2}{r_{\text{TF}}^2}\right), \text{ for } |r-r_M| < r_{\text{TF}}, \\ &= 0 \text{ everywhere else.} \end{aligned} \tag{5.31}$$

The column density takes the shape of an inverted parabola about a circle of radius r_M. The peak column density is given by

$$n_{2D,0} = n_{2D}(r = r_M, \phi) = \frac{\mu_0\sqrt{\pi} z_w}{g}, \tag{5.32}$$

in terms of the chemical potential μ_0. Integrating along r and ϕ, we get:

$$N = \frac{\mu_0\sqrt{\pi} z_w}{g} \times 2\pi r_M \frac{4}{3} r_{\text{TF}} = \frac{8\pi^{3/2}\mu_0}{3g} z_w r_M r_{\text{TF}}.$$

Substituting for r_{TF} and z_w, we get N in terms of the chemical potential and trap frequencies:

$$N = \frac{8\sqrt{2}\pi^{3/2}}{3}\frac{r_M\sqrt{\hbar}\mu_0^{3/2}}{mg\omega_r\sqrt{\omega_z}}. \tag{5.33}$$

5.4.c Fully Thomas-Fermi regime

We start with the 3D density distribution:

$$\begin{aligned} gn_{3D}(r,z,\phi) &= \mu_0 - \left(\tfrac{1}{2} m\omega_z^2 z^2 + \frac{1}{2} m\omega_r^2 (r-r_M)^2\right) \\ & \qquad \text{for } V(r,\phi,z) < \mu_0 \\ &= 0 \qquad \text{everywhere else} \end{aligned} \tag{5.34}$$

Integrating along z (see Appendix B), we get a column density given by:

$$\begin{aligned} gn_{2D}(r,\phi) &= \sqrt{\frac{32}{9m\omega_z^2}}\left(\mu_0 - \frac{m\omega_r^2(r-r_M)^2}{2}\right)^{3/2} \text{ for } |r-r_M| < r_{\text{TF}} \\ &= 0 \text{ everywhere else} \end{aligned} \tag{5.35}$$

where $r_{\text{TF}} = \sqrt{2\mu_0/m\omega_r^2}$, as defined earlier.

The 2D column density profile obtained is similar to the annular TF case expression, equation (5.31) except for a 3/2 power and therefore has a steeper drop-off. I will call the functional form of equation (5.35), the 3D-TF profile.

The peak 2D density is given by:

$$n_{2D,0} = n_{2D}(r = r_M, \phi) = \frac{4\sqrt{2}\mu_0^{3/2}}{3\sqrt{m\omega_z^2}g}. \tag{5.36}$$

We then setup the expression to integrate the 2D column density and obtain the number of atoms:

$$N = \int_{r_M - r_{\mathrm{TF}}}^{r_M + r_{\mathrm{TF}}} rdr \frac{4\sqrt{2}}{3g\sqrt{m\omega_z^2}}(\mu_0 - \frac{m\omega_r^2(r - r_M)^2}{2})^{3/2} \int d\phi,$$

Integrating over r and ϕ (see Appendix B), we obtain

$$N = r_M \frac{4\pi m\omega_r^3 r_{\mathrm{TF}}^4}{3g\omega_z} \times \frac{3\pi}{8}. \tag{5.37}$$

Finally, substituting for r_{TF} to express N in terms of μ_0, we arrive at

$$N = 2\pi^2 \frac{r_M \mu_0^2}{gm\omega_z\omega_r}. \tag{5.38}$$

Property	Harmonic Oscillator	Radial TF	Fully TF
n_{3D}	$n_{3D,0}e^{-z^2/z_w^2}e^{-s^2/r_w^2}$	$\frac{\mu_0 e^{-z^2/z_w^2}}{g}\left(1 - \frac{s^2}{r_{\mathrm{TF}}^2}\right)$	$\frac{\mu_0}{g}\left[1 - \left(\frac{z^2}{z_{\mathrm{TF}}^2} + \frac{s^2}{r_{\mathrm{TF}}^2}\right)\right]$
n_{2D}	$n_{3D,0}z_w\sqrt{\pi}e^{-s^2/r_w^2}$	$\frac{\mu_0\sqrt{\pi}z_w}{g}\left(1 - \frac{s^2}{r_{\mathrm{TF}}^2}\right)$	$\frac{4\mu_0 z_{\mathrm{TF}}}{3g}\left(1 - \frac{s^2}{r_{\mathrm{TF}}^2}\right)^{3/2}$
$n_{2D,0}$	$\sqrt{\pi}n_{3D,0}z_w$	$\frac{\sqrt{\pi}\mu_0 z_w}{g}$	$\frac{4\mu_0 z_{\mathrm{TF}}}{3g}$
N	$2\pi^2 n_{3D,0}z_w r_w r_M$	$\frac{8\pi^{3/2}\mu_0 r_{\mathrm{TF}}z_w r_M}{3g}$	$\frac{\mu_0\pi^2 r_{\mathrm{TF}}z_{\mathrm{TF}}r_M}{g}$
N	$\frac{2\pi^2 r_M\hbar}{m\sqrt{\omega_r\omega_z}}n_{3D,0}$	$\sqrt{\frac{128\pi^3 r_M^2\hbar}{9g^2m^2\omega_z\omega_r^2}}\mu_0^{3/2}$	$\frac{2\pi^2 r_M}{gm\omega_z\omega_r}\mu_0^2$

Table 5.2: The table summarizes the results for various parameters for the 3 simplified treatments of a ring BEC in our trap. I have used $s = r - r_M$, $r_w = \sqrt{\hbar/m\omega_r}$, $z_w = \sqrt{\hbar/m\omega_z}$, $r_{\mathrm{TF}} = \sqrt{2\mu_0/m\omega_r^2}$, $z_{\mathrm{TF}} = \sqrt{2\mu_0/m\omega_z^2}$.

5.4.d Sample BEC parameters for our trap

In this section, we will assume some typical values for our trap parameters, and obtain the BEC parameters for a given number of atoms. For our system, we typically had:

- $r_M = 20\ \mu\text{m}$,
- $\omega_r = (2\pi)110$ Hz, and
- $\omega_z = (2\pi)550$ Hz.
- For sodium, $m = 3.8 \times 10^{-26}$ kg
- and $g = 1.0 \times 10^{-50}\ \text{Jm}^3$.

For 150 000 atoms, the various properties are given in table 5.3. As seen in the table, the chemical potential goes roughly as $\mu \approx 2\omega_z$ and $\mu \approx 9\omega_r$. This implies that the BEC lies somewhere between the radial TF and the fully TF regimes. The harmonic oscillator BEC model is clearly not valid. One can see that the radial extent of the harmonic oscillator BEC is significantly less than that of the TF BECs, r_{TF}. The harmonic oscillator model also overestimates the peak 2D and 3D densities.

The radial TF and fully TF models are in rough agreement for the conditions given. This implies that they are both reasonable approximations for the conditions given. They both given a similar value for μ_0, and their radial and vertical dimensions are comparable. If the N were to increase, say to about 300 000, then the radial TF model would become less applicable and the fully TF model would become more applicable. However, if N were to decrease, the fully TF model would be less applicable. At low enough N, it is expected that the harmonic oscillator model would become applicable.

Property	Harmonic Oscillator	Radial TF	Fully TF
μ	-	$h \times 1000$ Hz	$h \times 890$ Hz
r_{TF} z_{TF}	4.0 μm † 1.8 μm $*$	8.5 μm 1.8 μm $*$	8.0 μm 1.6 μm
$n_{3D,0}$	$2.1{\times}10^{20}$ atoms/m^3	$6.6{\times}10^{19}$ atoms/m^3	$5.8{\times}10^{19}$ atoms/m^3
$n_{2D,0}$	$3.4{\times}10^{14}$ atoms/m^2	$1.0{\times}10^{14}$ atoms/m^2	$1.3{\times}10^{14}$ atoms/m^2

Table 5.3: The table gives the values of the various BEC parameters for the 3 simplified treatments of a ring BEC in our trap, assuming N=150 000 atoms. † - As the harmonic oscillator limit BEC has no TF lengthscale, I have used $2r_\omega = 2\sqrt{hbar/m\omega_r}$ to obtain the equivalent lengthscale. $*$ - As the harmonic oscillator and radial TF BECs have no TF lengthscale along z, I have used $2z_\omega = 2\sqrt{hbar/m\omega_z}$ to obtain the equivalent system size. The TF half-width corresponds to approximately twice the harmonic oscillator $1/e$ width.

5.5 Characterizing the ring BEC from time-of-flight expansion

While it took nearly a year of work to get a good, smooth ring trap (see section 5.6), we had some evidence of persistent currents almost right away, and within five months, had unambiguous persistent currents and preliminary data for the decay of superflow. Our characterization and understanding of the dynamics of the ring trap went a long way in getting a smooth trap and having the next few steps (see chapters 6 and 7) ready to be implemented. In this section, I will discuss how we characterized the various parameters of our trap from the time-of-flight expansion.

The time-of-flight (TOF) expansion of a cold atom cloud yields useful information of the cloud in the trap such as the temperature and mean field [109]. In fact, the slow and anisotropic expansion of the BEC (as well as its sudden onset) compared to the non-condensed thermal cloud[6] were the key signatures in identify-

---

[6] In some situations, the thermal cloud may be too faint to be seen, making the measurement of temperature difficult. In our system, we have seen both, regimes in which the thermal cloud

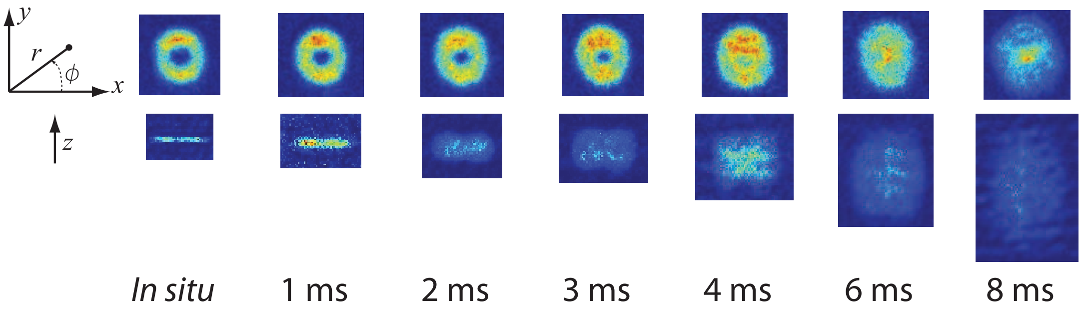

Figure 5.6: Time-of-flight expansion of the ring : In this sequence of 2 sets of PTAI images (top: from above, bottom: from the side), the ring is imaged after release from the trap in TOF. The BEC (thermal cloud is too weak to be detected) expands in all directions, filling up the central hole in about 6 ms. The coherence of the BEC can be seen in the enhancement of the peak central density at 8 ms and the diffraction-like fringes along the edges at the similar time.

ing the first BEC [41]. The expansion of the cloud depends on the trap parameters, the temperature and the chemical potential (or equivalently, the number of atoms).

The expansion of the condensate is shown in figure 5.6. The condensate expands in all directions, causing the ring to close upon itself. The focussing of the BEC at the center of the ring causes a prominent peak around 6 ms. The tight confinement (or compression) in the vertical direction causes far more expansion in the vertical than in the radial direction. We will now go into the more quantitative aspects of the TOF expansion.

While most standard BEC references assume a 3D harmonic trap [109, 212], we have to be careful since we have a multiply-connected geometry which cannot be directly mapped onto a simple 3D harmonic oscillator. As discussed earlier in this chapter, we assume our BEC to be in a toroidal harmonic trap. The validity of the assumption for the condensate depends on the next order term in the Taylor expansion of the trapping potential (equation (5.13) for the annular confinement). This term is smaller by an additional factor of $(r_{\mathrm{TF}}-r_M)/3r_M$ (for a TF condensate)

---

was clearly visible hence the temperature was measurable, and regimes in which the thermal cloud was not visible. For the latter cases, we ignored temperature and any possible thermal effects.

compared to the second order (quadratic or harmonic) term. For our system (see Appendix C.5 for sample parameters), the value of the (third order) quartic term is about 17% of the quadratic term at the TF radius. In the vertical direction (z), the quartic term scales as z_{TF}^2/z_0^2, which amounts to a correction of around 1% with respect to the harmonic term. This correction is small since the vertical trapping frequency is higher and hence the condensate sits close to the bottom of the trap, seeing minimal anharmonicity. In our system, the temperature was close to the condensate chemical potential and so similar corrections would apply to the thermal cloud also.

Since the system is more harmonic in the vertical direction and the trapping geometry is simple along that axis, we extracted the temperature and the mean field from the vertical expansion.

We will derive the expression for obtaining the temperature and mean field for the case of a general 3D harmonic oscillator, and then apply the expression for an individual axis to the vertical expansion of the cloud.

5.5.a The thermal cloud

The width of the thermal cloud in a particular direction, r_i, can be derived from the equipartition of energy. A 3D harmonic trap has 3 degrees of freedom, each having an average energy of $\frac{1}{2}k_B T$ per atom, where k_B is the Boltzmann's constant, and T is the temperature of the cloud. By equating the translational kinetic energy (equal to the potential energy for a harmonic oscillator) of the cloud to $\frac{1}{2}k_B T$, we get

$$\frac{1}{2}k_B T = \frac{1}{2}m\omega_i^2\langle r_i^2\rangle \tag{5.39}$$

where ω_i is the trap frequency in the relevant direction. Assuming a Gaussian profile for the thermal cloud, $\propto e^{-r_i^2/r_{i,0}^2}$, we get an expression for $\langle r_i^2\rangle$:

$$\langle r_i^2\rangle = \frac{\int_{-\infty}^{\infty} r_i^2 e^{-r_i^2/r_{i,0}^2} dr_i}{\int_{-\infty}^{\infty} e^{-r_i^2/r_{i,0}^2} dr_i} = (1/2)r_{i,0}^2. \tag{5.40}$$

Substituting $\langle r_i^2 \rangle$ back into equation (5.39), we obtain the Gaussian width of the *in situ* thermal cloud in terms of the temperature:

$$r_{i,0} = \sqrt{\frac{2k_BT}{m\omega_i^2}}. \tag{5.41}$$

The Gaussian width in TOF, at long time t can similarly be derived [109]:

$$r_i(t) = \sqrt{\frac{2k_BT}{m}}t. \tag{5.42}$$

By taking a fit of the Gaussian width of the expanding thermal cloud, we use equation (5.42) to obtain the temperature[7]. The precision is limited mainly by shot-to-shot fluctuations. Figure 5.7 shows the expansion of a cold atom cloud in the ring and the calculation of the temperature from the rate of expansion of the thermal cloud.

5.5.b The condensate

The *in situ* condensate wavefunction has been described in detail in section 5.4. Here, we will discuss the expansion of a TF cloud, since it is most relevant to our system. The harmonic oscillator case, and situations in between the TF and harmonic oscillator regimes also follow similar scaling, as has been derived by Castin and Dum [212]. In this section, I will use an energetics argument to obtain an expression for the vertical expansion of the BEC due to mean field.

The mean field energy of a TF condensate scales as the chemical potential μ_0. When atoms are released in TOF, all this energy is converted into kinetic energy, which gives a scaling

$$r_i(t) \propto \sqrt{\frac{2\mu_0}{m}}t\ . \tag{5.43}$$

In the case of highly anisotropic trap, most of the mean field energy goes in the direction of the tightest confinement. This is because the cloud is maximally com-

---

[7] We can interpolate between the two limits to get a generalized expression that can be used for fitting: $r_i(t) = \sqrt{\frac{2k_BT}{m}}\left(\frac{1}{\omega_i^2} + t^2\right)^{1/2}$. In practice, the small size of the *in situ* cloud in the vertical makes it difficult to extract ω_z due to optical resolution limits. Hence, we use equation (5.42) to obtain the temperature.

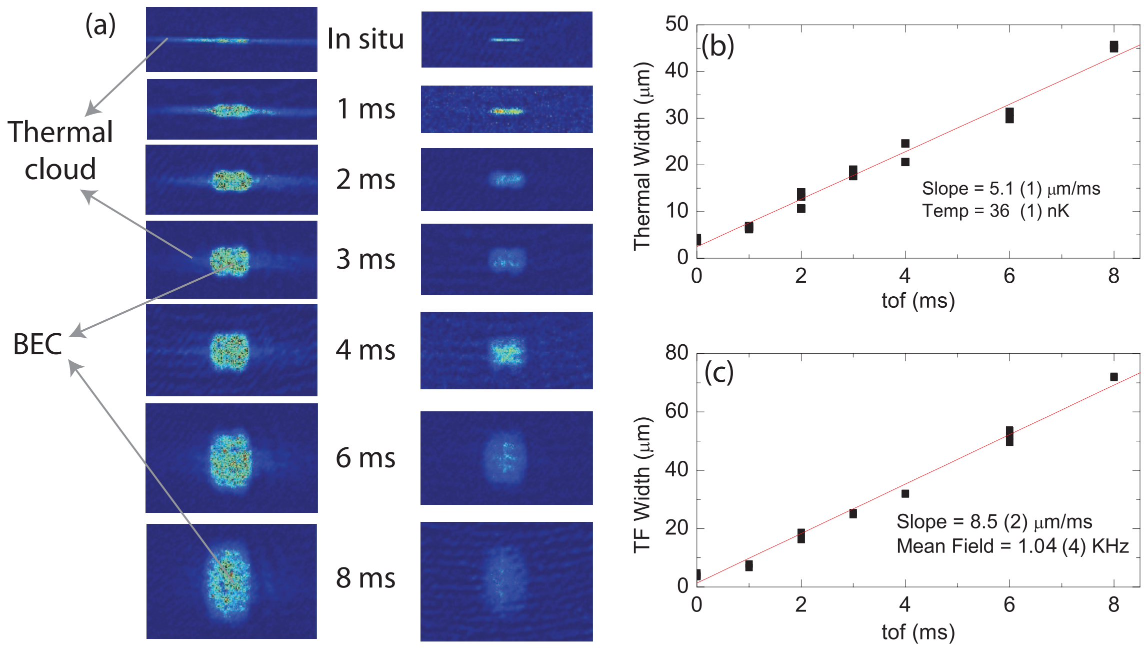

Figure 5.7: Obtaining temperature and mean field : (a) The vertical TOF of our BEC in the ring trap is shown. The left and right column show absorption images and PTAI images respectively. The absorption images are able to detect the thermal cloud. The PTAI images are able to profile the BEC accurately. (note : transfer fraction varies 1-20%) (b) Temperature of 38 nK obtained from the slope of a linear fit of the Gaussian $1/e$ radius of the thermal cloud using equation (5.42). (c) Mean field (or chemical potential) of 1.0 kHz obtained from the slope of a linear fit to equation (5.44) of the TF half-maximum radius of the BEC.

pressed in that direction, and hence the sudden release causes maximum expansion along that direction. The ratio of energy released in different directions is directly proportional to the trap frequency squared (see Ketterle *et al.* [109] for example). A trap frequency ratio of 4 is sufficient to have more than 90% of the energy released in the direction of tight confinement. In our experiment, we typically have $\omega_z/\omega_r \gtrsim 5$, and hence we assume

$$z(t) = \sqrt{\frac{2\mu_0}{m}}t \ . \tag{5.44}$$

The correction to the above expression in the calculation of the chemical potential is smaller than other calibration uncertainties. We use the above expression, along with *in situ* profile measurements (detailed in appendix C.5) to calibrate the chemical potential of our ring traps. Figure 5.7 also shows the calculation of the mean field from the rate of expansion of the TF condensate.

5.6 Azimuthal smoothness of the ring

In our trapping scheme, the BEC is very sensitive to bumpiness. The trapping potential has to be smooth on the scale of the mean field, which is an order of magnitude smaller than the average depth of the potential. Rough estimates suggest that the bumps need to be smaller than 10% of the beam intensity just to get an unbroken ring BEC. Unlike magnetic traps, which are intrinsically smooth due to the macroscopic long range potentials created by the current carrying coils that are located far away from the atoms, optical traps are prone to bumpiness on the order of the optical wavelength or longer. Such bumpiness can come from any number of sources: unclean optical surfaces, dust settled on optical elements, scratches on optical coatings, unwanted reflections from surfaces of optical elements, etc. While such bumpiness cannot be completely eliminated especially at the level of azimuthal smoothness required by the mean field, it can be greatly reduced by careful design of the optical beam path and the use of strategically placed irises to clean up the beam.

The tight confinement (with far-field optics) in the vertical direction (confining the cloud to <2 μm) down to lengthscales comparable to the trapping light wavelength prevents any structure in the trapped BEC in the vertical direction. The optics do not have the sufficient numerical aperture to cause any structures. However, bumpiness is present in the more weakly confined horizontal direction, which is reflected in the azimuthal profile of the ring BEC. There are several problems with this azimuthal bumpiness. Firstly, if the bumpiness is larger than the chemical potential of the BEC, the BEC becomes segmented and localized and no continuous ring BEC is formed. Secondly, even if we have a continuous BEC, the bumpiness causes an azimuthal variation of both the mean field and the trapping frequency. Any small perturbation of the BEC arising, for example, from the transfer of circulation as discussed in chapter 6, can cause different parts of the ring to oscillate out of phase, leading to further excitations that could facilitate the decay of flow for a circulating ring.

Thirdly, even if the azimuthal bumpiness were small enough to be robust against out-of-phase oscillations from small perturbations, the bumpiness may still limit the range of the chemical potentials for which one still has a continuous ring BEC. As varying the chemical potential is key in varying the superfluid flow velocity (see chapter 7), the bumpiness would ultimately limit the range of superfluid flow velocities that could be probed for the determination of the critical velocity (discussed in chapter 7). In addition, variations in the azimuthal density profile due to the bumps would lower the accuracy of the determined critical velocity. Hence, obtaining an azimuthally smooth ring is critical to studying superfluidity.

The bumpiness of the potential caused several visible and obvious problems. In performing a simple TOF of atoms in the ring trap, we would see complicated patterns emerge (figure 5.8 top and middle), presumably due to the non-uniform phase-evolution of the azimuthally varying BEC. In addition, when we transferred circulation (discussed in Chapter 6), oscillations due to the perturbation go out of phase with hold time, presumably due to the azimuthal variation of the annular trap frequency leading to possible decay of the flow (figure 5.8 bottom).

While the effects of bumpiness were easy enough to see, we still required an

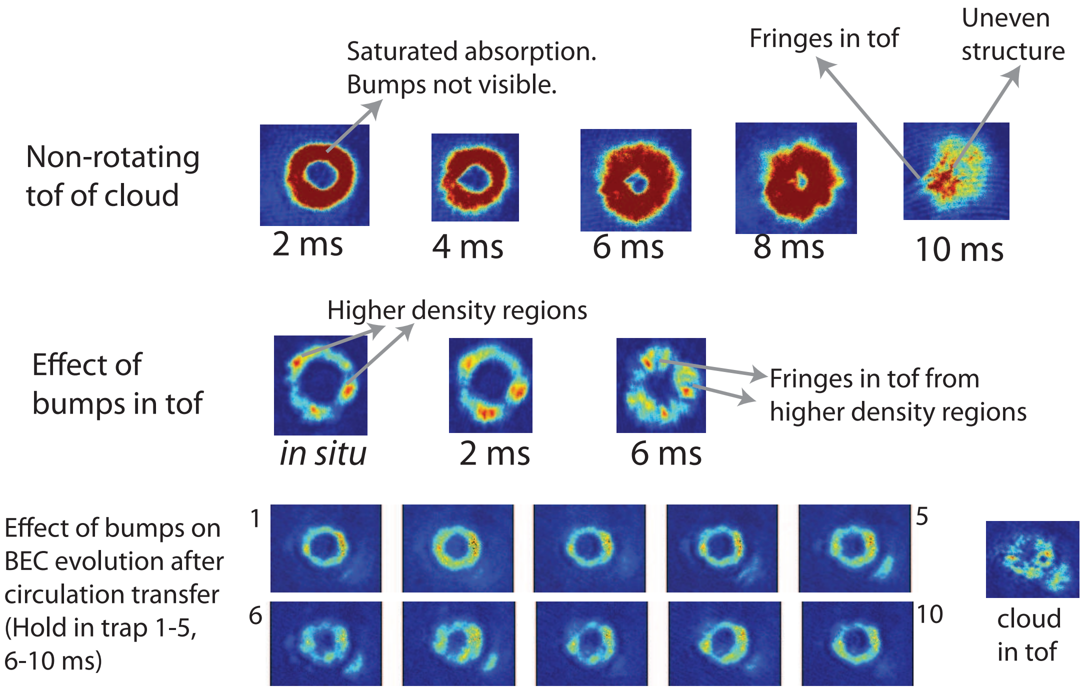

Figure 5.8: Effects of Azimuthal bumpiness: (top) Tof sequence of a bumpy ring - While spatial features of the cloud before 6 ms TOF are not visible due to severe attenuation of the probe, there are fringes and other uneven structure seen in 10 ms TOF that indicate the presence of bumps. (middle) Showing the effect more clearly - Variations in the *in situ* density cause different rates of phase evolution in TOF for different points. This causes interference which can be visible as fringes in TOF (here 6 ms), similar to those seen in the expansion of cigar-shaped clouds [187]. The interference fringes are more easily seen in higher density regions. (bottom) Effects of circulation transfer in the presence of bumps - While the ring is smoother in this case than the previous, the perturbation due to the transfer of circulation causes small oscillations (seen *in situ*) which then locally oscillate out of phase due to the azimuthal variation of the annular trap frequency leading to possible decay of the flow. The atoms seen in the bottom right corner of the image are those trapped in a stray local minimum of the sheet potential. The cloud in TOF after a short hold also shows a lot of structure.

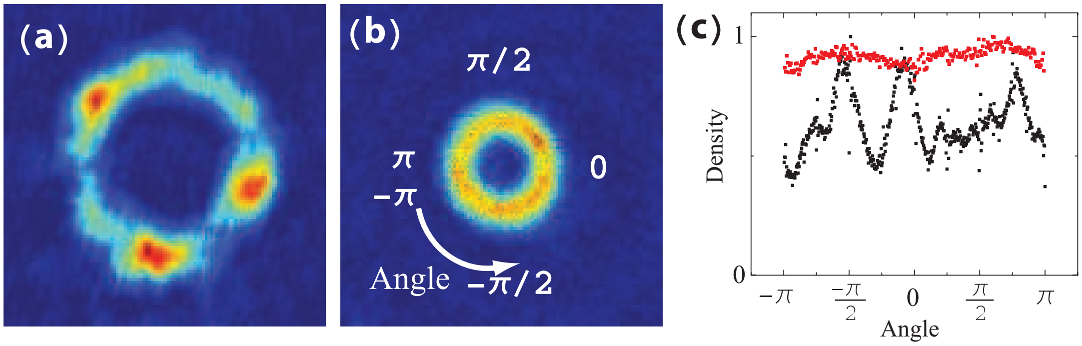

Figure 5.9: *In situ* azimuthal density profile of the ring BEC : The above figure shows the improvement in the smoothness of the ring from June 2009 (a) to May 2010 (b). The magnification and pixel size is the same for both images. We obtained a quantitative measure of the bumpiness by plotting the azimuthal density (c). (black - from (a), red - from (b)).

accurate diagnostic for the bumpiness. Taking the azimuthal profile of an *in situ* image (typically using PTAI) of the BEC in the ring trap gave us a good measure of the bumpiness (figure 5.9). The profile can be taken in two ways, either by summing over the transverse direction to get the number of atoms as a function of the angle, or by finding the peak density (either by a transverse fit or by the maximum density in a region, both giving similar results). Either way, we get a good measure of the bumpiness.

In the course of improving the smoothness from figure 5.9(a) to (b), we made several changes. We ensured that the sheet potential was smooth in the vicinity of the ring, and that the BEC in the sheet alone was as circular as possible. We made the ring smaller, which thereby saw a smaller area of the sheet and hence was less affected by potential variations in the sheet. The smaller ring also made the mean field higher, which made the bumps smaller relative to the mean field.

The biggest change was cleaning up the ring beam. In our initial setup, scattered light from the hologram ended up being refocussed onto the plane of the BEC. By suitably placing an iris in the path of the LG ring beam, and finely adjusting its position, we were able to obtain a very smooth ring with gentle undulations (as opposed to sharp bumps). The undulations were quadrupolar in nature, presumably due to the astigmatism in the optical path. Subsequently, by collimating the beam passing through the hologram to a smaller size, the scattered light was reduced. In addition, the smaller beam used a smaller aperture on subsequent optics lowering the effect of the astigmatism. By carefully placing an iris in the beam path, the astigmatism could be further reduced so that we could obtain smooth rings as shown in figure 5.9(b).

5.7 Sloshing and breathing oscillations

In the course of working with the BEC, we noticed that when perturbed, the BEC underwent radial oscillations. We took some time to briefly study them. Collective oscillations in BECs have been extensively studied [63, 136, 213]. Oscillations can be classified as sloshing (dipole), which is center-of-mass motion in a harmonic potential, and breathing (quadrupole), which is symmetric non-center-of-mass oscillation. While the former has a period equal to the trap frequency, the latter has a faster period which depends on the interactions and the dimensionality. For a non-interacting BEC, the breathing frequency is twice the trap frequency.

Breathing and sloshing excitations can provide useful information about the BEC. The sloshing oscillation gives a measure of the trap frequency. The ratio of the breathing and sloshing frequencies can indicate whether lower-dimensional and/or interaction effects are playing a role. The amplitude dependence of the sloshing oscillations can indicate the anharmonicity of the trap. The damping of the oscillations can indicate the coupling to the excited modes, give a measure of the temperature, and provide information on the superfluid nature of the BEC.

We excited sloshing modes (see figure 5.10) using the light-shift gradient from a large radius, pulsed red-detuned LG beam, and breathing modes (see figure 5.11) by suddenly removing a small fraction ($< 10\%$)of the cloud using a microwave pulse to transfer to the F=2 state and then applying imaging light. The radial sloshing

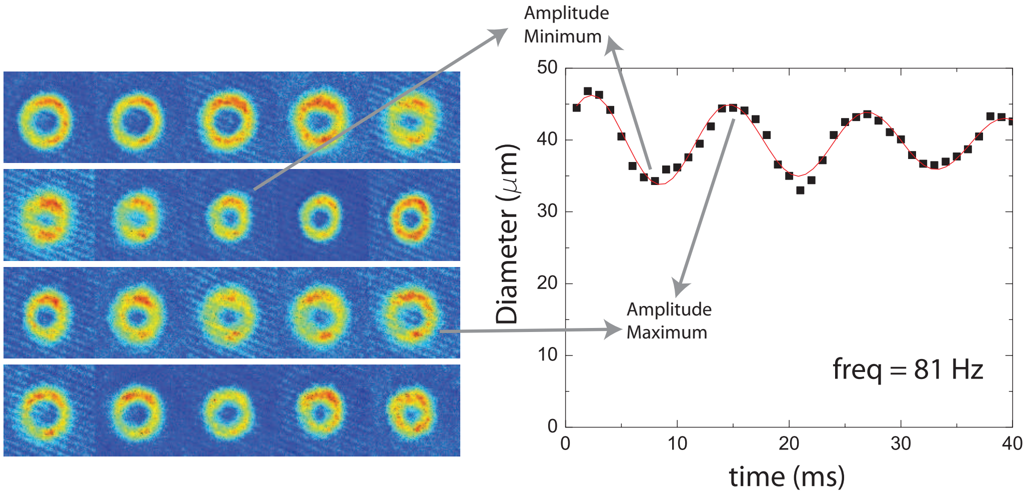

Figure 5.10: Radial sloshing oscillations in the ring BEC : On exciting center-of-mass oscillations using a spatially large, pulsed red-detuned LG beam, we observe the diameter of the ring BEC oscillate at a frequency of 81 Hz. Images are taken *in situ*. Each image is a separate BEC, for which we fit a ring TF density profile to extract the BEC diameter, which is plotted on the right. The oscillations have a damping time constant of about 50 ms.

frequency was 81 Hz, while the breathing frequency was 134 Hz, giving a ratio[8] of 1.65. Both oscillations have a damping time constant of 50 ms. This damping is presumed to be due to the anharmonicity and asymmetry of the ring trap, which causes energy to be lost to other excitation modes of trap. Ultimately, the energy of the oscillations is presumed to be converted into thermal energy. While we have made preliminary measurements studying breathing and sloshing, more care and precision is required to study useful physics.

---

[8] This can be compared to ratios calculated [214, 215] for a pure 2D gas (2.00), 2D TF gas ($\sqrt{10/3} = 1.82$) or a symmetric 3D TF gas ($\sqrt{2} = 1.41$), none of which exactly match our parameters.

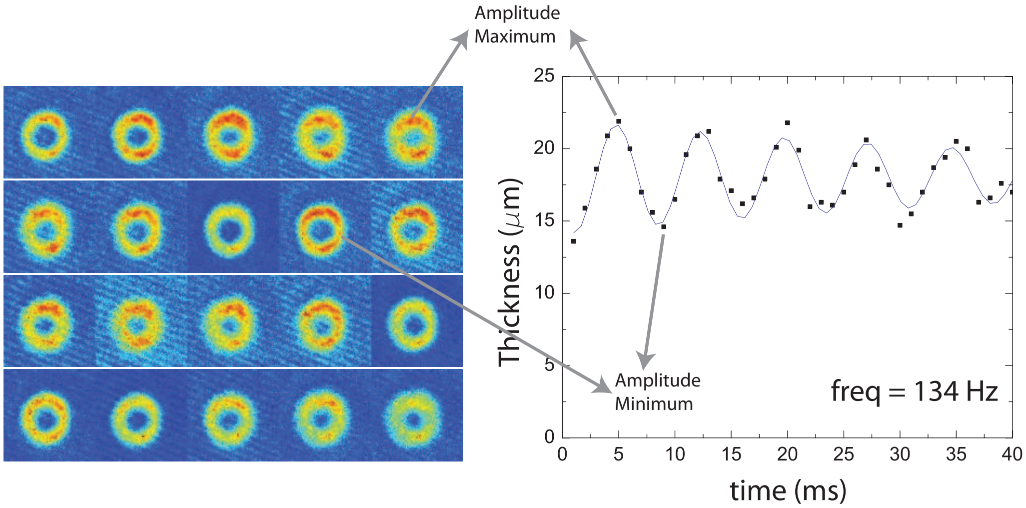

Figure 5.11: Radial breathing oscillations in the ring BEC : On suddenly removing a small fraction of the BEC, we observe the annular thickness of the ring BEC oscillate at a frequency of 134 Hz. Images are taken *in situ*. Each image is a separate BEC, for which we fit a ring TF density profile to extract the radial thickness, which is plotted on the right. The oscillations have a damping time constant of about 50 ms.

5.8 Conclusion

In this chapter, we have discussed the construction of the toroidal trap and the basic ring BEC expansion and dynamics. There have been several proposals on creating a toroidal potential. Of those, we have successfully realized a ring trap where the two axes of confinement, vertical and radial (about an annulus) are created separately. This has the advantage of being stable with respect to relative drift. We have also built the framework to measure and quantify smoothness, and have been successful in making the trap smooth to within 10% of the chemical potential.

Apart from the technical aspects in creating a smooth trap, there are several avenues for studying interesting physics. We pursued the study of superflow and persistent currents, which constitute the remainder of this thesis. However, there are interesting possibilities in the observation of phase fluctuations, the study of interactions in TOF (as we saw for a non-uniform condensate, figure 5.8 middle) and possibly *in situ* and the study of collective oscillations.

Besides being more stable to relative drift between different components of the trapping potential (similar to Ryu *et al.* [52]), the all-optical ring trap has other advantages over the "plugged" magnetic traps [52, 208]. For example, the dimensionality of the system can be easily changed by simply adjusting the relative intensities of the two trapping beams, and varying the chemical potential (number of atoms in practice) to choose the right regime. While this is also possible in the "plugged" magnetic traps, it is more difficult.

In exploring dimensionality using our ring trap, there are some problems that one is likely to encounter. For example, if one wanted to explore the quasi-1D limit, one needs to either lower the mean field or provide tighter radial confinement using higher ring beam power. Either way, the mean field would be reduced compared to the azimuthal bumps in the potential, making the BEC more bumpy. Azimuthal smoothness currently is limited by the astigmatism of the LG beam path. A careful realignment can further improve the smoothness, which would be necessary if one were trying to create a larger radius ring trap.

If exploring the quasi-2D limit or pushing for larger ring traps ($\sim$100 μm), the uniformity of the sheet potential and also its 800 μm Rayleigh range would limit the smoothness. This would require a redesign of the sheet beamline to create a larger uniform focal spot. It is important to note that any further increase in ring size would run into other technical limitations of the experimental apparatus, such as the number of atoms necessary for condensation in the ring, etc.

In contrast, observing superflow is easier with relatively weaker confinement, where the mean field is allowed to smooth over the bumps, and a smaller radius ring, since the flow velocities are higher for the same circulation (same phase winding over a smaller circumference leads to a higher phase gradient and therefore flow velocity). Hence, our $r_M \approx$20 μm ring, was well suited[9] for studying persistent currents, which we shall now look at.

---

[9] If the ring were any smaller, imaging *in situ* would become more difficult.

Chapter 6

Persistent currents in a BEC

In the previous chapter, we discussed our motivation for using toroidal geometry to observe superflow. We also discussed the various aspects of the ring-shaped condensate and our efforts in understanding the system and obtaining a smooth ring. In this chapter, we will detail our efforts towards the achievement of persistent currents in our ring BEC.

We begin with the previous persistent current experiment by Ryu *et al.* [52], where superflow was observed in a toroidal geometry. The persistent current was found to last 10 seconds, limited by the relative drift between the magnetic TOP trap and the optical "plug" beam. The previous work also looked at multiply-charged circulation in a BEC and the stability of a doubly-charged vortex around the central hole in the BEC.

Our current work was largely motivated by the previous work, where we sought to improve upon the earlier experiment. We used an all-optical trap (discussed in the previous chapter), which eliminated magnetic coils and thermal drift. The trapping beams were fiber coupled, so that any thermal drift from the laser translated only to a loss of laser power in the trap, but not misalignment. The new trap also had the independent confinement of the two axes, and so relative drift would not affect the shape of the trap. With the new trap, we were able to observe persistent currents lasting 40 seconds [54].

The chapter is organized as follows. In sections 6.1 and 6.2, we will go over some general background, discussing flow in a toroidal geometry and the various ways of transferring orbital angular momentum (OAM) to a BEC respectively. The next two sections will go into some of the specifics, namely the transfer of OAM using an LG beam (section 6.3) and the other experimental changes from the previous persistent current experiment [52] (section 6.4). Section 6.5 details some of the experimental considerations for clean and efficient transfer, while section 6.6 talks about our detection method. Finally, section 6.7 discusses the persistent currents we achieved and the lifetime of the flow, and is followed by section 6.8, which mentions some of our preliminary results on multiply-charged circulation.

6.1 Flow in a toroidal BEC

In chapter 2, we discussed the concept of flow in multiply-connected geometry, and found that such flow was quantized, based on equation (2.42), which is reproduced here:

$$\frac{m}{\hbar}\oint \mathbf{dl}\cdot v_s = 2\pi n, \tag{6.1}$$

where m is the mass of the atom, v_s is the superfluid flow velocity, and n is an integer. The integral represents any path enclosing the region of no superfluid. Applying the above equation to a circular path of radius r in a toroidal condensate, we obtain

$$\frac{m}{\hbar}\oint r\mathbf{d}\theta\cdot v_s = 2\pi n, \tag{6.2}$$

from which, using the cylindrical symmetry of the problem, we can express v_s in terms of the integer n:

$$v_s = \frac{\hbar n}{mr}. \tag{6.3}$$

Equation (6.3) is identical to the velocity profile of a cloud with a single vortex, shown in equation (2.44), except for the quantum number n. Hence, a single unit of circulation in a toroid has the same velocity profile[1] as that of a superfluid with a single vortex line. However, one should be careful in taking this equivalence too far since the toroidal BEC has no vortex core.

The lack of a vortex core has several implications. There is no region where there is a trade-off between the interaction energy (mean field) and the kinetic energy, which is responsible for the shape of the vortex core. The circulating kinetic energy is typically small compared to the interaction energy or kinetic energy from

---

[1] For the region where the BEC has a non-zero density.

confinement. Such circulation is also possible in a non-interacting BEC, but would be unstable.

6.2 Transferring orbital angular momentum to atoms

The methods of transferring OAM to a BEC can be broadly classified as:

1. Mechanical stirring methods : analogous to methods to create circulation in classical fluids.
2. Phase engineering methods : exploit the quantum nature of atoms to deterministically imprint a certain number of quanta (usually one or two) of phase winding, which translates into circulation.

The classification is not perfect as above categories do not cover all the methods of transferring OAM, and some methods fall in-between the two categories. Nevertheless, the classification is still instructive in that it points out what aspect of the fluid (classical or quantum) is being exploited.

In the first vortex experiment in an atomic BEC, Matthews *et al.* [44] created a vortex state through a coherent process involving the spatial and temporal control of the interconversion of a two-component BEC between two spin states (based on a scheme by Williams and Holland [216]). This experiment could be seen as both classical, in that there was a rotating beam, and quantum, in that there was an interconversion between the two components and that the vortex had exactly one unit of circulation. In the years following, several groups demonstrated vortices in BECs by mechanical stirring [45–47, 217–223]. While mechanical stirring may seem like a classical technique, it can also be understood in terms transfer of phase winding [224].

Vortices have also been nucleated by other perturbations to a BEC, such as inducing a defect [225], sweeping a defect through a BEC [51, 226], or superimposing an oscillating excitation to the trapping potential [227]

On the phase engineering front, Isoshima *et al.* [228] first proposed a scheme of using the spin degree of freedom of the order parameter of a BEC to create a vortex. Based on that, Akamatsu and Kozuma [229] transferred OAM to atoms in a vapor cell using a LG beam, and Leanhardt *et al.* [230] transferred two (or four) units OAM to a BEC by inverting the bias of an Ioffe-Pritchard trap. OAM transfer to BECs using LG beams have been demonstrated [52, 117, 126]. There have been recent proposals to continuously pump OAM into a BEC [231, 232]. Kuwamoto *et al.* [233] transferred 4 units of OAM, by inverting the bias field similar to earlier work [230]. Vortices have also been created by engineering the Hamiltonian using a spatial-dependent optical coupling between internal states [234].

The methods of transferring OAM discussed above involve the deliberate creation of circulation in a BEC. It is worth mentioning that vortices can also be created by the merging of independent condensates [235, 236] or by the condensation process itself [151, 208]. In these situations, the process is random, where thermal or quantum fluctuations of the phase determine the number of vortices and the sign of their rotation.

While both mechanical stirring and phase engineering have been successful in creating circulation and vortices, there are some important differences, which could make one technique or the other preferable. In general, mechanical stirring is inaccurate and one cannot precisely control the amount of circulation transferred. However, it can transfer large amounts (> 5 units) of angular momentum, necessary to observe effects such as vortex lattices [47], or large vortex aggregates [218], or to attain critical rotation where the rotation velocity is close to the radial trapping frequency [221].

Phase engineering is important in situations where one needs to transfer a fixed amount of rotation, usually one or two units. Transferring large amounts of circulation by the repeated use of phase engineering is difficult because of the perturbation to the cloud by each transfer process (discussed in section 6.5). Transfer of rotation by phase engineering has been used for observing persistent currents [52] and for sculpting a vortex state in a spinor BEC [237].

For our experiments, where we observed persistent currents and studied the decay of superflow (chapter 7), we used phase engineering to transfer circulation. We implemented phase engineering using a two-photon Raman[2] transfer with an LG beam [52, 117, 126], which transferred exactly one unit of circulation.

6.3 Transferring orbital angular momentum using a LG beam

Having already discussed the connection between circulation and phase winding, we will now talk about transferring OAM using LG beams. Light can carry two kinds of angular momentum: internal or spin angular momentum associated with its polarization and external or OAM associated with its spatial mode [240]. A light beam with a phase singularity, such as an LG beam, has a well-defined OAM along its propagation axis [241]. As with circulating atoms, LG beams have a phase winding around the central phase singularity, sometimes termed an optical vortex. Coherent transfer of atoms using such a beam will cause the atomic cloud to acquire the optical phase winding.

In order to perform a coherent transfer, one needs a stable final state. Such a state cannot be in the $^3P_{3/2}$ (D_2 transition) of sodium, as the excited state has a very short lifetime and the spontaneous emission is likely to destroy the condensate. Hence, two-photon transfers leading back into the $^3S_{1/2}$ state are needed. In a two-photon coherent transfer, the difference in the phase winding of the two beams is imprinted onto the atoms.

The two-photon transfer process works identically to the single photon Rabi flopping, which we discussed in section 3.1.a. The two laser beams used for the transfer have different frequencies, ω_1 and ω_2. The resonance condition is given by

$$\omega_1 - \omega_2 = \omega_{if}, \tag{6.4}$$

where ω_{if} is the energy separation between the initial and final states (shown in

---

[2] A Raman transition refers to a transition which involves the absorption of a photon by an atom (or molecule) and the emission of a photon of a slightly different color [238]. For a history of the Raman effect, see Krishnan and Shankar [239].

figure 6.2) of the atom[3].

The two-photon Rabi frequency Ω_R depends on the Rabi frequencies of the individual beams, Ω_1 and Ω_2 as well as their mutual detuning from the single-photon resonance (normalized by the transition half-linewidth $\Gamma/2$), $\tilde{\Delta}$ (see figure 6.2), and is given by [80]

$$\Omega_R = \frac{\Omega_1 \Omega_2}{\tilde{\Delta}\Gamma}. \tag{6.5}$$

For efficient coherent transfer and to ensure that four-photon or other multi-photon processes do not occur, the final state has to be energetically separated from the initial state[4]. The circulation by itself does not create a sufficient difference in energy. Previous experiments in our group [52, 117] used counter-propagating beams for the two-photon transfer, thereby giving a net momentum kick to the transferred cloud (see figure 6.1). Owing to the spatial separation of the transferred and remnant clouds, one could choose to either image one of the two clouds (shown in figure 6.1) or selectively remove the non-circulating component [52].

In our scheme, we make an internal-state transfer between two hyperfine states of the $^3S_{1/2}$ manifold (see figure 6.2) using co-propagating Gaussian and Laguerre-Gaussian beams (similar to Wright *et al.* [126]), exploiting the fact that optical dipole traps can trap all spin states. The transferred and remnant clouds are in the same momentum state (at rest), but in different internal states ($F = 1$ m_F=0 and $F = 1$ m_F=-1 respectively, as shown in figure 6.2). To selectively remove the remnant, we need to have the two clouds in different hyperfine manifolds (remnant in $F = 2$ and transferred component in $F = 1$), so that we can shine light resonant with only the remnant cloud. Choosing a final state that is already in a different hyperfine manifold would allow this selective removal. For situations where that is not the case (figure 6.2), we separate the clouds by choosing a suitable microwave transition ($|1, -1\rangle$ to $|2, -2\rangle$).

---

[3] $\omega_2 - \omega_1 = \omega_{if}$ works equally well. In such a situation, the imprinted phase winding and hence the rotation would be in the opposite direction.

[4] In principle, a suitable change in spin state would be sufficient to ensure that no multi-photon processes occur (say transfer from m_F=-1 to m_F=+1 of the $F = 1$ hyperfine manifold).

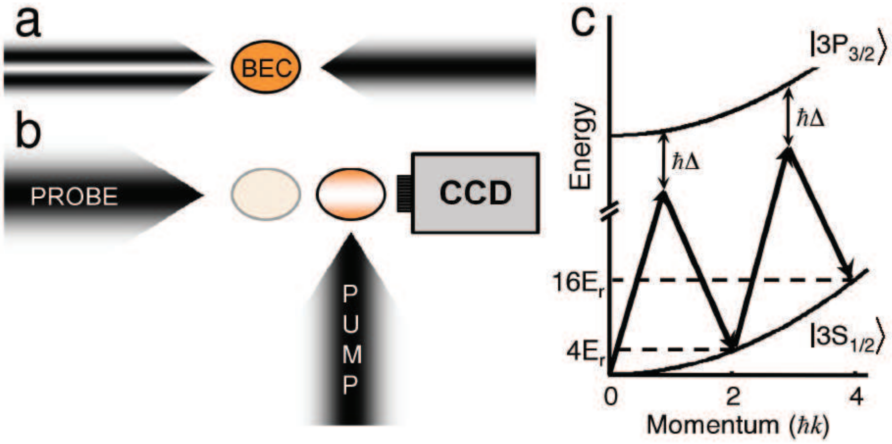

Figure 6.1: OAM transfer via counterpropagating beams [117]: (a) Counterpropagating LG_0^1 and Gaussian laser beams, with the same linear polarization and a frequency difference ($\omega_1 - \omega_2 = \omega_{if}$), were applied to a BEC. (b) The atoms that had undergone the Raman transition (right cloud) would separate from those that had not (left cloud). A spatially localized pump beam was used for independent imaging of each cloud by the absorption of a probe beam propagating along the direction of linear momentum transfer. (c) Diagram illustrating energy and linear momentum conservation of the 2-photon Raman process for one and two consecutive pulses ($\tilde{\Delta}$ here has not been normalized by $\Gamma/2$). For a single pulse $\hbar\omega_{if} = 4E_r$, where E_r is the recoil energy of the atom. The recoil energy is calculated from $E_r = \hbar^2 k^2/2m$, where $k \approx \omega_1/c \approx \omega_2/c$ is the momentum of the photon. (taken from Andersen *et al.* [117])

6.4 Changes from the previous experiment

Since the goal of our current experiment was to realize persistent currents, similar to Ryu *et al.* [52], it is useful to compare the similarities and differences between the two experiments. The two experiments were broadly the same. Both experiments observed persistent flow by looking at the decay of a single quantum of flow around a toroidal geometry. Both experiments used a two-photon Raman transfer with an LG beam for transferring OAM. Both experiments detected the survival of flow by looking for a density minimum in the time-of-flight (TOF) expansion of the cloud (discussed in section 6.6). However, despite the general similarity, there

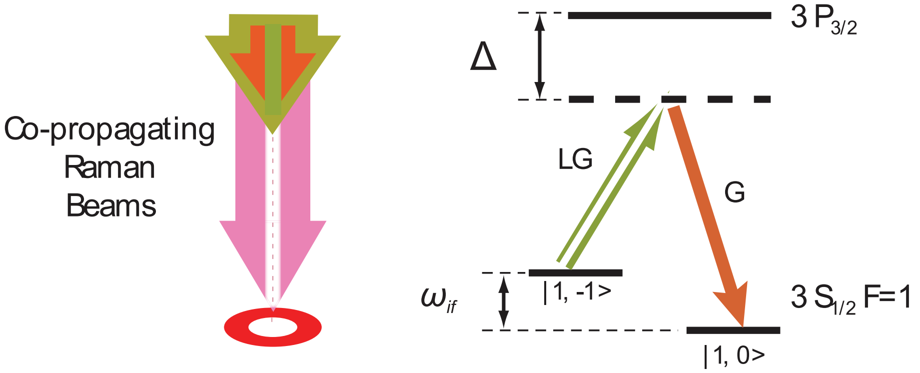

Figure 6.2: OAM transfer scheme : (left) We use co-propagating Gaussian and LG beams for the transfer of OAM, and hence do not transfer any linear momentum to the BEC. The beams travel along the same beam path as the trapping infrared LG beam. (right) The transfer occurs between the m_F=-1 and m_F=0 magnetic sublevels of the $^3\mathrm{S}_{1/2}$ $F = 1$ hyperfine manifold.

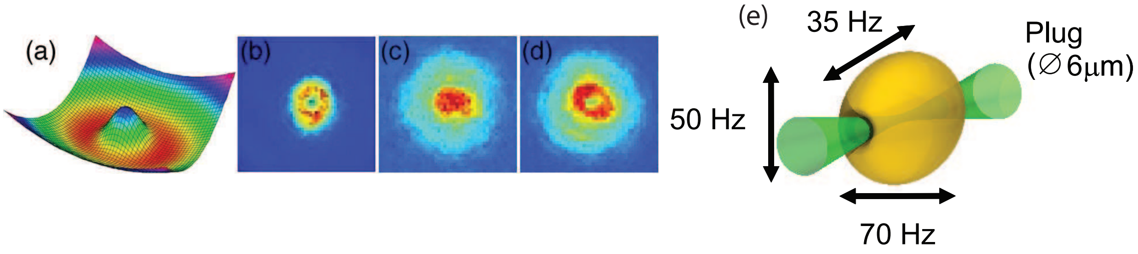

Figure 6.3: Plugged TOP trap : (a) Toroidal trap from the combined potentials of the TOP magnetic trap and Gaussian laser "plug" beam. (b) In-situ image of a BEC in the toroidal trap. (c) TOF image of a non-circulating BEC released from the toroidal trap. (d) TOF image of a circulating BEC, released after transfer of one unit of orbital angular momentum. (e) 3D rendering of the spheroidal trap and the optical plug. (from Ryu *et al.* [52])

were a few key differences:

- In the plugged TOP trap, the inner diameter of the BEC was around 10 μm (see figure 6.3). In our all-optical trap, it was around 20 μm. Since the atoms on the inner edge have the highest velocity, depending on the inner radius, this difference is important.
- In transferring circulation to the atoms via a two-photon transfer, the previous experiments used a change of momentum state to energetically separate the initial and final states. In the new experiments, we used a change of internal state (figure 6.2).
- In detecting circulation, the previous experiments did a simple 13 ms TOF. As a consequence of our relatively larger inner radius, we employed a slightly different scheme where we lowered the toroidal confinement before doing a 6 ms TOF.
- In the previous experiment, the persistent current lifetime was limited to 10 seconds by the relative drift between the magnetic trap and the optical plug. In the current experiment, we observed flow lasting up to 40 seconds (figure 6.8), limited by the lifetime of the BEC (see section 6.7).

Now that we understand the differences between the current and the previous persistent current experiments, we can move on to discuss some of the more practical considerations.

6.5 Practical considerations for the transfer of circulation

Before we arrived at our current scheme of transferring circulation to the atoms, we tried out several different initial and final state combinations. The current scheme was arrived at after optimizing the OAM transfer process to have the most efficient transfer to the final state, with minimum heating of the BEC and minimum perturbation to the cloud. I shall now go over some of the technical issues associated with the transfer process, and describe the changes implemented to overcome or minimize them.

6.5.a Single photon scattering

Although detuned far from resonance, the Raman beams still cause some single-photon off-resonant excitation. The number of atoms lost can be expressed as the number of photons absorbed, *i.e.* $N_l = \bar{M}_{\text{abs}}$. Applying the far-detuned limit, *i.e.* $\tilde{\Delta} \gg 1$, to the photon absorption $\bar{M}_{\text{abs}}$ by a cloud as described in equation (4.11), we obtain

$$N_l = \frac{\bar{M}\beta}{\tilde{\Delta}^2} = \frac{\bar{M}N\sigma_0}{A\tilde{\Delta}^2}, \tag{6.6}$$

where $\bar{M}$ is the incident number of photons and β is the on-resonant optical depth of the cloud, N is the number of atoms in the region of interest or area A. For a Rabi π-pulse, necessary to transfer the cloud to the circulating state, the pulse area (intensity × time) is given by

$$\Omega_R \tau = \pi, \tag{6.7}$$

where τ is the pulse duration. Using equation (6.5) and expressing the Rabi frequency in terms of I_{sat} (see section 3.1.c), we get

$$\frac{\Gamma\tau\sqrt{I_1 I_2}}{2I_{\text{sat}}\tilde{\Delta}} = \pi, \tag{6.8}$$

where I_1 and I_2 are the intensities of the two Raman beams. To express $\bar{M}$ in terms of intensity, we use

$$\bar{M} = I\tau A/\hbar\omega, \tag{6.9}$$

and assume that the two beams have roughly equal intensities, $I_1 \approx I_2$ and so, substituting $I = I_1, I_2$ from equation (6.8) into (6.9), we obtain

$$\bar{M} = 2\pi I_{\text{sat}}\tau A\tilde{\Delta}/\hbar\omega. \tag{6.10}$$

The frequency difference has been neglected for this calculation ($\omega = \omega_1 \approx \omega_2$). Finally, substituting $\bar{M}$ into equation (6.6), and using $\sigma_0 = \Gamma\hbar\omega/2I_{\text{sat}}$ from equation (4.2), we obtain

$$N_l = \frac{\pi}{\tilde{\Delta}}N. \tag{6.11}$$

For simplicity, we have assumed a 3-level system. The initial and final states couple via an intermediate excited state, which in the process also causes single photon scattering. In reality, there are multiple intermediate states, each with a different coupling strength. Not all intermediate states contribute to the two-photon process. Since the intermediate states have different energies, the detuning $\tilde{\Delta}$ also varies between the states. We are justified in the assumption of a 3-level system in that the detuning is typically much larger than the spacing of the intermediate states, and so they behave like an effective state, although the losses are typically higher than predicted, because of the many states only contributing to loss, but not two-photon coupling.

The single photon loss scales simply as a $\pi/\tilde{\Delta}$ fraction of the number of atoms. Hence, it is advantageous to detune as far from resonance as possible[5], so long as the laser power is still sufficient to drive the two-photon transition. We initially used a detuning of around $(2\pi) \times 500$ MHz ($\tilde{\Delta} \approx 100$), which gives a (lower bound) calculated loss of 3%. However, the actual losses were much more, ~20%, for reasons mentioned above. We later used a detuning of $(2\pi) \times 2.3$ GHz ($\tilde{\Delta} \approx 50$), which gives a calculated loss of 0.6%. The actual loss was around 5%.

6.5.b Dipole force

Apart from the single-photon scattering, the Raman beams individually also cause an energy shift. The spatial inhomogeneity of the beams translates to a gradient dipole force on the atoms. The dipole force can cause the BEC to be excited by breathing and sloshing oscillations (section 5.7), which leads to heating and loss of atoms.

As discussed in section 3.1.b, a far off-resonant beam causes an energy shift given by $\delta\epsilon = \hbar\Omega^2/2\Gamma\tilde{\Delta}$, which gives a total energy shift due to the two Raman

---

[5] In detuning very far from resonance, one must keep in mind possible coupling via other excited states, say the D_1 line, that may affect the overall coupling strength.

beams

$$\delta\epsilon = \frac{\Omega_1^2 + \Omega_2^2}{2\Gamma\tilde{\Delta}} \tag{6.12}$$

which, like the expression for the two-photon Rabi frequency has a $1/\tilde{\Delta}$ dependence. For $\Omega_1 \approx \Omega_2$, we get

$$\delta\epsilon = \frac{\Omega^2}{2\Gamma\tilde{\Delta}} = \frac{\Omega_R}{2}.$$

Since the energy shift scales with the Rabi frequency, changing the intensity or detuning does not make any difference to the magnitude of the light shift.

If we were to consider the case of two uniform beams, there would be a uniform light shift which would result in no dipole force since there would not be any field gradient. For that reason, we made the Gaussian beam large compared to the size of the BEC to make the light shift as uniform as possible. However, the LG beam necessarily has an intensity gradient with a length scale the size of the BEC. To minimize the dipole force due to the LG beam, we lowered the power of the LG beam, while increasing the power of the Gaussian beam to keep the two-photon Rabi frequency constant until the dipole force was smaller than other perturbations from the two-photon Raman process.

6.5.c Cleaning up the remnant

In our two-photon Raman transfer scheme, the transferred cloud and the remnant cloud, which are in different magnetic sub-levels, are both at rest and occupy the same area in physical space. In such a situation, interactions between atoms in different magnetic sub-levels play a role. In sodium, the inter-species scattering length (scattering between atoms in different magnetic sub-levels) is usually higher than the intra-species scattering length (scattering between atoms in the same magnetic sub-level) and hence any hyperfine mixture tends to spatially phase-separate [242]. This phase separation affects the condensate dynamics of both clouds and could cause the circulation to decay[6].

---

[6] We observed that phase separation of the cloud due to a significant remnant tended to break the continuity of the circulating cloud around the ring, causing the flow to decay.

While microwave or rf transfer processes can be made to transfer 100%, the transfer of circulation cannot be 100% because of the non-uniform radial intensity profile of the LG beam, and hence there will always be a remnant that must be removed from the trap.

The removal of atoms using resonant light occurs as follows. The atom absorbs a photon, acquiring a momentum $\hbar k$ from the photon, and correspondingly a recoil energy of $E_r = \hbar^2 k^2/2m$. The atom then spontaneously decays back to the ground state (not necessarily the state it started in) by emitting a photon in a random direction, acquiring another momentum kick $\hbar k$. From the two momentum kicks, the atom, on average, acquires translational kinetic energy of $2E_r$ [87].

At first sight, it might seem like as long as the transferred fraction and the remnant are in different hyperfine manifolds, we can simply shine light resonant with the remnant and eject those atoms. However, it is always better to have the remnant in the $F = 2$ state (and the transferred fraction in the $F = 1$), since the $F = 2$ can be removed with light resonant with the cycling transition, scattering many photons per atom, acquiring many recoil energies ($\approx nE_r$, where $n > 50$ for sodium) ensuring that the atom leaves the trap. If the remnant was in the $F = 1$ state and $F = 1$ to $F' = 2$ imaging light was shone, a good fraction of atoms would undergo only a single recoil event before decaying to the $F = 2$ state acquiring only a single recoil energy (0 to 4 E_r). Such atoms may not have sufficient energy to leave the trap and may collide with other atoms causing heating.

To give an estimate, $E_r = h \times 25$ kHz (calculated) for sodium. The total trap depth for our trap (from table 5.1) is 25 kHz. An atom absorbing a single recoil may not leave the trap, whereas an atom absorbing $n \approx 20$ recoils is almost certain to leave the trap. Hence, it is important to always remove the remnant using the $F = 2$ to $F' = 3$ cycling transition.

6.5.d Our optimized scheme

After several changes and improvements, we arrived at our optimized scheme, through which we could transfer 90% of the atoms to the circulating state. In our scheme (shown in figure 6.4), we make an internal-state transfer between two magnetic sublevels (m_F=-1 to m_F=0) of the $^3\mathrm{S}_{1/2}$ $F = 1$ hyperfine manifold. We then selectively perform a microwave transfer, transferring the remnant to the $^3\mathrm{S}_{1/2}$ $F = 2$ ($m_F = -2$), which can then be ejected using resonant light. Our Raman beams were detuned 2.3 GHz from single-photon resonance, limited by the various laser beam frequencies we had available[7]. We used a shallow trap (trap depth $\approx$ 25 kHz) so that single-photon scattered atoms could more easily leave the trap without causing heating.

At low magnetic fields, the energy difference between the m_F=-1 and m_F=0 states is equal to the difference between the m_F=0 to m_F=+1 states. It is not possible to ensure transfer only to the singly circulating m_F=0 state if the degeneracy is not broken. We break the degeneracy using the quadratic Zeeman effect (shown in figure 3.7) by applying a higher magnetic bias field ($\approx$ 5 G). The bias field strength was limited by the $\approx$ 1 A current that we were able to pass through the bias field producing current coils. At 4.9 G, the linear Zeeman shift caused a splitting of around 3.4 MHz, while the quadratic Zeeman shift caused the energy differences to be split by around 20 kHz, for which we used a 100 μs Raman pulse to minimize coupling to the m_F=+1 state.

We obtained a transfer efficiency of around 90% (see figure 6.5) to the final rotating state. There were some small oscillations created during the transfer of circulation due to the dipole force of the Raman beams and the sudden $\approx$ 10% loss of atoms due to the 90% transfer efficiency. These oscillations decayed in several 100 ms (similar to figure 5.11, when we deliberately excited them), and caused no problems to the circulation or its detection. However, as the energy of oscillations ultimately leads to heating, we typically waited a few seconds for the cloud to equilibriate in the trap before performing any further experiments.

---

[7] In the lab, the various laser beams used for the MOT, the Zeeman slower, absorption imaging, the Raman beams, etc. are all derived from two lasers, appropriately frequency shifted using acousto-optic modulators [114]. Acousto-optic modulators are limited in how much they can shift the frequency, thereby limiting how far from single-photon resonance the Raman beams can be detuned.

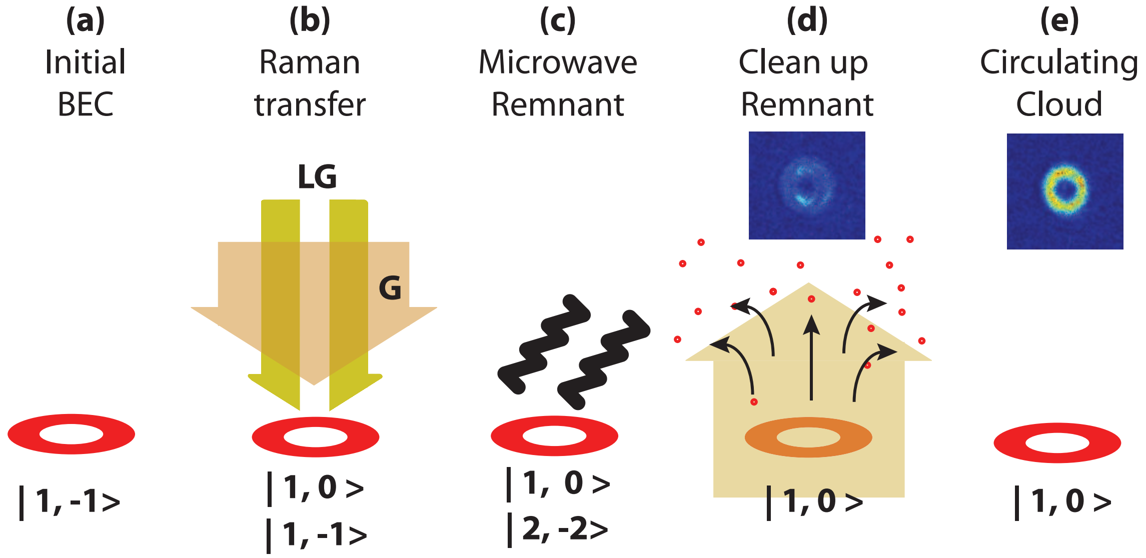

Figure 6.4: The OAM transfer with co-propagating Gaussian and LG beams is shown : We start with an initial $|F = 1, m_F = -1>$ BEC, which undergoes a 2-photon Raman transfer (b) to the $|1, 0>$ state. We then transfer the remnant $|1, -1>$ cloud to the $|2, -2>$ state via a microwave process (c) and then remove the remnant $|2, -2>$ atoms using $F = 2$ resonant light (d). The $F = 2$ resonant light, which is also used for absorption imaging of the final cloud, is used to obtain an image of the remnant (shown under (d)) to get information about the efficiency of the transfer process. Finally we obtain a circulating cloud in the $|1, 0>$ state (e). The circulating cloud does not look very different from the stationary cloud *in situ*.

6.6 Detecting the circulation

Vortices in a BEC are usually detected by doing a simple TOF (for example see Madison *et al.* [45]). The vortex core, with a characteristic size given by the condensate healing length, is too small to be resolved by an *in situ* image. In TOF, the vortex core expands and one can see a clear central hole.

Since circulation was detected by a simple 13 ms TOF in the previous persistent currents experiment [52], we initially tried to detect circulation by a simple similar TOF. However, we overlooked a crucial difference between our current experiment and the previous persistent current experiment, which delayed our detection

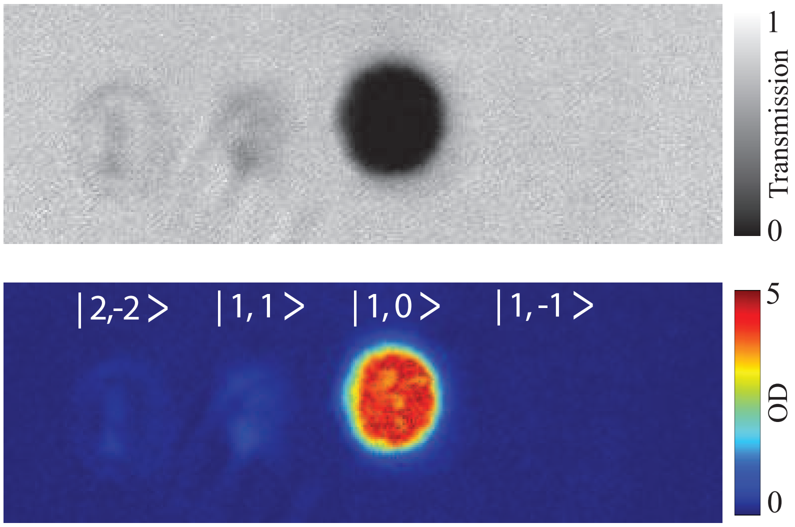

Figure 6.5: OAM transfer efficiency : The figure shows the distribution of atoms in the various spin states after the transfer of OAM. The atoms are transferred from the initial non-circulating $|F = 1, m_F = -1\rangle$ state to the circulating $|1, 0\rangle$ state via a two-photon Raman transfer process. In the process, some atoms ($<$ 4% of initial number) undergo a four-photon transfer to the $|1, 1\rangle$ state with two units of circulation. The $|1, -1\rangle$ remnant ($<$ 5%) is then transferred to the $|2, -2\rangle$ state via a microwave pulse. The different spin states are then split by applying a magnetic field gradient and releasing the cloud in TOF.

of circulation and persistent flow by more than four months! In performing a simple TOF for the circulating cloud (see figure 6.6 top), we found that the central hole did not persist. It appeared to close in TOF (due to mean-field driven ballistic expansion), qualitatively indistiguishable from the behavior of a non-circulating cloud (figure 5.6).

The reason for vortices to be visible in a simply-connected BEC in TOF is as follows: The velocity of flow around a vortex has a $1/r$ dependence (r is the distance from the center of circulation)[8]. Due to the mean-field of the cloud in the trap, atoms can climb the $1/r^2$ (comes from the v_s^2 scaling of the kinetic energy) centrifugal pseudo-potential of the vortex, acquiring a kinetic energy comparable

---

[8] Here, I am assuming a lengthscale small compared to the size of the condensate or any other perturbation.

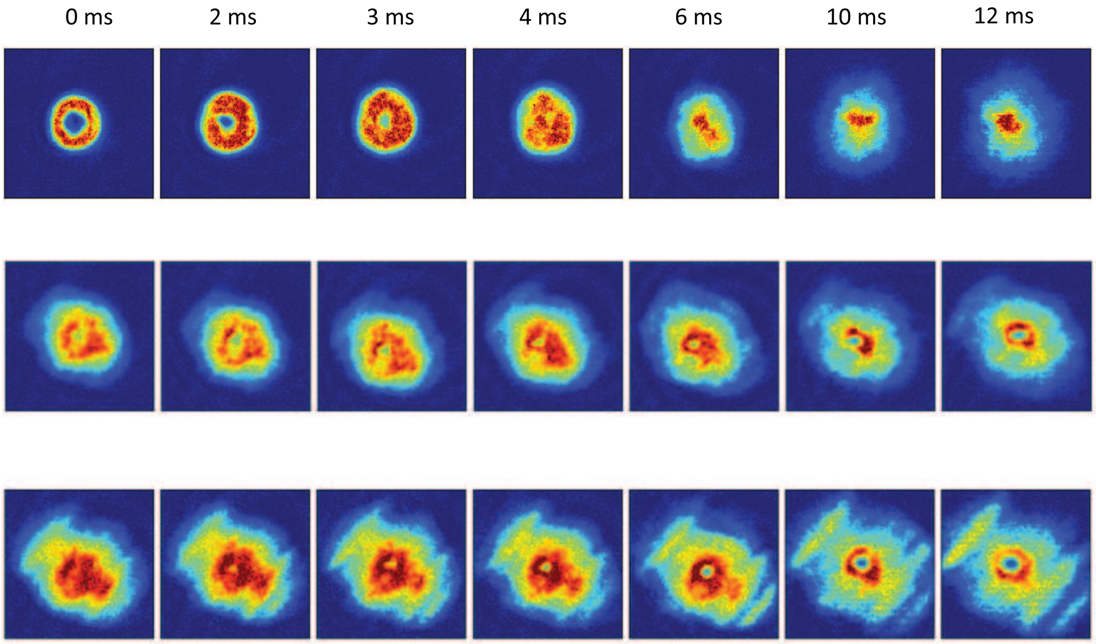

Figure 6.6: TOF sequence after relaxing radial confinement : The figure shows TOF sequences of a circulating cloud with no relaxation (top), after relaxing the strength of the radial confinement to 28% of the unrelaxed value (middle) and relaxing to 7% (bottom) respectively. With no relaxation (top), the TOF is indistinguishable from that of a non-rotating cloud. The hole due to circulation becomes larger and more resolvable with increasing relaxation. The fringe-like structure on the top left and bottom right of some of the images is due to inhomogeneities in the sheet beam potential, and does not affect the detection of circulation. The sheet beam propagation axis is at 45 degrees, from bottom left to top right, and hence there are no structures along that direction.

to the mean-field[9]. In TOF, for the bulk of the cloud, the mean-field energy is distributed amongst the three axis in the form of kinetic energy, causing expansion. For the atoms close to the vortex core, there is a strong outward expansion due to

---

[9] In fact, the radius r_μ at which the kinetic energy of the vortex pseudo-potential equals the BEC mean-field, $\hbar^2/2mr_\mu^2 = \mu \Rightarrow r_\mu = \sqrt{\hbar^2/2\mu m} = (8\pi\rho a)^{-1/2}$, is the healing length ξ. Hence, for estimates of the energy of a vortex, the vortex core size can be taken to be the condensate healing length.

the tangential velocity of circulation. This expansion is primarily responsible for the visibility of a vortex.

In our ring trap, since the inner radius of the cloud is 10 μm, the tangential velocity of such atoms is ≈ 0.3 mm/s for one unit of circulation. Given a mean-field of about 1 kHz, our in-plane expansion velocities (directed radially for a ring shaped cloud) are nearly an order of magnitude higher. Expansion is radially symmetric in TOF and atoms acquire little additional tangential velocity as the cloud expands towards the center. Since the radial velocity is much higher than the tangential velocity, atoms get very close to the center of circulation. While the singularity persists in TOF, atoms nevertheless get very close to it preventing us from optically resolving the hole due to the singularity. The tangential velocities due to circulation are too small to have any impact on the TOF expansion for the durations probed.

To overcome this issue, we adiabatically relax the radial confinement over 100 ms to less than 10% of its initial value before doing a release into TOF. This does three things. It allows atoms to move closer to the center gaining a higher tangential velocity. It lowers the mean-field and hence the radial velocity in TOF. Finally, by lowering the annular confinement (ω_r), it causes more mean-field energy to be released along the vertical direction than the radial direction (discussed in section 5.5.b), further lowering the radial velocity. This allowed us to clearly resolve the hole due to circulation (see figure 6.6).

To give an estimate of numbers for the above argument, consider a typical trap, $\omega_z = 2\pi \times 550$ Hz, $\omega_r = 2\pi \times 110$ Hz, $N = 2 \times 10^5$, r_M =20 μm. The chemical potential $\mu_0 = 1$ kHz (see table 5.2). The initial TF radius r_{TF}=9 μm. This gives a circulating velocity of 0.25mm/s for atoms on the inner of the condensate. The velocity of radial expansion of the condensate (see section 5.5.b) is $\approx$ 1.2mm/s, a factor of 5 more than the velocity of circulation.

On relaxing the radial confinement to 10% of its initial value, $\omega_r = 2\pi \times 35$ Hz, for the same number of atoms, $\mu_0 \approx 580$ Hz. We get r_{TF}=20 μm, which is equal to the radius of the ring, r_M, implying that the inner edge reaches the center and hence the local healing length ($\xi \approx$0.6 μm). The circulating velocity becomes 2.7 mm/s.

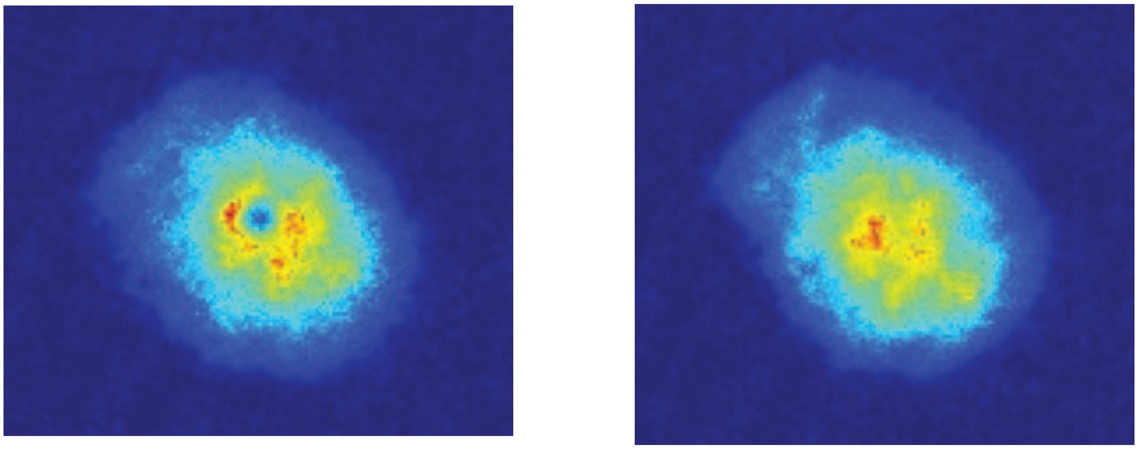

Figure 6.7: Distinguishing between circulation and no circulation : After our standardized sequence of adiabatically relaxing the radial confinement to 5% of its initial value followed by a 6 ms TOF, we could clearly distinguish a circulating cloud (left) from a non-circulating cloud (right) by its central hole.

The velocity of radial expansion for this configuration is 0.3 mm/s which is a factor of 10 smaller than the circulation velocity. Hence, relaxing the radial confinement lets the circulating velocity to play a greater role in the BEC expansion, allowing us to more easily detect the presence of flow.

6.7 Lifetime of persistent currents

We settled upon a a sequence where we relax the radial confinement to around 5% of its initial value, followed by a 6 ms TOF. We could clearly distinguish the case of a circulating cloud vs a non-circulating cloud (see figure 6.7).

Once we realized how to detect the flow, we had no difficulty in observing the persistent currents. We found the current to last 40 seconds (figure 6.8). The lifetime of the current was limited by the lifetime of the BEC, which was ≈ 30 s for the data shown in figure 6.8. In our apparatus, the lifetime of the BEC was limited by background gas scattering due to imperfect vacuum. On days when the vacuum limited lifetime of the BEC was shorter, the lifetime of the persistent current was shorter.

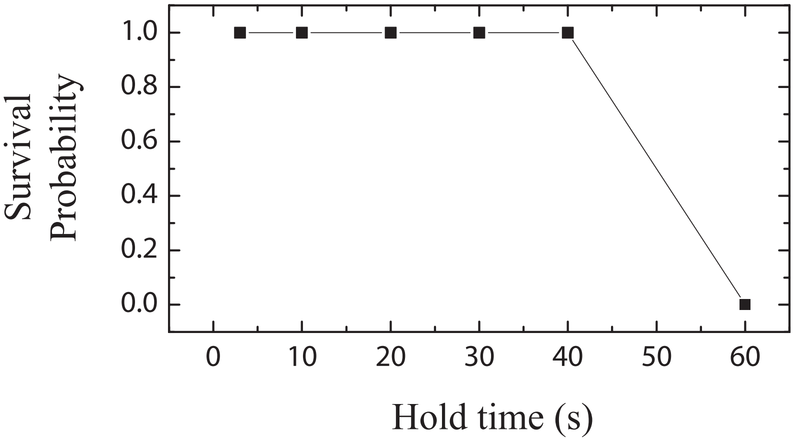

Figure 6.8: 40 second persistent current : We find that the persistent current lasted 40 seconds, limited only by atom loss from the BEC due to background gas scattering. The vacuum limited trap lifetime of the atoms was ≈ 30 s for the above measurements. The number of points for each time, from shortest to longest hold times are 4 (for 3 s), 5, 2, 2, 5 and 1 (for 60 s) respectively.

The above paragraph may imply that the persistent current survives as long as there is some BEC. This is not the case. The flow decays when the chemical potential reaches the level of bumps in the potential, breaking the continuity of the annulus. The reader may be curious to know the exact decay mechanism, whether the flow decays just before continuity is broken or just after, etc. The next chapter investigates precisely this point, and so a discussion here, with the limited data that we have, would not give a complete picture.

6.8 Multiply-charged circulation

Having successfully demonstrated transferring and detecting circulation, one of the next things to try was transferring multiple units of circulation. We did so by repeating the transfer process multiple times. After each transfer, we moved atoms back to the m_F=-1 state using an rf pulse (figure 6.9). In this manner, we successfully transferred up to 3 units of circulation.

While transferring multiple units of circulation was straightforward, detection

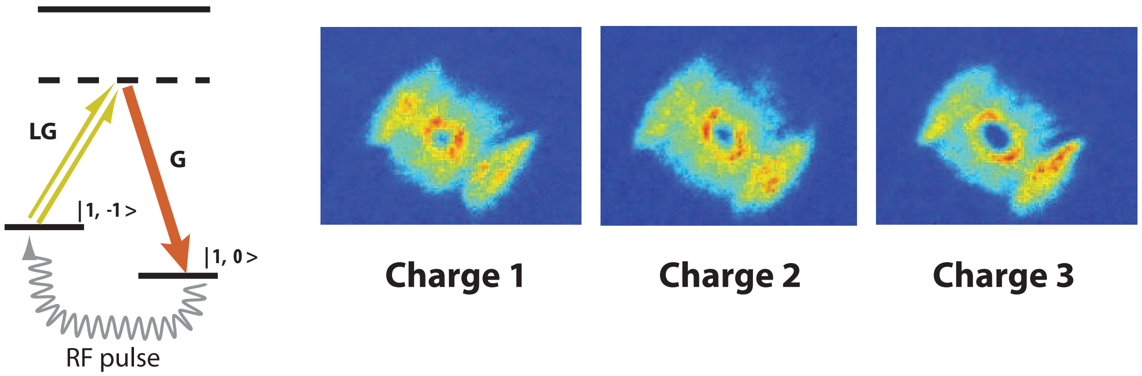

Figure 6.9: Multiply-charged circulation : By repeating the process of transfer of circulation (using an rf pulse to get the atoms back to the $|1,-1\rangle$ state), we were able to observe transfer of up to 3 units of circulation. The larger rotational kinetic energy due to the higher circulation causes a larger central hole in TOF, when the cloud is controlled to have about the same number of atoms. The BEC peripheral "lobes" on the top left and bottom right of the main “lobe” that contains the hole, are due to inhomogeneities in the sheet potential. They do not affect the measurement of circulation.

was more tricky. In performing our standard relaxation and TOF, the difference between no circulation and one unit of circulation is simply the appearance of a hole in TOF (figure 6.7). The difference between one unit and say two units of circulation is the size of the hole, as the cloud with two units of circulation has four times the kinetic energy. The size of the hole gets larger with additional units of circulation, as shown in figure 6.7. However, the size of the hole also depends on the radial relaxation. Accurately distinguishing the different levels of circulation requires more care and calibration, which is one of the future directions of the experiment.

Another possibility for detecting multiply-charged circulation is to remove the radial confinement and allow the BEC to become simply connected[10]. In a simply-connected geometry, it is energetically favorable for a multiply-charged vortex to break up into individual vortices [52]. In some of our preliminary attempts, we

---

[10] Even in the absence of toroidal confinement, the sheet beam confines the BEC in the horizontal. See section 3.6.a.

were not able to find a suitable relaxation time after removing the annular confinement, when the multiply-charged vortex split into individual vortices without any individual vortices leaving the system[11]. In our attempts, we found that either the multiply-charged vortex had not split up, or one of the individual vortices had already left the system. However, with a better understanding of the vortex dynamics, it may be possible to find a suitable relaxation sequence that would allow us to determine the presence of multiply-charged circulation.

6.9 Conclusion

We were able to create and observe persistent currents lasting 40 seconds, limited only by the vacuum lifetime of the BEC. In a toroidal BEC, circulation is quantized and hence, on transferring only one unit of circulation, the survival of flow indicates that there is no dissipation (not counting the loss of atoms). This is unambiguous evidence of superflow and hence superfluidity.

From a practical stand point, we found the persistent currents to be remarkably robust. We found them to survive even in bumpy traps (discussed quantitatively in chapter 7) and sub-optimal conditions such as misaligned beams (the LG Raman beam misaligned by half a radius from the center), imperfect detuning of the Raman beams (even for transfer fractions of around 40%) and lower mean-field (so long as there was continuity in the BEC around the ring). It usually took something severely wrong for persistent currents not to work. This is also a testament to superfluidity and dissipationless flow. We look forward to the day when, just like how making a BEC is so reliable, making a persistent current also becomes a routine part of the process.

While making a clean ring trap merely set the stage for creating persistent currents, obtaining a reliable persistent current was an important milestone and opened the door to several experiments. The most obvious experiment is studying the decay of flow in the presence of a barrier, which constitutes the next chapter.

---

[11] Vortices in a simply-connected trapped BEC are by nature unstable excitations.

However, there are other possibilities, two of which I shall briefly mention.

Although the kinetic energy of a single vortex is much lower than the mean-field and has no impact on the radial spatial distribution of the BEC, going to high units of circulation can significantly increase the kinetic energy. It would be interesting to know how much circulation the ring could sustain, and if there was any effect of the high kinetic energy on the radial spatial profile of the BEC [47, 218].

Primordial circulation is also interesting [151, 208]. Primordial circulation refers to circulation that was entrapped during the BEC condensation process. As with persistent currents, any such circulation is expected to be stable and last the lifetime of the BEC. During the initial experiments of persistent currents, we noticed some false positives (around 1 in 10) in vortex formation, which we later realized were due to primordial circulation from the condensation process. We could eliminate such circulation (to prevent it from interfering with our measurement) by putting a barrier in the flow path of the initial BEC to break the continuity of the ring. Nevertheless, primordial circulation is interesting and has implications on critical fluctuations.

There are also interesting physics in the ring trap that can be studied using the spinor degree of freedom, which are yet to be explored. However, rather than describe other possible experiments, it suffices to say that having realized persistent currents, there are lots of interesting possibilities. We shall now move on to studies of the critical velocity of flow.

Chapter 7

Superfluid flow in the presence of a barrier

Having successfully observed superflow and persistent currents, we went on to make a more quantitative test of superfluidity by introducing a barrier in the flow path of the ring. Given the superfluid nature of the BEC, for a weak barrier in the flow path, the superfluid property should ensure that there is no dissipation. In the opposite limit, that of a high barrier, the ring is no longer continuous and hence cannot sustain flow. Somewhere in between, there is a critical point at which the flow decays.

The breakdown of superfluidity can be understood in terms of the Landau criterion (discussed in section 2.4), which states that dissipation occurs at a critical flow velocity when it is energetically favorable to create excitations. Naturally, such excitations are expected to be from the low-energy excitation spectrum, which could be phonons or vortex-like excitations. For low-level phononic excitations, the critical velocity is the speed of sound in the condensate[1]. For vortex-like excitations, one can use Feynman's approximate expression for the critical velocity.

Before we go on to the details of the experiment and how the various critical velocities could play a role, let us take a look at previous related work. The breakdown of superfluidity in BECs has been experimentally probed in different ways. Experiments at MIT [48, 49] scanned a blue detuned laser beam back and forth through a BEC and found that excitations were created when the scan speed crossed a certain critical velocity. Engels and Atherton [50] swept a penetrable

---

[1] Often, this velocity is termed as the Landau critical velocity, which I feel is incorrect for two reasons. Firstly, it takes away credit from Landau, who stated the general expression for any excitation *and then* took the specific case of liquid helium considering phonons and rotons [13]. Secondly, until Bogoliubov's theory of weakly-interacting gases [16], the expression for the sound velocity in a BEC as well as the possibility of pure phononic (without rotons) breakdown did not exist.

barrier along a cigar-shaped BEC and observed that excitations in the wake of the beam were created when sweep speed crossed a certain critical velocity. Experiments at the University of Arizona [51] forced a Gaussian obstacle through a superfluid and found that at a critical velocity, a vortex-antivortex pair was nucleated. In all experiments, the inhomogeneity and finite size of the sample were such that the breakdown of superfluidity could not be simply explained in terms of a phononic or vortex-like critical velocity for a uniform system.

Our current work has three key differences from previous work:

- The superfluid is made to flow, while the barrier is stationary. While in the frame of reference of the atoms, this should not matter, our experiment is closer to the original superfluidity experiments [9, 10].
- In our experiment, the superfluid is in a metastable circulating state, which is different from the stationary ground state. Previous work had the BEC in the ground state.
- In contrast to the previous work, which looked for signs of excitations in the BEC, the current work detects the survival of flow. In that sense, the detection does not depend on whether we can see the excitations or heating, and with the additional feature of a binary detection (flow survives or does not), our detection of dissipation is more direct and sensitive.

Given the binary detection of the breakdown of flow, our data does not reveal the decay mechanisms, and hence, we need a good understanding of our system. In the following sections, I will first discuss the various aspects of superflow in a toroidal geometry, the stability of the persistent current and the concept of phase slips. I will then describe the dimensionality aspects of the problem, particularly with respect to quasi-2D physics, and in that context, describe some of our previous experiments on 2D Berezinskii-Kosterlitz-Thouless physics. Following that, I will go into the experimental details, our observations, the analysis of the data and subsequently make comparisons to the phononic and vortex-like critical velocities, before concluding.

7.1 Superfluid flow in a toroidal condensate

In the previous chapter, we discussed the velocity profile of a uniform toroidal condensate with one unit of OAM (equation (6.3)). The flow profile, **J**, defined as the number of atoms moving through a unit cross-section in unit time, is given by

$$\mathbf{J}(r,\theta,z) = \frac{\hbar}{mr}|\psi(r,\theta,z)|^2\hat{\theta}. \tag{7.1}$$

As mentioned previously, the $1/r$ dependence comes from the fact that as one goes further from the center of circulation, the phase winding is distributed over a larger circumference leading to a lower gradient and hence lower flow. The expression holds for any system with cylindrical symmetry.

The case of a ring with a barrier (non-uniform ring) is more complicated, since one cannot simply use the symmetry of the problem. Before we solve the problem of flow in a ring with a barrier, let us first look at the effect of a barrier in the ring.

7.1.a Effect of a barrier

The barrier, in effect locally changes the potential of the trap. The effect can be easily seen in an *in situ* image (figure 7.1a). For a BEC, particularly if it is radially TF, this causes a decrease in the local mean field of the condensate (figure 7.1b). The decrease in mean field thereby causes fewer atoms to be present at the location of the barrier, which is accentuated by the transverse TF profile (radially integrated number of atoms, $n_{1D} \sim \mu^2$ from table (5.2), where μ is the mean field)), as can be seen in the azimuthal atom distribution of figure 7.1c.

A second consequence of lowering the mean field of the (TF) condensate, is a slight constriction in the transverse directions (radial and vertical) of the BEC at the location of the barrier. This may seem counter-intuitive at first since we are not actively squeezing the condensate at the location of the barrier. However, because of the harmonic condition, (nearly) uniformly raising the potential at the location of the barrier causes some regions to be raised beyond the chemical potential. As the condensate is TF, particularly in the transverse direction, this leads to the

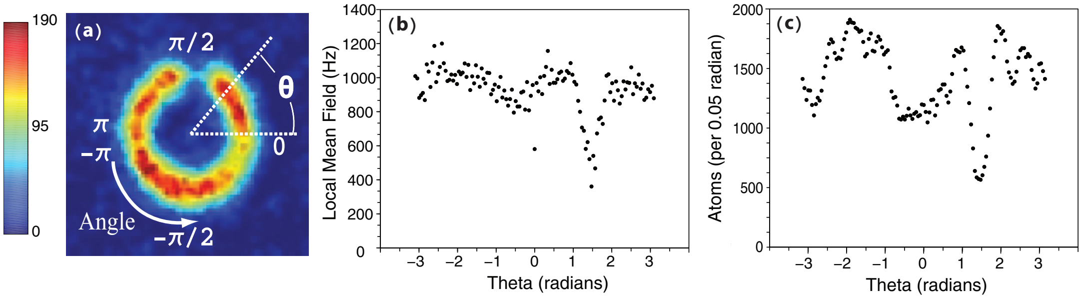

Figure 7.1: Effect of a barrier on a toroidal BEC: (a) PTAI image of the BEC (colorbar shows column density in atoms/μm^2). The barrier has been inserted at an azimuthal position of $\pi/2$. (b) Azimuthal plot of the condensate mean field (see appendix C.7 for details). The condensate was broken down into 128 angular sections of 0.1 radians each, and a fully ring TF profile (column density distribution given by equation (5.35)) was fitted to each section to obtain a peak height, which was related to the mean field using equation (5.36). The barrier causes a strong reduction in the local mean field. (c) Azimuthal plot of the distribution of the number of atoms. The effect of the barrier is more pronounced because of the transverse TF profile and causes a sharper dip in the region of the barrier (for a TF BEC, radially integrated number of atoms, $n_{1D} \sim \mu^2$, see table (5.2)).

condensate having a smaller transverse extent at the location of the barrier[2].

The change in shape and density of the condensate at the location of the barrier breaks the azimuthal symmetry of the problem and prevents us from using equation (7.1) to obtain the flow pattern. However, all is not lost. Some general assumptions are still valid:

- Steady state condition: If one assumes an steady state configuration where the density distribution does not change with time, flow has to be conserved for any path along a direction of flow[3]. For a given flow path $\mathbf{l}(s)$, where s is

---

[2] In principle, the displacement of atoms from the barrier region should cause the overall chemical potential to increase. However, in practice, for our system, this effect was small ($< 5\%$) and we chose to ignore it in light of our nearly 10% calibration uncertainty.

[3] This assumes a well defined flow velocity vector at all points in the BEC. Starting at any point, one can follow the flow velocity vector around the ring, which for a steady state should form a path around the ring that closes upon itself.

a parameter defining the location on the flow path:

$$
\begin{aligned}
\mathbf{J}(s) \,.\, \hat{\mathbf{dl}} &= J_0 = \text{ const} && (7.2)\\
\mathbf{v}(s) \,.\, \hat{\mathbf{dl}} &= \frac{J_0}{|\psi(\mathbf{l}(s))|^2} && (7.3)\\
\int \mathbf{v} \,.\, \hat{\mathbf{dl}} &= \frac{\hbar}{m} 2\pi \quad 2\pi \text{ phase winding,} && (7.4)
\end{aligned}
$$

where $\hat{\mathbf{dl}}$ refers to a unit vector along $\mathbf{dl}$.

- No flow across boundary: This is a corollary to the steady state condition. The flow being parallel to the boundary implies that there is no phase gradient normal to the boundary. Lines of constant phase are normal to the boundaries. One can use

  $$v(\mathbf{l}(s)) \propto \frac{1}{|\psi(\mathbf{l}(s))|^2}, \qquad (7.5)$$

  to obtain the flow velocity at any given point.

While the exact flow pattern for a ring with a barrier cannot be simply solved, we can still learn some things. The most obvious, from equation (7.5), is that the flow velocity at the location of the barrier is higher than that of the rest of the ring due to the local depletion of the density. This effect can also be understood in terms of conservation of flow from classical fluid dynamics. The purpose of this section is to give the reader the gist of what happens when a barrier is introduced, and now we will move on to other aspects of flow in a toroidal potential. We will return to this topic when we actually try to obtain a flow velocity.

7.1.b Stability of flow in a ring

So far, we have talked about superfluidity breaking down by the dissipation of flow into low-energy excitations. An implicit assumption in this picture is that the flow is somehow fixed. This assumption is valid if there is an external driver of flow, as is the case for the original superfluidity experiments [9, 10], where gravity (or a pressure difference) was used to make helium flow from one container to another via a narrow path. In such situations, a dissipation event leads to a loss of energy from the flow, but will not stop the flow itself. In considering the local flow in the constrained narrow path, the flow is not expected to dissipate into other excitations if it is below the critical velocity.

We could use the above picture for our toroidal BEC, and state that superflow is expected to dissipate if the local velocity at some points exceeds a critical velocity. However, unlike the case of flowing helium, the flow is not fixed and any dissipation in one part of the ring not only causes local excitations, but also causes the stopping of flow everywhere in the ring. Hence, any dissipation is a global effect, not just a local effect. The question that arises is: Is there any validity to a local critical velocity for the onset of dissipation?

Taking a global picture, the stationary non-circulating BEC is the ground state. On transferring one unit of circulation to the ring, the BEC is no longer in the ground state. If one were to apply an energetics argument, the BEC is expected to decay to the ground state, which has lower energy. Then, how is it that we see stable flow? The answer to the question is that the flow is not stable, but metastable. The reason for metastability becomes more obvious if one looks at a phase plot of a circulating condensate (see figure 7.2b). The 2π phase winding of a circulating condensate gives it topological stability and does not allow any simple continuous relaxation to cause decay to the ground state (figure 7.2a). Hence, even though the circulating BEC is not in the ground state, the topology yields a metastability that allows for persistent currents.

7.1.c Phase slips

Having arrived at the metastability of flow from a global picture, we shall now look at phase slips, which are necessary to cause decay of the circulating state to the non-circulating ground state. A phase slip event results in the phase of a particular location shifting by 2π, and for a ring geometry, it results in a change of the phase winding around the ring. As can be seen in figure 7.2, a phase slip event causes a change in the phase winding, changing the phase pattern in (b) to that of (d). The phase pattern in (d) has no phase winding, and can subsequently continuously relax

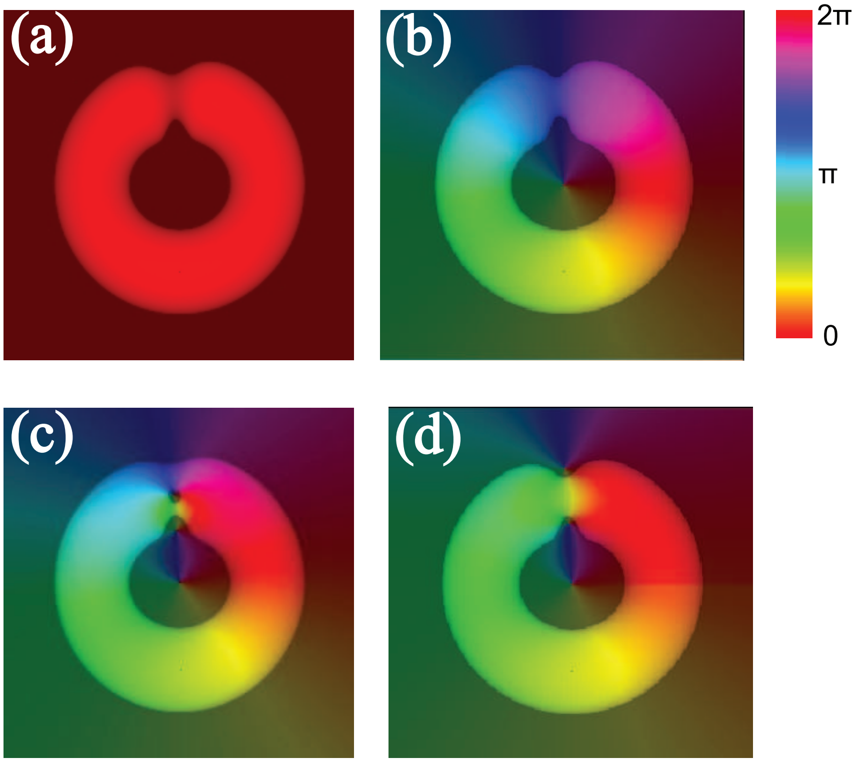

Figure 7.2: (Note: Plot is in color) Flow stability and phase slips: (a) Phase plot of a stationary BEC in a ring with a barrier. (b) Phase plot of a BEC with one unit of circulation. There is no simple, continuous deformation of the phase from the circulating state that would lead to the non-circulating state. This topological stability leads to persistent currents in the metastable circulating state. (c) and (d) show an example of a phase slip event via a single vortex moving from the inside to the outside of the annulus. In (c), the vortex, shown by a hole in the ring, is at the location of the barrier. For a path around the annulus that passes on the inside of the vortex (does not enclose the vortex), the phase winding is zero. The phase is always below *pi* (see colorbar). For a path that passes on the outside of the vortex, the phase winding is still 2*pi* (passes through all colors). After the vortex moves to the outside of the annulus, the phase winding is zero as seen in (d). The phase can subsequently relax to a uniform phase (stationary BEC) as in (a). (generated using Scilab)

to (a). Phase slip events are known to occur in superconductors [1] and have also been seen in superfluids [33, 34].

Tinkham [1] describes a phase slip as an event where the coherence is momentarily broken at a location in a superconductor (often at a Josephson junction), during which time the local phase changes by a multiple of 2π. Phase slips are quantum in nature [243], and in superconductors, phase slips have been found to interfere across junctions [244]. In superfluids, phase slips can have spatial structure. Experiments studying helium superflow through small apertures by Avenel and Varoquaux [33] and Amar *et al.* [34] have shown evidence of a phase slip mechanisms similar to dissipation via vortex rings.

Coming back to our system, a phase slip is most likely to occur at the location of the barrier since the density is low, and hence the phase coherence can be more easily broken. In principle, it is possible for the phase slip to occur via the momentary formation of a plane of zero density (line when projected to a 2D plane as shown in the plots of figure 7.2) across a part of the torus, during which time the phase changes by 2π. However, an energy cost for such a mechanism is high given the width of the condensate even at the barrier. The energetics of a phase slip via the vortex movement through the barrier region are more favorable.

Figure 7.2(c) illustrates a phase slip occurring via a single vortex moving through the barrier from the inside to the outside of the ring. As the vortex moves through the barrier, paths around the annulus that do not enclose the vortex (or equivalently, paths that the vortex has cut across) have zero phase winding, while the paths that do enclose the vortex (paths which the vortex has not cut across) still have a 2π phase winding. Once the vortex reaches the outside of the BEC, all paths around the annulus have a zero phase winding as seem in figure 7.2(d). This way, a vortex moving through the BEC causes the circulation to decay[4]. We will discuss the role of vortices for flow decay in the context of quasi-2D physics (section 7.2.e).

---

[4] A vortex passing through the BEC can be seen as a mechanism for the continuous decay of flow.

7.2 Dimensionality and quasi-2D physics

Until now, through all the discussions of the ring trap and persistent currents, we have implicitly assumed our BEC to be a three-dimensional (3D) system. In section 5.1.b, we briefly discussed the possibility of studying quasi-1D physics as motivation for the ring trap. As mentioned before, highly anistropic 3D condensates can exhibit certain 1D-like behavior [184, 186]. In that context, it is worth exploring the dimensionality aspect of the system and how it plays a role.

For the persistent current experiments we used, the dimensions of the ring were approximately

- Circumference : 120 μm
- Radial TF full width : 18 μm
- Vertical TF full width : 3 μm

While the above conditions were typical, we could increase the radial confinement (ω_r) by up to a factor of 2 and the vertical (ω_z) by up to a factor of 3. The radial confinement could also be decreased by a factor of 3, as is done when we relax the radial confinement for detecting flow. In addition, by changing the focusing of the LG trapping beam, the ring diameter could be increased by a factor of two. The current aspect ratio, along with the extent we can vary different parameters implies the following:

- Excitations in different directions have different energy scales (energy scales approximately as $1/r_i^2$, where r_i is the length scale in a particular axis). For example, azimuthal excitations ($\sim$ 1 Hz) have lower energy than the radial excitations ($\sim \omega_r = 100$ Hz), which have lower energy than vertical excitations ($\sim \omega_z = 500$ Hz).
- Depending on the temperature, it is possible to be in a regime where the condensate has thermal phase fluctuations in 1 or 2 dimensions [193].

Finally, in inserting a barrier in the ring, the density depletion causes the local mean field to drop to well below the vertical trapping frequency, while still above the radial trapping frequency (see figure 7.1b). This localized region has dimensions of around $9 \times 9 \times 2$ μm, with the condensate being mainly in the vertical harmonic oscillator ground state, making it susceptible to quasi-2D physics. As this region is important in the decay of flow, we shall now spend some time on quasi-2D physics. While on the topic, I will also mention some of our previous experiments studying the phase transition of a quasi-2D gas [53], which were performed on the same setup, with just the sheet beam (no annular confinement).

7.2.a Superfluidity and the BKT transition

The origins of quasi-2D (Bose gas) physics can be understood better if one started from a true 2D system. In this section, we will study the superfluid transition of a 2D gas, before moving on to the case of a quasi-2D gas in the next.

While it was understood in the 1950s that a 2D Bose gas would not Bose-condense at finite temperature [245], Berezinskii [246] and Kosterlitz and Thouless [247] showed that a 2D neutral superfluid would undergo a phase transition to a non-superfluid state at a temperature $T = T_{\mathrm{BKT}}$ at a universal value

$$n_s \lambda_T^2 = 4, \tag{7.6}$$

where n_s is the 2D superfluid density and λ_T is the thermal de Broglie wavelength given by

$$\lambda_T = \sqrt{\frac{2\pi\hbar^2}{m k_B T}}. \tag{7.7}$$

The BKT transition is more general than just the 2D neutral superfluid and also occurs for defects in a 2D crystal and magnetism for spins in the 2D XY model [247].

For a neutral superfluid, the microscopic mechanism of the BKT transition is based on vortex excitations in a 2D system. The energy of a single vortex in a 2D

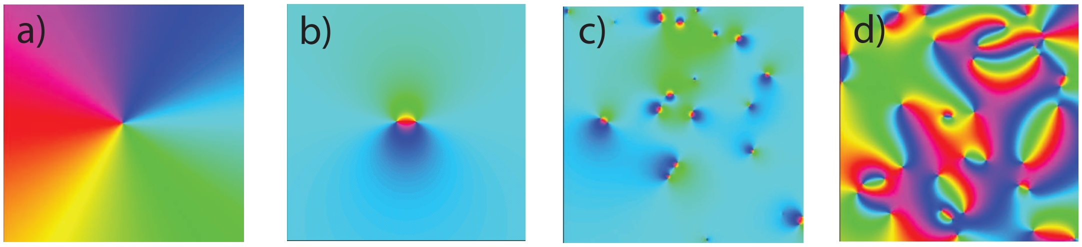

Figure 7.3: The phase profile of a 2D superfluid for a) single vortex, b) single vortex anti-vortex pair, c) a 2D Bose gas below the BKT transition ($T < T_{\mathrm{BKT}}$) with only vortex pair excitations, and d) a 2D Bose gas above the BKT transition ($T > T_{\mathrm{BKT}}$). c) and d) were created for illustrative purposes only, with vortex pais and free vortices put in at random. Colorbar same as figure 7.2. Since the flow velocity is given by the gradient of phase, changes in color correspond to kinetic energy. For a single vortex (a), there is flow even at distances far from the center, while for a vortex pair (b), superfluid far away from it is not affected. Similarly, there is a clear qualitative difference between only vortex pair excitations (c) and free vortex excitations (d). (Generated using Scilab)

superfluid is given by:

$$\begin{aligned} E_{\mathrm{vortex}} &= \int_{r_v}^{R} \frac{n_s \hbar^2}{2mr^2} 2\pi r dr, \\ E_{\mathrm{vortex}} &= \frac{n_s \hbar^2 \pi}{m} \log \frac{R}{r_v}, \qquad (7.8) \end{aligned}$$

where r_v is the size of the vortex core and R is the system size. The energy of a vortex diverges with system size. If one were to consider the energy of a vortex anti-vortex pair, one obtains:

$$E_{\mathrm{pair}} = \frac{n_s \hbar^2 2\pi}{m} \log \frac{r_s}{r_v}, \qquad (7.9)$$

where r_s is the separation between the vortex and the anti-vortex. This energy is independent of the system size for a large enough system size ($R \gg r_s, r_v$), which is what one expects since for large distances, the flow field of the vortex cancels the one from the antivortex. One can look at a pictorial representation of the two cases (see figure 7.3 (a) and (b)).

For a 2D Bose gas at constant temperature, the free energy of a single vortex determines whether such an excitation is favored. The free energy of an excitation is given by:

$$F = E - TS, \tag{7.10}$$

where F is the free energy and S is the entropy. The entropy of an excitation can be expressed as the number of degenerate ways, Ω, in which the excitation can occur

$$S = k_B \log \Omega. \tag{7.11}$$

For a vortex, whose size scales as r_v^2 relative to the system size R^2, the entropy is given by

$$S_{\text{vortex}} = 2k_B \log\left(\frac{R}{r_v}\right). \tag{7.12}$$

As one can see from equations (7.8) and (7.12), both the energy and the entropy of a vortex scale similarly with system size. For the creation of a vortex to be favorable, the free energy has to be negative:

$$\begin{aligned} F_{\text{vortex}} = \frac{n_s \hbar^2 \pi}{m} \log \frac{R}{r_v} - T 2k_B \log\left(\frac{R}{r_v}\right) < 0, \\ \Rightarrow T > \frac{n_s \hbar^2 \pi}{2mk_B}. \end{aligned} \tag{7.13}$$

Hence, free vortices can be spontaneously created at temperatures $T > T_{\text{BKT}}$, given by

$$T_{\text{BKT}} = \frac{n_s \hbar^2 \pi}{2mk_B}, \tag{7.14}$$

which is identical to equation (7.6).

In contrast to a uniform, homogeneous BEC, where phase coherence does not decay at long distances, the BKT superfluid phase has an algebraic decay of coherence[5]. In the limit of $T \to 0$, the coherence length goes to infinity like a true BEC. With increasing temperature, the coherence length gets shorter, and as the gas goes through the BKT transition, the coherence function changes from algebraic to exponential. With further increasing temperature, the coherence length further decreases until the gas has a coherence length determined by the single

---

[5] For a system with algebraic decay of coherence, the correlation function $\langle\psi(r)\psi(r+\delta r)\rangle$ scales as $(\delta r)^{-\alpha}$, where $\alpha > 0$. In contrast, for a system with exponential decay of coherence, $\langle\psi(r)\psi(r+\delta r)\rangle \sim \exp(-\delta r/r_c)$, where r_c is correlation length.

particle de Broglie wavelength. The coherence function and its derivation from vortex excitations is discussed extensively in Kosterlitz and Thouless [247].

Equations (7.14) and (7.6) express the transition in terms of the superfluid density. In terms of the total density, n, the corresponding expression is [245, 248]

$$n\lambda_T^2 = \log(C/u), \tag{7.15}$$

where C is a constant and u is the 2D interaction strength. Although the transition point in terms of the superfluid density is universal, the transition point in terms of the total density depends on interactions.

7.2.b Case of a quasi-2D Bose gas

Since we live in a 3D world, no gas can be truly confined to 2 dimensions, and we have to consider the more realistic quasi-2D case. A gas can be said to be quasi-2D if excitations along one of the dimensions are frozen out. A simple way to picture this is by having a 3D Bose gas harmonically confined in one dimension, having energy sufficiently low that all the atoms are in the ground state in the trapped dimension. In such a system, one needs to treat the gas in the 2D picture, with a dimensionless interaction (coupling) constant, g_{2D}, given by Petrov *et al.* [249]

$$g_{2D} = \sqrt{8\pi}\frac{a}{a_{\text{ho}}}, \tag{7.16}$$

where a is the 3D atom-atom s-wave scattering length, $a_{\text{ho}} = \sqrt{\hbar/m\omega_0}$, and ω_0 is the trapping frequency of the confining potential. Using the above expression, one can treat the quasi-2D case identical to the 2D case and hence a BKT transition is expected to occur. The BKT superfluid density still satisfies equation (7.6) and the total density satisfies an equation similar to equation (7.15):

$$n\lambda_T^2 = \log(C/g_{2D}). \tag{7.17}$$

Using Monte-Carlo calculations, the constant C was calculated to be 380 [250].

While BKT theory deals with the phase transition from a state without free vortices to a state with, it does not talk about the high temperature limit. A quasi-

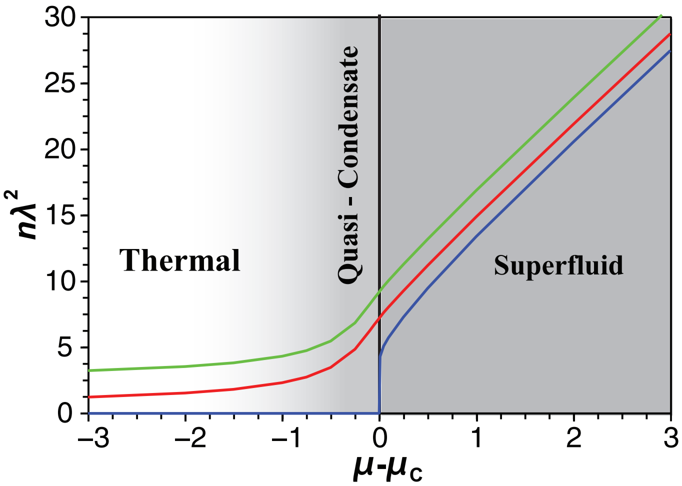

Figure 7.4: The phases of a quasi-2D gas: Calculated total density (green), quasi-condensate density (red) and superfluid density (blue). The chemical potential is normalized by g_{2D}/λ_T^2 with the BKT transition occurring at $\mu = \mu_c$, where the superfluid density jumps and is given by $n_s\lambda_T^2 = 4$. (based on Prokof'ev and Svistunov [251])

2D Bose gas at temperatures well above the BKT transition temperature is expected to behave like a classical gas. However, as one approaches the transition from above, there is an appearance of a non-superfluid quasi-condensate [251] phase, which has some coherence before a sudden transition to a superfluid quasi-condensate state. A quasi-condensate can be understood as a phase which behaves like a true condensate at short length scales, but does not have long range order.

In figure 7.4, the phases of a quasi-2D gas are plotted. Until now, we have talked about the transition in terms of temperature. The BKT transition can also be discussed in terms of phase-space density $(n\lambda_T^2)$ as a function of the chemical potential. When the chemical potential is near the critical point, the conditions given by equations (7.6) and (7.17) are satisfied. As one can see, prior to the transition, there is the appearance of a significant (non-superfluid) quasi-condensate.

The quasi-condensate *component* is indistinguishable from a condensate except that it has quasi-long range order (short coherence length) as opposed to the true long range order of a BEC. At a local level, it behaves like a condensate. The

Phase	Appearance	Coherence	ξ
Thermal	Classical gas	Gaussian	λ_T
Quasi-condensate	QC component with fluctuations	exponential	$> \lambda_T$
Superfluid	SF and QC components	algebraic	longer

Table 7.1: Brief summary of the different phases of a quasi-2D Bose gas. This table is only to give a general picture. Coherence refers to the functional form of the coherence decay. ξ is the coherence length. QC = quasi-condensate. SF = superfluid.

quasi-condensate *region* in figure 7.4 is characterized by large scale fluctuations.

7.2.c Previous experiments studying the BKT transition

In one of the earliest experiments on BKT physics in neutral superfluids, Bishop and Reppy [252] studied the superfluid transition of a thin superfluid helium film adsorbed on an oscillating substrate. Analysis of the superfluid mass and dissipation supported a dynamic theory of an oscillating superfluid based on the BKT picture [253, 254]. Estimates of the change in superfluid density were in good agreement with predictions of the BKT theory.

There have been several studies of the BKT transition for the 2D XY model using Josephson junction arrays. Resnick *et al.* [255] reported evidence for the BKT transition in triangular planar arrays of proximity coupled Pb-Sn junctions. Shaw *et al.* [256] saw a change in the characteristic of the magnetic flux noise in a Josephson junction array as one crossed the BKT transition. Leemann *et al.* [257] studied the ac response of large two-dimensional arrays of proximity-effect Josephson junctions to an oscillating driving field as a function of temperature, applied transverse magnetic field, and frequency. They observed that for an integer number of flux quanta per unit cell, a peak in dissipation and a drop in superfluid density are observed near the superconducting transition of the array. They concluded that these features and their frequency dependence provided clear evidence for the vortex-unbinding BKT transition.

With ultracold gases, there were two path-breaking experiments in Paris studying the BKT transition in quasi-2D trapped Rubidium. In Hadzibabic *et al.* [258], using a matter wave heterodyning technique, the long-wavelength fluctuations of the quasi-condensate phase and free vortices were observed. Starting at low temperatures, where the gas is quasi-coherent on the length scale set by the system size, there was a loss of long-range coherence that coincided with the onset of the proliferation of free vortices as the temperature was increased, providing experimental evidence for the microscopic mechanism underlying the BKT theory. In Krüger *et al.* [259], the critical atom number for condensation[6] in an array of harmonically trapped two-dimensional (2D) Bose gases of rubidium atoms was measured at different temperatures. The critical atom number being 5 times higher than that predicted by the semiclassical theory of Bose-Einstein condensation (BEC) in the ideal gas, the authors found that a simple heuristic model based on the Berezinskii-Kosterlitz-Thouless theory of 2D superfluidity and the local density approximation accounted well for the experimental results.

While studying similar physics to the Paris experiments, our experiment differed in key ways. We studied the quasi-2D Bose gas in a single plane, imaging perpendicular to the plane of interest. In addition, we used a homodyne technique to measure the coherence length in contrast to the heterodyne technique used in Paris. The reader should note that there have been recent experimental work on the quasi-2D Bose gas by the Paris group [260], studying the quasi-2D Bose gas with even tighter confinement. Also, Eric Cornell's group at JILA [261] recently studied the *in situ* position and momentum distribution of a 2D Bose gas more carefully, to clearly observe non-mean-field physics in the non-superfluid quasi-condensate phase.

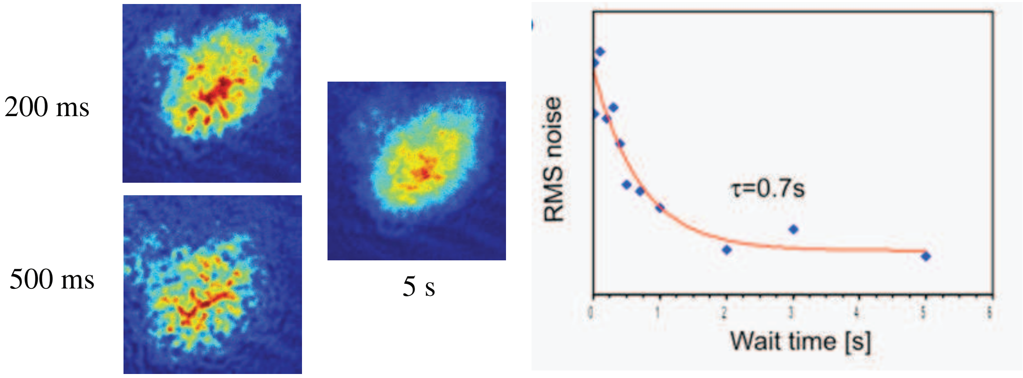

Figure 7.5: Excitations in a 2D BEC: On transferring a BEC from our magnetic TOP trap to the optical sheet, there are excitations which damp out over time. Images are taken after a certain wait in the optical trap followed by a 5 ms TOF. The 2D BEC seems more susceptible to density fluctuations.

7.2.d NIST experiments in the quasi-2D trap

Our trap was created by just the sheet beam (see section 3.6.a). The z trapping frequency was ≈ 1 kHz, and the horizontal trapping frequencies were ≈ 20 Hz, giving an aspect ratio of 1:50.

In preliminary experiments in the quasi-2D trap, we were able to get a condensate in our trap, identified by the clear signature of a bimodal distribution (condensed and thermal atoms) in TOF. Our first indications of quasi-2D physics were excitations in the BEC. In contrast to a 3D BEC where the thermal fraction can be taken as an indicator of heating or the presence of excitations, we noticed that excitations in the form of large density ripples (see figure 7.5) seen in 5 ms TOF. If we waited a few seconds, the density ripples were reduced.

Furthermore, by deliberately exciting the quasi-2D BEC when there were few other excitations, we could see "holes" (figure 7.6, image of 5 ms TOF) in the cloud in TOF. The BEC was excited by pulsing a strong magnetic field gradient to transfer impulse. On allowing the BEC to expand in 8 and 10 ms times-of-flight,

---

[6] It was determined by the appearance of a narrow feature, akin to a BEC, above the broad Gaussian thermal distribution of a gas in TOF.

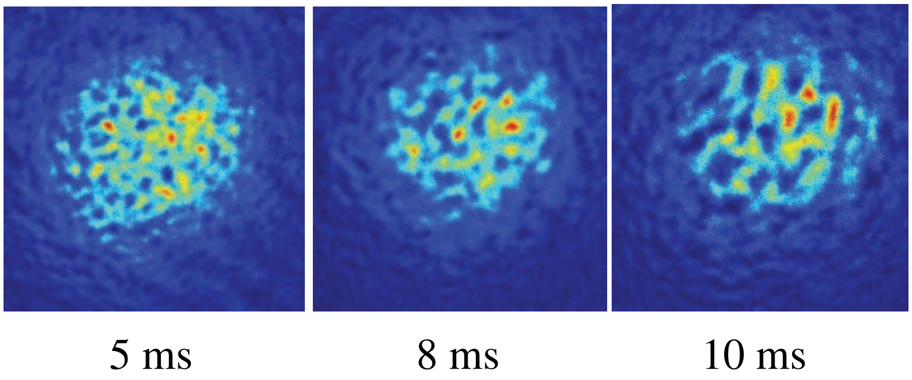

Figure 7.6: Deliberate excitations in a 2D BEC: We deliberately cause excitations to the BEC by pulsing a strong magnetic field gradient, giving it a momentum impulse. There are "hole"-like density ripples suggestive of vortices. The merging of these in longer times-of-flight (TOF indicated below figure) is similar to what one would expect if there were vortex-antivortex pairs.

there were fewer, but larger holes, implying that some of the smaller holes "merged" together, as one would expect of vortex-antivortex pairs. The nature of excitations was indicative of something different from 3D BECs, and suggestive of quasi-2D vortex excitations.

We performed a set of measurements of the quasi-2D condensate varying the number of atoms (or equivalently, the chemical potential μ) close to the apparent transition point. From the absorption images obtained, we performed a bimodal fit to the cloud. The cloud fit well to a bimodal double Gaussian (wide and narrow Gaussian modes superposed). The wide Gaussian fit the non-condensed (or thermal) cloud, and stayed constant, both in width and amplitude[7], across the range of the number of atoms probed for a given trap depth, indicating that the temperature was constant.

The narrow Gaussian fit the quasi-condensed atoms. For a 5 ms TOF (figure 7.7 (left)), we found that the width of the narrow Gaussian initially decreased

---

[7] Any change was immeasurably small. This is similar to a 3D BEC at equilibrium with a thermal cloud, where, on adding more atoms, the thermal cloud changes little while the BEC changes in height, and consequently in width and shape due to mean field repulsion.

as a function of μ or equivalently the peak 2D column density in TOF (presumably due to fewer phase fluctuations) and subsequently increased (due to mean field). The sharp change in the sign of the slope was indicative of a phase transition (elbow point in fitted lines in figure 7.7 (left)). The obtained critical points agreed with predictions of the BKT theory (figure 7.7 right), although only after correcting for excitations in the tight confinement direction based on Holzmann *et al.* [262]. We also observed the expansion of the cloud for longer TOF. At 10 ms TOF, we observed a sudden appearance of a narrow peak (above the bimodal distribution), which was consistent with the sudden appearance of superfluid fraction at the BKT transition [53]. Such measurements were subsequently performed more carefully by the JILA group [261]. Phase coherence measurements also indicated an increase of coherence from the thermal de Broglie wavelength to the size of the condensate [53].

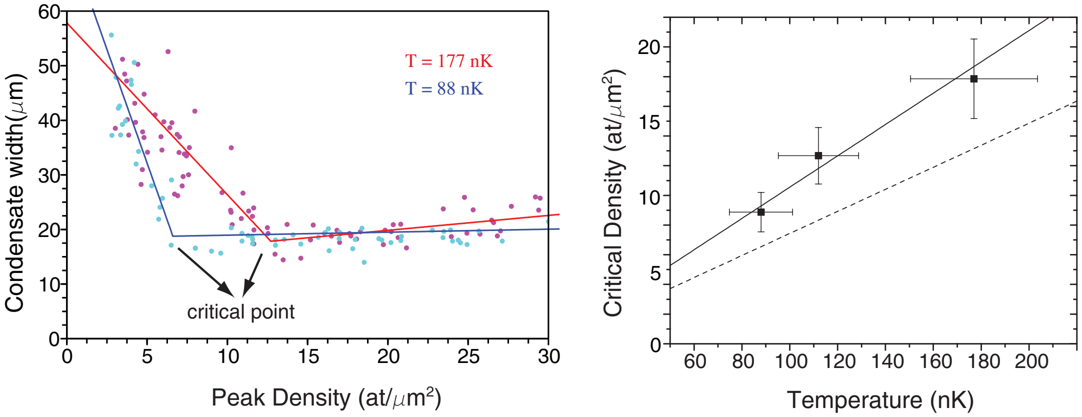

Figure 7.7: Critical density: (left) We obtain the critical density by finding the minimum width (elbow point) in a plot of the condensate width vs the peak density. The data is taken after 5 ms TOF for two different temperatures shown. (right) On comparing the critical density (translating the 5 ms TOF to *in situ*) to BKT theory, we find that our data is systematically higher than that predicted by BKT theory (dashed line: $n\lambda_T^2 = \log(380/g_{2D})$ for our conditions). However, if one were to correct the theory for excitations (occupation of higher modes) in the vertical direction based on Holzmann *et al.* [262], one gets better agreement (solid line).

In effect, we identified three regions for a quasi-2D Bose gas near the critical point. The gas underwent a phase transition at a point which agreed with the predictions of BKT theory. Our measurements were indirect in the sense that we could not directly observe free vortices or vortex-antivortex pairs or observe the change in functional form of the coherence, which some experts would consider as the hallmarks of the BKT transition. Also, our experiments (or any other atomic gas experiments) did not look at any superflow. Nevertheless, our measurements were in good quantitative and qualitative agreement with the quasi-2D BKT theory, and have been further confirmed by subsequent simulations by Bisset and Blakie [263].

Our experiments observed the quasi-2D gas near the critical point differently from the Paris experiments [258, 259]. Imaging perpendicular to the plane, we obtained a 2D image of the cloud, and could directly measure the 2D (column) density. We could therefore perform a 2D Gaussian fit to the cloud, and obtain the peak 2D density of the cloud, indicative of the chemical potential μ. Hence, our determination of the critical point was based on the minimum width of the narrow mode of the bimodal distribution as a function of the peak 2D density. In the Paris eperiments, it was based on the change in functional form of the correlation function [258] or the appearance of a bimodal distribution [259].

More importantly, our experiments were able to clearly identify the three phases; the thermal, the non-superfluid quasi-condensate and the superfluid quasi-condensate. The critical point separated the quasi-condensate and the superfluid phases. The quasi-condensate was distinguished from the thermal cloud by nature of its coherence length being longer than the thermal de Broglie wavelength λ_T.

7.2.e Effects of BKT physics and quasi-2D dimensionality

The BKT experiments [53] have shown that our vertical confinement by the sheet beam is sufficient to observe quasi-2D physics and even the BKT transition. As mentioned previously, the barrier region is particularly susceptible to quasi-2D excitations due to the reduced mean field interactions there. We will now look at what are the possible effects due to the quasi-2D nature of the gas in the barrier region.

As discussed earlier in the chapter, the circulating state can decay to the non-circulating state via a phase slip, which in our system is believed to be vortex motion through the region of the barrier. A vortex moving through the condensate has an energy barrier, which is the cost of putting a vortex at the center of the annulus. The energy of such a vortex is

$$E = \pi \frac{\hbar^2 n_{2D}}{m} \log \frac{r_t}{\xi}, \tag{7.18}$$

where r_t is of the order of the width of the annulus at the location of the barrier, ξ is the healing length of the condensate[8] at the location of the vortex and n_{2D} is the mean column density of the condensate in the region of the barrier. The exact energy depends on various parameters such as the exact shape and density profile of the condensate near the barrier and so equation (7.18) should be taken as the first approximation.

As one can see, increasing the height of the barrier would cause the local density, n_{2D} to decrease and the healing length, ξ to increase, both of which lower the energy barrier for a vortex to leave.

While one could have a vortex (of the same sign as the circulation) pass from the inside of the annulus to outside or an anti-vortex pass the other way, the mechanism with the lowest energy barrier would be a vortex from the inside and an anti-vortex from the outside coming in and annihilating each other at the center. This is also consistent with the low energy excitation spectrum for a quasi-2D gas that is superfluid, which consists of vortex-antivortex pairs. Such a pair would have minimal effect on regions away from the barrier, which have high density. While the cost of putting a vortex and an anti-vortex in the middle of the condensate is higher than the cost of keeping them at the edge of the condensate, such a pair would have an attraction which would lower the overall energy barrier. The condensate flow causes an additional attractive force between the vortex and the antivortex[9]. The

---

[8] For simplicity, the vortex core size r_v can be taken as the healing length of the condensate [264]. The error in this approximation is small compared to that arising from other approximations we will make.

[9] From a classical perspective, this is the Magnus force [265]. The sign of the Magnus force

energy of a vortex-antivortex pair in the annulus can be expressed as [266, 267]

$$E = 2\pi \frac{\hbar^2 n_{2D}}{m} \log \frac{r_s}{\xi} - 2\pi\hbar n_{2D} v_f r_s, \tag{7.19}$$

where r_s is the distance between the pair and v_f is the velocity of flow[10]. We assume that the pair starts at a distance $2r_t$, which is the width of the annulus and attempts to move inward. The flow velocity causes an attractive force between pair, while the energy barrier is the cost of putting a vortex and an anti-vortex in the center of the annulus, where the density is maximum. Flow at the critical velocity causes the attractive force to overcome the energy barrier, which leads to the decay of circulation.

If the superfluid already had thermally excited vortex-antivortex pairs, the flow could decay by causing a pair to split and leave in opposite directions[11]. In such a situation, the velocity term of equation (7.19) would oppose the vortex-antivortex interaction energy term. The critical velocity would depend on the temperature, which determines the initial separation of the pair.

We have discussed some of the possible mechanisms for the decay of flow and how dimensionality may play a role. We shall now move on to the critical velocity experiments and will return to this discussion in the context of our experimental results.

7.3 Experimental setup and procedure

Our experiment determined flow survival in the presence of a barrier. The barrier consisted of an elliptical blue-detuned 532 nm beam that intersected the annulus. The barrier beam was measured to be about 15 μm by 4.3 μm ($1/e^2$ radii), with the long dimension extending from nearly the center of the ring across the atoms

---

depends on the sign of the vortex, and hence, the force on the vortex is of the opposite sign to the force of the antivortex. This is an additional force to the vortex pair attraction; a mutual attraction or repulsion or shear force depending on the direction of flow.

[10] The sign of the velocity dependent energy term depends on the direction of flow.

[11] If the direction of flow were such that it initially caused attraction between a vortex pair, the vortex pair would reorient and the force would then become repulsive.

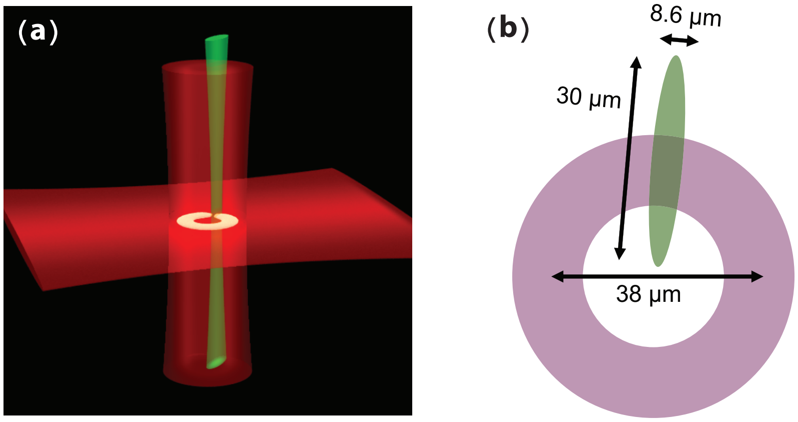

Figure 7.8: Schematic of the barrier beam: (a) 3D rendering of the barrier beam and its effect on the BEC. (b) Relative orientation of the elliptical barrier beam with respect to the trapping LG beam. The barrier is sufficiently elongated in the transverse (radial) direction so that the BEC cannot flow around it.

to well outside the annulus (figure 7.8) so that the atoms could not flow around it. The barrier was much larger than the condensate healing length ($\xi < 0.5\mu$m) in bulk and so we can model the depletion using TF formalism. Our experiment consisted of creating a persistent current, then turning on the barrier for 1-2 seconds, followed by turning it off and checking to see if the flow survived. By taking several data points at each of a range of different barrier heights and chemical potentials, we were able to obtain the critical point for the breakdown of flow.

The procedure for taking data was the following (see figure 7.9). We created a BEC in the ring trap. After holding for about 3 seconds in the ring trap, we performed the Raman transition, obtaining a circulating cloud in the $|1, 0\rangle$ state. After allowing the ring to relax, and excitations from the transfer process (discussed in section 6.5) to settle down, we then turned on the barrier and adiabatically ramped it to its full height, V_b in 100 ms. After holding the barrier at its maximum value for 2 seconds, we ramped down the barrier in 100 ms and turned it off completely. We then detected circulation (see section 6.6) by ramping down the ring and doing a 6 ms TOF.

Rather than finding the critical barrier for a fixed BEC, we found it eas-

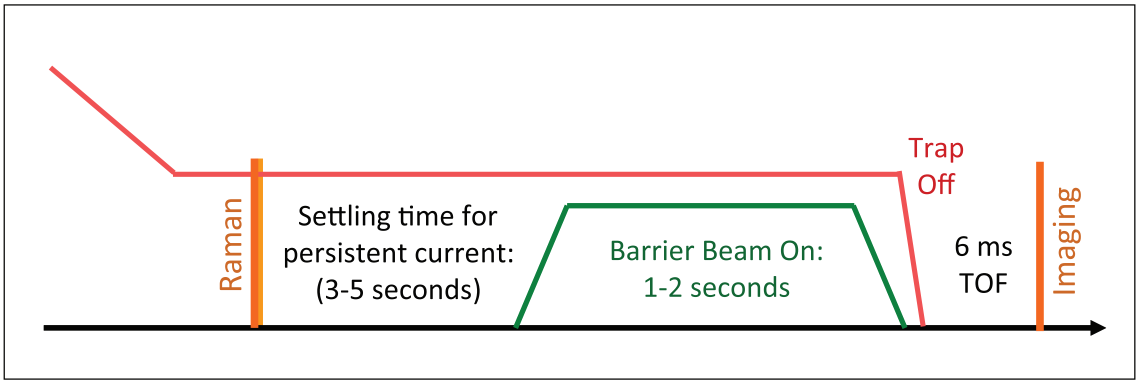

Figure 7.9: Experimental sequence studying critical flow. The sloped lines indicate intensity ramps of the barrier beam with adiabatic turn on/off in ≈100 ms. The full sequence time is 30-40 seconds including around 25 seconds required to create the BEC.

ier to vary the chemical potential μ_0 for a fixed V_b and find the critical chemical potential, μ_c that was sufficient to overcome the barrier and allow the persistent current to survive. The chemical potential depends on the number of atoms, $\mu_0 = \sqrt{(1/2\pi^2)Ng\omega_z\omega_r/mr_M}$, (from equation (5.38) assuming a fully TF BEC), which we varied in a controlled way (in addition to uncontrolled shot-to-shot fluctuations) over a large range by doing one or more of the following:

1. Adding delays before or after the Raman process : Since the vacuum lifetime was about 15 seconds for many of the runs, a 3 second extra delay would lower the atom numbers by about 20%. By varying the delay, we could accurately control the range of the number of atoms. However, delays made the sequence time longer slowing down the rate of data and so for large changes, we needed other methods.

2. Doing a microwave cut : By removing a fixed fraction of atoms, we can deterministically lower the number of atoms. While in principle, we could have cut any fraction we wanted, large cuts (more than 25%) caused excitations which could lead to heating, and hence we limited cuts to 25%. After any cut, we waited at least 3 seconds for the excitations to damp out.

3. Lowering the Zeeman slower current : This works by lowering the number of atoms we load into our MOT and is thereby useful in significantly lowering the number of atoms. The only practical limit to this method was that we needed a sufficient number of atoms in the BEC to sustain a persistent current before the barrier was turned on.

We interspersed our critical flow data with calibration data, necessary for calibrating μ_0 and V_b. Calibration data was taken using an identical procedure, except that we imaged the cloud *in situ* while the barrier is still on. Since the cloud was optically thick, we used partial-transfer absorption imaging (see chapter 4), typically transferring 8-42% of the cloud. The calibrations are detailed in appendix C.

7.4 Observation of the breakdown of flow

From each experimental run we obtain two pieces of information: a binary (survival or not) of flow and the number of atoms in the cloud (by integrating the atom column density over the area of the cloud), which correspondingly gives μ_0. We find that for a given barrier height, the survival probability clearly depends on μ_0 (figure 7.10). The flow survival dependence on the chemical potential can be divided into three regions. At high μ_0, the flow always survives (above 1100 Hz for $V_b/h = 780$ Hz, shown in figure 7.10, number of atoms $N > 225 \times 10^3$). Below that is a critical region, where the probability of survival increases with atom number (1000 to 1100 Hz for $V_b/h = 780$ Hz, $N \approx 185 - 225 \times 10^3$ atoms). At the low end, the flow always decays (below 1000 Hz for $V_b/h = 780$ Hz, $N < 185 \times 10^3$). For a lower barrier height (figure 7.10 (top), for $V_b/h = 650$ Hz), the behavior is identical except that the critical region occurs at a lower point μ_0 (800-950 Hz).

In figure 7.11, we plot the critical chemical potential as a function of the barrier height. For each experimental run we calculate the chemical potential, μ_0, assuming an annular Thomas-Fermi condensate profile, where N is the number of atoms, g is the interaction strength, r_M is the radius of the annulus and ω_z and ω_r are the

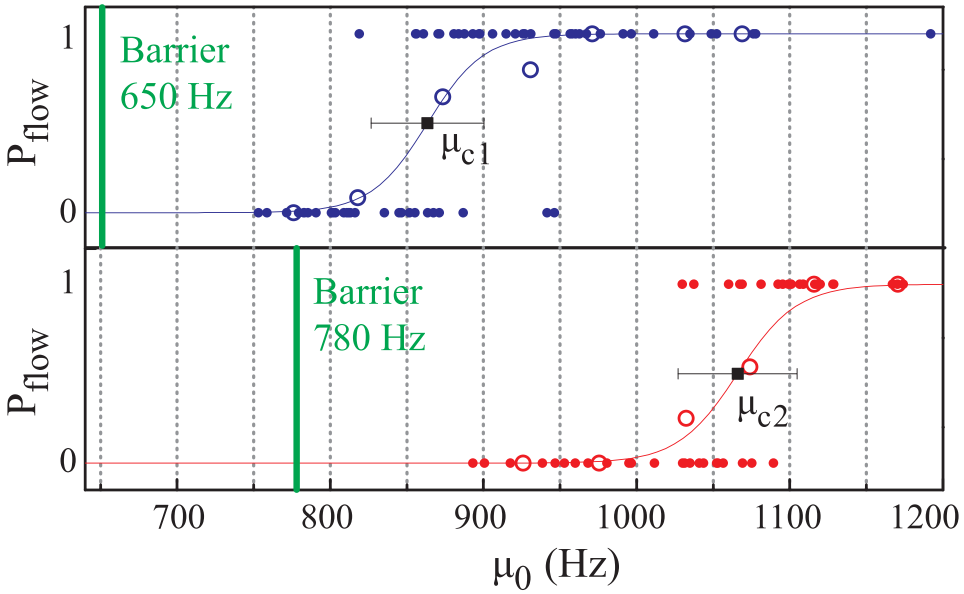

Figure 7.10: Flow survival as a function of chemical potential, μ_0, for two barrier heights: (Upper, blue) $V_b/h = 650$ Hz (barrier beam power = 75 μW), and (lower, red) $V_b/h = 780$ Hz (barrier beam power = 91 μW). Presence or absence of flow for a single condensate is shown by closed circles. Open circles are the average of data within the bins (vertical lines), representing the flow survival probability (P_{flow}) of each bin. A critical chemical potential μ_c for stable flow is found from a sigmoidal fit (solid lines) to the data for each V_b/h. The width of the sigmoidal is believed to be primarily due to temporal drift of the trapping potential that causes the effective height of the barrier to vary (see appendix C.7). The vertical green lines indicate the height of the barrier (to compare against the chemical potential).

vertical and radial trapping frequencies respectively. Here, we have neglected the azimuthal variations in μ and the volume of the barrier, which has a $< 4\%$ effect on the calculated chemical potential. We fit a sigmoidal $[1+\exp(\mu_c - \mu/\mu_w)]^{-1}$ function to the data obtaining a critical chemical potential μ_c and the $1/(1+e^2)$ half-width of the critical region, $2\mu_w$.

We obtain the barrier height relative to the chemical potential by analyzing its effect on the BEC. We take a series of *in situ* images (figure 7.1a) of the BEC with varying barrier beam power. For each image, we divide the annulus into angular

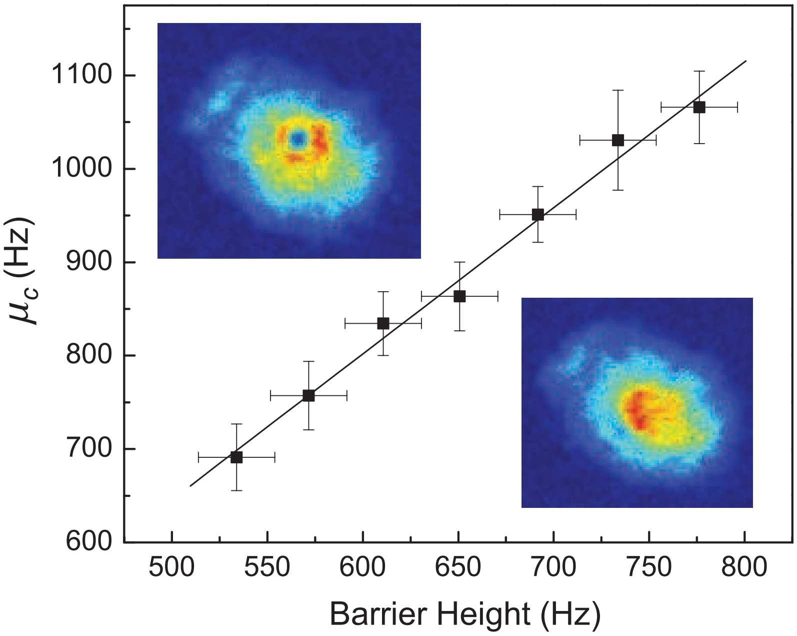

Figure 7.11: Critical chemical potential vs barrier height (V_b): The chemical potential at the critical point (μ_c) is plotted against the barrier height. We find a linear scaling with a slope of 1.6 (continuous line). The chemical potential is calculated based on the number of atoms in the trap. For each barrier height, we fit a sigmoidal $[1 + \exp(\mu_c - \mu/\mu_w)]^{-1}$ to obtain the critical chemical potential μ_c and critical region width, μ_w. The vertical uncertainty is of size $\pm 2\mu_w$ (from sigmoidal fit), and the horizontal uncertainty is ±20 Hz, based on our calibration uncertainty. The images indicate regions of flow survival (top left) and regions of flow decay (bottom right)

sections and measure the local peak mean field ($gn_{3D,\max}$ for the section), μ_l, as a function of the azimuthal coordinate, θ (see figure 7.1b). We use the fully Thomas-Fermi approximation to obtain $\mu_l = \left((9/32)n_{2D,l}^2 m\omega_z^2 g^2\right)^{1/3}$ (equation (5.35)) from the peak column density, $n_{2D,l}$, of each section.

For regions of the cloud close to the barrier, where the Thomas-Fermi approximation is clearly not valid ($\mu_l < \hbar\omega_z$), we assume a harmonic oscillator ground state profile along z giving $\mu_l = \sqrt{\pi\hbar\omega_z/m} \times n_{2D,l}$ (equation (5.32)).

To get the barrier height, we use

$$V_b = \mu_0 - \min(\mu_l), \tag{7.20}$$

where min(μ_l) is the minimum μ_l as a function of θ. We correct for our imaging resolution which is expected to cause our barrier to appear around 15% wider (see appendix C.7).

We find that the critical chemical potential scales approximately linearly with the barrier height (figure 7.11) over the full range of barrier heights and chemical potentials. This supports that the breakdown of flow occurs due to a depletion of density in the barrier region, which can be compensated by raising the chemical potential. The linear dependence of μ_c on the barrier height has slope of 1.6, which indicates that it is not simply a matter of the barrier cutting off the flow. The > 1 slope indicates some sort of flow velocity dependence, based on flow conservation, which leads to excitations and dissipation.

Taking our analysis to the next step, we need to obtain the flow velocity so that we can compare the critical velocity to different criteria.

7.5 Flow velocity of a circulating ring

We return to the problem of obtaining the flow pattern in a circulating ring. By imposing the conditions of phase winding, no flow across boundaries and steady-state flow, we could calculate the complete flow profile. However, since the purpose of the experiment is more to understand the physics rather than make a precision measurement, it is more useful to employ a simple model where the physics is easier to see. Also, since our calibrations of the barrier height and the chemical potential have significant uncertainties, there is little benefit from a precisely calculated flow velocity.

We make the following simplification. We treat the ring as a 1D object by integrating out the transverse directions. That is, we neglect the r (and z) variation of the ring and assume it to be fixed at $r = r_M$ (and $z = 0$). The phase at any angle θ is fixed, and hence the flow and the flow velocity have only a θ dependence. We then use equations (7.3) and (7.4) to obtain the flow velocity. Due to the depleted 1D density at the location of the barrier, the velocity is maximum there.

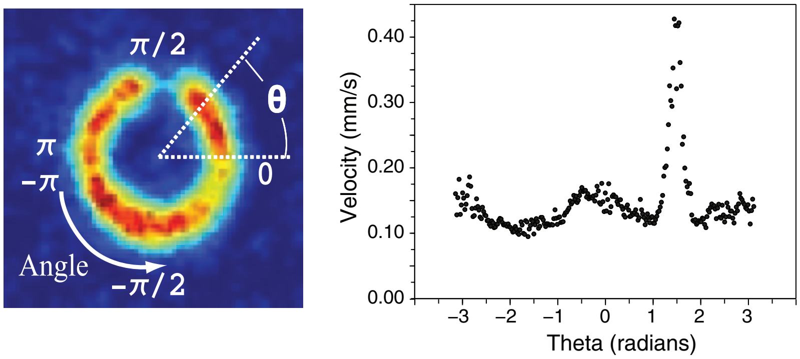

Figure 7.12: Sample flow velocity profile: We plot the azimuthal flow profile of a cloud computed after integrating the transverse profiles of the ring to create a 1D object. Conservation of flow leads to the flow velocity being maximum at the location of the barrier, as seen by the prominent peak reaching nearly 3 times the velocity for the rest of the ring. The above plot does not correct for optical resolution.

In the absence of the quantization condition, if flow was fixed (if it was externally driven for example), the (transverse integrated) 1D density at the barrier would be sufficient to determine the peak flow velocity (such a system is considered in Watanabe *et al.* [268]). However, because of the quantization condition, given in equation (7.4), the peak flow velocity depends on the complete density distribution.

To illustrate the point, we start with our ring in the absence of a barrier, which is azimuthally more or less uniform. The flow velocity everywhere is $\approx \hbar/mr_M =$ 0.15 mm/s (ignoring the minor azimuthal non-uniformities). On adding a single barrier, we obtain the distribution shown in figure 7.12, which has a peak of $\approx$0.4 mm/s and the flow at other regions to average $<$ 0.15 mm/s. If another barrier was added somewhere else in the annulus, the overall average flow would further decrease. The peak flow velocity would also decrease, even though nothing changed in the vicinity of the barrier. If the entire ring had a potential as high as the peak of the barrier, the flow velocity would go back to case of a uniform ring and hence the velocity everywhere would be $\hbar/mr_M$.

The counter-intuitive nature of the flow velocity and its dependence on the density distribution of the entire ring ties in with the global picture for dissipation of flow. Both the condition for the dissipation of flow and the complete stoppage of flow are global in nature, and depend on and affect the flow in the entire ring.

The flow velocity at the barrier follows directly from the density distribution (shown in figure 7.12). Using our *in situ* data and barrier calibration, we were able to obtain a density distribution for a given number of atoms (or μ_0) and barrier height. This was then used to obtain the flow velocity at the barrier. As mentioned earlier in the context of the azimuthal smoothness of the ring, azimuthal variations in the density profile lower the accuracy to which we can determine the flow velocity. Hence, the smooth ring was key to a good measurement of the superfluid flow velocity.

7.6 The critical velocity

While one may argue that the phononic critical velocity is irrelevant, as there needs to be a phase slip and hence vortex-like mechanisms are the likely cause of dissipation, I feel that it is still necessary to put the phononic critical velocity in the right context. As discussed earlier, the phononic critical velocity of a BEC is the speed of sound. The speed of sound in bulk has a physical meaning and is easy to calculate. Since the phononic critical velocity is nearly the same for all phononic modes (see section 2.2.c), flow at the speed of sound is likely to excite several modes and is almost certain to cause severe dissipation. Hence, the speed of sound serves as an upper bound on the critical velocity. For a BEC, the speed of sound c is given by [16, 269]

$$c = \sqrt{\frac{\mu_l}{m}}, \tag{7.21}$$

where μ_l is the local mean field, and the size of the sample is large enough for c to be meaningful.

In comparing our critical velocity to the sound speed, there is one detail: Our condensate has an inhomogeneous density distribution (given in equation (5.24)) and so the speed of sound is also spatially varying. Taking a cross-section of the ring, one finds that the local speed of sound is zero at the edges. Since the flow velocity is non-zero across the cross-section, there is some point at which the flow velocity exceeds the critical velocity purely by virtue of an inhomogeneous profile. How do we resolve this inconsistency?

The Landau criterion for the dissipation of flow is based upon the lowest energy excitations. If we were to take a step back and try to see what kinds of excitations are possible, we immediately notice that the transverse excitations (along r and z) have much higher energy than the longitudinal excitations (along θ). Hence, the longitudinal phononic excitations are the lowest energy phononic excitations and need to be considered separate from the other excitations. In our inhomogeneous system with a TF cross-section, the longitudinal effective speed of sound at the barrier is given by [215, 270, 271]

$$c_{\text{eff}} = \frac{c}{\sqrt{2}} = \sqrt{\frac{\mu_l}{2m}}, \tag{7.22}$$

where μ_l is the (peak) local mean field at the location of the barrier.

Plotting our obtained critical velocity vs c_{eff} (see figure 7.13), we see that our data spans a range of sound speeds (1.1 to 1.6 mm/s) and critical flow velocities (0.7 to 1.0 mm/s). This was possible because of the azimuthal smoothness of the ring that allowed us to vary the chemical potential and therefore flow velocity by a large range. We find that the critical flow velocity is around 60% of c_{eff}. This is consistent with it being lower than the sound speed. This is also to be compared to the measurement of ≈15% for the Washington State University experiment [50], and ≈25% (correcting for the cylindrical shape of the laser beam [48]) for the MIT experiments [49] and the University of Arizona experiments [51]. Experiments in superfluid helium have also found superflow to breakdown at velocities well below the critical velocity due to phonon and roton excitations (see Wilks [272] or Varoquaux [32]).

Coming to the critical velocity of vortex-like excitations, we look at the energy cost of putting a vortex-antivortex pair with separation r_s at the middle of the annulus in the barrier region. From equation (7.19), we can see that the energy is

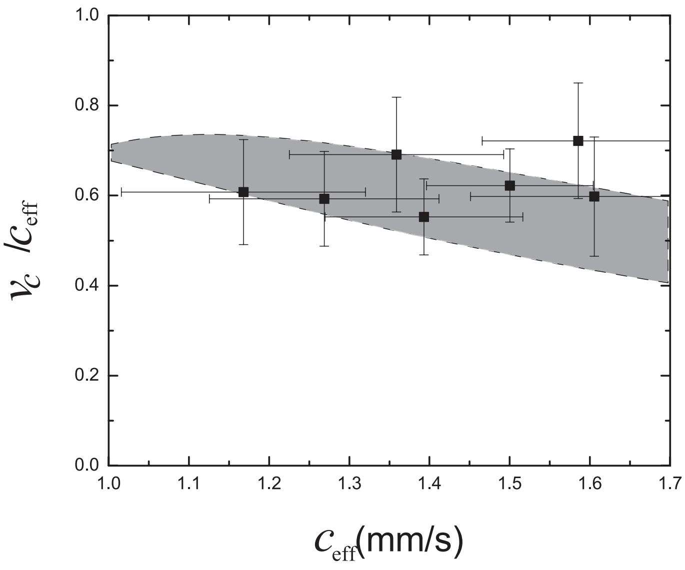

Figure 7.13: Critical velocity comparison: The critical velocity v_c normalized by the effective local sound speed, c_{eff} is plotted. The flow breaks when the flow velocity is around 60% of the effective sound speed. The gray band shows the predicted (2D) Feynman critical velocity.

negative if[12]

$$v_f \geq \frac{\hbar}{m r_s} \log \frac{r_s}{\xi}, \tag{7.23}$$

where ξ is the healing length. Again, we have the problem of the inhomogeneous density profile, and hence ξ varies across the cross-section. For any vortex-pair recombination, the vortices have to pass through the center of the annulus, and hence the peak density and the corresponding ξ are relevant. The $\log(r_s)/r_s$ dependence of v_f makes it relatively insensitive to r_s for the range of r_s in our system (TF width at the barrier), and so the choice of r_s is less critical.

We set[13] $r_s = 2r_{\mathrm{TF}} = 2\sqrt{2\mu/m\omega_r^2}$ and $\xi = \sqrt{\hbar^2/2\mu m}$, where $\mu_l/2 \leq \mu \leq \mu_l$ is the transverse variation of the mean field at the location of the barrier. Plotted against our data (see figure 7.13), we can see that our data lies within the gray band

---

[12] This expression is very similar to Feynman's [24] expression for the critical velocity for creating vortices in a channel (discussed in section 2.5.b). The difference is a factor of 2 (r_s is the full width of the channel), which arises from the quasi-2D nature of our condensate near the barrier.

[13] While the condensate may not be TF along z, it is still TF along r.

indicative of the (2D Feynman) critical velocity for a vortex-pair excitation. The specified range of μ is a best guess to accommodate the inhomogeneous transverse profile, where the mean field varies from μ_l at the center and 0 at the edge.

While the match looks good, it must be kept in mind that both the expression for the Feynman critical velocity, and the calculation of the critical flow velocity are approximate, and a more careful calculation of the various parameters and the energetics are needed. Still, that all the points fall within the band (within error bars) is suggestive of the mechanism of flow decay by vortex production. Simulations of systems similar to ours [273], although with circulation of $8\hbar$, indicate decay of flow by a vortex entering the ring. This could be compoared to the annhilation of a vortex-antivortex pair at the center of the annulus. In their case, presumably due to the high circulation, the vortices were dragged along with the flow, which should not happen in our experiment since we have only one unit of circulation.

Experiments studying helium superflow through small apertures by Avenel and Varoquaux [33] and Amar *et al.* [34] have also shown evidence of a phase slip mechanism, although the 3D nature of these systems makes vortex rings more likely. The critical velocities for such events have been in agreement with the Feynman critical velocities (discussed extensively in Varoquaux [32]).

7.7 Conclusion and future work

In conclusion, we have been able to clearly identify the decay of flow due to the presence of a barrier. Our estimates of the critical velocity match well with that necessary for the decay via a vortex-antivortex pair.

Our critical velocity experiment is a first step to studying several phenomenon. In the experiment, we worked with a cloud that was effectively at zero temperature. A possible experiment is studying the effect of temperature, which could lead to decay of flow via a different mechanism, the splitting of thermally excited vortex-antivortex pairs. Another possibility is studying the effect of dimensionality by varying the radial and vertical confinement.

Recently, we have had success in testing an acousto-optic deflector (AOD) to generate arbitrarily shaped potentials. By engineering the barrier using the AOD, we could change the dimensionality of the BEC in the barrier region; that would allow us to explore the channel width dependence of the critical velocity. We could also create a definite constriction with nearly hard walls, which would more closely approach the superfluid helium experiments allowing more direct comparisons. Using the AOD, we could also create a moving barrier. Such a barrier could be used to deterministically stir the condensate, as described in Brand and Reinhardt [224].

Josephson effects have been observed in BECs separated by a weak link [274, 275]. The barrier in our setup serves as a weak link, and hence the weak link in a superfluid circuit constitutes a first step towards the atom analog of a superconducting SQUID. A possible scheme for sensing rotation is to rotate the barrier around the ring close to the critical velocity for one unit of circulation. Small changes in the rotation speed would then translate to circulation being imparted to the BEC or not. Such changes could arise from the rotation of the apparatus as a whole or even the rotation of the earth, thereby creating a rotation sensor.

As I conclude this thesis, I would say that our journey these last 4+ years has been quite long. From our first days of creating an all-optical toroidal potential, we now have very good control of the ring BEC, from how to create it to how to characterize it. We also now have a good understanding of what sustains a persistent current, and what it takes for the flow to breakdown. Along with being able to measure the critical velocity, we are well poised to perform experiments with moving barriers and atom SQUIDs. The future looks bright with possibilities of creating rotation sensors or other “atomtronic” devices (atom analogs of electronic devices). With that, I would like to thank you for reading this thesis.

Appendices

Appendix A

Analyzing PTAI images

A.1 Calculating the uncertainty of measurement using PTAI

In this section, we calculate the uncertainty of measurement using PTAI. We start with the expression for the total noise (equation (4.18)), and use it to determine the uncertainty, $\delta\beta_m$. The area of interest in the cloud has an OD of β. We transfer a fraction γ, giving a transferred OD of $\beta_f = \gamma\beta$. By imaging the transferred fraction, we obtain an inferred optical depth, $\bar{\beta}_m$, which can be expressed in terms of the photon counts on the detector $\eta\bar{M}_t$[1], the latter being the measured quantity:

$$\bar{\beta}_m = \frac{\beta_f}{\gamma} = -\frac{1}{\gamma}\log\frac{\eta\bar{M}_t}{\eta\bar{M}} \tag{A.1}$$

Correspondingly, the uncertainty in the measurement, $\delta\beta_m$, can be expressed in terms of the statistical variation of the transmitted probe light. We assume that the reference signal, $\eta\bar{M}$, which comes from the image of the probe beam on CCD in the absence of atoms has been averaged over several realizations and so has no uncertainty associated with it:

$$\delta\beta_m = \frac{1}{\gamma}\frac{\delta(\eta M_t)}{\eta\bar{M}_t}. \tag{A.2}$$

From the limit to the number of photons, eq. (4.17), we get:

$$\eta\bar{M}_t = \frac{\alpha\eta N_f e^{-\beta_f}}{1-e^{-\beta_f}} \tag{A.3}$$

The variation in the detected photon counts comes from the noise, eq. (4.18).

$$\delta(\eta M_t) = \sqrt{\frac{\alpha N_f \eta e^{-\beta_f}}{1-e^{-\beta_f}}\left(1+\frac{\alpha\eta\beta_f^2 e^{-\beta_f}}{1-e^{-\beta_f}}\right)} \tag{A.4}$$

---

[1] The bar indicates an average, assuming an average over several realizations. The uncertainty is based on a single realization and hence in the notation, I do not use a bar.

Substituting equations (A.4) and (A.3) into equation (A.2), the uncertainty in the measurement can be calculated:

$$\begin{aligned}
\delta\beta_m &= \frac{1}{\gamma}\sqrt{\frac{\left(1+\frac{\alpha\eta\beta_f^2 e^{-\beta_f}}{1-e^{-\beta_f}}\right)}{\frac{\alpha\eta N_f e^{-\beta_f}}{1-e^{-\beta_f}}}} \\
\delta\beta_m &= \frac{1}{\gamma}\sqrt{\frac{1-e^{-\beta_f}+\alpha\eta\beta_f^2 e^{-\beta_f}}{\alpha\eta N_f e^{-\beta_f}}} \qquad \text{(A.5)}
\end{aligned}$$

where, the last step is only an algebraic simplification. Equation (A.5) expresses the uncertainty in measurement, $\delta\beta_m$ as a function of the OD of the cloud (β), the transferred fraction (β_f) and the pixel resolution (one can express N_f in the denominator as $\beta_f A/\sigma_0$). The first two terms in the numerator under the square-root come from the photon shot noise, while the last term comes from the atom shot noise. Depending on which term is larger, the respective shot noise will dominate.

A.2 Calculating the uncertainty in measurement using PCI

In this section, we calculate the uncertainty in measurement of phase-contrast imaging as a function of the OD of the cloud and the perturbation to the sample. We choose a region of interest identical to the PTAI case, having an area, A, N atoms and an (on-resonant) OD β. In phase-contrast imaging, the probe light is usually far detuned from resonance, $(\omega-\omega_0)/(\Gamma/2)=\Delta \gtrsim 10$. Applying $\Delta^2 \gg 1$ to equations (4.10, 4.11 and 4.12), we obtain (see Lye *et al.* [140] for example):

$$\begin{aligned}
\bar{M}_t &= \bar{M}e^{-\beta/\Delta^2} \qquad \text{(A.6)} \\
\bar{M}_{abs} &= \bar{M}(1-e^{-\beta/\Delta^2}) \qquad \text{(A.7)} \\
\delta\phi &= \frac{N}{A}\sigma_0\frac{1}{2\Delta} = \frac{\beta}{2\Delta} \qquad \text{(A.8)}
\end{aligned}$$

To retain sensitivity at higher optical depths and not have the phase wrap around, we have to also ensure that $\delta\phi < \pi/4$. This puts a further condition on the detuning, Δ, at very high optical depths, i.e. $\beta \gtrsim 60$:

$$\begin{aligned} \frac{\beta}{2\Delta} &< \frac{\pi}{4}, \\ \Delta &> \frac{2\beta}{\pi}. \end{aligned} \tag{A.9}$$

This condition ensures that $e^{-\beta/\Delta^2} \approx 1$, and so, the absorption of photons through the sample can be expressed as,

$$\bar{M}_{abs} = \bar{M}\frac{\beta}{\Delta^2} \tag{A.10}$$

Since the absorption of photons through the sample is low, we can assume that there is very little change in the number of photons in the probe beam as it passes through the sample, i.e. $M_t \approx M$.

A.2.a Photon shot noise

For simplicity of calculation, we will assume the following setup. The transmitted probe beam, $\bar{M}\eta$, interferes with a reference local oscillator of $\bar{M}_L$ photons on the detector. The calculation holds for the more typical phase-contrast imaging setups [136], if one uses a large enough probe beam and an appropriate interference scheme. Deviations from these ideal conditions causes some distortion, which is beyond the scope of this thesis. For our model interference setup, the detected number of photons is:

$$\bar{M}_d = \bar{M}_L + \eta\bar{M} + 2\sqrt{\bar{M}_L\eta\bar{M}}\cos(\phi_0 + \delta\phi) \tag{A.11}$$

where $\bar{M}_d$ is the detected number of photons and ϕ_0 is the native phase shift between the beams. For maximum detectability, we set the relative phase $\phi_0 = \frac{\pi}{2}$. This simplifies equation (A.11):

$$\bar{M}_d = \bar{M}_L + \eta\bar{M} - 2\sqrt{\bar{M}_L\eta\bar{M}}\sin(\delta\phi) \tag{A.12}$$

In the absence of atoms, the number of photons incident on the detector is:

$$\bar{M}_{d,0} = \bar{M}_L + \eta\bar{M}, \tag{A.13}$$

which is the reference signal.

Substituting the phase shift $\delta\phi$ from equation (A.8), we obtain the detected number of photons, $\bar{M}_d$, as a function of the OD, β:

$$\bar{M}_d = \bar{M}_L + \eta\bar{M} - 2\sqrt{\bar{M}_L\eta\bar{M}}\sin\left(\frac{\beta}{2\Delta}\right). \tag{A.14}$$

The photon shot noise goes as the square root of the number of photons incident on the detector, $\bar{M}_d$. The photon shot noise for phase-contrast imaging is:

$$\aleph_{phot} = \sqrt{(\bar{M}_L + \eta\bar{M}) - 2\sqrt{\bar{M}_L\eta\bar{M}}\sin\left(\frac{\beta}{2\Delta}\right)} \tag{A.15}$$

A.2.b Uncertainty in the measured optical depth

Analogous to the PTAI case, we start with an expression for the measured OD, $\bar{\beta}_m$, and obtain an expression for the uncertainty $\delta\beta_m$ arising from the photon shot noise, $\aleph_{phot}$. From equations (A.8),(A.12) and (A.13) we obtain an expression for the measured OD, $\bar{\beta_m}$:

$$\bar{\beta}_m = 2\Delta\sin^{-1}\left(\frac{\bar{M}_{d,0} - \bar{M}_d}{2\sqrt{\bar{M}_L\eta\bar{M}}}\right), \tag{A.16}$$

where $\bar{M}_L$ and $\eta\bar{M}$ are measured prior to taking the image. We assume that these quantities have been measured repeatedly and so have no shot noise associated with them.

Again, we assume that the reference is averaged over several images and so has no shot noise associated with it ($\delta M_{d,0} = 0$). Differentiating equation (A.16) with respect to the signal, $\bar{M}_d$, we get:

$$\delta\beta_m = 2\Delta\left(1 - \left(\frac{\bar{M}_{d,0} - \bar{M}_d}{2\sqrt{\bar{M}_L\eta\bar{M}}}\right)^2\right)^{-\frac{1}{2}}\frac{\delta M_d}{2\sqrt{\bar{M}_L\eta\bar{M}}} \tag{A.17}$$

Substituting the variation in photon number, $\delta\bar{M}_d$ from equation (A.15), the uncertainty in measurement is:

$$\delta\beta_m = \Delta\frac{\sqrt{(\bar{M}_L + \eta\bar{M}) - 2\sqrt{\bar{M}_L\eta\bar{M}}\sin\left(\frac{\beta}{2\Delta}\right)}}{\cos\left(\frac{\beta}{2\Delta}\right)\sqrt{\bar{M}_L\eta\bar{M}}} \tag{A.18}$$

In order to obtain the minimum uncertainty without increasing the amount of light passing through the atom cloud, we set $\bar{M}_L >> \bar{M}$. This assumes a sufficient dynamic range of the detector, $\gtrsim 2\bar{M}_L$. Equation (A.18) simplifies to

$$\delta\beta_m = \Delta\ \frac{1}{\cos\left(\frac{\beta}{2\Delta}\right)}\sqrt{\frac{1}{\eta\bar{M}}}. \tag{A.19}$$

Although we detect only the phase-shift of the beam, there is some absorption of light (see equation (A.7)). Expressing the number of incident photons in terms of the absorption through the cloud, we find:

$$\delta\beta_m = \frac{1}{\cos\left(\frac{\beta}{2\Delta}\right)}\sqrt{\frac{\beta}{\eta\bar{M}_{abs}}}. \tag{A.20}$$

Each absorbed photon corresponds to an atom undergoing a recoil event. For ultracold gases, even a single recoil event transfers kinetic energy much higher than the temperature and other energy scales. We can set $\bar{M}_{abs} = N_d$, where N_d is the number of atoms undergoing recoil events, which is a measure of the perturbation of the sample. We express the absorbed light in terms of the number of atoms undergoing recoil. We obtain:

$$\delta\beta_m = \frac{1}{\cos\left(\frac{\beta}{2\Delta}\right)}\sqrt{\frac{\beta}{\eta N_d}}, \tag{A.21}$$

which expresses the uncertainty of measurement in terms of the OD and the number of atoms undergoing recoil.

A.3 Change in transmitted intensity due to optical pumping

In performing PTAI, there is some optical pumping due to off-resonant excitation. The optical pumping can be accounted for by solving for the change in optical depth as a function of time given an certain incident intensity. However, as seen in section 4.6.b, the differential equation is more easily cast in terms of the transmitted intensity $I_t(\tau)$ than the optical depth $\beta(\tau)$. In this section, we will solve for $I_t(\tau)$, given an incident probe intensity I_i. We start with the basic differential equation, reproduced from equation (4.27):

$$\frac{dI_t(\tau)}{d\tau}\left(\frac{1}{I_t(\tau)}+\frac{1}{I_{\text{sat}}}\right)=-\frac{\sigma_b}{\hbar\omega\tilde{\Delta}^2}\left(I_i-I_t(\tau)+\frac{I_i^2-I_t^2(\tau)}{2I_{\text{sat}}}\right).$$

We will now make a suitable change of variables to make the algebra simple:

$$\begin{aligned} x &= \frac{I_t(\tau)}{I_{\text{sat}}}+1, \\ B &= \frac{I_i}{I_{\text{sat}}}+1, \text{ and} \\ A &= \frac{\sigma_b I_{\text{sat}}}{\hbar\omega\tilde{\Delta}^2}. \end{aligned}$$

Equation (4.27) then becomes:

$$\frac{dx}{d\tau}\left(\frac{1}{x-1}+1\right)=-A\left(B-1-(x-1)+\frac{(B-1)^2-(x-1)^2}{2}\right), \tag{A.22}$$

which then simplifies to

$$\frac{dx}{d\tau}\left(\frac{x}{x-1}\right)=-\frac{A}{2}(B^2-x^2). \tag{A.23}$$

Equation (A.23) can be solved by first moving all x containing terms to the left-hand side,

$$\frac{xdx}{(x-1)(B^2-x^2)}=-\frac{Ad\tau}{2}, \tag{A.24}$$

then splitting the terms into partial fractions,

$$\frac{dx}{2(B^2-1)}\left(\frac{2}{x-1}+\frac{B-1}{B+x}+\frac{B+1}{B-x}\right)=-\frac{Ad\tau}{2}, \tag{A.25}$$

and finally integrating the equation to give

$$\frac{dx}{2(B^2-1)}\log\left(\frac{(x-1)^2(B+x)^{B-1}}{(B-x)^{B+1}}\right)=-\frac{A\tau}{2}+C, \tag{A.26}$$

where C is the constant of integration. Substituting for $I_t(\tau)$, and using the $\tau=0$ condition for C, we finally obtain

$$\begin{aligned} \frac{1}{\tilde{I}_i(\tilde{I}_i+2)}\log\left(\frac{I_t(\tau)^2(I_i+I_t(\tau)+2I_{\text{sat}})^{\tilde{I}_i}}{(I_i-I_t(\tau))^{(\tilde{I}_i+2)}}\right) &= A\tau + \\ \frac{1}{\tilde{I}_i(\tilde{I}_i+2)}\log\left(\frac{I_t(0)^2(I_i+I_t(0)+2I_{\text{sat}})^{\tilde{I}_i}}{(I_i-I_t(0))^{(\tilde{I}_i+2)}}\right)&, \end{aligned} \tag{A.27}$$

where $\tilde{I}_i = I_i/I_{\text{sat}}$.

The solution is not particularly insightful, and is presented here just for completeness.

Appendix B

Fully Thomas-Fermi condensate in the ring trap

In this appendix, we will calculate the relationship between the number of atoms and the chemical potential for a fully Thomas-Fermi condensate. The potential is given by

$$V(r,z,\theta) = \frac{1}{2}m\omega_z^2 z^2 + \frac{1}{2}m\omega_r^2 (r-r_M)^2.$$

We start with the 3D density distribution:

$$\begin{aligned} gn_{3D}(r,z,\theta) &= \mu_0 - \left(\frac{1}{2}m\omega_z^2 z^2 + \frac{1}{2}m\omega_r^2(r-r_M)^2\right) \text{ for } \mu_0 > V(r,z,\theta) \quad \text{(B.1)} \\ &= 0 \text{ everywhere else} \end{aligned}$$

For integrating along z, one needs to be aware that the limit of integration depends on the radial coordinate r. In the region of the condensate, we set up the integral with limits:

$$gn_{2D}(r,\theta) = \int_{-z_r}^{z_r} dz \left(\mu_0 - \left(\frac{1}{2}m\omega_z^2 z^2 + \frac{1}{2}m\omega_r^2(r-r_M)^2\right)\right), \quad \text{(B.2)}$$

where $z_r = \sqrt{\frac{\mu_0 - \frac{1}{2}m\omega_r^2(r-r_M)^2}{m\omega_z^2/2}}$ is the distance up to which the condensate extends at a radial location r.

$$\begin{aligned} gn_{2D}(r,\theta) &= \left(\mu_0 - \frac{m\omega_r^2(r-r_M)^2}{2}\right) z|_{-z_r}^{z_r} - \frac{1}{6}m\omega_z^2 z^3|_{-z_r}^{z_r} \\ &= \left(\mu_0 - \frac{m\omega_r^2(r-r_M)^2}{2}\right) 2z_r - \frac{1}{6}m\omega_z^2 2z_r^3 \end{aligned}$$

Substituting z_r, we get

$$\begin{aligned} gn_{2D}(r,\theta) &= 2\frac{(\mu_0 - \frac{1}{2}m\omega_r^2(r-r_M)^2)^{3/2}}{\sqrt{m\omega_z^2/2}} \\ &\quad -\frac{1}{3}m\omega_z^2\left(\frac{\mu_0 - \frac{1}{2}m\omega_r^2(r-r_M)^2}{m\omega_z^2/2}\right)^{3/2} \\ gn_{2D}(r,\theta) &= \frac{4\sqrt{2}}{3\sqrt{m\omega_z^2}}(\mu_0 - \frac{m\omega_r^2(r-r_M)^2}{2})^{3/2} \quad \text{(B.3)} \end{aligned}$$

The 2D column density profile obtained scales as a 3/2 power of the expression for the radial TF case (see equation (5.31)), which makes it similar in shape except for a steeper drop-off near the TF width. I will call this functional form the 3D-TF profile.

The peak 2D density is given by:

$$n_{2D}(r = r_M, \theta) = \frac{4\sqrt{2}\mu_0^{3/2}}{3\sqrt{m\omega_z^2 g}}. \tag{B.4}$$

We then set up the integral to integrate the 2D column density to get the number of atoms:

$$N = \int_{r_M - r_{TF}}^{r_M + r_{TF}} r dr \frac{4\sqrt{2}}{3g\sqrt{m\omega_z^2}}(\mu_0 - \frac{m\omega_r^2(r - r_M)^2}{2})^{3/2} \int d\theta, \tag{B.5}$$

where $r_{TF} = \sqrt{\frac{2\mu_0}{m\omega_r^2}}$, as defined in chapter 5.

Since the trap is radially symmetric, we can easily integrate over θ to obtain:

$$N = \int_{r_M - r_{TF}}^{r_M + r_{TF}} r dr \frac{8\sqrt{2}\pi}{3g\sqrt{m\omega_z^2}}(\mu_0 - \frac{m\omega_r^2(r - r_M)^2}{2})^{3/2}. \tag{B.6}$$

In order to integrate over r, we first express μ_0 in terms of r_{TF}:

$$N = \int_{r_M - r_{TF}}^{r_M + r_{TF}} r dr \frac{4\pi m\omega_r^3}{3g\omega_z}(r_{TF}^2 - (r - r_M)^2)^{3/2}. \tag{B.7}$$

We will now make a change of variable. We then set $q = r - r_M$. The change in integrand and limits of integration are given by:

$$dq = dr, \tag{B.8}$$

$$\text{for } \; r = r_M - r_{TF} \;\; \Rightarrow q = -r_{TF}, \text{ and} \tag{B.9}$$

$$\text{for } \; r = r_M + r_{TF} \;\; \Rightarrow q = r_{TF}. \tag{B.10}$$

Substituting the above expressions in equation (B.7), we get:

$$N = \int_{-r_{TF}}^{r_{TF}} r_M dq \frac{4\pi m\omega_r^3}{3g\omega_z}(r_{TF}^2 - q^2)^{3/2}. \tag{B.11}$$

Since the integral is symmetric about $q = 0$, only r_M, which is the even part of $r_M + q$ (comes from r in equation (B.7)) survives, and so the term containing q has not been shown in equation (B.11).

We then make a further change of variables and set $\tilde{q} = \frac{q}{r_{TF}}$. This gives us:

$$N = \int_{-1}^{1} r_M d\tilde{q} \frac{4\pi m \omega_r^3 r_{TF}^4}{3g\omega_z}(1 - \tilde{q}^2)^{3/2}. \tag{B.12}$$

We can then use a trignometric integral to solve, setting $\sin\alpha = \tilde{q}$, which gives:

$$\begin{aligned}
\cos\alpha \; d\alpha &= d\tilde{q}, && \text{(B.13)} \\
\tilde{q} = \pm 1 \Rightarrow \alpha &= \pm\pi/2, \text{ and} && \text{(B.14)} \\
\cos\alpha &= \sqrt{1 - \tilde{q}^2}. && \text{(B.15)}
\end{aligned}$$

Substituting these expressions for $\tilde{q}$, we get:

$$N = \int_{-\pi/2}^{\pi/2} r_M d\alpha \frac{4\pi m \omega_r^3 r_{TF}^4}{3g\omega_z}(\cos\alpha)^4. \tag{B.16}$$

This is a known trignometric integral giving us:

$$N = r_M \frac{4\pi m \omega_r^3 r_{TF}^4}{3g\omega_z} \times \frac{3\pi}{8}. \tag{B.17}$$

Substituting for r_{TF}, we obtain:

$$N = 2\pi^2 \frac{r_M \mu_0^2}{g m \omega_z \omega_r}. \tag{B.18}$$

Appendix C

Calibrations for critical velocity

This appendix explains the various calibration procedures used.

C.1 Time calibration

Our PulseBlaster board was tested against various (calibrated) oscilloscopes, and the timing was found to be accurate to the limit of the measuring device. This makes our knowledge of time (for Raman or microwave pulses and time of flight) the most accurate measurement, better than 10^{-4} (specified to be accurate to 10 ns). In the remainder of this section, I will neglect any inaccuracies in our knowledge of time, and treat time as perfectly known.

C.2 Length calibration and pixel size

Since we know the imaging system we have in place, we can determine the magnification and pixel size purely from the location of various optical elements. However, it is usually more accurate to measure a property of the atoms to determine the lengthscale.

The simplest such method is to image a cloud falling under gravity. We first calibrate our horizontal imaging system to watch the change in position of a cloud falling in time of flight, and then use that to calibrate the vertical imaging system.

C.2.a Calibrating the horizontal imaging system using gravity

In data taken on October 29 2008, we took a series of measurements watching the cloud fall under gravity (see figure C.1). Our camera pixel size is given as 6.45 μm. Since our imaging system consists of a 20 cm focal length lens followed by a 50 cm lens (both convex achromatic doublets), we estimate an initial pixel size (size

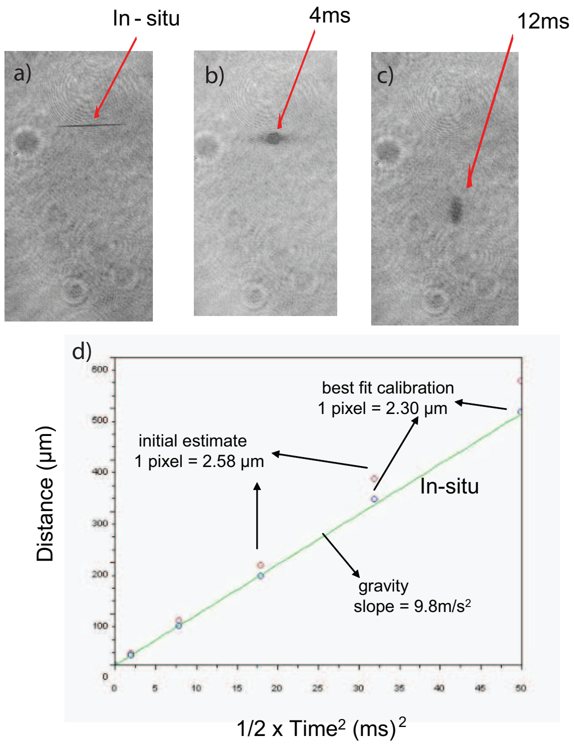

Figure C.1: Calibrating length scale using gravity. Absorption images (a), (b) and (c) show the cloud at different times of flight. We match the pixel size to acceleration due to gravity. As one can see, all points fall on the straight line.

at the plane of the BEC corresponding to one pixel on the camera) of 2.58 μm. Matching the location of the cloud on the camera with what is expected of a freely falling object ($\frac{1}{2}gt^2$, where t is the time-of-flight and $g = 9.8m/s^2$ is the acceleration due to gravity), we obtain a calibrated pixel size of 2.30 μm (figure C.1(d)).

Our pixel size calibration agrees with our initial estimate, the difference arising from the first lens not being at the proper focal distance from the BEC. The distance between the two lenses were not the sum of focal lengths (analogous to 4F imaging), and so the magnification is sensitive to minor displacements of the lens. The difference between the predicted and actual pixel size correspond to the first lens being placed 1 cm closer to the plane of the BEC than the focal length. The discrepancy is quite plausible as the BEC sits inside vacuum in a 2 cm glass cell (see figure 3.8), and so its precise position cannot be determined.

C.2.b Calibrating the vertical imaging system by matching cloud size

The horizontal and vertical images share a common axis (which is along the Zeeman slower). If one were to take an image of the same cloud using both cameras and integrate out the non-common axis in the respective images, one should get an identical line profile from each camera. Taking a set of 3 images from each camera, we compare and match up line profiles to get the calibration of the vertical camera (figure C.2). We get a pixel size (at a 5x zoom lens setting) of 1.2 μm. The uncertainty in the calibration is estimated to be less than 10%. The calibration matches what one would expect from an estimate of the magnification of the imaging set up.

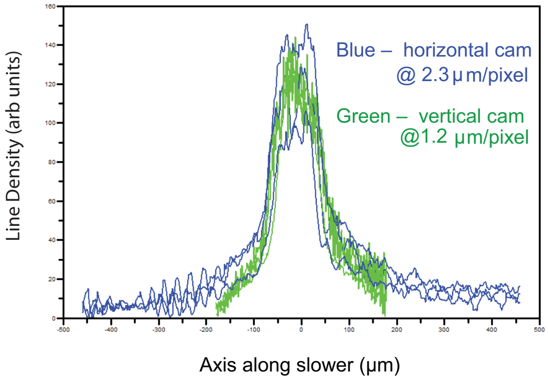

Figure C.2: Matching the line profiles from the two cameras. By adjusting the x-axis scales of the vertical camera, we match up the line profiles of 6 ms time-of-flight images to get a calibration of the pixel size of the vertical camera from the known calibration of the horizontal camera. We use 3 images of each to get a fair sample size. While the regions of line density may not match up as the regions of high optical depth are not accurately measured, the slope at the edge of the cloud matches well.

C.3 Measuring the trap frequencies

We measured trap frequency by parametric heating. By summing a small AC signal to the amplitude control of the AOM driver for the ring or the sheet beam, we could modulate the dipole trap. We sum a 20-50 mV signal (1-4%) for a time varying between 100 ms and 2 s. Modulating a beam at the corresponding trap frequency causes parametric heating. In our system, the trap depth is relatively low and only a weak diffuse thermal cloud can be contained. Therefore, it was easier to detect heating by looking at the loss of atoms from the trap (particularly the BEC) due to thermal excitation. We measured the number of atoms *in situ* immediately after the parametric heating. As we required only a relative measurement of the heating, this measurement sufficed for us to determine the trapping frequency.

C.3.a Vertical trapping frequency

The vertical confinement is due to the sheet beam[1]. Due to non-uniformities in the beam believed to be due to interference fringes from a secondary reflection as the beam passes through the glass cell, parametric heating occurs for a broad range of frequencies (more than 50 Hz $1/e^2$ full width in 540 Hz). However, when we performed the same experiment with the ring beam turned on, we were able to narrow the range. We measured the sheet trapping frequency, ω_z on June 9 2010. ω_z was found to be 545±5 Hz (uncertainty in mean) for a sheet beam power of 135 mW, which was the configuration we did our critical velocity experiments in. Measuring the trap frequency at different sheet beam intensities, we obtained values consistent with the relation $\omega \propto \sqrt{P}$ ($\omega/2\pi$ is the trap frequency, and P is the beam power). We also measured heating at close to twice the fundamental frequency.

C.3.b Radial trapping frequency

The annular confinement is due to the LG ring beam. Performing a similar process for the LG beam (performed on June 11 2010), we found the radial trapping frequency, ω_r to be 107±2 Hz for a ring beam power of 27 mW (our typical

---

[1] While it may seem that parametric heating should not occur in this direction at the trap frequency ω_z because of the symmetry in the beam, a combination of the gravitational potential and the anharmonicity of the trap is believed to allow parametric heating to take place.

experimental condition). We verified the $\omega \propto \sqrt{P}$ scaling for the ring beam power also.

C.4 Measuring imaging parameters

In getting any quantitative measurement of atom column density out of absorption imaging, one needs to know the scattering cross-section (σ_0), the incident and transmitted light intensities (I_i and I_t) and, to correct for the effects of saturation, the saturation intensity (I_{sat}, see section 4.2). While it may seem more logical to get the scattering cross-section first, it is more complicated. Saturation intensity, on the other hand can be determined by comparing the uncorrected measured atom number for different the incident intensities of the light, without knowing anything else.

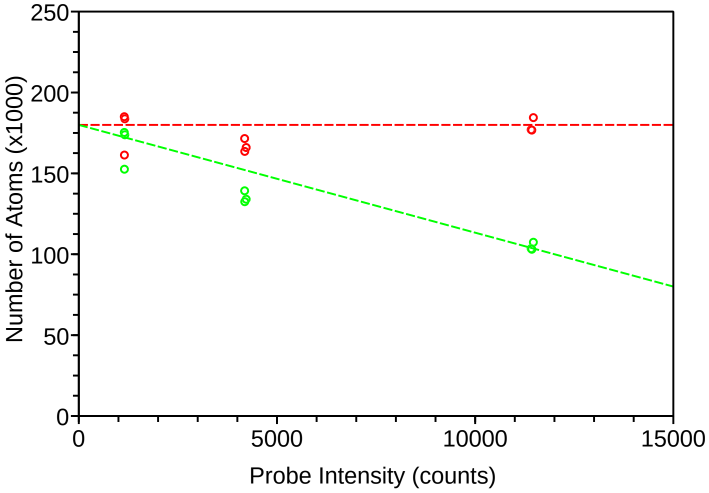

Figure C.3: Calibrating the saturation intensity: For a set of 6 images of nearly identical clouds, at varying probe intensity, we plot the number of atoms against the average probe count (green). We then make a correction (red), setting the saturation intensity to 10000 counts. The dotted lines are a guide to the eye.

C.4.a Measuring saturation intensity

To determine the saturation intensity, we take a set of absorption images of nearly identical atom clouds (data taken on May 6 2010) and different probe intensities. The clouds are imaged in time-of-flight with full optical repump. To correct for saturation, we take an overall average correction factor as opposed to an individual pixel-by-pixel correction factor. This is because certain variations in the probe intensity are due to optics downstream of the atom cloud. We calculate the probe intensity by averaging the pixel counts of the reference probe image (in the absence of atoms) over the region of atoms, and using that average value $\bar{I}_i$ (equation (4.9)) as the incident intensity for all pixels. We correct using

$$\beta_c(x,y) = \beta_u(x,y) + \frac{\bar{I}_i}{I_{\text{sat}}}(1 - e^{-\beta_u(x,y)}), \tag{C.1}$$

where $\beta_u(x,y) = -\log(I_t(x,y)/I_i(x,y))$ is the uncorrected optical depth and $\beta_c(x,y)$ is the corrected optical depth. We iteratively correct for I_{sat} as shown in figure C.3.

We obtain a saturation intensity of 10 000±1000 digital detector counts per pixel (figure C.3). This value is consistent with the estimated intensity (≈ 10 mW/cm^2) of the probe beam at the location of the atoms based on the calibration of the camera measuring the intensity at the atoms.

C.4.b Calibrating optical pumping for PTAI images

For *in situ* images, imaging with partial-transfer absorption imaging (PTAI), we need to correct for optical pumping because we cannot use repumping light (see section 4.6). The reader should note that although off-resonant excitation is sufficiently large so as to cause optical pumping, it is nevertheless small compared to resonant excitation and so does not contribute to the scattering cross-section. We use the calibration for saturation from the time-of-flight, optically repumped images and then apply another correction for optical pumping. While an exact analytic expression for optical pumping is not possible, we use the approximation in equation (4.30), which acts as a simple overall scaling factor and which works well for low transfer optical depth.

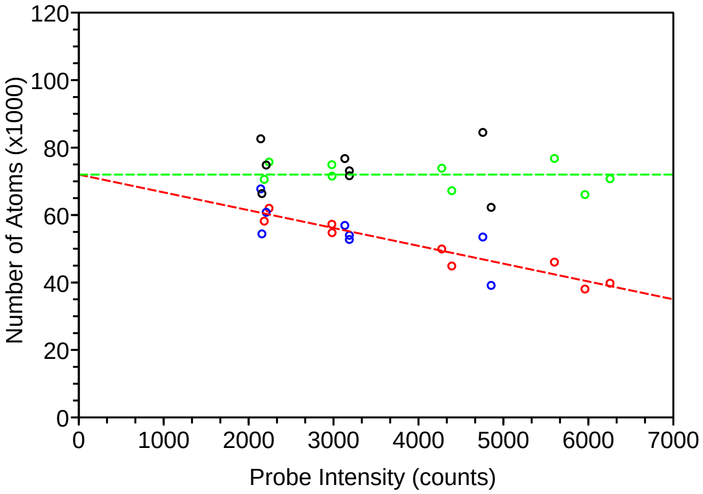

Figure C.4: Calibrating the optical pumping: For a series of 17 partial transfer images taken of nearly identical clouds, we plot the saturation-corrected number of atoms as a function of probe intensity (blue and red). We are able to correct for optical pumping to obtain the atom number independent of the probe intensity (black and green). While the correction is not linear, for this limited range of probe intensities, it appears so. The dotted lines are a guide to the eye. The blue (and corresponding black) points were taken with a 23% microwave transfer, while the red (and green) were taken with a 34% transfer. As one can see, the lower transfer fraction gives a higher scatter in atom number.

We took a series of measurements of an *in situ* cloud (data taken on May 28 2010) with varying probe power. We found optical pumping to be a factor of 3 more than the calculated value for the given intensity of light assuming isotropic light polarization. We do not have an explanation for this. The corrected and uncorrected plots are shown in figure C.4.

We also test our calibration, which was only based on imaging *in situ* data at various probe intensities, against optically repumped images (figure C.5). On June 14 2010, we took several sets of images of identical clouds imaging certain clouds *in situ* by PTAI and others in time-of-flight using optical repump. By taking the sets in quick succession, we avoid long term drifts in atom number due to varying conditions of oven temperature or transfer fractions. The atom numbers determined by the two methods were found to agree. The PTAI images had more shot to shot fluctuations. This is presumed to be due to atoms *in situ* giving a smaller signal. Checks taken closely in time agreed well. Those that were not taken closely in time did not agree as well, presumably due to other systematic drifts of experimental conditions during the time interval between the checks.

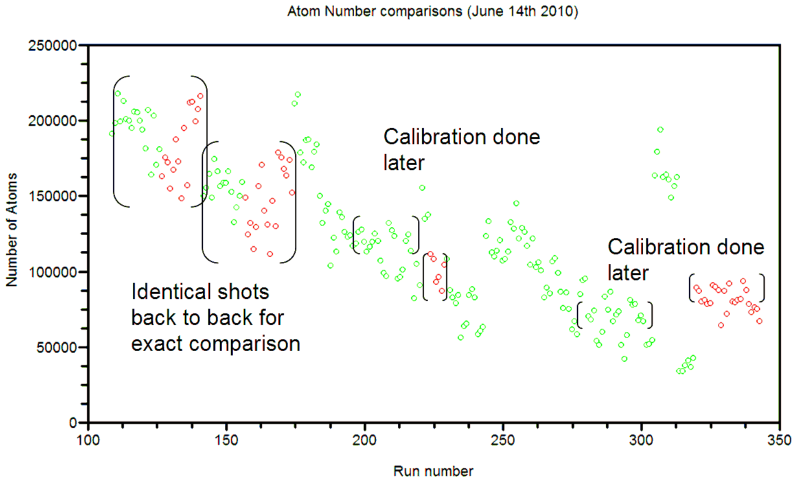

Figure C.5: Verifying the optical pumping calibration : We take a series of *in situ* partial transfer images (red) and time-of-flight optically repumped images (green). We compare shots taken under similar conditions (indicated on graph). The measured number of atoms of images taken back to back by the two techniques agree very well, while those taken some duration apart agree, but not as well.

C.4.c Measuring the scattering cross-section

The natural next step in imaging calibration is determining the scattering cross-section. When imaging with a cycling transition, each atom absorbs several photons, undergoing spontaneous decay during the process. Given the polarization of light and the initial state of the atom, one can calculate the scattering cross-section from the transition dipole moment and the appropriate Clebsch-Gordon coefficients. However, when an atom undergoes spontaneous decay, one cannot predict which state it will decay to and so cannot determine in which state an atom is starting from.

Certain special cases can be calculated (see Steck [156]).

- $|F = 2, m_F = \pm 2\rangle \rightarrow |F' = 3, m_F = \pm 3\rangle$ with $\sigma_\pm$ circularly polarized light, magnetic sub-level cycling transition : In this case, spin selection rules specify that the atom stays in the cycling transition, which keeps the initial state fixed allowing one to calculate the scattering cross-section. For sodium, this value is 1.657×10^{-13} m^2 [156]. This transition uses the highest transition dipole matrix element and so is the upper bound for the scattering cross-section.
- $F = 2 \rightarrow F' = 3$ isotropic light polarization: In this case, the distribution is averaged over all magnetic sublevels, and the scattering cross-section is averaged over all the transition dipole matrix elements. For sodium, this value is 0.7734×10^{-13} m^2 [156].

In our system, we use circularly polarized light. However, our bias field (∼1 G) is perpendicular to the direction of propagation of light and so our system does not map on to either of the above mentioned cases. We expect our scattering cross-section to be in-between the above mentioned values. To determine the exact value, we use our observed atom-atom repulsion to independently determine the density of atoms. Knowing the density, one can calculate the scattering cross-section from the absorption of light going through the cloud.

C.5 Calibrating the mean field

At ultracold temperatures, the interaction between sodium atoms can be characterized by a single parameter, the s-wave scattering length (see Tiesinga *et al.* [101]):

$$a = 2.75\text{nm} \tag{C.2}$$

Using mean field theory, in the TF regime, one can define a position dependent mean field energy for a BEC. For a condensate of density $n_{3D}(\mathbf{r})$, where $\mathbf{r}$ is the position in space, the mean field energy, $\mu(\mathbf{r})$ is given by

$$\mu(\mathbf{r}) = g n_{3D}(\mathbf{r}), \tag{C.3}$$

where $g = 4\pi\hbar^2 a/m$. To know the shape of our atom cloud, given the trapping potential and mean field interaction, we use the time-independent Gross-Pitaevskii (GP) equation (see Dalfovo *et al.* [63]):

$$E\psi(\mathbf{r}) = -\frac{\hbar^2}{2m}\nabla^2\psi(\mathbf{r}) + V_{\text{ext}}(\mathbf{r})\psi(\mathbf{r}) + g|\psi(\mathbf{r})|^2\psi(\mathbf{r}) \tag{C.4}$$

where ψ is the condensate wavefunction, E is the energy of the eigenstate and V_{ext} is the trapping potential. The GP equation is a non-linear Schrodinger equation. The first term on the right is the kinetic energy, the second term is the potential energy and the third term is the mean field energy. The lowest energy eigenstate of the GP equation is the ground state.

The GP equation cannot in general be solved analytically. In the limit of low interaction ($g|\psi|^4 \ll \frac{\hbar^2}{2m}|\nabla\psi|^2$), one gets the linear Schrodinger equation, which can be solved exactly for a harmonic oscillator. In the limit of high interaction energy (Thomas-Fermi approximation) compared to the kinetic energy, ($g|\psi|^4 \gg \frac{\hbar^2}{2m}|\nabla\psi|^2$), one gets a simple analytic solution:

$$n_{3D}(\mathbf{r}) = |\psi(\mathbf{r})|^2 = \frac{1}{g}\left(\mu_0 - V_{\text{ext}}(\mathbf{r})\right), \tag{C.5}$$

where μ_0 is the energy per particle (or chemical potential of the system). The Thomas-Fermi (TF) approximation breaks down at the edge of the condensate ($\mu_0 = V_{\text{ext}}(\mathbf{r})$), due to the sharp discontinuity in the derivative of the condensate density. While this can be corrected for, its overall effect on the shape of the cloud away from the edge and on the peak cloud density is usually negligible.

In this analysis, we use the Thomas-Fermi approximation. We perform various cross-checks and discuss possible corrections to account for deviations from the TF regime.

Our trap can be approximated as (see chapter 5)

$$V(r, z, \theta) = \frac{1}{2}m\omega_z^2 z^2 + \frac{1}{2}m\omega_r^2(r - r_0)^2 \tag{C.6}$$

where ω_z is the vertical trapping frequency and ω_r is the annular trapping frequency. We use cylindrical coordinates (r, z, θ). Using equation (C.5), we obtain the condensate density:

$$\begin{aligned} gn_{3D}(r,z,\theta) &= \mu_0 - \left(\frac{1}{2}m\omega_z^2 z^2 + \frac{1}{2}m\omega_r^2(r-r_0)^2\right) \text{ for } \mu_0 > V(r,z,\theta) \\ &= 0 \text{ everywhere else} \end{aligned} \tag{C.7}$$

The column density for such a profile would be (see equation (5.35) in chapter 5)

$$\begin{aligned} gn_{2D}(r,\theta) &= \frac{4\sqrt{2}}{3\sqrt{m\omega_z^2}}(\mu_0 - \frac{m\omega_r^2(r-r_0)^2}{2})^{3/2} \text{ for } (r-r_0) < r_{TF} \\ &= 0 \text{ everywhere else,} \end{aligned} \tag{C.8}$$

where $r_{TF} = \sqrt{\frac{2\mu_0}{m\omega_r^2}}$. If one were to fit the above profile to a cloud and obtain r_{TF}, one could determine the chemical potential μ_0 as

$$\mu_0 = \frac{1}{2}m\omega_r^2 r_{TF}. \tag{C.9}$$

The peak column density can be related to the chemical potential (equation (5.36) in chapter 5):

$$n_{2D}(r=r_0,\theta) = \frac{4\sqrt{2}\mu_0^{3/2}}{3\sqrt{m\omega_z^2}g}. \tag{C.10}$$

Rearranging this expression, one can obtain the chemical potential from the peak column density:

$$\mu_0 = \left(\frac{9n_{2D,0}^2 m\omega_z^2 g^2}{32}\right)^{1/3}. \tag{C.11}$$

Similarly, the number of atoms can also be related to the chemical potential (equation (5.38) in chapter 5)

$$N = 2\pi^2\frac{r_0\mu_0^2}{gm\omega_z\omega_r}. \tag{C.12}$$

One can also obtain the chemical potential from the number of atoms:

$$\mu_0 = \sqrt{\frac{g\omega_z\omega_r N}{2\pi^2 r_0}} \tag{C.13}$$

Equations (C.9), (C.11) and (C.13) provide 3 distinct (but not entirely independent) ways of determining the chemical-potential. We can calibrate the scattering cross-section by comparing the chemical potential obtained from the 3 ways.

C.6 Using the chemical potential to calibrate Absorption Scattering Cross-section

We fit the 3D-TF function to our *in situ* data. We assume a scattering cross-section of 1.1×10^{-13} m^2 to begin with and plot the chemical potential as a function of the atom number obtained by the 3 methods (see figure C.6).

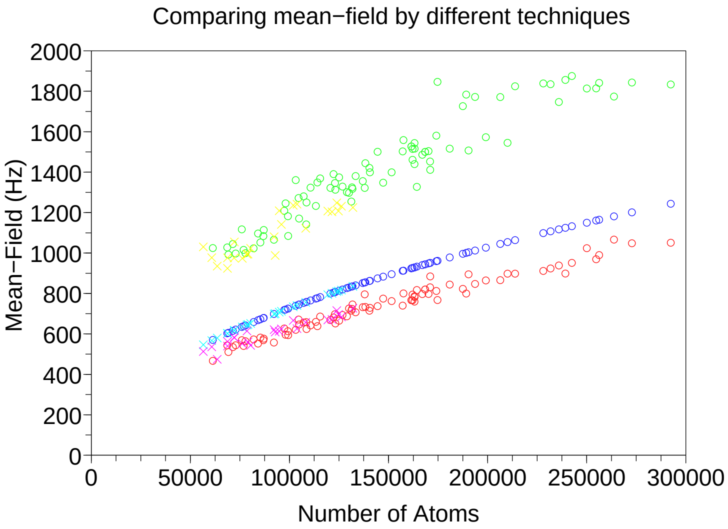

Figure C.6: Comparing the uncorrected chemical potential obtained by different methods : The blue/cyan points, red/magenta points and green/yellow points are based on the number of atoms, the peak 2D column density and the TF width respectively. As the blue/cyan points are a function of the number of atoms only, they are independent of shape, and hence for a neat curve in the above plot. The cyan, yellow and magenta points were taken with a 10 μs long probe pulse, while the blue, red and green points were taken with a 15 μs long probe pulse. While the curves have a similar scaling with the number of atoms, the μ_0 based on the TF width is significantly higher.

There are two major correction factors for the TF width:

- Resolution: The TF width is convolved with our resolution point spread function. To first order, one can correct it by subtracting the square of the point spread function width from the square of the TF width.

$$r_{\text{corr}} = \sqrt{r_{TF}^2 - p^2}, \tag{C.14}$$

where p is the resolution point spread function width. We apply a best guess correction using a point spread function width of 4 μm full width at half maximum.

- Smearing due to motion while imaging: During the imaging process, atoms scatter photons and undergo recoil. The motion of the atoms due to this additional energy (or momentum) causes the BEC to expand during the imaging pulse making it appear larger than the true *in situ* size. Assuming that the atoms scatter photons at a constant rate, the root-mean-square velocity goes as $v_{\text{rms}} \propto \sqrt{\tau}$, and the BEC size increases as $\delta r\ propto \tau^{3/2}$. On close analysis of images taken with a 10 μs imaging pulse and a 15 μs imaging pulse respectively, we find that the 15 μs images are 5% wider. We apply a small correction of a 10% smear for the 15 μs pulses and a 5% smear for the 10 μs pulses. To conserve number, we correct the 2D peak density correspondingly.

We plot the comparisons of the chemical potential with the above corrections applied (see figure C.7). The corrections led to a better agreement between the methods. We assume that the remaining disagreement is largely due to our incorrect guess for the scattering cross-section. We set $\sigma_0 = 0.91 \times 10^{-13}$ m^2, chosen by hand to minimize the disagreement in the calculation of the between the different methods, and replot the chemical potential calibration (see figure C.8). As one can see, all the methods agree closely. We attribute the remaining disagreement to the TF assumption and the uncertainty in some of our prior calibrations.

C.7 Calibrating the effect of the barrier

Having calibrated the scattering cross-section and the chemical potential, we can now go ahead to determine the effect of the barrier beam power on the density depletion at the location of the barrier. Taking an *in situ* image of the BEC with the

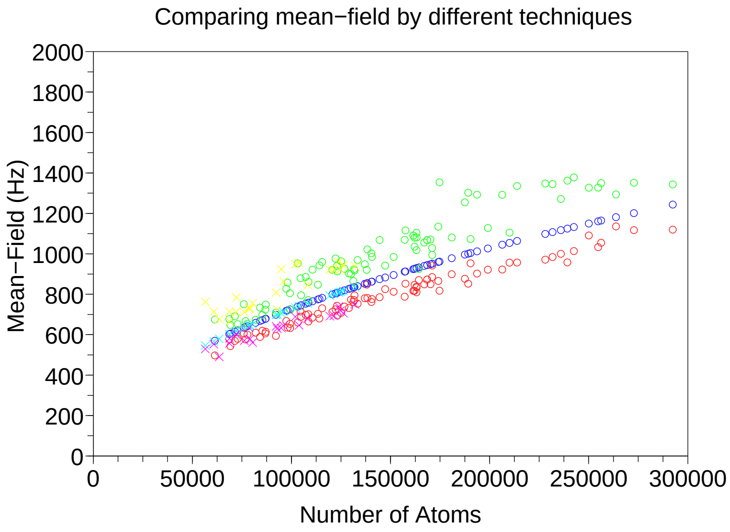

Figure C.7: Comparing the chemical potential obtained by different methods after correcting for resolution and smearing: The blue/cyan points, red/magenta points and green/yellow points are based on the number of atoms, the peak 2D column density and the TF width respectively. The cyan, yellow and magenta points were taken with a 10 μs long probe pulse, while the blue, red and green points were taken with a 15 μs long probe pulse.

barrier beam turned on is a direct measurement of the effect of the barrier. While one could, in principle, obtain the same from calculating the optical potential, given the dimensions of the beam, such a calculation is indirect and is highly dependent on our precise understanding of the beam propagation through the focusing optics. We start with a partial transfer image of the cloud (inset of figure C.9).

In the first round of calculations, I will ignore the effects due to the limited resolution of the imaging system. I will assume that the height of the barrier increases linearly with optical power in the beam. The calculation also assumes a local density mean field dominated (TF) approach, where the barrier height V_b is given by

$$V_b = \mu_0 - \mu_b, \tag{C.15}$$

where μ_0 is the chemical potential of the system and μ_b is the mean field at the

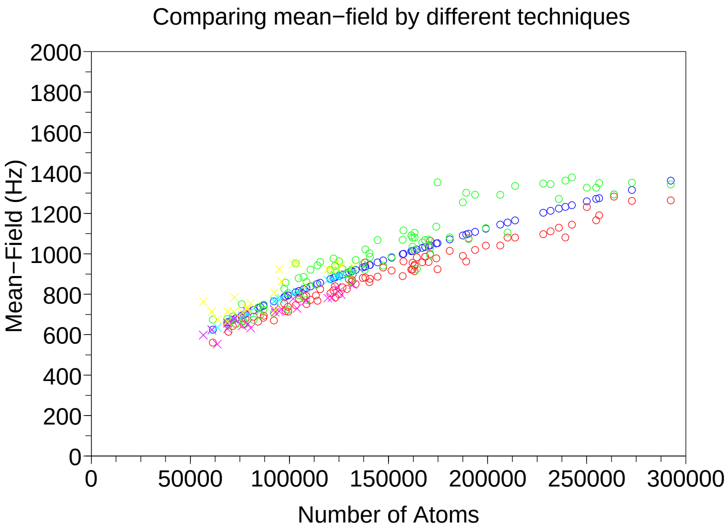

Figure C.8: Comparing the chemical potential obtained by different methods after the necessary corrections and calibrations: A different scattering cross-section was used. The blue/cyan points, red/magenta points and green/yellow points are based on the number of atoms, the peak 2D column density and the TF width respectively. The cyan, yellow and magenta points were taken with a 10 μs long probe pulse, while the blue, red and green points were taken with a 15 μs long probe pulse.

location of the barrier. While there are multiple ways of obtaining the chemical potential, I use the number of atoms (from equation (C.13)), since it is independent of imaging artifacts. While the expression assumes a uniform ring without a barrier, the effect of the barrier in decreasing the ring volume was found to be less than 4%, which is smaller than other uncertainties.

To obtain the local mean field at the location of the barrier, I perform 2D sectional fits to the column density of the BEC, assuming a ring 3D TF profile (equation (5.35)), to obtain the peak column density as a function of the azimuthal coordinate. By oversampling the azimuthal coordinate (256 overlapping sections of size 0.025 radians each), I can accurately obtain the density dip due to the effect of the barrier (figure C.9). While the fit to the radial width was found to be fluctuating (~ 20 %) due to the small number of sample points, the height of the fit was more

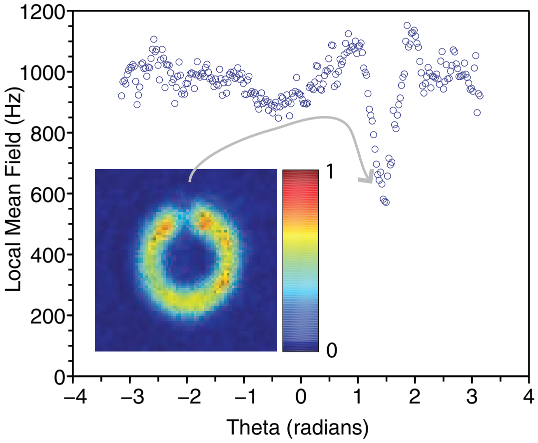

Figure C.9: Azimuthal mean field profile of cloud: By taking the difference between the chemical potential and the local mean field of the cloud at the barrier, the height of the barrier can be calculated. In this image, $N = 230 \times 10^3$, $\mu_0 = 1100$ Hz, $\mu_b = 570$ Hz, giving a barrier height, $V_b = 530$ Hz. The barrier beam power was 74 μW. The inset shows the partial transfer image of the cloud, with the location of the barrier indicated by the gray arrow.

consistent. The height of the fit was also found to be independent of the fitting potential (2D or 3D TF fits).

For simplicity, I assumed a simple 3D TF profile in calculating the local mean field from the peak column density (expression in equation (C.11)). For regions close to the barrier where the 3D TF profile is clearly not valid ($\mu_b < \hbar\omega_z$), I used the expression for the annular TF profile (from equation (5.31)), giving

$$\mu_b = \frac{g n_{2D,0}}{\sqrt{\pi\hbar/m\omega_z}}. \tag{C.16}$$

For the range of barrier heights and chemical potentials probed, the difference between the 3D TF and the radial TF fitting functions did not change the local mean field appreciably.

In figure C.9, an azimuthal mean field profile used to obtain a sample calibration data point of the barrier height is shown. Taking several such images, one can obtain a calibration for the effect of the barrier. We took several calibration images of varying atom number and barrier height (see figure C.10). For a typical barrier beam power, taking around 10 data points, the barrier height was found to have a standard deviation of around 30-50 Hz giving a standard deviation of the mean of around 10-15 Hz. The spread in points is believed to be due to shot-to-shot fluctuations in the trap potential and noise in the imaging process.

The *in situ* data also yielded some other interesting facts, which I am going to mention but not get too deep into.

1. Astigmatism in the ring trapping beam causes a sinusoidal (quadrupole) azimuthal variation of the trap (see figure 5.9c upper curve) of amplitude 100 Hz.

2. There is an overall tilt in the potential of the order of 50-100 Hz in the direction of propagation of the sheet beam, that varies from shot to shot. This is seen in figure C.10, in the variation of the barrier height at a fixed barrier beam power. This variation is comparable to the width of the critical region in measuring the critical chemical potential in section 7.4. Had the potential fluctuated less, it is possible that the width of the sigmoidal fit in figure 7.10 would have been smaller.

In figure C.10, I have fit a straight line to the measured barrier height vs beam power. The line had a slope of 6.4 ± 0.7 Hz/μW. Using this calibration, given an atom number and applied barrier beam power, one can obtain the local mean field at the barrier region. The alert reader may have noticed that the line has a non-zero intercept. This intercept arises from the azimuthal variation of the trapping potential that was ignored in the calculation of μ_0. The intercept is the height of the potential at the barrier region (in the absence of the barrier beam) with respect to the average potential zero around the annulus.

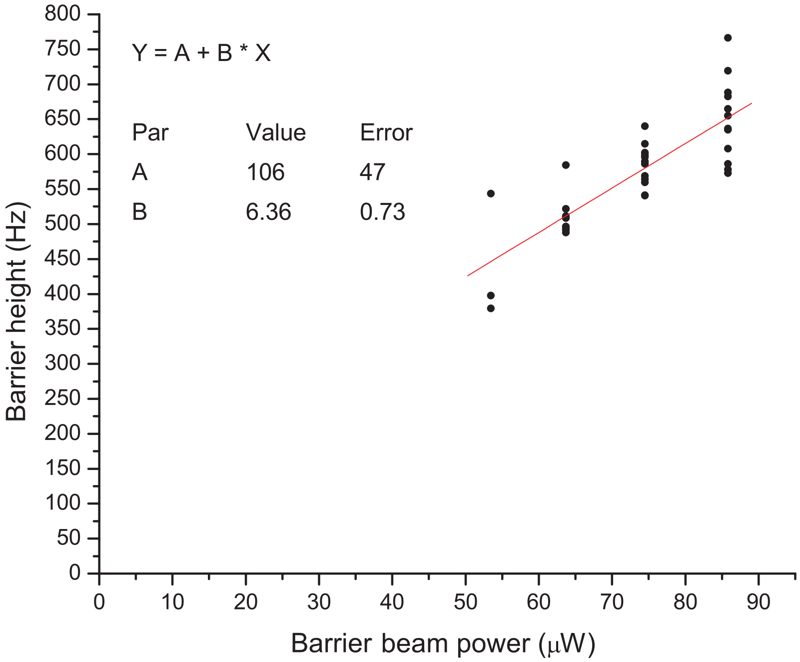

Figure C.10: Calibration of barrier beam: By plotting the depletion in the condensate mean field ($V_b = \mu_0 - \mu_b$) at the location of the barrier as a function of the barrier beam power, we obtain a linear calibration (red line) for the effect of the barrier, having a slope of 6.4 Hz/μW.

Bibliography

[1] M. Tinkham. *Introduction to superconductivity.* Dover Pubns, 2004.

[2] A. J. Leggett. Superfluidity. *Reviews of Modern Physics*, 71(2):S318–S323, 1999.

[3] H. K. Onnes. On the sudden rate at which the resistance of mercury disappears. *Akad. van Wetenschappen*, 14(113):818, 1911.

[4] D. J. Quinn and W. B. Ittner. Resistance in a Superconductor. *Journal of Applied Physics*, 33:748, 1962.

[5] C. Zhuang, C. Gu, D. X. Chen, and Z. Han. Persistent current of bi2223/ag closed coil in 77 k. *Applied Superconductivity, IEEE Transactions on*, 17(2): 3125–3128, 2007.

[6] S. N. Bose. Plancks gesetz und lichtquantenhypothese. *Zeitschrift fr Physik A Hadrons and Nuclei*, 26:178–181, 1924.

[7] A. Einstein. *Sitzungsber. K. Preuss. Akad. Wiss., Physics Math*, Kl. 261, 1924.

[8] A. Einstein. *Sitzungsber. K. Preuss. Akad. Wiss., Physics Math*, Kl. 3, 1925.

[9] P. Kapitza. Viscosity of liquid helium below the λ-point. *Nature*, 141(3558): 74, 1938.

[10] J. F. Allen and A. D. Misener. Flow of liquid helium II. *Nature*, 141(3558): 75, 1938.

[11] F. London. The-phenomenon of liquid helium and the Bose-Einstein degeneracy. *Nature, London*, 141:643–644, 1938.

[12] L. Tisza. Transport phenomena in helium II. *Nature*, 141(3577):913, 1938.

[13] L. Landau. Theory of the superfluidity of helium ii. *Physical Review*, 60(4): 356–358, 1941.

[14] V. Peshkov. Second sound in helium II. *J. Physics USSR*, 8:381, 1944.

[15] V. L. Ginzburg and Landau L. D. *Zh. Eksp. Teor. Fiz.*, 20:1064, 1950.

[16] N. N. Bogoliubov. On the theory of superfluidity. *J. Physics(USSR)*, 11(23): 4–2, 1947.

[17] O. Penrose and L. Onsager. Bose-einstein condensation and liquid helium. *Physical Review*, 104(3):576–584, 1956.

[18] H. W. Jackson. Reexamination of evidence for a bose-einstein condensate in superfluid ^{4}he. *Physical Review A*, 10(1):278–294, 1974.

[19] A. Griffin. *Excitations in a Bose-condensed liquid*. Cambridge Univ Pr, 1993. ISBN 0521432715.

[20] K. R. Atkins. *Liquid helium*. University Press, 1959.

[21] D. V. Osborne. The rotation of liquid helium II. *Proceedings of the Physical Society. Section A*, 63:909, 1950.

[22] H. E. Hall. The Angular Acceleration of Liquid Helium. II The Angular Acceleration of Liquid Helium. II (pp. 359-385). *Philosophical Transactions of the Royal Society of London. Series A, Mathematical and Physical Sciences*, 250:980, 1957.

[23] L. Onsager. Statistical hydrodynamics. *Il Nuovo Cimento (1943-1954)*, 6: 279–287, 1949.

[24] R. P. Feynman. Application of quantum mechanics to liquid helium. *Progress in Low Temperature Physics*, 1:17–53, 1955.

[25] W. F. Vinen. Detection of single quanta of circulation in rotating helium II. *Nature*, 181:1524–1525, 1958.

[26] W. F. Vinen. Vortex lines in liquid helium II. *Progress in Low Temperature Physics*, 3:1–57, 1961.

[27] W. A. Steyert, R. D. Taylor, and T. A. Kitchens. Direct measurements of multiple quantization in he ii. *Physical Review Letters*, 15(13):546–549, 1965.

[28] R. E. Packard and T. M. Sanders. Observations on single vortex lines in rotating superfluid helium. *Physical Review A*, 6(2):799–807, 1972.

[29] G. A. Williams and R. E. Packard. Photographs of quantized vortex lines in rotating He II. *Physical Review Letters*, 33(5):280–283, 1974.

[30] E. J. Yarmchuk and R. E. Packard. Photographic studies of quantized vortex lines. *Journal of Low Temperature Physics*, 46:479–515, 1982.

[31] F. Wagner. Does a persistent current exist in a superfluid helium film? *Journal of Low Temperature Physics*, 13(1):185–193, 1973.

[32] É. Varoquaux. Critical velocities in superfluids and the nucleation of vortices. *Comptes Rendus Physique*, 7(9-10):1101–1120, 2006.

[33] O. Avenel and E. Varoquaux. Observation of singly quantized dissipation events obeying the josephson frequency relation in the critical flow of superfluid ^4he through an aperture. *Physical Review Letters*, 55(24):2704–2707, 1985.

[34] A. Amar, Y. Sasaki, R. L. Lozes, J. C. Davis, and R. E. Packard. Quantized phase slippage in superfluid ^4he. *Physical Review Letters*, 68(17):2624–2627, 1992.

[35] E. Varoquaux and O. Avenel. Vortex nucleation in phase-slippage experiments in ultrapure superfluid ^4he below 0.5 k. *Physical Review B*, 68(5):054515, 2003.

[36] A. J. Leggett. A theoretical description of the new phases of liquid ^3he. *Reviews of Modern Physics*, 47(2):331–414, 1975.

[37] D. Vollhardt and P. Wölfle. *The superfluid phases of helium 3*. CRC, 1990.

[38] K. R. Atkins and I. Rudnick. Third Sound. *Progress in Low Temperature Physics*, 6:37–76, 1970.

[39] R. E. Packard and S. Vitale. Principles of superfluid-helium gyroscopes. *Physical Review B*, 46(6):3540–3549, 1992.

[40] O. Avenel, P. Hakonen, and E. Varoquaux. Detection of the rotation of the earth with a superfluid gyrometer. *Physical Review Letters*, 78(19):3602–3605, 1997.

[41] M. H. Anderson, J. R. Ensher, M. R. Matthews, C. E. Wieman, and E. A. Cornell. Observation of Bose-Einstein Condensation in a Dilute Atomic Vapor. *Science*, 269(5221):198–201, 1995.

[42] K. B. Davis, M. O. Mewes, M. R. Andrews, N. J. van Druten, D. S. Durfee, D. M. Kurn, and W. Ketterle. Bose-einstein condensation in a gas of sodium atoms. *Physical Review Letters*, 75:3969–3973, 1995.

[43] C. C. Bradley, C. A. Sackett, J. J. Tollett, and R. G. Hulet. Evidence of bose-einstein condensation in an atomic gas with attractive interactions. *Physical Review Letters*, 75(9):1687–1690, 1995.

[44] M. R. Matthews, B. P. Anderson, P. C. Haljan, D. S. Hall, C. E. Wieman, and E. A. Cornell. Vortices in a bose-einstein condensate. *Physical Review Letters*, 83(13):2498–2501, 1999.

[45] K. W. Madison, F. Chevy, W. Wohlleben, and J. Dalibard. Vortex formation in a stirred bose-einstein condensate. *Physical Review Letters*, 84(5):806–809, 2000.

[46] K. W. Madison, F. Chevy, W. Wohlleben, and J. Dalibard. Vortices in a stirred Bose-Einstein condensate. *Journal of modern optics*, 47(14):2715–2723, 2000.

[47] J. R. Abo-Shaeer, C. Raman, J. M. Vogels, and W. Ketterle. Observation of vortex lattices in Bose-Einstein condensates. *Science*, 292(5516):476, 2001.

[48] C. Raman, M. Köhl, R. Onofrio, D. S. Durfee, C. E. Kuklewicz, Z. Hadzibabic, and W. Ketterle. Evidence for a critical velocity in a Bose-Einstein condensed gas. *Physical Review Letters*, 83(13):2502–2505, 1999.

[49] R. Onofrio, C. Raman, J. M. Vogels, J. R. Abo-Shaeer, A. P. Chikkatur, and W. Ketterle. Observation of superfluid flow in a bose-einstein condensed gas. *Physical Review Letters*, 85(11):2228–2231, 2000.

[50] P. Engels and C. Atherton. Stationary and nonstationary fluid flow of a bose-einstein condensate through a penetrable barrier. *Physical Review Letters*, 99 (16):160405, 2007.

[51] T. W. Neely, E. C. Samson, A. S. Bradley, M. J. Davis, and B. P. Anderson. Observation of vortex dipoles in an oblate bose-einstein condensate. *Physical Review Letters*, 104(16):160401, 2010.

[52] C. Ryu, M. F. Andersen, P. Cladé, Vasant Natarajan, K. Helmerson, and W. D. Phillips. Observation of persistent flow of a bose-einstein condensate in a toroidal trap. *Physical Review Letters*, 99(26):260401, 2007.

[53] P. Cladé, C. Ryu, A. Ramanathan, K. Helmerson, and W. D. Phillips. Observation of a 2d bose gas: From thermal to quasicondensate to superfluid. *Physical Review Letters*, 102(17):170401, 2009.

[54] A. Ramanathan, K. C. Wright, S. R. Muniz, M. Zelan, W. T. Hill, C. J. Lobb, K. Helmerson, W. D. Phillips, and G. K. Campbell. Superflow in a toroidal Bose-Einstein condensate: an atom circuit with a tunable weak link. *Phys. Rev. Lett.*, 106(13):130401, 2011.

[55] A. Ramanathan, S. Muniz, K. Wright, W. D. Phillips, K. Helmerson, and G. Campbell. Partial transfer absorption imaging of ultracold atomic gases. *"Partial Transfer Absorption Imaging of ultracold atomic gases"*, In preparation.

[56] L. D. Landau and E. M. Lifshitz. *Statistical Physics: Course of Theoretical Physics, Vol. 5.* Pergamon, 1980.

[57] J. G. Daunt and R. S. Smith. The problem of liquid helium—some recent aspects. *Reviews of Modern Physics*, 26(2):172–236, 1954.

[58] I. M. Khalatnikov. *An introduction to the theory of superfluidity.* Westview Press, 2000.

[59] D. R. Tilley and J. Tilley. *Superfluidity and superconductivity.* CRC Pr I Llc, 1990.

[60] L. P. Pitaevskii and S. Stringari. *Bose-Einstein Condensation.* Oxford University Press, USA, 2003. ISBN 0198507194.

[61] E. A. Cornell, J. R. Ensher, and C. E. Wieman. Experiments in dilute atomic Bose-Einstein condensation. *Arxiv preprint cond-mat/9903109*, 1999.

[62] D. M. Stamper-Kurn. *Peeking and Poking at a new quantum fluid : Studies of gaseous Bose-Einstein condensates in magnetic and optical traps*. PhD thesis, Massachusetts Institute of Technology, 2000.

[63] F. Dalfovo, S. Giorgini, L. P. Pitaevskii, and S. Stringari. Theory of Bose-Einstein condensation in trapped gases. *Reviews of Modern Physics*, 71(3): 463–512, 1999.

[64] Vanderlei Bagnato, David E. Pritchard, and Daniel Kleppner. Bose-einstein condensation in an external potential. *Physical Review A*, 35(10):4354–4358, 1987.

[65] C. Pethick and H. Smith. *Bose-Einstein condensation in dilute gases*. Cambridge Univ Pr, 2002.

[66] J. Weiner, V. S. Bagnato, S. Zilio, and P. S. Julienne. Experiments and theory in cold and ultracold collisions. *Reviews of Modern Physics*, 71(1):1–85, 1999.

[67] P. G. Gennes. *Superconductivity of Metals and Alloys*. Advanced Book Program, Perseus Books, 1966.

[68] E. Gross. Structure of a quantized vortex in boson systems. *Il Nuovo Cimento (1955-1965)*, 20:454–477, 1961.

[69] E. P. Gross. Hydrodynamics of a superfluid condensate. *Journal of Mathematical Physics*, 4:195, 1963.

[70] L. P. Pitaevskii. Vortex lines in an imperfect Bose gas. *Sov. Physics JETP*, 13(2):451–454, 1961.

[71] J. J. Sakurai. *Modern Quantum Mechanics, revised edition*. Addison Wesley, 1993.

[72] L. H. Thomas. The calculation of atomic fields. In *Mathematical Proceedings of the Cambridge Philosophical Society*, volume 23, pages 542–548. Cambridge University Press, 1927.

[73] E. Fermi. Un metodo statistico per la determinazione di alcune priorieta dell'atome. *Rend. Accad. Naz. Lincei*, 6(602-607):32, 1927.

[74] W. I. Glaberson and R. J. Donnelly. Structure, Distributions and Dynamics of Vortices in Helium II*. *Progress in Low Temperature Physics*, 9:1–142, 1986.

[75] H. Lamb. *Hydrodynamics*. Cambridge Univ Pr, 1932.

[76] V. P. Peshkov. Critical Velocities and Vortices in Superfluid Helium. *Progress in Low Temperature Physics*, 4:1–32, 1964.

[77] M. Kozuma, L. Deng, E. W. Hagley, J. Wen, R. Lutwak, K. Helmerson, S. L. Rolston, and W. D. Phillips. Coherent splitting of bose-einstein condensed atoms with optically induced bragg diffraction. *Physical Review Letters*, 82 (5):871–875, 1999.

[78] M. O. Scully and M. S. Zubairy. *Quantum optics*. Cambridge University Press.

[79] H. J. Metcalf and P. van der Straten. *Laser cooling and trapping of neutral atoms*. Wiley Online Library.

[80] D. A. Steck. Quantum and atom optics, available online at. *http://atomoptics.uoregon.edu/d̃steck/teaching/quantum-optics*, 2007.

[81] V. Weisskopf and E. Wigner. Berechnung der natürlichen Linienbreite auf Grund der Diracschen Lichttheorie. *Zeitschrift für Physik A Hadrons and Nuclei*, 63(1):54–73, 1930.

[82] P. W. Milonni and M. L. Shih. Zero-point energy in early quantum theory. *American Journal of Physics*, 59:684, 1991.

[83] R. K. Shankar and K. P. Sinha. Photon-Induced Electron Pairing. *Physical Review B*, 7:4291–4293, 1973.

[84] J. D. Jackson. Classical Electrodynamics John Wiley & Sons. *Inc., New York*, 1962.

[85] T. W. Hänsch and A . L. Schawlow. Cooling of gases by laser radiation. *Optics Communications*, 13(1):68–69, 1975.

[86] D. Wineland and H. Dehmelt. Proposed 1014$\delta\nu/\nu$ laser fluorescence spectroscopy on Tl+ mono-ion oscillator. *Bulletin American Physics Society*, 20 (637):136, 1975.

[87] D. J. Wineland, R. E. Drullinger, and F. L. Walls. Radiation-pressure cooling of bound resonant absorbers. *Physical Review Letters*, 40(25):1639–1642, 1978.

[88] W. Neuhauser, M. Hohenstatt, P. Toschek, and H. Dehmelt. Optical-sideband cooling of visible atom cloud confined in parabolic well. *Physical Review Letters*, 41(4):233–236, 1978.

[89] C. Cohen-Tannoudji. Atomic motion in laser light in Fundamental Systems in Quantum Optics, edited by Dalibard J., Raimond J.-M. and Zinn-Justin J. 1992.

[90] J. Dalibard and C. Cohen-Tannoudji. Laser cooling below the Doppler limit by polarization gradients: simple theoretical models. *Journal of the Optical Society of America B*, 6(11):2023–2045, 1989.

[91] P. D. Lett, R. N. Watts, C. I. Westbrook, W. D. Phillips, P. L. Gould, and H. J. Metcalf. Observation of atoms laser cooled below the Doppler limit. *Physical Review Letters*, 61(2):169–172, 1988.

[92] P. D. Lett, W. D. Phillips, S. L. Rolston, C. E. Tanner, R. N. Watts, and C. I. Westbrook. Optical molasses. *Journal of the Optical Society of America B*, 6 (11):2084–2107, 1989.

[93] C. Salomon, J. Dalibard, W. D. Phillips, A. Clairon, and S. Guellati. Laser cooling of cesium atoms below 3 μK. *EPL (Europhysics Letters)*, 12:683, 1990.

[94] P. J. Ungar, D. S. Weiss, E. Riis, and S. Chu. Optical molasses and multilevel atoms: theory. *Journal of the Optical Society of America B*, 6(11):2058–2071, 1989.

[95] C. N. Cohen-Tannoudji. Nobel Lecture: Manipulating atoms with photons. *Reviews of Modern Physics*, 70(3):707–719, 1998.

[96] William D. Phillips. Nobel lecture: Laser cooling and trapping of neutral atoms. *Reviews of Modern Physics*, 70(3):721–741, 1998.

[97] L. I. Schiff. *Quantum mechanics 3rd ed.* McGraw-Hill, 1968.

[98] W. R. Johnson. *Atomic structure theory: lectures on atomic physics.* Springer Verlag, 2007.

[99] R. S. Krishnan. Fine Structure of the Rayleigh Line in Amorphous Substances. *Nature*, 165(4206):933–934, 1950.

[100] M. E. Weeks. The discovery of the elements. XII. Other elements isolated with the aid of potassium and sodium: Beryllium, boron, silicon, and aluminum. *Journal of Chemical Education*, 9:1386, 1932.

[101] E. Tiesinga, C. J. Williams, P. S. Julienne, K. M. Jones, P. D. Lett, and D. William. A spectroscopic determination of scattering lengths for sodium atom collisions. *Bose-Einstein Condensation: An Introduction*, 101(4):505, 1996.

[102] D. S. Durfee. *Dynamic properties of dilute Bose-Einstein condensates.* PhD thesis, Massachusetts Institute of Technology, 1999.

[103] A. P. Chikkatur. *Colliding and Moving Bose-Einstein Condensates: Studies of superfluidity and optical tweezers for condensate transport.* PhD thesis, Massachusetts Institute of Technology, 2002.

[104] J. R. Ensher. *The first experiments with Bose-Einstein condensation of 87Rb.* PhD thesis, University of Colorado, 1998.

[105] T. Weber. *Bose-Einstein Condensation of Optically Trapped Cesium–.* PhD thesis, Universität Innsbruck, 2003.

[106] K. M. R. Van Der Stam, E. D. Van Ooijen, R. Meppelink, J. M. Vogels, and P. Van der Straten. Large atom number Bose-Einstein condensate of sodium. *Reviews of Scientific Instruments*, 78:013102, 2007.

[107] E. W. Streed, A. P. Chikkatur, T. L. Gustavson, M. Boyd, Y. Torii, D. Schneble, G. K. Campbell, D. E. Pritchard, and W. Ketterle. Large atom number Bose-Einstein condensate machines. *Reviews of Scientific Instruments*, 77:023106, 2006.

[108] Y. J. Lin, A. R. Perry, R. L. Compton, I. B. Spielman, and J. V. Porto. Rapid production of ^{87}Rb Bose-Einstein condensates in a combined magnetic and optical potential. *Physical Review A*, 79(6):63631, 2009.

[109] W. Ketterle, D. S. Durfee, and D. M. Stamper-Kurn. Making, probing and understanding Bose-Einstein condensates. In *Proceedings of the International School of Physics-Enrico Fermi*, page 67, 1999.

[110] Wolfgang Petrich, Michael H. Anderson, Jason R. Ensher, and Eric A. Cornell. Stable, tightly confining magnetic trap for evaporative cooling of neutral atoms. *Physical Review Letters*, 74(17):3352–3355, 1995.

[111] L. G. Gouy. Sur une propriété nouvelle des ondes lumineuses Compt. *Comptes Rendus de l'Académie des Sciences, Paris*, 110:1251–3, 1890.

[112] L. Mandel and E. Wolf. *Optical coherence and quantum optics*. Cambridge Univ Pr, 1995.

[113] A. Siegman. *Lasers*. University Science Books, 1986.

[114] A. K. Ghatak and K. Thyagarajan. *Optical electronics*. Cambridge Univ Pr, 1989. ISBN 0521314089.

[115] F. Pampaloni and J. Enderlein. Gaussian, Hermite-Gaussian, and Laguerre-Gaussian beams: A primer. *Arxiv preprint physics/0410021*, 2004.

[116] L. Allen, M. W. Beijersbergen, R. J. C. Spreeuw, and J. P. Woerdman. Orbital angular momentum of light and the transformation of laguerre-gaussian laser modes. *Physical Review A*, 45(11):8185–8189, 1992.

[117] M. F. Andersen, C. Ryu, Pierre Cladé, Vasant Natarajan, A. Vaziri, K. Helmerson, and W. D. Phillips. Quantized rotation of atoms from photons with orbital angular momentum. *Physical Review Letters*, 97(17):170406, 2006.

[118] S. Fürhapter, A. Jesacher, S. Bernet, and M. Ritsch-Marte. Spiral interferometry. *Optics Letters*, 30(15):1953–1955, 2005.

[119] G. Foo, D. M. Palacios, and G. A. Swartzlander Jr. Optical vortex coronagraph. *Optics Letters*, 30(24):3308–3310, 2005.

[120] H. He, M. E. J. Friese, N. R. Heckenberg, and H. Rubinsztein-Dunlop. Direct observation of transfer of angular momentum to absorptive particles from a laser beam with a phase singularity. *Physical Review Letters*, 75(5):826–829, 1995.

[121] Jennifer E. Curtis and David G. Grier. Structure of optical vortices. *Physical Review Letters*, 90(13):133901, 2003.

[122] P. Török and P. Munro. The use of Gauss-Laguerre vector beams in STED microscopy. *Optics Express*, 12(15):3605–3617, 2004.

[123] K. I. Willig, S. O. Rizzoli, V. Westphal, R. Jahn, and S. W. Hell. STED microscopy reveals that synaptotagmin remains clustered after synaptic vesicle exocytosis. *Nature*, 440(7086):935–939, 2006.

[124] G. Gibson, J. Courtial, M. J. Padgett, M. Vasnetsov, V. Pasko, S. M. Barnett, and S. Franke-Arnold. Free-space information transfer using light beams carrying orbital angular momentum. *Nature*, 412:313, 2001.

[125] A. Mair, A. Vaziri, G. Weihs, and A. Zeilinger. Entanglement of the orbital angular momentum states of photons. *Nature*, 412(6844):313–316, 2001.

[126] K. C. Wright, L. S. Leslie, and N. P. Bigelow. Optical control of the internal and external angular momentum of a bose-einstein condensate. *Physical Review A*, 77(4):041601, 2008.

[127] K. T. Gahagan and G. A. Swartzlander, Jr. Optical vortex trapping of particles. *Optics Letters*, 21(11):827–829, 1996.

[128] Y. Song, D. Milam, and W. T. Hill III. Long, narrow all-light atom guide. *Optics Letters*, 24(24):1805–1807, 1999.

[129] J. Arlt, T. Hitomi, and K. Dholakia. Atom guiding along Laguerre-Gaussian and Bessel light beams. *Applied Physics B: Lasers and Optics*, 71(4):549–554, 2000.

[130] J. Arlt, K. Dholakia, J. Soneson, and E. M. Wright. Optical dipole traps and atomic waveguides based on Bessel light beams. *Physical Review A*, 63(6): 63602, 2001.

[131] Takahiro Kuga, Yoshio Torii, Noritsugu Shiokawa, Takuya Hirano, Yukiko Shimizu, and Hiroyuki Sasada. Novel optical trap of atoms with a doughnut beam. *Physical Review Letters*, 78(25):4713–4716, 1997.

[132] D. P. Rhodes, D. M. Gherardi, J. Livesey, D. Mcgloin, H. Melville, T. Freegarde, and K. Dholakia. Atom guiding along high order Laguerre-Gaussian light beams formed by spatial light modulation. *Journal of modern optics*, 53 (4):547–556, 2006.

[133] K. Bongs, S. Burger, S. Dettmer, and K. Sengstock. Manipulation of Bose-Einstein condensates by dipole potentials. *Journal of Modern Optics, 47*, 14 (15):2697–2713, 2000.

[134] M. Uchida and A. Tonomura. Generation of electron beams carrying orbital angular momentum. *Nature*, 464(7289):737–739, 2010.

[135] B. J. McMorran, A. Agrawal, I. M. Anderson, A. A. Herzing, H. J. Lezec, J. J. McClelland, and J. Unguris. Electron Vortex Beams with High Quanta of Orbital Angular Momentum. *Science*, 331(6014):192, 2011.

[136] M. R. Andrews, M.-O. Mewes, N. J. van Druten, D. S. Durfee, D. M. Kurn, and W. Ketterle. Direct, Nondestructive Observation of a Bose Condensate. *Science*, 273(5271):84–87, 1996.

[137] C. C. Bradley, C. A. Sackett, and R. G. Hulet. Bose-einstein condensation of lithium: Observation of limited condensate number. *Physical Review Letters*, 78(6):985–989, 1997.

[138] S. Kadlecek, J. Sebby, R. Newell, and T. G. Walker. Nondestructive spatial heterodyne imaging of cold atoms. *Optics Letters*, 26(3):137–139, 2001.

[139] L. D. Turner, K. F. E. M. Domen, and R. E. Scholten. Diffraction-contrast imaging of cold atoms. *Physical Review A*, 72(3):031403, 2005.

[140] J. E. Lye, J. J. Hope, and J. D. Close. Nondestructive dynamic detectors for bose-einstein condensates. *Physical Review A*, 67(4):043609, 2003.

[141] J. L. Roberts, N. R. Claussen, S. L. Cornish, and C. E. Wieman. Magnetic field dependence of ultracold inelastic collisions near a feshbach resonance. *Physical Review Letters*, 85(4):728–731, 2000.

[142] J. H. Huckans, J. R. Williams, E. L. Hazlett, R. W. Stites, and K. M. O'Hara. Three-body recombination in a three-state fermi gas with widely tunable interactions. *Physical Review Letters*, 102(16):165302, 2009.

[143] Tino Weber, Jens Herbig, Michael Mark, Hanns-Christoph Nägerl, and Rudolf Grimm. Three-body recombination at large scattering lengths in an ultracold atomic gas. *Physical Review Letters*, 91(12):123201, 2003.

[144] T. Kraemer, M. Mark, P. Waldburger, J. G. Danzl, C. Chin, B. Engeser, A. D. Lange, K. Pilch, A. Jaakkola, H.-C. Nägerl, and R. Grimm. Evidence for Efimov quantum states in an ultracold gas of caesium atoms. *Nature*, 440 (7082):315–318, 2006.

[145] M. Zaccanti, B. Deissler, C. DErrico, M. Fattori, M. Jona-Lasinio, S. Müller, G. Roati, M. Inguscio, and G. Modugno. Observation of an Efimov spectrum in an atomic system. *Nature Physics*, 5(8):586–591, 2009.

[146] Peter Krüger, Zoran Hadzibabic, and Jean Dalibard. Critical point of an interacting two-dimensional atomic bose gas. *Physical Review Letters*, 99(4): 040402, 2007.

[147] K Henderson, C Ryu, C MacCormick, and M G Boshier. Experimental demonstration of painting arbitrary and dynamic potentials for bose-einstein condensates. *New Journal of Physics*, 11(4):043030, 2009.

[148] D. McKay, M. White, M. Pasienski, and B. DeMarco. Phase-slip-induced dissipation in an atomic bose-hubbard system. *Nature*, 453(7191):76, 2008.

[149] G. Reinaudi, T. Lahaye, Z. Wang, and D. Guéry-Odelin. Strong saturation absorption imaging of dense clouds of ultracold atoms. *Optics Letters*, 32(21): 3143–3145, 2007.

[150] K. M. Mertes, J. W. Merrill, R. Carretero-González, D. J. Frantzeskakis, P. G. Kevrekidis, and D. S. Hall. Nonequilibrium dynamics and superfluid ring excitations in binary bose-einstein condensates. *Physical Review Letters*, 99 (19):190402, 2007.

[151] D. V. Freilich, D. M. Bianchi, A. M. Kaufman, T. K. Langin, and D. S. Hall. Real-Time Dynamics of Single Vortex Lines and Vortex Dipoles in a Bose-Einstein Condensate. *Science*, 329(5996):1182–1185, 2010.

[152] M. Gehm. Properties of Lithium. 2003.

[153] C. J. Sansonetti, B. Richou, R. Engleman Jr, and L. J. Radziemski. Measurements of the resonance lines of ^{6}Li and ^{7}Li by Doppler-free frequency-modulation spectroscopy. *Physical Review A*, 52(4):2682–2688, 1995.

[154] T. G. Tiecke. Properties of Potassium. 2010.

[155] C. N. Weiler, T. W. Neely, D. R. Scherer, A. S. Bradley, M. J. Davis, and B. P. Anderson. Spontaneous vortices in the formation of Bose–Einstein condensates. *Nature*, 455(7215):948–951, 2008.

[156] D. A. Steck. Sodium D line data. *Report, Los Alamos National Laboratory, Los Alamos*, 2000.

[157] L. D. Turner. *Holographic Imaging of Cold Atoms*. PhD thesis, University of Melbourne, School of Physics, 2004.

[158] B. P. Anderson, P. C. Haljan, C. E. Wieman, and E. A. Cornell. Vortex precession in Bose-Einstein condensates: Observations with filled and empty cores. *Physical Review Letters*, 85(14):2857–2860, 2000.

[159] A. D. Cronin, J. Schmiedmayer, and D. E. Pritchard. Optics and interferometry with atoms and molecules. *Reviews of Modern Physics*, 81(3):1051–1129, 2009.

[160] A. Peters, K. Y. Chung, and S. Chu. High-precision gravity measurements using atom interferometry. *Metrologia*, 38:25, 2001.

[161] D. S. Weiss, B. C. Young, and S. Chu. Precision measurement of the photon recoil of an atom using atomic interferometry. *Physical Review Letters*, 70 (18):2706–2709, 1993.

[162] D. S. Weiss, B. C. Young, and S. Chu. Precision measurement of $\hbar$/m Cs based on photon recoil using laser-cooled atoms and atomic interferometry. *Applied Physics B: Lasers and Optics*, 59(3):217–256, 1994.

[163] A. Wicht, J. M. Hensley, E. Sarajlic, and S. Chu. A preliminary measurement of the fine structure constant based on atom interferometry. *Physica Scripta*, 2002:82, 2002.

[164] R. Battesti, P. Cladé, S. Guellati-Khélifa, C. Schwob, B. Grémaud, F. Nez, L. Julien, and F. Biraben. Bloch oscillations of ultracold atoms: A tool for a metrological determination of h/m$_{Rb}$. *Physical Review Letters*, 92(25):253001, 2004.

[165] P. Cladé, E. De Mirandes, M. Cadoret, S. Guellati-Khélifa, C. Schwob, F. Nez, L. Julien, and F. Biraben. Determination of the fine structure constant based on bloch oscillations of ultracold atoms in a vertical optical lattice. *Physical Review Letters*, 96(3):33001, 2006.

[166] J. B. Fixler, G. T. Foster, J. M. McGuirk, and M. A. Kasevich. Atom interferometer measurement of the Newtonian constant of gravity. *Science*, 315 (5808):74, 2007.

[167] A. Bertoldi, G. Lamporesi, L. Cacciapuoti, M. De Angelis, M. Fattori, T. Petelski, A. Peters, M. Prevedelli, J. Stuhler, and G. M. Tino. Atom interferometry gravity-gradiometer for the determination of the Newtonian gravitational constant G. *The European Physical Journal D-Atomic, Molecular, Optical and Plasma Physics*, 40(2):271–279, 2006.

[168] G. Lamporesi, A. Bertoldi, L. Cacciapuoti, M. Prevedelli, and G. M. Tino. Determination of the Newtonian gravitational constant using atom interferometry. *Physical Review Letters*, 100(5):50801, 2008.

[169] M. G. Sagnac and M. E. Bouty. "l'éther lumineux démontré par l'effet du vent relatif d'éther dans un interféromètre en rotation uniforme" and "sur la preuve de la réalite de l'éther lumineux par l'expérience de l'intérferographe tournant". *Comptes Rendus Acad. Scienc*, pages 708–710, 1410–1413.

[170] A. Lenef, T. D. Hammond, E. T. Smith, M. S. Chapman, R. A. Rubenstein, and D. E. Pritchard. Rotation sensing with an atom interferometer. *Physical Review Letters*, 78(5):760–763, 1997.

[171] T. L. Gustavson, P. Bouyer, and M. A. Kasevich. Precision rotation measurements with an atom interferometer gyroscope. *Physical Review Letters*, 78(11):2046–2049, 1997.

[172] T. L. Gustavson, A. Landragin, and M. A. Kasevich. Rotation sensing with a dual atom-interferometer Sagnac gyroscope. *Classical and Quantum Gravity*, 17:2385, 2000.

[173] B. Canuel, F. Leduc, D. Holleville, A. Gauguet, J. Fils, A. Virdis, A. Clairon, N. Dimarcq, C. J. Bordé, A. Landragin, and P. Bouyer. Six-axis inertial sensor using cold-atom interferometry. *Physical Review Letters*, 97(1):10402, 2006.

[174] T. Müller, M. Gilowski, M. Zaiser, P. Berg, C. Schubert, T. Wendrich, W. Ertmer, and E. M. Rasel. A compact dual atom interferometer gyroscope based on laser-cooled rubidium. *The European Physical Journal D*, 53(3):273–281, 2009.

[175] Y. J. Wang, D. Z. Anderson, V. M. Bright, E. A. Cornell, Q. Diot, T. Kishimoto, M. Prentiss, R. A. Saravanan, S. R. Segal, and S. Wu. Atom Michelson interferometer on a chip using a Bose-Einstein condensate. *Physical Review Letters*, 94(9):90405, 2005.

[176] S. Wu, E. Su, and M. Prentiss. Demonstration of an area-enclosing guided-atom interferometer for rotation sensing. *Physical Review Letters*, 99(17): 173201, 2007.

[177] O. Garcia, B. Deissler, KJ Hughes, J. M. Reeves, and C. A. Sackett. Bose-Einstein-condensate interferometer with macroscopic arm separation. *Physical Review A*, 74(3):31601, 2006.

[178] P. J. Martin, B. G. Oldaker, A. H. Miklich, and D. E. Pritchard. Bragg scattering of atoms from a standing light wave. *Physical Review Letters*, 60 (6):515–518, 1988.

[179] K. L. Moore. *Ultracold atoms, circular waveguides, and cavity QED with millimeter-scale electromagnetic traps.* PhD thesis, University of California, 2007.

[180] J. Clarke and A. I. Braginski. *The SQUID handbook*, volume 1. Wiley-Vch, 2006. ISBN 3527402292.

[181] R. W. Simmonds, A. Marchenkov, E. Hoskinson, J. C. Davis, and R. E. Packard. Quantum interference of superfluid 3He. *Nature*, 412(6842):55–58, 2001.

[182] E. Hoskinson, Y. Sato, and R. Packard. Superfluid ^{4}He interferometer operating near 2K. *Physical Review B*, 74(10):100509, 2006.

[183] N. J. Van Druten and W. Ketterle. Two-step condensation of the ideal Bose gas in highly anisotropic traps. *Physical Review Letters*, 79(4):549–552, 1997.

[184] D. S. Petrov, G. V. Shlyapnikov, and J. T. M. Walraven. Phase-fluctuating 3d Bose-Einstein condensates in elongated traps. *Physical Review Letters*, 87 (5):50404, 2001.

[185] V. Dunjko, V. Lorent, and M. Olshanii. Bosons in cigar-shaped traps: Thomas-Fermi regime, Tonks-Girardeau regime, and in between. *Physical Review Letters*, 86(24):5413–5416, 2001.

[186] F. Gerbier, J. H. Thywissen, S. Richard, M. Hugbart, P. Bouyer, and A. Aspect. Momentum distribution and correlation function of quasicondensates in elongated traps. *Physical Review A*, 67(5):51602, 2003.

[187] S. Dettmer, D. Hellweg, P. Ryytty, J. J. Arlt, W. Ertmer, K. Sengstock, D. S. Petrov, G. V. Shlyapnikov, H. Kreutzmann, L. Santos, and M. Lewenstein. Observation of phase fluctuations in elongated Bose-Einstein condensates. *Physical Review Letters*, 87(16):160406, 2001.

[188] D. Hellweg, L. Cacciapuoti, M. Kottke, T. Schulte, K. Sengstock, W. Ertmer, and J. J. Arlt. Measurement of the spatial correlation function of phase fluctuating Bose-Einstein condensates. *Physical Review Letters*, 91(1):10406, 2003.

[189] M. Hugbart, J. A. Retter, F. Gerbier, A. F. Varón, S. Richard, JH Thywissen, D. Clément, P. Bouyer, and A. Aspect. Coherence length of an elongated condensate. *The European Physical Journal D-Atomic, Molecular, Optical and Plasma Physics*, 35(1):155–163, 2005.

[190] S. Richard, F. Gerbier, J. H. Thywissen, M. Hugbart, P. Bouyer, and A. Aspect. Momentum spectroscopy of 1D phase fluctuations in Bose-Einstein condensates. *Physical Review Letters*, 91(1):10405, 2003.

[191] U. Al Khawaja, N. P. Proukakis, J. O. Andersen, M. W. J. Romans, and H. T. C. Stoof. Dimensional and temperature crossover in trapped Bose gases. *Physical Review A*, 68(4):43603, 2003.

[192] F. Gerbier. Quasi-1D Bose-Einstein condensates in the dimensional crossover regime. *EPL (Europhysics Letters)*, 66:771, 2004.

[193] L. Mathey, A. Ramanathan, K. C. Wright, S. R. Muniz, W. D. Phillips, and Charles W. Clark. Phase fluctuations in anisotropic bose-einstein condensates: From cigars to rings. *Physical Review A*, 82(3):033607, 2010.

[194] F. M. H. Crompvoets, H. L. Bethlem, R. T. Jongma, and G. Meijer. A prototype storage ring for neutral molecules. *Nature*, 411(6834):174–176, 2001.

[195] J. A. Sauer, M. D. Barrett, and M. S. Chapman. Storage ring for neutral atoms. *Physical Review Letters*, 87(27):270401, 2001.

[196] S. Wu, W. Rooijakkers, P. Striehl, and M. Prentiss. Bidirectional propagation of cold atoms in a stadium-shaped magnetic guide. *Physical Review A*, 70(1): 13409, 2004.

[197] S. Gupta, K. W. Murch, K. L. Moore, TP Purdy, and D. M. Stamper-Kurn. Bose-Einstein condensation in a circular waveguide. *Physical Review Letters*, 95(14):143201, 2005.

[198] A. S. Arnold, C. S. Garvie, and E. Riis. Large magnetic storage ring for Bose-Einstein condensates. *Physical Review A*, 73(4):41606, 2006.

[199] S. E. Olson, M. L. Terraciano, M. Bashkansky, and F. K. Fatemi. Cold-atom confinement in an all-optical dark ring trap. *Physical Review A*, 76(6):61404, 2007.

[200] Luigi Amico, Andreas Osterloh, and Francesco Cataliotti. Quantum many particle systems in ring-shaped optical lattices. *Physical Review Letters*, 95 (6):063201, 2005.

[201] E. Courtade, O. Houde, J. F. Clément, P. Verkerk, and D. Hennequin. Dark optical lattice of ring traps for cold atoms. *Physical Review A*, 74(3):31403, 2006.

[202] A. R. Carter, M. Babiker, M. Al-Amri, and D. L. Andrews. Generation of microscale current loops, atom rings, and cubic clusters using twisted optical molasses. *Physical Review A*, 73(2):021401, 2006.

[203] Asa Hopkins, Benjamin Lev, and Hideo Mabuchi. Proposed magnetoelectrostatic ring trap for neutral atoms. *Physical Review A*, 70(5):053616, 2004.

[204] T. Fernholz, R. Gerritsma, P. Krüger, and R. J. C. Spreeuw. Dynamically controlled toroidal and ring-shaped magnetic traps. *Physical Review A*, 75(6): 63406, 2007.

[205] I. Lesanovsky and W. von Klitzing. Time-averaged adiabatic potentials: versatile matter-wave guides and atom traps. *Physical Review Letters*, 99(8): 83001, 2007.

[206] W. H. Heathcote, E. Nugent, B. T. Sheard, and C. J. Foot. A ring trap for ultracold atoms in an RF-dressed state. *New Journal of Physics*, 10:043012, 2008.

[207] B. E. Sherlock, M. Gildemeister, E. Owen, E. Nugent, and C. J. Foot. Time-averaged adiabatic ring potential for ultracold atoms. *Arxiv preprint arXiv:1102.2895*, 2011.

[208] C. N. Weiler, T. W. Neely, D. R. Scherer, A. S. Bradley, M. J. Davis, and B. P. Anderson. Spontaneous vortices in the formation of Bose–Einstein condensates. *Nature*, 455(7215):948–951, 2008.

[209] H. J. Miesner and W. Ketterle. Bose-Einstein condensation in dilute atomic gases. *Solid State Communications*, 107(11):629–637, 1998.

[210] S. R. Muniz and C Raman. Arbitrary shaped bose-einstein condensates. *Unpublished*, 2007.

[211] R. Grimm, M. Weidemüller, and Y. B. Ovchinnikov. Optical dipole traps for neutral atoms. *Advances in atomic, molecular, and optical physics*, 42:95–170, 2000. ISSN 1049-250X.

[212] Y. Castin and R. Dum. Bose-Einstein condensates in time dependent traps. *Physical Review Letters*, 77(27):5315–5319, 1996.

[213] D. S. Jin, J. R. Ensher, M. R. Matthews, C. E. Wieman, and E. A. Cornell. Collective excitations of a Bose-Einstein condensate in a dilute gas. *Physical Review Letters*, 77(3):420–423, 1996.

[214] T. Kimura. Breathing modes of Bose-Einstein condensates in highly asymmetric traps. *Physical Review A*, 66(1):013608, 2002.

[215] S. Stringari. Dynamics of bose-einstein condensed gases in highly deformed traps. *Physical Review A*, 58(3):2385–2388, 1998.

[216] J. E. Williams and M. J. Holland. Preparing topological states of a Bose-Einstein condensate. *Nature*, 401(6753):568–572, 1999.

[217] P. C. Haljan, I. Coddington, P. Engels, and E. A. Cornell. Driving bose-einstein-condensate vorticity with a rotating normal cloud. *Physical Review Letters*, 87(21):210403, 2001.

[218] P. Engels, I. Coddington, PC Haljan, V. Schweikhard, and E. A. Cornell. Observation of long-lived vortex aggregates in rapidly rotating Bose-Einstein condensates. *Physical Review Letters*, 90(17):170405, 2003.

[219] V. Schweikhard, I. Coddington, P. Engels, S. Tung, and E. A. Cornell. Vortex-lattice dynamics in rotating spinor Bose-Einstein condensates. *Physical Review Letters*, 93(21):210403, 2004.

[220] V. Schweikhard, I. Coddington, P. Engels, V. P. Mogendorff, and E. A. Cornell. Rapidly rotating Bose-Einstein condensates in and near the lowest Landau level. *Physical Review Letters*, 92(4):40404, 2004.

[221] P. Rosenbusch, D. S. Petrov, S. Sinha, F. Chevy, V. Bretin, Y. Castin, G. Shlyapnikov, and J. Dalibard. Critical rotation of a harmonically trapped Bose gas. *Physical Review Letters*, 88(25):250403, 2002.

[222] E. Hodby, G. Hechenblaikner, S. A. Hopkins, O. M. Marago, and C. J. Foot. Vortex nucleation in Bose-Einstein condensates in an oblate, purely magnetic potential. *Physical Review Letters*, 88(1):10405, 2001.

[223] S. R. Muniz, D. S. Naik, and C. Raman. Bragg spectroscopy of vortex lattices in Bose-Einstein condensates. *Physical Review A*, 73(4):041605, 2006.

[224] J. Brand and W. P. Reinhardt. Generating ring currents, solitons and svortices by stirring a Bose-Einstein condensate in a toroidal trap. *Journal of Physics B: Atomic, Molecular and Optical Physics*, 34:L113, 2001.

[225] Z. Dutton, M. Budde, C. Slowe, and L. V. Hau. Observation of quantum shock waves created with ultra-compressed slow light pulses in a Bose-Einstein condensate. *Science*, 293(5530):663, 2001.

[226] S. Inouye, S. Gupta, T. Rosenband, A. P. Chikkatur, A. Görlitz, T. L. Gustavson, A. E. Leanhardt, D. E. Pritchard, and W. Ketterle. Observation of vortex phase singularities in bose-einstein condensates. *Physical Review Letters*, 87(8):080402, 2001.

[227] E. A. L. Henn, J. A. Seman, E. R. F. Ramos, M. Caracanhas, P. Castilho, E. P. Olímpio, G. Roati, D. V. Magalhães, K. M. F. Magalhães, and V. S. Bagnato. Observation of vortex formation in an oscillating trapped bose-einstein condensate. *Physical Review A*, 79(4):043618, 2009.

[228] Tomoya Isoshima, Mikio Nakahara, Tetsuo Ohmi, and Kazushige Machida. Creation of a persistent current and vortex in a bose-einstein condensate of alkali-metal atoms. *Physical Review A*, 61(6):063610, 2000.

[229] Daisuke Akamatsu and Mikio Kozuma. Coherent transfer of orbital angular momentum from an atomic system to a light field. *Physical Review A*, 67(2): 023803, 2003.

[230] A. E. Leanhardt, A. Görlitz, A. P. Chikkatur, D. Kielpinski, Y. Shin, D. E. Pritchard, and W. Ketterle. Imprinting vortices in a bose-einstein condensate using topological phases. *Physical Review Letters*, 89(19):190403, 2002.

[231] Z. F. Xu, P. Zhang, C. Raman, and L. You. Continuous vortex pumping into a spinor condensate with magnetic fields. *Physical Review A*, 78(4):043606, 2008.

[232] Mikko Möttönen, Ville Pietilä, and Sami M. M. Virtanen. Vortex pump for dilute bose-einstein condensates. *Physical Review Letters*, 99(25):250406, 2007.

[233] T. Kuwamoto, H. Usuda, T. Satoshi, and T. Hirano. Dynamics of Quadruply Quantized Vortices in 87Rb Bose–Einstein Condensates Confined in Magnetic and Optical Traps. *Journal of the Physical Society of Japan*, 79(3):034004, 2010.

[234] Y. J. Lin, R. L. Compton, K. Jiménez-García, J. V. Porto, and I. B. Spielman. Synthetic magnetic fields for ultracold neutral atoms. *Nature*, 462(7273):628–632, 2009.

[235] D. R. Scherer, C. N. Weiler, T. W. Neely, and B. P. Anderson. Vortex formation by merging of multiple trapped Bose-Einstein condensates. *Physical Review Letters*, 98(11):110402, 2007.

[236] V. Schweikhard, S. Tung, and E. A. Cornell. Vortex proliferation in the Berezinskii-Kosterlitz-Thouless regime on a two-dimensional lattice of Bose-Einstein condensates. *Physical Review Letters*, 99(3):30401, 2007.

[237] K. C. Wright, L. S. Leslie, A. Hansen, and N. P. Bigelow. Sculpting the Vortex State of a Spinor BEC. *Physical Review Letters*, 102(3):30405, 2009.

[238] C. V. Raman and K. S. Krishnan. A new type of secondary radiation. *Nature*, 121(3048):501–502, 1928.

[239] R. S. Krishnan and R. K. Shankar. Raman effect: History of the discovery. *Journal of Raman Spectroscopy*, 10(1):1–8, 1981.

[240] V. B. Berestetskii, E. M. Lifshitz, and L. P. Pitaevskii. *Quantum electrodynamics*. Butterworth-Heinemann, 1982.

[241] L. Allen, M. W. Beijersbergen, R. J. C. Spreeuw, and J. P. Woerdman. Orbital angular momentum of light and the transformation of laguerre-gaussian laser modes. *Physical Review A*, 45(11):8185–8189, 1992.

[242] C. J. Myatt, E. A. Burt, R. W. Ghrist, E. A. Cornell, and C. E. Wieman. Production of two overlapping Bose-Einstein condensates by sympathetic cooling. *Physical Review Letters*, 78(4):586–589, 1997.

[243] A. Bezryadin, C. N. Lau, and M. Tinkham. Quantum suppression of superconductivity in ultrathin nanowires. *Nature*, 404(6781):971–974, 2000.

[244] IM Pop, I. Protopopov, F. Lecocq, Z. Peng, B. Pannetier, O. Buisson, and W. Guichard. Measurement of the effect of quantum phase slips in a Josephson junction chain. *Nature Physics*, 2010.

[245] V. N. Popov. Functional integrals in quantum field theory and statistical physics. 1983.

[246] V. L. Berezinskii. *Soviet Physics JETP*, 34:610, 1972.

[247] J. M. Kosterlitz and D. J. Thouless. Ordering, metastability and phase transitions in two-dimensional systems. *Journal of Physics C: Solid State Physics*, 6:1181, 1973.

[248] Daniel S. Fisher and P. C. Hohenberg. Dilute bose gas in two dimensions. *Physical Review B*, 37(10):4936–4943, 1988.

[249] D. S. Petrov, D. M. Gangardt, and G. V. Shlyapnikov. Low-dimensional trapped gases. 116:5–44, 2004.

[250] Nikolay Prokof'ev, Oliver Ruebenacker, and Boris Svistunov. Critical point of a weakly interacting two-dimensional bose gas. *Physical Review Letters*, 87 (27):270402, 2001.

[251] Nikolay Prokof'ev and Boris Svistunov. Two-dimensional weakly interacting bose gas in the fluctuation region. *Physical Review A*, 66(4):043608, 2002.

[252] D. J. Bishop and J. D. Reppy. Study of the superfluid transition in two-dimensional ^4he films. *Physical Review Letters*, 40(26):1727–1730, 1978.

[253] B. A. Huberman, R. J. Myerson, and S. Doniach. Dissipation near the Critical Point of a Two-Dimensional Superfluid. *Physical Review Letters*, 40(12):780–782, 1978.

[254] V. Ambegaokar, B. I. Halperin, D. R. Nelson, and E. D. Siggia. Dissipation in two-dimensional superfluids. *Physical Review Letters*, 40(12):783–786, 1978.

[255] D. J. Resnick, J. C. Garland, J. T. Boyd, S. Shoemaker, and R. S. Newrock. Kosterlitz-thouless transition in proximity-coupled superconducting arrays. *Physical Review Letters*, 47(21):1542–1545, 1981.

[256] T. J. Shaw, M. J. Ferrari, L. L. Sohn, D.-H. Lee, M. Tinkham, and John Clarke. Dynamic scaling of magnetic flux noise near the kosterlitz-thouless-berezinskii transition in overdamped josephson junction arrays. *Physical Review Letters*, 76(14):2551–2554, 1996.

[257] Ch. Leemann, Ph. Lerch, G. A. Racine, and P. Martinoli. Vortex dynamics and phase transitions in a two-dimensional array of josephson junctions. *Physical Review Letters*, 56(12):1291–1294, 1986.

[258] Z. Hadzibabic, P. Krüger, M. Cheneau, B. Battelier, and J. Dalibard. Berezinskii–Kosterlitz–Thouless crossover in a trapped atomic gas. *Nature*, 441(7097):1118–1121, 2006.

[259] Peter Krüger, Zoran Hadzibabic, and Jean Dalibard. Critical point of an interacting two-dimensional atomic bose gas. *Physical Review Letters*, 99(4): 040402, 2007.

[260] S. P. Rath, T. Yefsah, K. J. Günter, M. Cheneau, R. Desbuquois, M. Holzmann, W. Krauth, and J. Dalibard. Equilibrium state of a trapped two-dimensional Bose gas. *Physical Review A*, 82(1):013609, 2010.

[261] S. Tung, G. Lamporesi, D. Lobser, L. Xia, and E. A. Cornell. Observation of the Presuperfluid Regime in a Two-Dimensional Bose Gas. *Physical review letters*, 105(23):230408, 2010.

[262] M. Holzmann, M. Chevallier, and W. Krauth. Semiclassical theory of the quasi–two-dimensional trapped Bose gas. *EPL (Europhysics Letters)*, 82: 30001, 2008.

[263] R. N. Bisset and P. B. Blakie. Transition region properties of a trapped quasi-two-dimensional degenerate Bose gas. *Physical Review A*, 80(3):35602, 2009.

[264] P. W. Anderson. Considerations on the flow of superfluid helium. *Reviews of Modern Physics*, 38(2):298–310, 1966.

[265] G. Magnus. Ueber die Abweichung der Geschosse, und: Ueber eine auffallende Erscheinung bei rotirenden Körpern. *Annalen der Physik*, 164(1):1–29, 1853.

[266] P. W. Adams and W. I. Glaberson. Vortex dynamics in superfluid helium films. *Physical Review B*, 35(10):4633, 1987.

[267] C. J. Lobb. Private communication.

[268] G. Watanabe, F. Dalfovo, F. Piazza, L. P. Pitaevskii, and S. Stringari. Critical velocity of superfluid flow through single-barrier and periodic potentials. *Physical Review A*, 80(5):053602, 2009.

[269] T. D. Lee, Kerson Huang, and C. N. Yang. Eigenvalues and eigenfunctions of a bose system of hard spheres and its low-temperature properties. *Physical Review*, 106(6):1135–1145, 1957.

[270] E. Zaremba. Sound propagation in a cylindrical Bose-condensed gas. *Physical Review A*, 57(1):518–521, 1998.

[271] G. M. Kavoulakis and C. J. Pethick. Quasi-one-dimensional character of sound propagation in elongated Bose-Einstein condensed clouds. *Physical Review A*, 58(2):1563–1566, 1998.

[272] J. Wilks. *The Properties of Liquid and Solid Helium, Clarendon.* Oxford, 1967.

[273] F. Piazza, L. A. Collins, and A. Smerzi. Vortex-induced phase-slip dissipation in a toroidal Bose-Einstein condensate flowing through a barrier. *Physical Review A*, 80(2):21601, 2009.

[274] S. Levy, E. Lahoud, I. Shomroni, and J. Steinhauer. The ac and dc Josephson effects in a Bose–Einstein condensate. *Nature*, 449(7162):579–583, 2007.

[275] M. Albiez, R. Gati, J. Fölling, S. Hunsmann, M. Cristiani, and M. K. Oberthaler. Direct observation of tunneling and nonlinear self-trapping in a single bosonic josephson junction. *Physical Review Letters*, 95(1):10402, 2005.